INFORMATION TO USERS

This manuscript has been reproduced from the microfilm master. UMI films the text directly from the original or copy submitted. Thus, some thesis and dissertation copies are in typewriter face, while others may be from any type of computer printer.

The quality of this reproduction is dependent upon the quality of the copy submitted. Broken or indistinct print, colored or poor quality illustrations and photographs, print bleedthrough, substandard margins, and improper alignment can adversely affect reproduction.

In the unlikely event that the author did not send UMI a complete manuscript and there are missing pages, these will be noted. Also, if unauthorized copyright material had to be removed, a note will indicate the deletion.

Oversize materials (e.g., maps, drawings, charts) are reproduced by sectioning the original, beginning at the upper left-hand corner and continuing from left to right in equal sections with small overlaps. Each original is also photographed in one exposure and is included in reduced form at the back of the book.

Photographs included in the original manuscript have been reproduced xerographically in this copy. Higher quality 6" x 9" black and white photographic prints are available for any photographs or illustrations appearing in this copy for an additional charge. Contact UMI directly to order.

UMI

A Bell & Howell Information Company
300 North Zeeb Road, Ann Arbor MI 48106-1346 USA
313/761-4700 800/521-0600

Tropical Dynamics near the Stratopause: the Two-day Wave and Its Relatives

by

Varavut Limpasuvan

A dissertation submitted in partial fulfillment of
the requirements for the degree of

Doctor of Philosophy

University of Washington

1998

Approved by 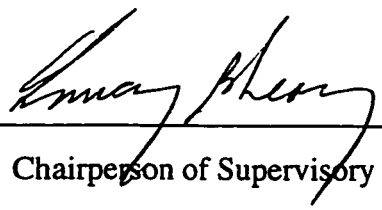

Chairperson of Supervisory Committee

Program Authorized
to Offer Degree ATMOSPHERIC SCIENCES

Date MAY 14, 1998

Doctoral Dissertation

In presenting this dissertation in partial fulfillment of the requirements for the Doctoral degree at the University of Washington, I agree that the Library shall make its copies freely available for inspection. I further agree that extensive copying of this dissertation is allowable only for scholarly purposes, consistent with "fair use" as prescribed in the U.S. Copyright Law. Requests for copying or reproduction of this dissertation may be referred to University Microfilms, 1490 Eisenhower Place, P.O. Box 975, Ann Arbor, MI 48106, to whom the author has granted "the right to reproduce and sell (a) copies of the manuscript in microform and/or (b) printed copies of the manuscript made from microform."

Signature 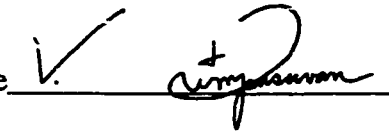

Date MAY 14, 1998

University of Washington

Abstract

Tropical Dynamics near the Stratopause: the Two-day Wave and Its Relatives

by Varavut Limpasuvan

Chairperson of the Supervisory Committee
Professor Conway B. Leovy
Department of Atmospheric Sciences

The two-day wave is observed in the Upper Atmosphere Research Satellite (UARS) Microwave Limb Sounder (MLS) temperature and water vapor data. During a 3-year period (Dec.1991-Sep.1994), the wave signature is prominent semiannually after each solstice and is comprised of a zonal wavenumber 3 component with ~2.0- day period and a wavenumber 4 component with ~1.8-day period. Intra-annually, the wavenumber 3 amplitude during the austral summer is nearly twice as strong as during the boreal summer. The wavenumber 4 component however can be equally strong in both summers. The wavenumber 3 signal tends to be dominant during the austral summer while the wave 4 component is dominant during the boreal summer. The derived zonal wind structure suggests that the Charney-Stern inflection instability mechanism is responsible for generating the two-day wave whose amplitude resides mainly on the equatorward flank of the summer easterly jet.

In some seasons, momentum redistribution by inertial instability appears to destabilize the easterly jet from which the barotropically unstable two-day wave grows. In these instances, an independent study using the UARS Cryogenic Limb Array Etalon Spectrometer (CLAES) temperature (Hayashi et al., 1998) coincidently identifies "pancake" structures associated with inertial instability. A possible connection between inertial instability and the two-day wave has been discussed by Hitchman (1985) and Orsolini et al. (1997).

The National Center for Atmospheric Research (NCAR) Community Climate Model version 2 (CCM2) mechanistic model is used to simulate this connection. Model experiments show that, for a prescribed initial wind condition with strong horizontal wind shear in the tropics, inertial instability can trigger the two-day wave. An increase in easterly wind curvature fostered by inertial instability circulation destabilizes the jet in low summer latitudes and allows first the growth of the wavenumber 4 then the wavenumber 3 component of the two-day wave. Near the stratopause, the two-day wave energy propagation is directed equatorward away from the wave's critical line source and westerly momentum is fluxed into the easterly jet core by the wave. While much of the wavenumber 4 activity is confined near the stratopause, the wavenumber 3 energy can propagate upward well into the mesosphere where strong Rayleigh damping is imposed. The simulated waves' spatial and spectral characteristics are fairly realistic.

TABLE OF CONTENTS

LIST OF FIGURES

LIST OF TABLES

ACKNOWLEDGEMENTS

I would like to express my deepest gratitude to Professor Conway Leovy for his support and guidance. Throughout my graduate school tenure, he has always shown great confidence in my ability and allowed me to explore different avenues of my research. The help of Dr. Byron Boville is greatly appreciated in the use of the NCAR CCM2 mechanistic model. The help of Dr. Pablo Canziani is also valuable in my understanding of the MLS data. I thank Professors James Holton and Dennis Hartmann for reading the initial manuscript and providing fruitful comments. I also thank Dr. Jeffrey Richey for serving as the Graduate School Representative and Drs. Joan Alexander, Yvan Orsolini, and Charles McLandress for showing continual interest in my research. Computing assistance from Marc Michelsen, David Warren, and Dr. Harry Edmon is also acknowledged. Finally, special thanks go to my wife, Lourdes, for her unconditional love and understanding.

DEDICATION

This thesis is dedicated to two men who I respect most: my father, *Yotin*, and my advisor, *Conway*. They always point me in the right directions.

CHAPTER 1

INTRODUCTION

Many interesting phenomena exist around the low latitude stratopause region. Mid-latitude quasi-stationary planetary (Rossby) waves are known to propagate meridionally into the region. Equatorially trapped Kelvin waves, originating from below, are also present. Upon nearing their critical surfaces, where their phase speed matches the zonal wind, these waves can break and irreversibly mix air constituents. The resulting mechanical damping along with thermal damping of the wave amplitudes can drive residual mean circulations that govern much of the vertical and latitudinal transport in the region. In addition, mean wind acceleration by Kelvin waves as well as mid-latitude Rossby waves and by the ubiquitous gravity waves are believed to be crucial in explaining the semiannual oscillation (SAO) circulation. Other dynamical features have also been identified in the low latitude stratopause region. In particular, two prominent planetary wave types have been observed. They are wave disturbances associated with inertial instability ("inertial waves") and quasi-two-day oscillations (collectively defined as the "two-day wave"). At the present time, details concerning these waves are unclear.

Inertially unstable features are observed in regions where the summer easterly winds intrude into the winter hemisphere (Hitchman et al., 1987; Fritts et al., 1992; Hayashi et al., 1998). Their appearance is intimately connected with mid-latitude quasi-stationary Rossby waves. As these waves propagate into the low winter latitudes, they tend to locally draw the easterlies across the equator and, in the process, initiate the instability by meridionally displacing air parcels. The resulting inertial instability produces vertically stacked patterns of anomaly extrema with vertical peak-to-peak scale of 5-14 km. These disturbances persist for about 7-14 days, and the associated circulation can mix tracers effectively (O'Sullivan and Hitchman, 1992; Orsolini et al., 1997).

The two-day wave is observed in the summer subtropical easterlies. The wave appears

regularly several weeks after the solstice and lasts for several weeks. Satellite observations show that it consists of westward propagating zonal wavenumber 3 and 4 components (Rodgers and Prata, 1981; Burks and Leovy, 1986; Wu et al., 1996). In some years, it is accompanied by a low frequency zonal wavenumber 1 disturbance. Given its large wind amplitudes and the possibility of wave breaking, the two-day wave can actively mix long-lived chemical constituents in the low latitude band during the austral summer (Plumb et al., 1987). Theories accounting for the two-day wave are still underdeveloped. The wavenumber 3 component can arise as a neutral normal mode amplified locally by the easterly zonal flow structure around the solstice (Salby, 1981c). The zonal wind structure can also promote modal instability of a wavenumber 3 disturbance (Plumb, 1983). The wavenumber 4 disturbance appears to be a manifestation of barotropic instability and does not correspond to a neutral normal mode.

The two-day wave and inertial wave may not be entirely independent of one another as first pointed out by Hitchman (1985). Inertial instabilities may foster favorable conditions in the easterly winds that allow instability growth of the two-day wave (Orsolini et al., 1997). Circulations associated with inertial instabilities tend to flux westerly momentum toward the summer hemisphere. In the process, the curvature of the mean wind can be significantly increased in the low latitude summer hemisphere, contributing to possible modal instability though the reversal of mean potential vorticity gradient.

In light of the discussed phenomena, this thesis focuses on the two-day wave. In the first part of the thesis, temperature and water vapor data from the Upper Atmosphere Research satellite (UARS) Microwave Limb Sounder (MLS) along with the United Kingdom Meteorological Office (UKMO) analyses are used to identify and record the wave appearance over a three year period. To resolve the wave's high frequencies in the satellite soundings, the asynoptic mapping method (Salby, 1982b) is employed. Wave structures and interannual and intra-annual features are elucidated in the observations. Relationships between the wave and the mean wind are examined. The final part of the thesis details a numerical study of the two-day wave. The study is performed using a mechanistic model

based on the National Center Atmospheric Research (NCAR) Community Climate Model (CCM) with relevant physical parameters kept to a minimum. The goal is to simulate the two-day wave and conduct sensitivity experiments to relate the wave behavior to both winter planetary forcing and zonal flow structure. Further understanding of the wave characteristics, propagation, and variability is facilitated by the latter study. Two pertinent questions regarding the two-day wave are addressed in this study:

- What mechanisms control the presence and structure of the two-day wave?
- Does a relationship exist between the inertial waves and the two-day wave? If so, what is their connection?

CHAPTER 2

BACKGROUND

This chapter reviews some of the observational and theoretical aspects of the two-day wave. The observational review is mainly restricted to those studies based on satellite measurements. The reader is referred to the Masters thesis of Burks (1986) for a background on earlier station observations. Proposed explanations for the two-day wave are presented. These explanations are based on theories of neutral normal modes, baroclinic-barotropic instability, and wave-wave interaction involving atmospheric tides. Model simulated two-day waves will also be discussed along with various phenomena appearing in conjunction with the waves, including inertial instability.

2.1 SATELLITE OBSERVATION OF THE TWO-DAY WAVE

Polar-orbiting satellites have been extremely useful in the global observation of the middle atmosphere. Planetary scale (zonal wavenumber 1-6) wave motions with period greater (slower) than 1 day can theoretically be resolved (Salby, 1982a). However, since the satellite is constantly in motion while scanning the atmosphere, aliasing problems in the observations must be carefully handled. Analytical techniques dealing with these problems are discussed in Chapter 3. Despite this limitation, satellite observations have been valuable in providing a clear picture of the two-day wave that is consistent with single station observations.

The earliest satellite observations of the two-day wave were reported by Rodgers and Prata (1981) using the brightness temperature field derived from radiance measurements of the Selective Chopper Radiometer (SCR) and Pressure Modulator Radiometer (PMR) aboard the Nimbus 5 and Nimbus 6 satellites, respectively. Time series of night-time and day-time measurements were Fourier analyzed and compared to determine the wave signal (this analytical technique is discussed in Chapter 3). Mainly data from Channel 2100

of the PMR was analyzed. The Channel's weighting function peaked around 62 km. For the SCR, the main data source came from Channel B12 whose weighting function maximized around 42 km. Hence, their study is confined between the upper stratosphere and lower mesosphere.

For July 1975, Rodgers and Prata's analysis of the PMR data identified the zonal wavenumber 3 component of the two-day wave with westward period around 2.0 days. Their analysis of the SCR data during January 1973 found similar wavenumber 3 signal but of smaller amplitude at lower altitude. The wavenumber 3 two-day wave structure had its largest amplitude in the tropical latitudes of the summer hemisphere. Figure 2.1 shows the amplitude-time evolution of this signal for 1973-1977 in both instruments. The amplitudes were computed from band-pass filtered data and averaged between latitudes 16°-32° of each hemisphere. Consistently, the wave signal peaks shortly after the solstice. Its amplitude is most pronounced in the southern hemisphere during the austral summer (January-February) and in the northern hemisphere during the boreal summer (July-August). The austral summer wave peak is consistently larger than the boreal summer peak. Interannual variability is also obvious for the boreal summer peaks.

Incidentally, Rodgers and Prata (1981) referred to the wavenumber 3 signal as the "two-day wave", and their study ultimately focused on this wavenumber 3 component. Their analysis of the PMR data for July 1975, however, also identified a wavenumber 4 peak with period near 1.7 days. As shown below, satellite observations following their study have indicated that a wavenumber 4 signal (with period near 2.0 days) consistently appears in conjunction with the wavenumber 3 signal at least near the stratopause. For this reason, the "two-day wave" definition used in this thesis will encompass both wavenumber components as mentioned in the Introduction.

The meridional structure of the temperature disturbance associated with the two-day wave was elucidated by Burks and Leovy (1986). They analyzed the 1979 austral summer temperature data derived from the Limb Infrared Monitor of the Stratosphere (LIMS) on

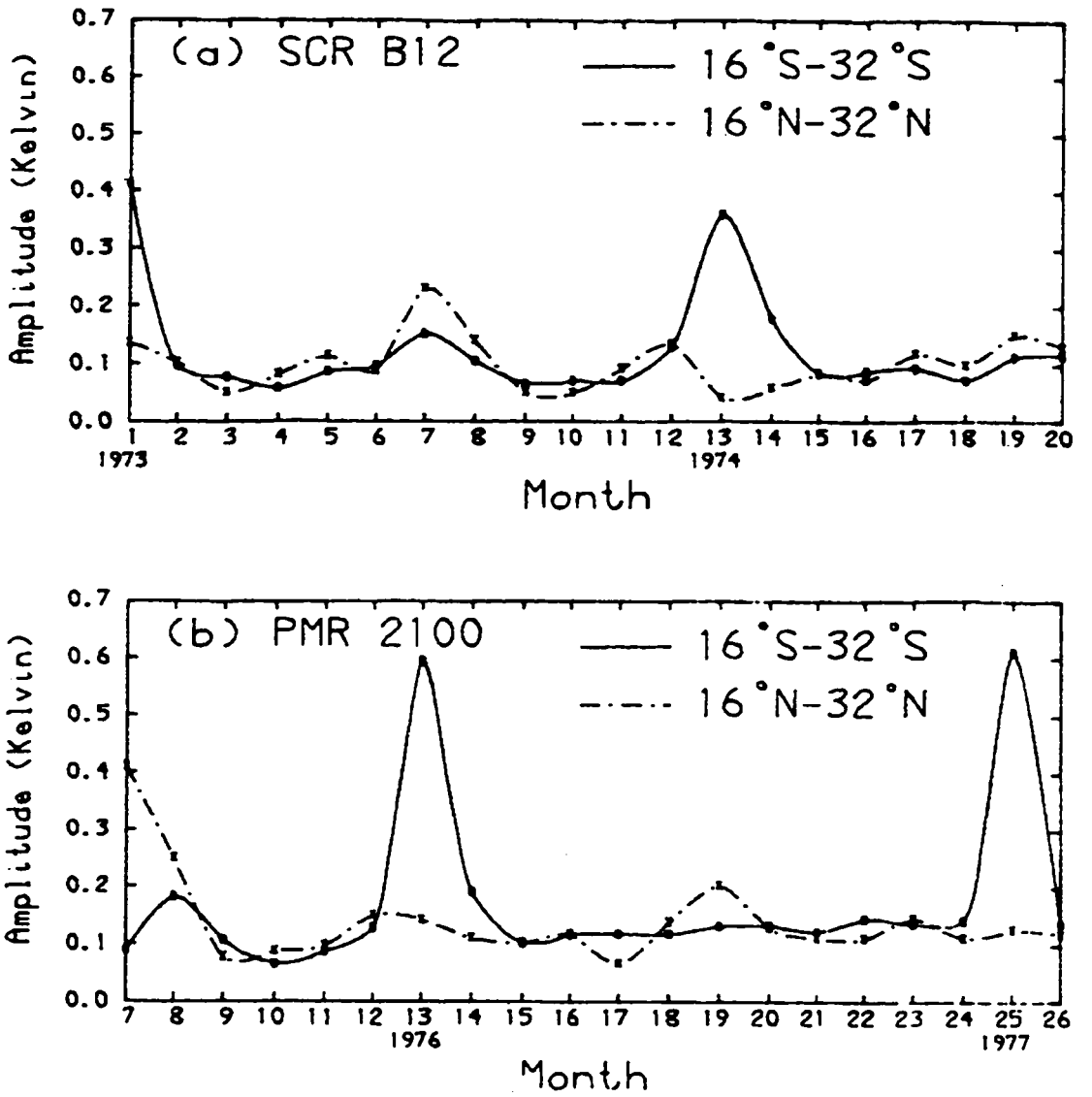

Figure 2.1: Variability of the brightness temperature two-day wave amplitude (wavenumber 3 component only) observed from the Nimbus satellites: (a) signal from the SCR instrument on Nimbus 5 near 42 km (~2.4 hPa) and (b) signal from the PMR instrument on Nimbus 6 near 62 km (~0.14 hPa). Signals are latitudinally averaged over the indicated band. [After Rodgers and Prata (1981).].

the Nimbus 7 satellite. The analytical method of Rodgers and Prata (1981) was used. This analysis identified both components of the two-day wave. The zonal wavenumber 3 and 4 signals had westward period of 2.08 (± 0.08) and 1.82 (± 0.06) days, respectively. Both components were prominent between 5 hPa (37 km) and 0.1 hPa (64 km).

The wavenumber 3 temperature structure generally slants poleward with height in the summer hemisphere (Figure 2.2a). Just below 1 hPa, the wave structure is confined near the summer subtropics. This structure broadens slightly with height and maximizes (at the amplitude of 1.3 K) near 0.7 hPa at 15°S. In these regions, the phase lines decrease slightly with height indicating a weak westward tilt. At higher altitude, a second maximum (amplitude of 1.3 K) resides in the mesosphere near 0.1 hPa and 30°S. The wave phase variation associated with the latter structure is quite uniform. Overall, the entire structure in the summer hemisphere resembles a "wedge" that is found to tilt with the equatorward shear zone of the summer easterly jet. A significant winter mesosphere signal (albeit weak) is seen in near quadrature with the summer signal.

The wavenumber 4 temperature structure exhibits a similar wedge-like characteristic (Figure 2.2b). Again, a poleward tilt with height is evident, and the entire structure follows the equatorward shear zone of the easterly jet. The amplitude increases with height and maximum amplitude (~2.6 K) is located at the top of the observed domain. Above 0.5 hPa, the wave tilts slightly westward with height. In other regions, phase variations are small. Overall, the structure is confined entirely in the summer hemisphere and is stronger than the wavenumber 3 structure particularly in the mesosphere.

Burks (1986) discussed details of the time evolution of the wave components presented in Burks and Leovy (1986). For the 1979 austral summer, the wave 4 component appeared as a pulse starting from early January and ending in early February. The wave 3 component pulse was also observed as the wave 4 component continued to grow. The latter pulse began in mid January and peaked around early February. The latitudinal extent of these components remained nearly fixed in the low summer latitudes throughout their

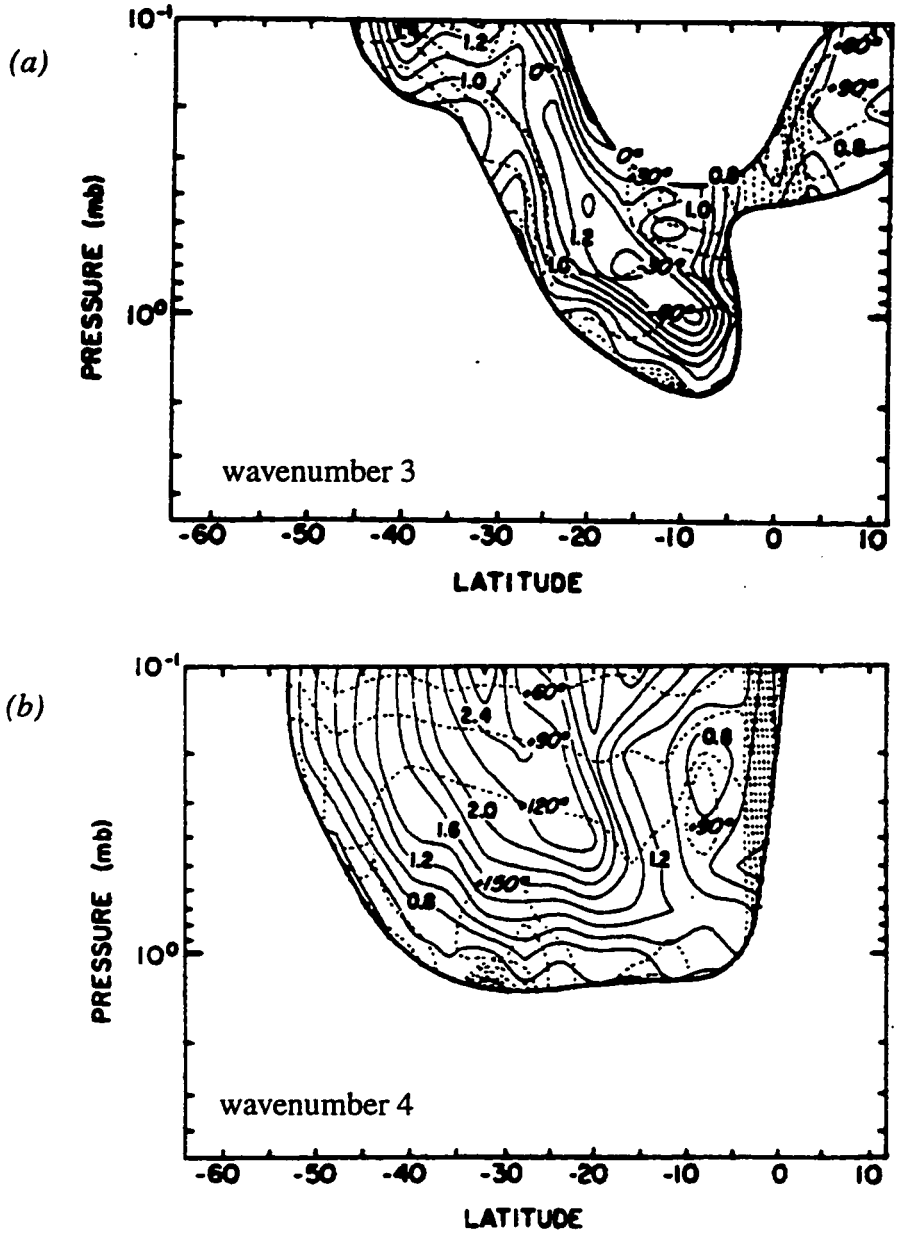

Figure 2.2: LIMS temperature two-day wave amplitude-phase structure during austral summer of 1978-79: (a) the zonal wavenumber 3 component; and (b) the zonal wavenumber 4 component. The amplitude is given by the solid contours in 0.1 K intervals for (a) and 0.2 K intervals for (b). The phase is shown as dashed contours in intervals of 30°. Only statistically significant regions are shown. [After Burks and Leovy (1986).].

duration.

Recent observational work of Wu et al. (1996) on the temperature two-day wave revealed the intra-annual variability of both two-day wave components. For data, they used a special version of the temperature field derived from the Microwave Limb Sounder (MLS) aboard the Upper Atmosphere Research Satellite (UARS). This special version contained data retrieved from 46 hPa up to 0.046 hPa (~21-70 km). The two-day wave was resolved using a least squares fitting technique of Wu et al. (1995). The study concentrated on the austral and boreal summer seasons of 1993. The computed wave spectrum for the period of January 10-30 showed a strong signature at wavenumber 3 and westward period of 2.00 days. A considerably weaker wavenumber 4 signature had a westward period of 1.89 days. The spectrum for the period of June 7-July 7 also revealed westward propagating peaks at wavenumber 3 and 4. The stronger wave 4 peak was located at 1.87 days while the wave 3 peak was at 2.08 days.

Latitude-time structures of the wavenumber 3 and 4 two-day wave amplitude during the 1993 austral summer are shown in Figure 2.3. The wave 4 two-day wave peaks first in the season around Christmas and at 0.46 hPa. This early appearance of wave 4 concurs with the two-day wave evolution examined by Burks (1986) during the 1979 austral summer. After the first wave 4 episode subsides, the wave 3 grows and then dominates the wave 4 component for the remainder of season. Generally, the peaks of both components are confined near 15°S at 0.464 hPa. At higher altitude, the peaks shift slightly poleward, so the meridional structures of these components appear similar to the ones observed by Burks and Leovy (1986). By mid-February, the two-day wave episodes have completely subsided.

About six months later, during the 1993 boreal summer, both components are again present as multiple pulses (Figure 2.4). The wave structure is now centered around 30°N at 0.46 hPa and shifts slightly poleward with height. In contrast to the austral summer, the wave 4 component is now dominant over much of the season. Comparison with Figure 2.3

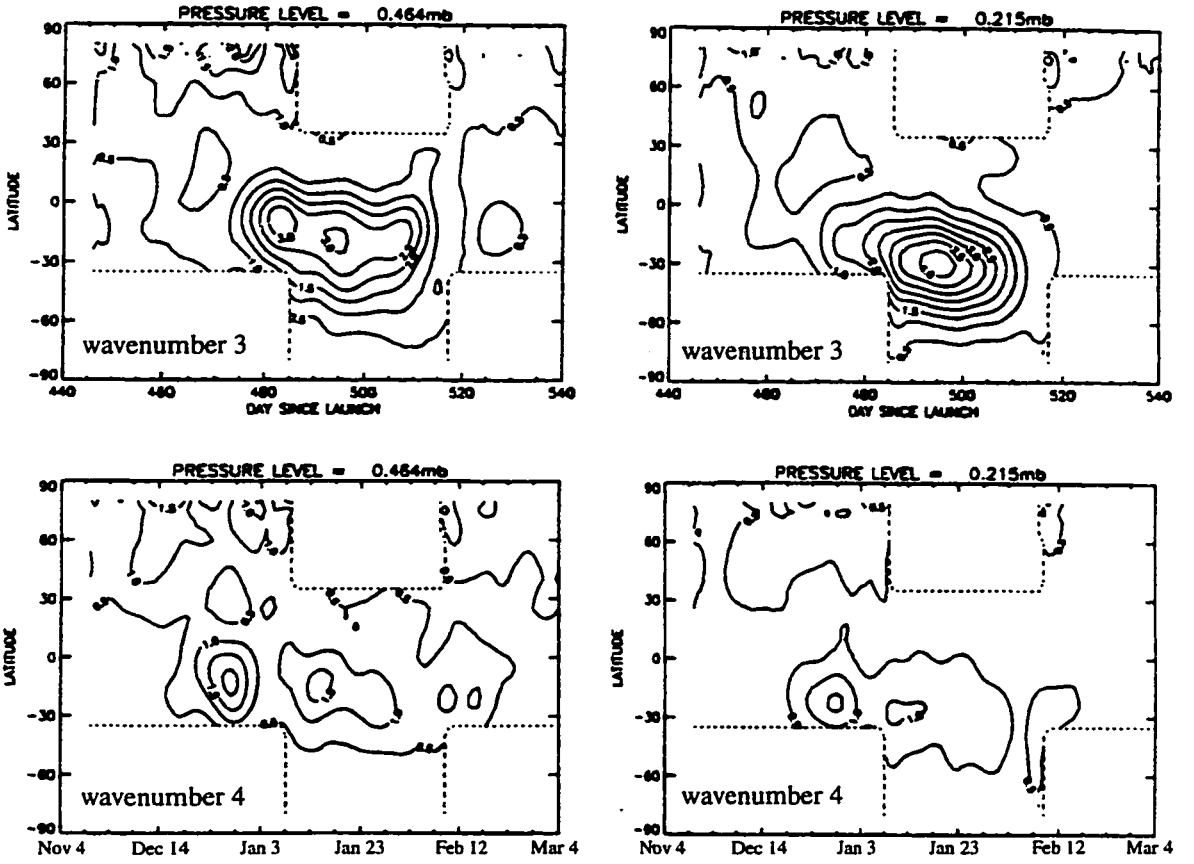

Figure 2.3: The MLS two-day wave temperature amplitude evolution at 0.464 hPa (~54 km) and 0.215 hPa (~59km) during 1992-93 austral summer. The top (bottom) panels show the evolution of the wavenumber 3 (4) component of the two-day wave. The contours are labeled every 0.5 K starting from 0.5 K. Dotted lines indicate the boundaries of the observations. [After Wu et al. (1996).].

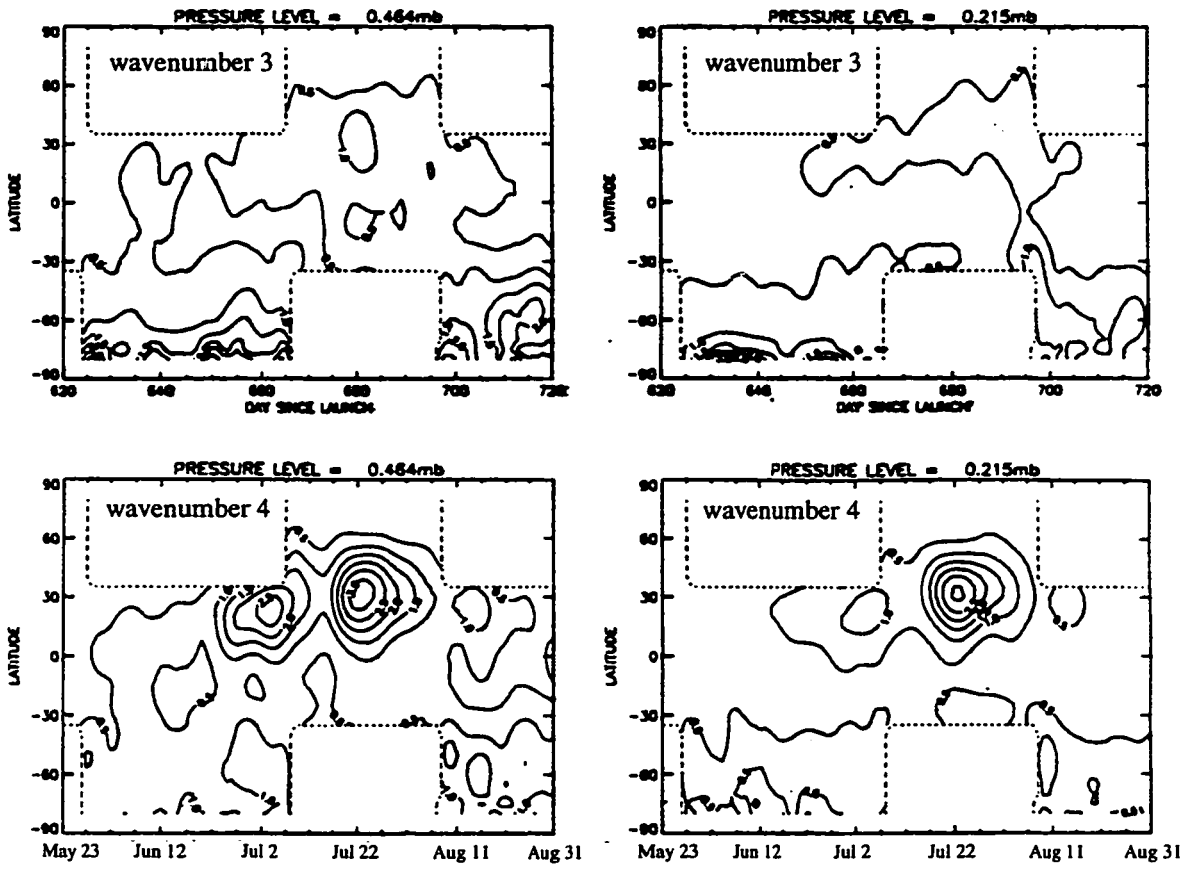

Figure 2.4: The MLS two-day wave temperature amplitude evolution at 0.464 hPa (~54 km) and 0.215 hPa (~59km) during 1993 boreal summer. The top (bottom) panels show the evolution of the wavenumber 3 (4) component of the two-day wave. The contours are labeled every 0.5 K starting from 0.5 K. Dotted lines indicate the boundaries of the observations. [After Wu et al. (1996).].

shows that the boreal wave 3 component is significantly weaker than its austral counterpart and the opposite is true for the wave 4 component. The intra-annual behavior of the wave 3 component agrees with the observation of Rodgers and Prata (1981). Again, the wave 4 component peaks earlier in the season (around July 4) than the wave 3 component.

The only known satellite analysis of winds associated with the two-day wave is that of Wu et al. (1993). They analyzed horizontal wind measurements from the High Resolution Doppler Imager (HRDI) aboard UARS using a least squares fitting technique of Wu et al. (1995). The data coverage was mainly in the upper mesosphere and lower thermosphere (between ~60-105 km). Only the zonal wavenumber 3 two-day wave was reported in their study.

The observed meridional structure of the horizontal wind is presented in Figure 2.5. The zonal wind amplitude has a node near the equator. The amplitude peak of about 30 ms^{-1} resides around 95 km in the low latitudes of both hemispheres. The phase lines are complicated, but, near the amplitude peak, they decrease with height, indicating a slight westward tilt. On the other hand, the meridional wind amplitude peaks near the equator. The maximum amplitude is about 65 ms^{-1} near 95 km. A secondary peak is evident at higher summer latitudes. The meridional wind phase lines indicate a westward tilt with height and the vertical wavelength tends to be shortest at the lowest latitudes.

In summary, these satellite observations have elucidated the following preliminary characteristics about the two-day wave. At least in the upper stratosphere and lower mesosphere region, both zonal wavenumber 3 and 4 components are present during the summer season. In the austral summer, the wave 3 component has a westward period of ~2.0 days. The wave 4 component has a slightly higher frequency with a period of ~1.7-1.89 days. During the boreal summer, the wave 3 component may propagate at slightly lower frequency. The intraannual differences in their amplitudes are evident. The wave 3 component tends to be stronger during the austral summer than the boreal summer. The wave 4 component is apparently stronger during the boreal summer. In a given summer season, it

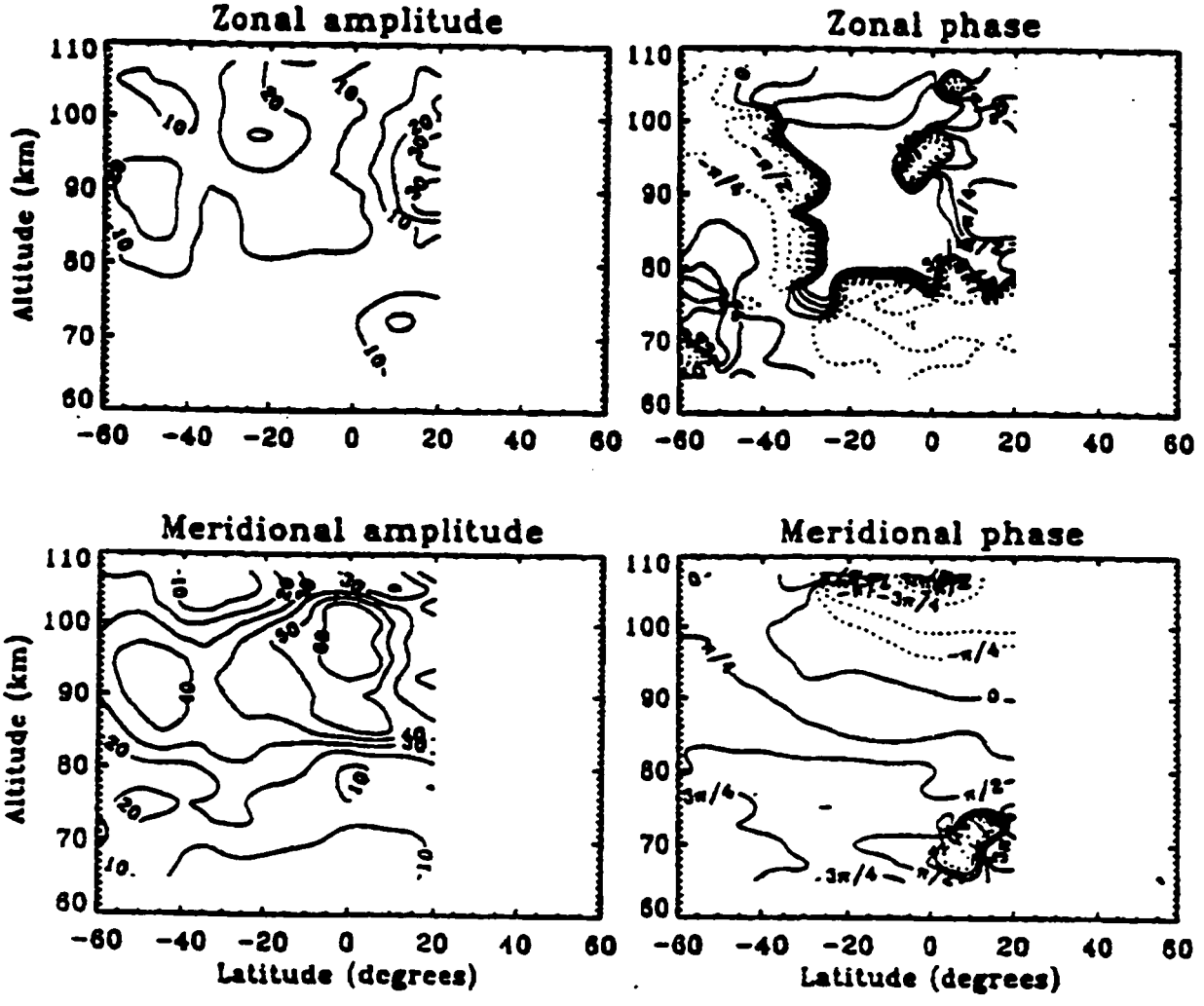

Figure 2.5: The HRDI wavenumber 3 two-day wave wind amplitude-phase meridional structure during January 24-31, 1993: zonal wind (top panels) and meridional wind (bottom panels). The contours are labeled every 10 ms^{-1} for amplitude and every π/4 for phases. [After Wu et al. (1993).].

is not entirely clear which component dominates the two-day wave evolution. However, the wave 4 component is seen to occur earlier in the season. The temperature structure of both components tilts poleward with height along the shear zone of the summer easterly jet. The wave 3 zonal wind structure appears to behave similarly. The wave 3 meridional wind structure, on the other hand, tends to focus over the equator.

2.2 PROPOSED EXPLANATIONS OF THE TWO-DAY WAVE

While the exact nature of the two-day wave is still uncertain, three theoretical explanations of its origin have been proposed. All seemingly can account for some of the observed wave characteristics. The first explanation describes a neutral normal mode and its amplification in the summer easterly jet. The second explanation relates instability wave growth to the unstable easterly jet. Observational studies discussed in the previous section usually cite one or both explanations to account for the observed two-day wave. A third explanation is based on nonlinear wave-wave interactions with atmospheric tides. These theoretical interpretations are briefly reviewed here.

2.2.1 THIRD ROSSBY-GRAVITY NORMAL MODE

Neutral normal modes are non-growing solutions to the linearized, adiabatic, and non-dissipative fluid dynamics equations. In the simplest case, the linearization is based on a motionless and isothermal basic state (Andrews et al., 1987). The solutions are obtained by separation of variables under the assumption that the lower boundary is flat and the wave solutions are evanescent (their energy density decays with height). The vertical part of the solution has no vertical phase tilt and grows vertically as $exp(\kappa z/H)$ where $\kappa \equiv (\gamma-1)/\gamma$. Here, γ is the ratio of specific heats, H is the scale height, and z is the log-pressure height. The horizontal part of the solution is solved from Laplace's tidal equation.

Given a temperature of the atmosphere, an equivalent depth (h) is computed from the relationship $h = (1-\kappa)^{-1}H$. Then, for each zonal wavenumber (s), the neutral normal modes

supported by this idealized atmosphere are discrete wave solutions with corresponding eigenfrequencies. These solutions are distinguished by their meridional index $n = s, s+1, \cdots$. By definition, the gravest mode (when $n = s$) is called the "Rossby-gravity mode". Zonal wavenumber 3 normal modes are shown in Figure 2.6 for different equivalent depths. The eigenfrequencies can be read from the intersection of the constant equivalent depth line and the various curves. The gravest zonal wavenumber 3 mode (n=s=3) is the third Rossby-gravity mode.

Assuming an isothermal atmospheric temperature of ~240 K (H = 7 km), the equivalent depth is then 10 km. From Figure 2.6, the westward propagating third Rossby-gravity mode (s=n=3) would have an eigenfrequency of 0.24, corresponding to a period of ~2.1 days. The zonal wind and geopotential fields associated with this mode exhibit nodes at the equator and maxima at low latitudes (Figure 2.7). The associated meridional wind field is considerably stronger with a maximum at the equator. From this simple theory, it is evident that the third Rossby-gravity mode in an idealized atmosphere shows remarkable similarity to the observed wavenumber 3 component of the two-day wave structure discussed in Section 2.1 (see Figure 2.5).

However, the neutral normal modes in a more realistic atmosphere (with height and latitude variation in wind and temperature fields) can differ from the idealized normal modes (Geisler and Dickinson, 1976; Salby, 1981abc; Hagan et al., 1993). The mode's spectral signature can be less sharp and peak at slightly different eigenfrequency due to wind variations. In this realistic case, the governing equations are non-separable, but one can still speak of the horizontal structure at each height and vertical structure at each latitude. While the horizontal structure of the neutral normal mode is largely insensitive to the background variation, its vertical structure can be altered from the simple Lamb structure of $exp(\kappa z/H)$ vertical growth and evanescence of the idealized case.

In particular, the normal mode's vertical growth is enhanced from the Lamb structure at levels where the zonal mean zonal wind ($\bar{u}$) is weakly eastward (i.e. westerly) with

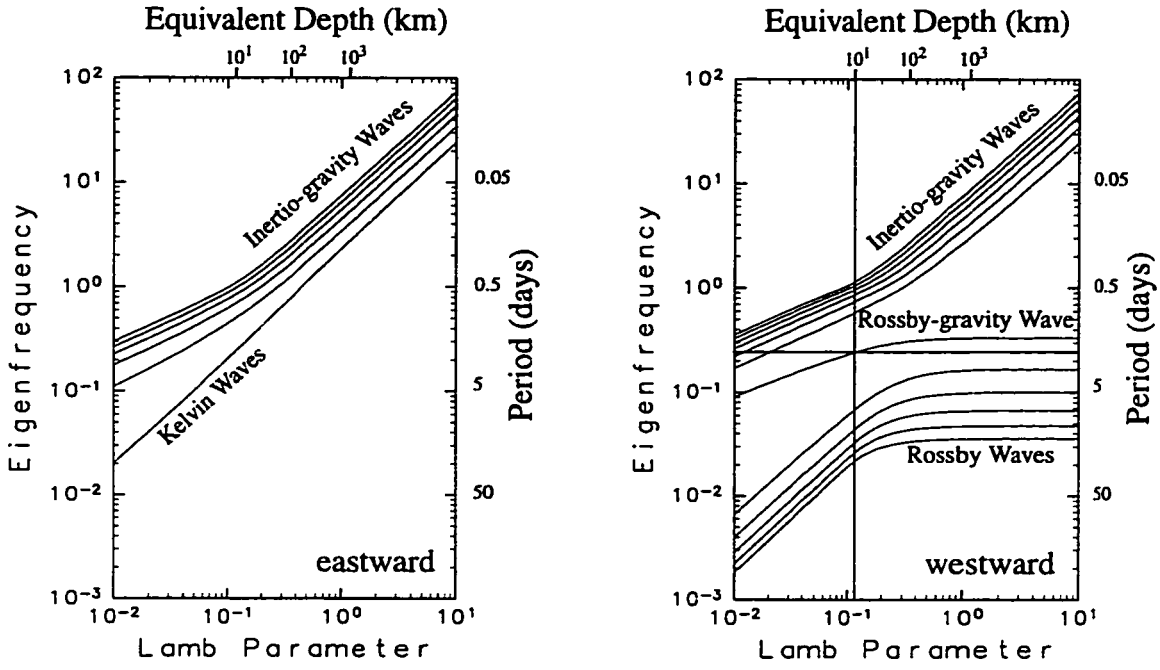

Figure 2.6: Plots of equivalent depth versus period for zonal wavenumber 3 neutral normal modes. The inverse of twice the eigenfrequency gives the mode period in days. The Lamb's parameter ($\gamma^{0.5}$) is related to the equivalent depth (h) through the relationship: $\gamma^{0.5}=(gh)^{0.5}/2\Omega a$, where g, Ω, and a are gravitational acceleration, Earth's rotational frequency, and Earth's radius, respectively. The lines where h=10km and period is 2.08 days are denoted in the right diagram. [Courtesy of T. Horinouchi.].

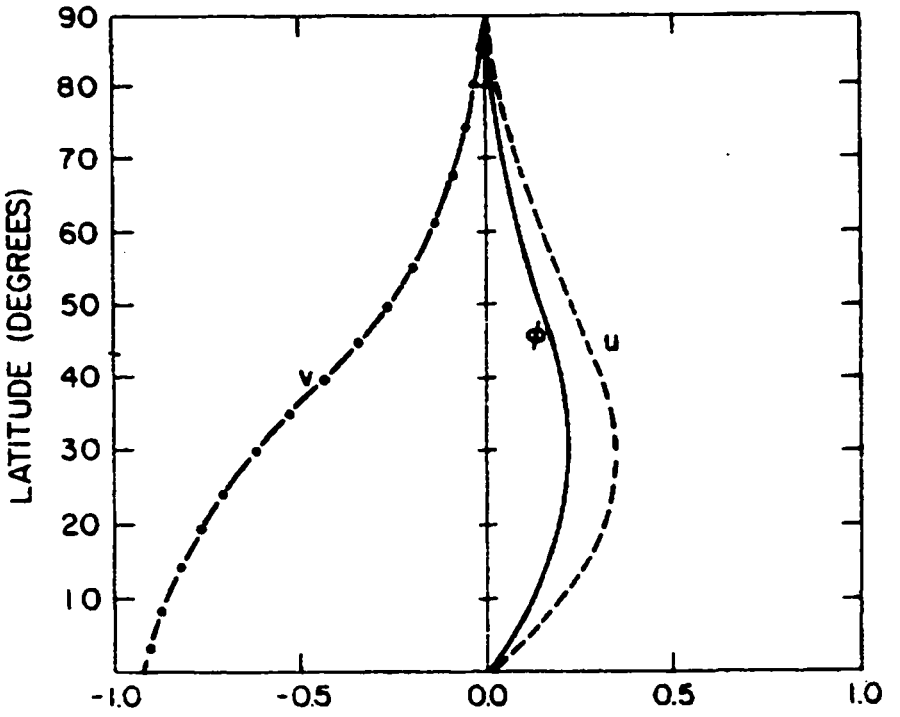

Figure 2.7: Meridional distribution of the geopotential (ϕ), zonal (u), and meridional velocity (v) fields associated with the third Rossby-gravity normal mode for windless, isothermal atmosphere. [After Salby (1981c).].

respect to the mode. The mode phase speed is Doppler shifted toward the zonal wind so that $\bar{u}$-c and the wave's intrinsic frequency are small. Where $\bar{u}$-c is small, the wave's evanescence is attenuated as a result of increased index of refraction. The wave's evanescence can be increased in regions where the zonal mean zonal wind is strongly westerly with respect to the mode ($\bar{u}$-c large). In regions of strong easterlies, the zonal wind can be Doppler shifted through zero. A linear absorbing critical surface (where $\bar{u}$=c) then exists, damping out the mode's amplitude. These effects are most obvious in the middle atmosphere (above ~15 km).

The third Rossby-gravity mode supported by a realistic atmosphere was investigated by Salby (1981c). For prescribed solstitial basic wind configurations (Figure 2.8b), the third Rossby-gravity solution has a period near 2.22 days. Considerable hemispheric asymmetry is present in the summer upper stratosphere and mesosphere (Figure 2.8c). The mode's geopotential height amplitude is enhanced in regions where the winds are weak westerly relative to the wave and intrinsic frequency and $\bar{u}$-c are small. The phase progression generally increases with altitude indicating an upward energy flux. Horizontally, the structure is antisymmetric about the equator as evidenced by the 180° phase jump. Near the critical surface, the amplitude is removed and the phase lines converge. The associated zonal wind and temperature mode structures show similar hemispheric asymmetry although the meridional wind has no apparent nodes near the equator (Figure 2.9). For the equinox condition, when westerly mesospheric jets are present in both hemispheres, the third Rossby-gravity mode's large amplitude above the stratopause is absent.

In the atmosphere, a steady forcing mechanism of a two-day period is not known. Without a steady forcing mechanism (as in the case of tides or quasi-stationary planetary waves), the recurrent temporal and spatial characteristics of the two-day wave are perhaps results of a preferred state of atmospheric oscillation, a normal (resonant) mode whose structure is amplified in the summer mesosphere. Neutral normal mode waves may be initially (and/or continually) excited by some forcing. Possible tropospheric forcing sources are latent heating, variations in the mean winds, and random processes (Andrews et al.,

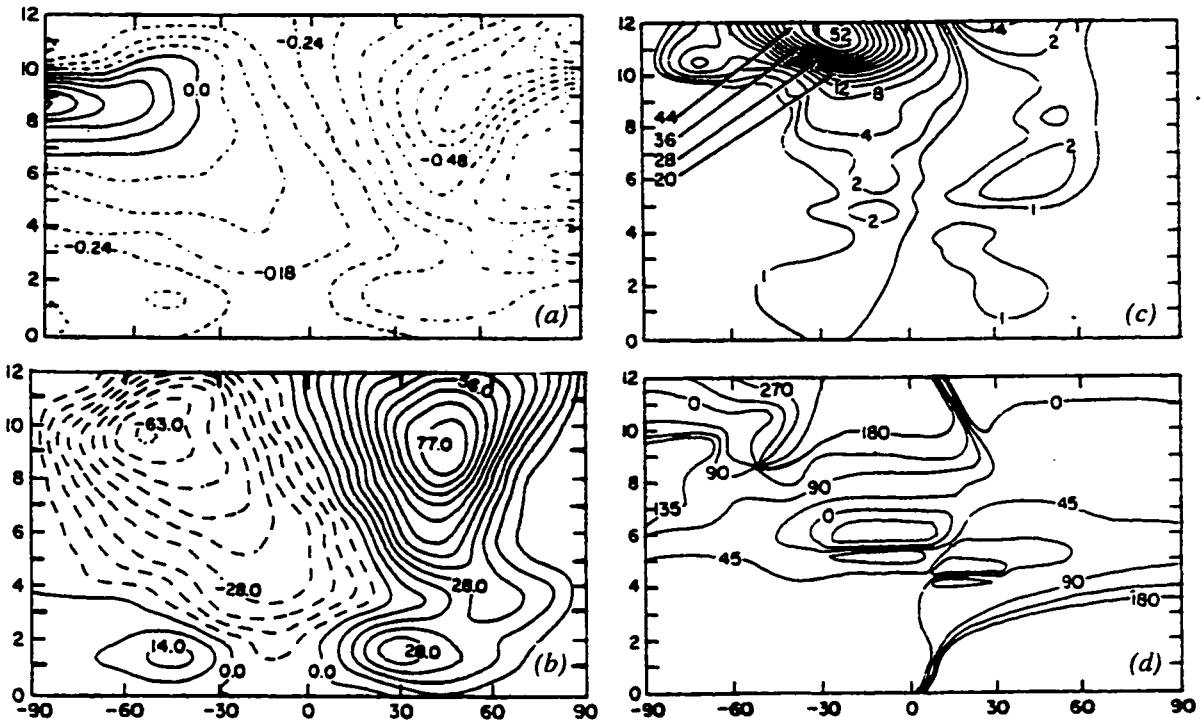

Figure 2.8: Meridional structure of the third Rossby-gravity mode in realistic solstice condition (austral summer). (a) The non-dimensionalized intrinsic frequency (negative regions indicate winds are westerly relative to the wave, positive regions indicate winds are easterly relative to the wave, and the critical surface is located at the zero contour); (b) zonal wind field in ms^{-1}; (c) the geopotential height amplitude structure; and (d) the corresponding phase in degrees of the third Rossby-gravity mode. [Adapted from Salby (1981c).].

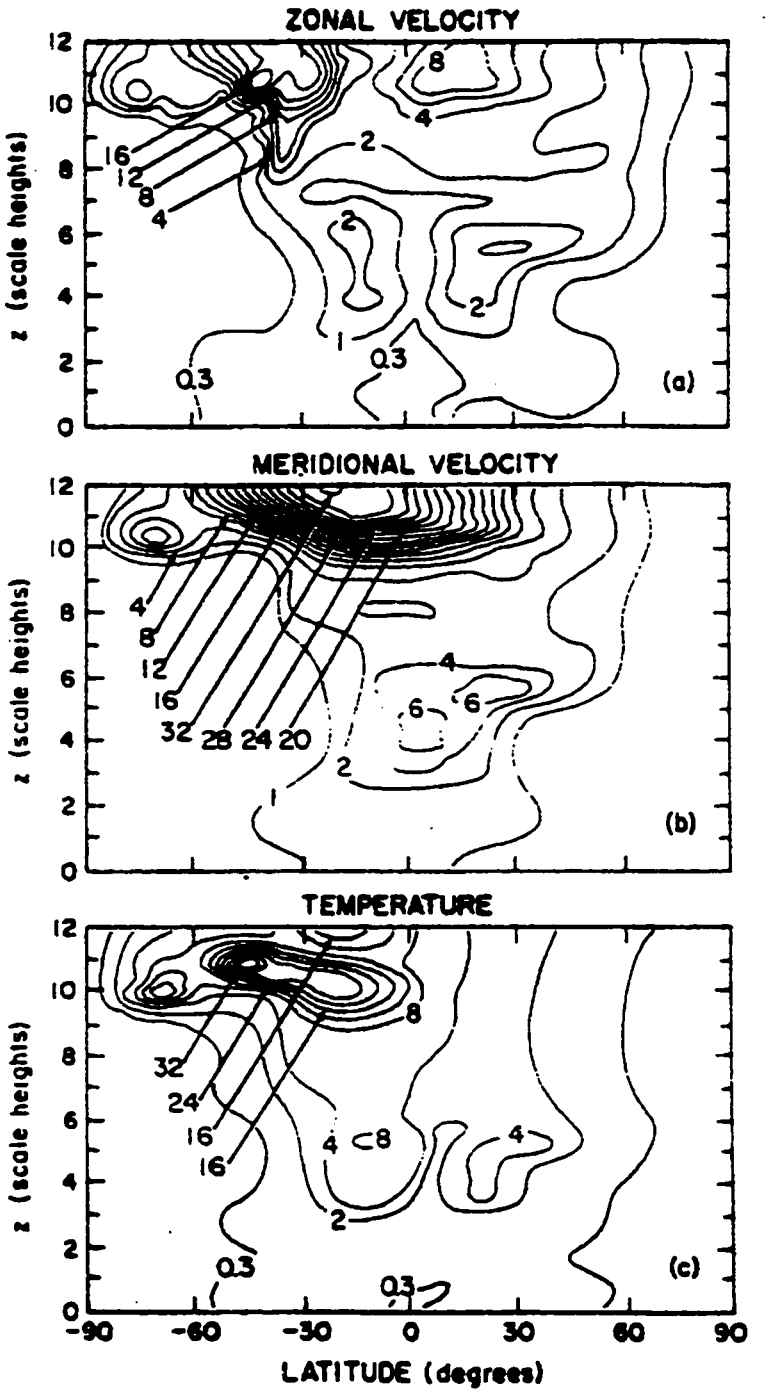

Figure 2.9: Meridional structure of the zonal wind (a), meridional wind (b), and temperature (c) associated with the third Rossby-gravity mode in realistic solstice condition shown in Figure 2.8b (austral summer). [After Salby (1981c).].

1987). They may also be excited in the middle atmosphere by local atmospheric instability and breaking planetary waves (Wu et al., 1996). In either case, the forcing needs to be rather strong because the two-day wave is observed to have rapid growth in a highly dissipative environment (due to strong radiative damping and, possibly, gravity wave mixing). Based on the third Rossby-gravity mode structure, an interpretation of the observed wavenumber 3 component of the two-day wave as a normal mode is a favorable one.

2.2.2 INSTABILITY GROWTH

Alternatively, the two-day wave has been rationalized to be a growing Rossby wave caused by internal mean flow instability. The summer easterly jet, where the two-day wave has been observed to reside, is known to be barotropically and baroclinically unstable depending on the horizontal or vertical curvature of the zonal wind (Pfister, 1985). In theory, these types of instability are mathematically similar and their necessary condition is that the meridional gradient of potential vorticity on an isentropic surface changes sign somewhere in the domain of interest (Charney and Stern, 1962; Andrews et al., 1987). Instability growth would seem to account for the observed growth of the two-day wave.

Instability waves grow by drawing energy (extracting enstrophy) from the mean flow. Barotropic instability is associated with the horizontal curvature of the mean flow and involves the redistribution of momentum by the growing wave activity. Internal baroclinic instability, on the other hand, is related to mean flow vertical curvature and/or vertical shear and mainly involves the wave redistribution of heat. In the early stage, instability growth from an infinitesimal perturbation is non-modal with arbitrary structures. The growth initially occurs in a linear fashion as the unstable amplitude is not too large. The instability eventually becomes modal (describable as a superposition of normal modes) during the late stages of the linear growth. A dominant wave mode will usually outgrow others and becomes readily observed. As the dominant wave mode amplitude continues to grow, it interacts with the mean flow and stabilizes the mean flow condition from which it grew. That is, the sign of the meridional gradient of potential vorticity becomes uniform

by the wave mixing. Eventually, the fastest growing mode ceases to grow and wave saturation is said to occur. Non-linear interactions among the waves are also possible.

In barotropic-baroclinic (inflection) instability, most vigorous wave vorticity flux occurs at the critical line where the phase speed of the fastest growing mode matches the background wind (Newman, 1991). At the critical line, the wave does not drift with respect to the ambient flow so it can effectively extract energy from the mean wind and grow at its expense. The growing wave activity appears to emanate from the critical line that exists in or near regions where the meridional gradient of potential vorticity changes sign. That is, the critical line acts like a wave source for the unstable wave case as opposed to a wave absorber (or reflector) for the linear stable wave case (Dickinson, 1973). The position of the critical layer gradually shifts with time as the mean flow is modified by the wave flux divergence and saturation is approached. Faster unstable ambient flow tends to produce unstable waves of higher frequency (Pedlosky, 1987). This is because a faster wave phase is needed to match the ambient flow in or near the region of reversed potential vorticity gradient to allow effective mean enstrophy extraction.

The mechanics of barotropic-baroclinic instability have been also interpreted in terms wave over-reflection (Lindzen and Tung, 1978; Tung, 1981;Lindzen and Barker, 1985). The concept of wave over-reflection is intimately related to the wave's critical layer and the meridional gradient reversal of potential vorticity. As a weak stable Rossby wave propagates (vertically or meridionally) towards its critical layer, if the critical layer acts as an over-reflecting surface, the return (over-reflected) wave energy will be greater than the incident wave. Given a reflecting boundary condition in the region of the incident wave, the over-reflected wave can be reflected back toward the critical surface. This scenario can lead to a self-maintained disturbance or an unstable growth that continually extracts mean flow energy near the critical layer.

For the critical layer to act as an over-reflector, certain conditions are usually necessary. The mean flow region beyond the critical layer must accommodate wave propaga-

tion. This is needed to allow wave activity flux through the critical layer (Lindzen and Barker, 1985). That is, "tunneling" across the critical layer must be allowed. The meridional gradient of potential vorticity must also change sign somewhere in the domain near or containing the critical layer. Specifically, for normal-mode instabilities (a subset of a more general set of wave instability structures), the wave over-reflected from the critical layer and the wave reflected from the boundary in the incident wave region must be appropriately in phase for constructive interference to occur. This so-called "quantization" requirement determines which of the normal modes of the over-reflected waves will actually lead to instability. Evidence of over-reflection can be seen as wave energy flux directed away from the critical layer.

The proposal of instability growth as a two-day wave mechanism was initiated by Plumb (1983) using a one dimensional baroclinic instability model. For a mesospheric westerly shear greater than 6 $ms^{-1}km^{-1}$, the fastest growing unstable mode in the presence of realistic radiative damping can have a horizontal scale of ~10,000 km and a westward phase velocity of 60 ms^{-1}. This corresponds to an instability wave of zonal wavenumber 3 with a period of 2 days at middle latitudes. Baroclinic wave growth may also occur at zonal wavenumber 4 with similar phase speed. The e-folding growth times for these modes are less than 8 days.

Pfister (1985) confirmed Plumb's study and allowed for latitudinal variations in the mean flow configuration in his baroclinic instability model. For his most realistic basic wind, the easterly jet core is centered at 65 km and 45° and tilts poleward with height. Characteristics of the most unstable modes under adiabatic conditions are summarized in Table 2.1. The wavenumber 3 geopotential amplitude peaks above and poleward of the jet core (Figure 2.10). The phase lines generally increase with height (westward tilt) near the amplitude peak, showing poleward heat flux by the wave. Downgradient momentum flux is also indicated by the phase lines near 50-60° latitude and 70-80 km which tend to reduce the latitudinal easterly shear and eliminate the jet core slope. The instability wave source is located where the wave's critical surface intersects the region of negative potential vor-

Table 2.1: Stability Analysis of Basic Wind Shown in Figure 2.10b

	zonal wavenumber	period (days)	e-folding growth time (days)
most unstable mode	3	2.15	4.1
second most unstable mode	4	1.66	5.5

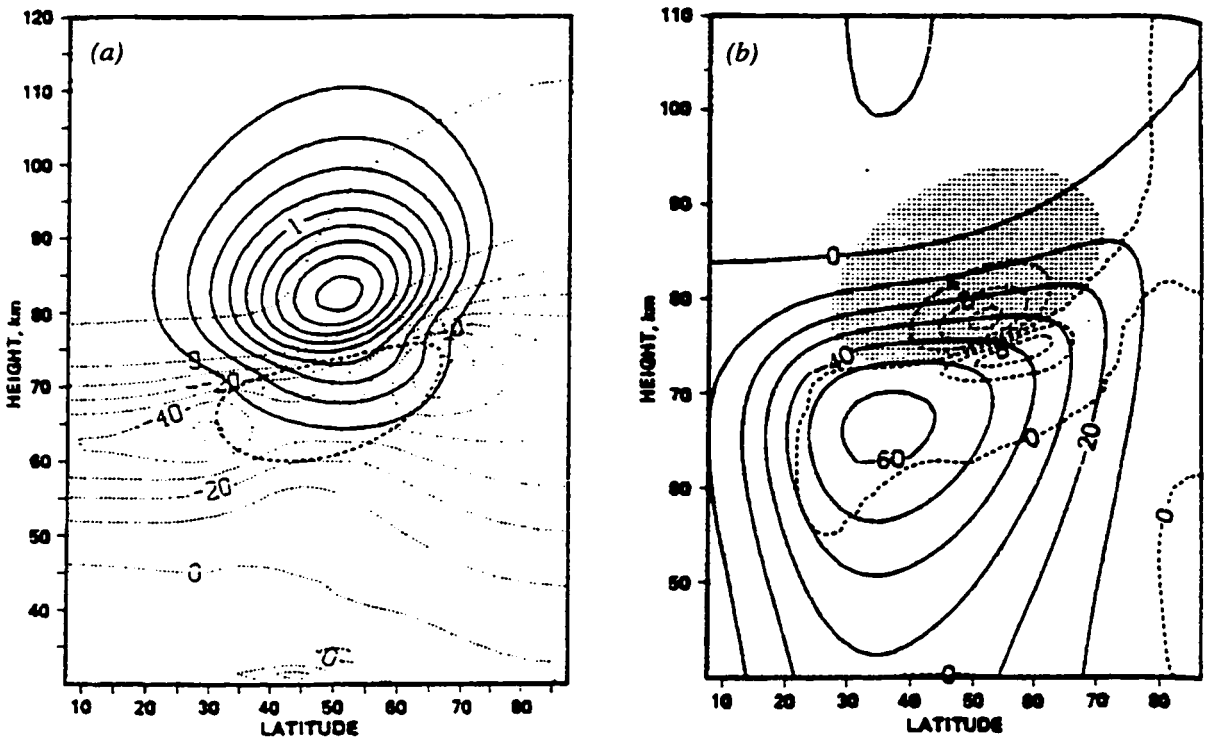

Figure 2.10: The most unstable mode structure for a realistic basic wind: zonal wavenumber 3 and westward propagating period of 2.15 day. (a) The amplitude (solid lines) and phase (dotted lines) structure; the dashed line shows the position of the critical surface. (b)The corresponding zonal mean zonal wind (solid lines) and divergence of the Eliassen-Palm (EP) flux per unit mass (dashed lines). The region of EP flux convergence is shaded while the region of EP divergence is not. [Adapted from Pfister (1985).].

ticity gradient. Above this region, convergence of the upward-equatorward pointing Eliassen-Palm flux vector is evident.

Pfister also conducted sensitivity studies on the above results. The inclusion of reasonable radiative damping through Newtonian cooling retards the unstable wave's e-folding growth rate by almost half (doubling the growth time) while the modal structure remains largely intact. Removal of the jet tilt decreases the growth rates as the tilting introduces horizontal wind shear that contributes barotropically to the overall flow instability. Finally, widening the horizontal width of the jet tends to shift the most unstable mode toward smaller zonal scale (i.e. zonal wavenumber 4) with lower period.

One dimensional barotropic instability study of the upper stratosphere summer easterly jet by Manney et al. (1988) likewise found fastest growing disturbances reminiscent of the two-day wave. Their study used zonal wind meridional profiles similar to that in summer upper stratosphere and mesosphere with regions of negative potential vorticity gradient. The most unstable modes were generally westward propagating, zonal wavenumber 3 and 4 disturbances with period ranging from 1.9-4.7 days. The periods were determined to depend mainly on the strength of the easterly jet. The unstable wave structure peaked between 10°-40° summer latitudes adjacent to the region of negative potential vorticity gradient. Secondary peaks often appeared on the equatorward side of the jet with amplitude spreading well into the winter hemisphere.

Although these instability studies examined mean wind structures with realistic features, the actual mean wind structure around the solstice is still poorly known. Unfortunately, the unstable mode structures are predicated upon details of the zonal mean wind. The wind shears govern the location of possible mean flow instability and hence the central location of wave activity. The wind strength determines the unstable mode frequency. This may explain why the theoretical unstable modes do not match the observed two-day wave structure very well. Nevertheless, these studies were able to demonstrate that the zonal scale and period of the unstable mode agree reasonably well with observation. The

recurrent nature of the phenomenon implies the ability of the atmosphere to reproduce similar easterly jet structure around the solstice.

Observation from LIMS suggested instability growth to be associated with the two-day wave (Burks and Leovy, 1986). The wavenumber 4 structure of the two-day wave was observed to be located on the equatorward side of the summer easterly jet where horizontal and vertical shears are greatest. In that same location, a large region of potential vorticity gradient reversal existed satisfying the necessary condition for barotropic-baroclinic instability (Charney and Stern, 1962). In addition, the critical layer of the wave was co-located with this unstable region, indicating possible generation of wave activity from the critical layer. No critical layer for the wavenumber 3 component was seen since the jet derived from the LIMS data was relatively weak. However, the observed wavenumber 3 structure suggested that an instability signature may be observed above the LIMS observational limits.

2.2.3 TIDAL INTERACTION

Cooperative efforts between various stations deduced the observed two-day oscillation signal between 80-110 km to have a zonal wavenumber 3 structure (Glass et al., 1975; Muller and Nelson, 1978). Apparently, in these altitudes, only the wavenumber 3 component of the two-day wave is observed. Interestingly, long-term partial-reflection radar observations have shown the unique nature of the two-day wave signal above 80 km in the austral summer. During onset of a large wave amplitude, the signal grows rapidly with nearly stabilized period of 48 hours and appears to be phase locked in local time (e.g. Harris and Vincent, 1993; Harris, 1994). That is, a given phase of the signal (e.g. the time of maximum northward wind) tends to occur at the same local time from cycle to cycle. While the discussed wave instability and neutral normal mode theories offer plausible explanation for the onset of the two-day wave, these mechanisms cannot account for the observed phase locking and period stability of the wave (Walterscheid and Vincent, 1996).

The phase-locked nature of the two-day wave strongly suggests a connection with diurnally varying phenomena. Walterscheid and Vincent (1996) proposed that the two-day wave is nonlinearly generated through a triad parametric resonance mechanism driven by tides. Conditions for parametric resonance (PR) are the same as the conditions for a resonant wave-wave interaction (Drazin and Reid, 1981). The triad consists of a primary wave and two secondary waves. The necessary conditions for PR instability from which the secondary waves grow from infinitesimal amplitudes are (for one dimensional case):

$$\sigma_1 + \sigma_2 = \sigma_0, \qquad k_1 + k_2 = k_0 \tag{2.1}$$

where σ is the wave frequency (in cycles per day), k is the zonal wavenumber, and the subscripts (1, 2) and (0) denote the two secondary waves and one primary wave, respectively. A degenerate subclass of PR instability is called the self-excited instability where:

$$\sigma_1 = \sigma_2 = \frac{1}{2}\sigma_0, \qquad k_1 = k_2 = \frac{1}{2}k_0 \tag{2.2}$$

Theoretically, the wavenumber 3 two-day wave can be involved with zonally symmetric, nonmigrating (not Sun-synchronous) diurnal tide and a zonal wavenumber 3 westward propagating wave with 16-hour period (1.5 cpd) through PR instability. Indeed, Harris and Vincent (1993) have reported observations of a 16-hour oscillating signal with maximum amplitude of ~20 ms^{-1} in connection with the two-day wave. In the low-latitude middle atmosphere, significant signatures of zonally symmetric diurnal tide have also been observed (e.g. Lieberman, 1991). Alternatively, it is possible for the two-day wave to be self-excited with a nonmigrating diurnal tide with zonal wavenumber 6. This particular tidal mode propagates zonally at the same phase speed as the two-day wave but has not been seen in past observations.

Other types of nonlinear interactions between the two-day wave and diurnal tides may also be possible. In the mesosphere and lower thermosphere, model simulations and

observations of zonal wavenumber 1, migrating diurnal tide have shown semiannual amplitude variation characterized by equinoctial maxima and solstitial minima (e.g. Vincent et al., 1988; McLandress et al. 1996; McLandress, 1997). General circulation model simulations of Norton and Thuburn (1997) show occurrences of large two-day wave amplitude during the solstice when diurnal tide is weak, suggesting that interactions between these waves may be responsible for weak tidal amplitudes. However, using the Canadian middle atmosphere general circulation model, McLandress (1997) does not observe the two-day wave but the semiannual variability of the diurnal tidal amplitude is nonetheless evident in the model.

2.3 TWO-DAY WAVE IN MODELS AND INERTIAL INSTABILITY

Features similar to the two-day waves have been observed in general circulation models (Hunt, 1981ab; Norton and Thuburn, 1997) and global models which had assimilated real observations (Randel, 1994; Orsolini et al., 1997). Evidence from these models has provided additional insights into the nature of the wave.

Hunt (1981a) first reported a serendipitous finding of a wave disturbance identifiable with the wavenumber 3 component of the two-day wave in the middle and low latitudes of the summer mesosphere. His global circulation model was set up for perpetual January conditions, retaining only 15 zonal wavenumbers and 40 meridional points from pole-to-pole. Evidence of two-day wave amplitude was suggested by a signature extending from 65 km and up to 100 km, the model top. The structure of the simulated two-day wave pointed to baroclinic instability as a possible source of the wave. Synoptic maps of the meridional wind showed a westward tilt with height indicative of a limited region of baroclinic instability in the summer mesospheric jet.

Hunt's model also indicated that the simulated two-day wave component was strongly coupled to tropical fluctuations. Six hourly synoptic maps of the meridional wind at 90 km (given in Figure 2.11) showed the pulsation between the mid summer latitude two-day

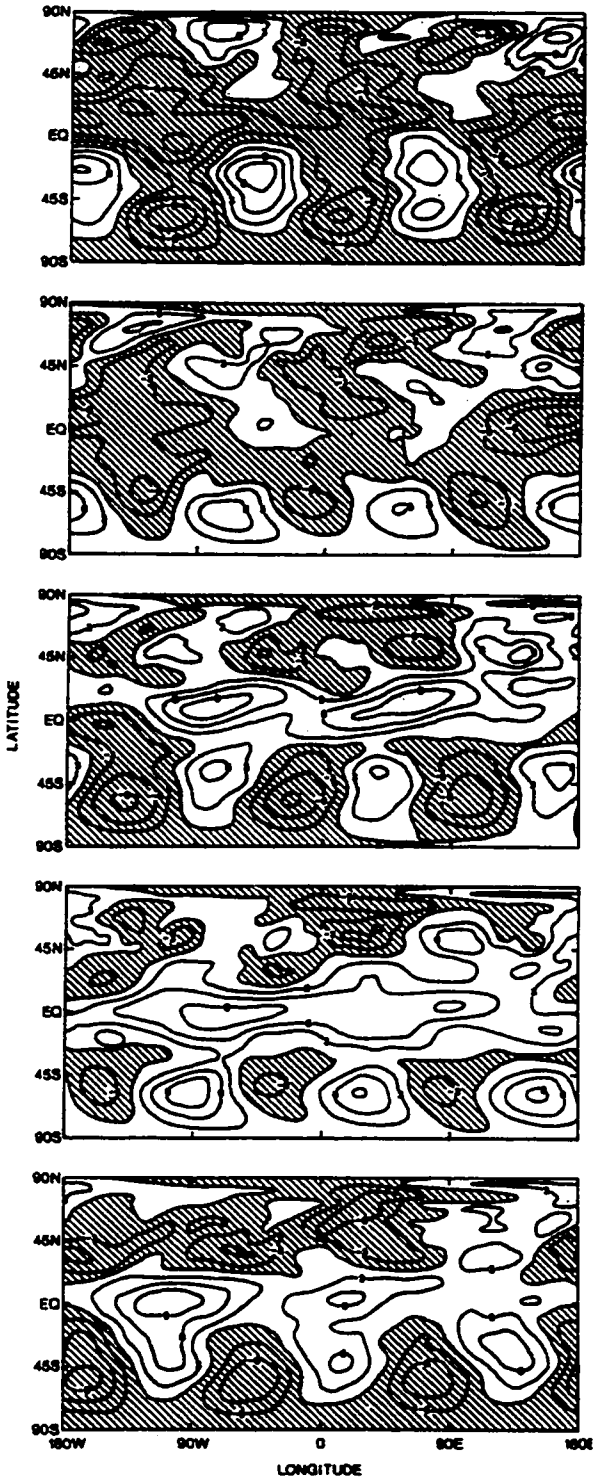

Figure 2.11: Six hours synoptic maps of the meridional wind (ms^{-1}) at 90 km. The contour interval is 3 ms^{-1}. Northerly winds are hatched. Time increases from top to bottom. [After Hunt (1981a).].

wave and the tropical systems. The southerly wind began to encroach the tropical areas during the first 12 hours. Eventually, southerly wind dominated the entire equatorial region and combined with the propagating two-day signal in the summer hemisphere during the last 12 hours. This coupling to the tropical fluctuation by the two-day wave was not well understood in the model. It may illustrate the neutral normal mode nature of the two-day wave in the upper mesosphere as suggested by Hunt. The presence of the wave critical surface (where the wave zonal phase speed is Doppler-shifted to zero by the mean wind) in the low summer latitudes may cause the amplification and extension of the third Rossby-gravity mode into the winter hemisphere (see Figure 2.9b).

At lower altitudes (30-78km), pronounced equatorial structures were also observed. They were believed to be signatures of strong inertial instability produced in the model run (Hunt, 1981b). The instability resulted from intense meridional mean wind shear that reversed the usual gradient of the angular momentum in the equatorial regions. The mean structures associated with the instability appeared as vertically stacked cells with vertical scale of twice the model resolution (~5 km). The synoptic features of inertial instability were observed to appear in close latitude proximity to the two-day wave in the lower mesosphere similar to the relationship between the tropical wind variability and the two-day wave as shown in Figure 2.11.

In general, inertial instability is a parcel instability due to an imbalance between pressure gradient force and centrifugal force. From a zonally symmetric point of view, the instability is expected to occur in regions of strong mean wind shear where the local Coriolis parameter is exceeded. This condition can be expressed as $f(f\text{-}a^{-1}\overline{u}_{\varphi}) < 0$, where f, a, and $\overline{u}_{\varphi}$ are Coriolis parameter, Earth's radius, and the partial change in mean zonal wind with respect to latitude, respectively. When this condition is met, the meridional gradient of the absolute angular momentum increases toward the pole. In the atmosphere, this condition is observed in the equatorial upper stratosphere and lower mesosphere during the winter season. The strong equatorial wind shear is promoted by cross equatorial advection of summer easterlies by mean circulation. Mean meridional motion imposed on the air

parcel in this region can release the instability by accelerating the parcel. The resulting disturbance appears as a zonally symmetric stacked structure with alternating anomalies (see Figure 2.12). The structure's latitudinal extent is bounded by the equator and the latitude where $f = a^{-1}\bar{u}_{\varphi}$. The momentum redistribution by the overturning circulation transports westerly momentum meridionally toward the equator (Dunkerton, 1981; Andrews et al., 1987) and reduces the equatorial wind shear.

As observed by Hitchman et al. (1987) and Hayashi et al. (1998), inertial instability in the atmosphere tends to be zonally asymmetric. Nonetheless, the instability features occur in regions of strong equatorial wind shear. Winter planetary waves propagating barotropically toward the equator interact strongly with the strong wind shear. In the process, they tend to locally draw easterlies across the equator. Air parcels are thus displaced meridionally and inertially accelerated along the meridional phase tilt of the encroaching planetary waves. To diagnose the localized parcel acceleration, a generalized inertial instability criterion is suggested by O'Sullivan and Hitchman (1992) and Hayashi et al. (1998) to be $f(f+\zeta) < 0$, where ζ is the relative vorticity. In isentropic coordinates, this condition simply states that the instability is expected to occur in region of anomalous Ertel's potential vorticity (P) which is written as $P = -g(f+\zeta)\theta_p$, where g and θ_p are gravity and the partial change of potential temperature with respect to pressure, respectively (Hoskins et al., 1985). Here, anomalous P refers to values with the opposite sign than expected values in each hemisphere (i.e. negative (positive) in the northern (southern) hemisphere). Thus, the associated overturning cells and structures appear localized and are embedded in the vertically deep regions of anomalous P (see Figure 2.13). The momentum redistribution by the cells will also transport westerly momentum equatorward.

A possible connection between the two-day wave and inertial instability in the upper stratosphere and lower mesosphere was recently explored by Orsolini et al. (1997). They used the United Kingdom Meteorological Office (UKMO) assimilated data and an off-line transport model to examine these phenomena. Possible features associated with inertial instability were observed as overturning cells with high zonal wavenumber (10-12). These

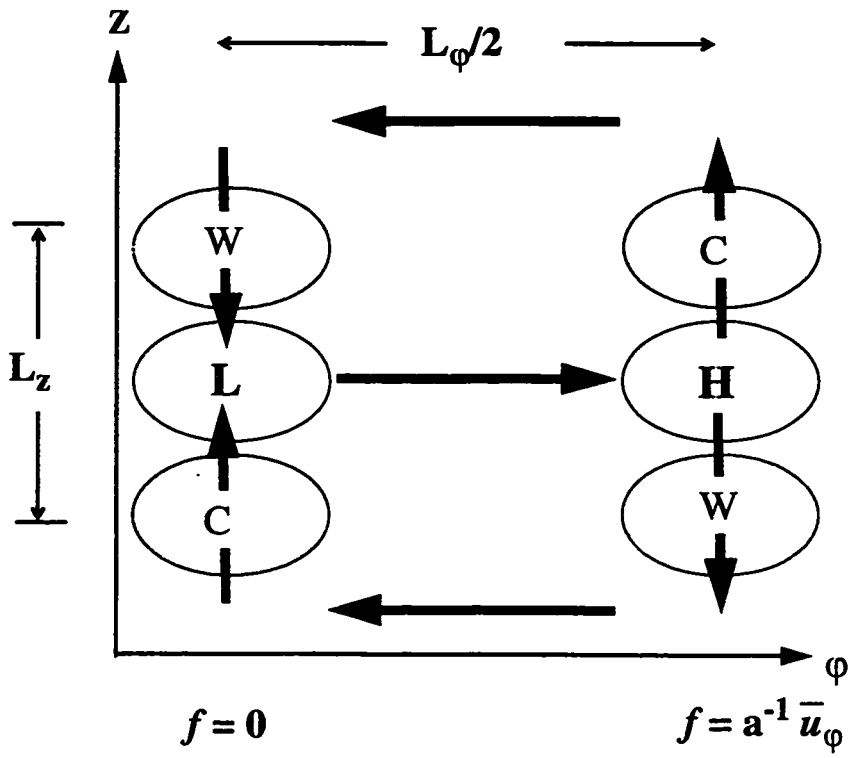

Figure 2.12: Schematic of zonally symmetric inertial circulation in the meridional plane. The arrows show the flow induced by inertial instability. The letter W (C) denotes warm (cold) temperature anomalies, and H(L) indicates high (low) geopotential height anomalies. The letter L_z (L_φ) represents the structure's vertical (meridional) scale.

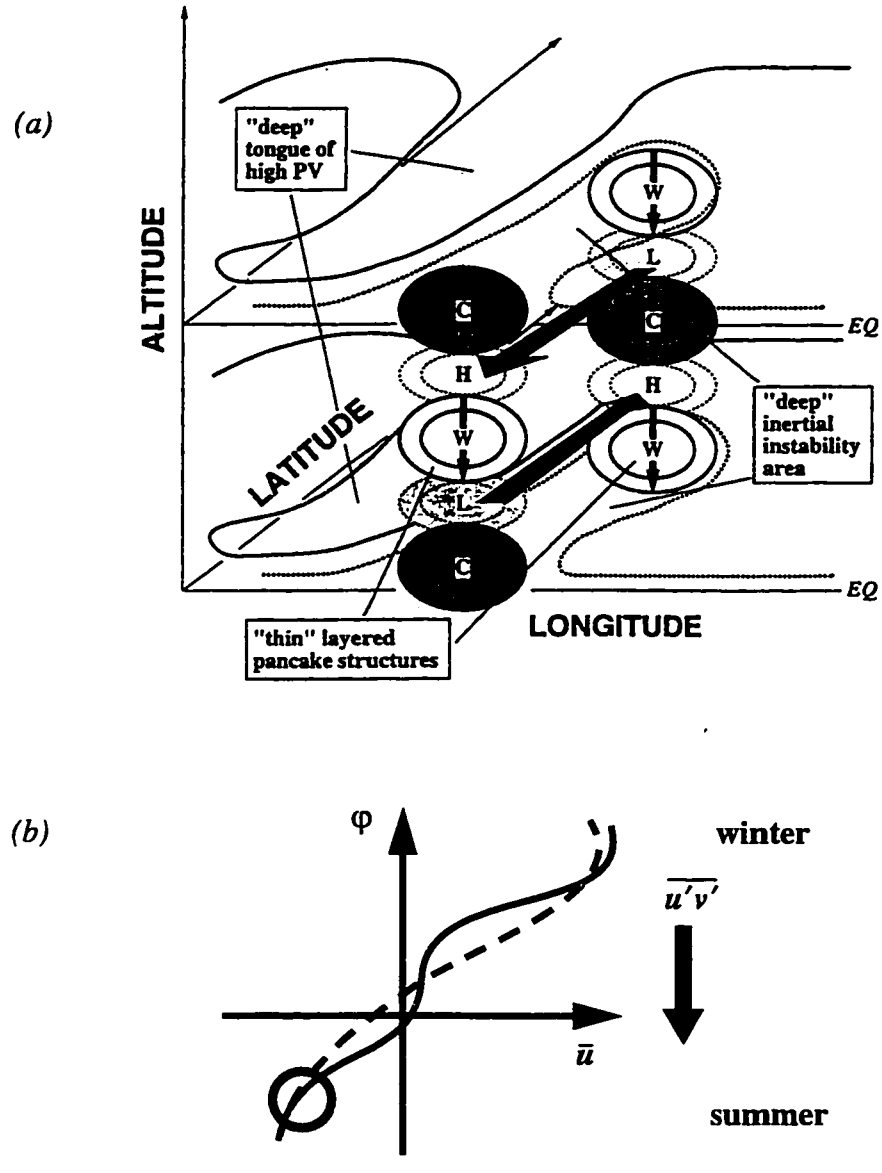

Figure 2.13: (a) Relationship between inertial structure and winter planetary wave in the northern hemisphere. Solid contours indicate the high ("normal") P tongue due to planetary wave breaking. The dotted contours show the negative ("anomalous") P tongue that confines the inertial instability region. The symbols and arrows are identical to Figure 2.12. [Taken from Hayashi et al. (1998).]. (b)Schematic effects of inertial activity on the mean wind. Dashed (solid) profile is mean zonal wind at time before (after) inertial activity. Thick arrow indicates the direction of zonal momentum flux. The circle highlights the region where the positive curvature of the profile is increased in the summer hemisphere.

cells ("inertial eddies") appeared on the westward flank of a wide tongue of dry air drawn away from the tropics into the winter hemisphere (shown by the low water vapor mixing ratio in the 225°-275°E longitudinal band of Figure 2.14). The winter planetary wave activity was responsible for this northward advection of dry air. A clear wavenumber 3 two-day signature was evident in the low summer latitude and confirmed by spectral analysis. Barotropic instability appeared to be the main source of the two-day wave generation.

Although not conclusive, their study suggested that the inertial eddies and two-day wave may be intimately connected. Momentum redistribution associated with the inertial cells has been suggested to alter the curvature of the mean flow and contribute to the barotropic destabilization of the summer easterlies (Hitchman, 1985). In eliminating the strong meridional wind shear over the equatorial region (hence removing inertial instability), these eddies tend to transport westerly momentum toward the easterlies (see Figure 2.13b). Consequently, the meridional curvature of the low latitude summer easterlies is increased as the easterlies are being accelerated and the westerlies decelerated. Barotropically unstable regions can occur in association with the increased curvature. Unstable disturbances with a two-day wave characteristic may appear as discussed in Section 2.2.2. Latitude-time plots of inertial wave variance at 1hPa (see figure 3 of Orsolini et al., 1997) showed considerable inertial wave activity to consistently appear prior to each two-day wave peak. The inertial circulations in the tropics may serve as a link between the winter planetary wave activity and the summer hemisphere disturbances. Planetary wave amplification governs the activation of inertial instabilities which then create regions of strong wind curvature in the summer subtropics, a condition favorable for the generation of the 2-day wave.

A direct connection between the two-day wave and the winter planetary wave may be present in observed data. Wu et al. (1996) reported precursor two-day wave signals in the high latitude winter upper stratosphere spreading across the equator prior to the peaking of the two-day wave in the lower summer mesosphere (see Figure 2.3 and Figure 2.4). They

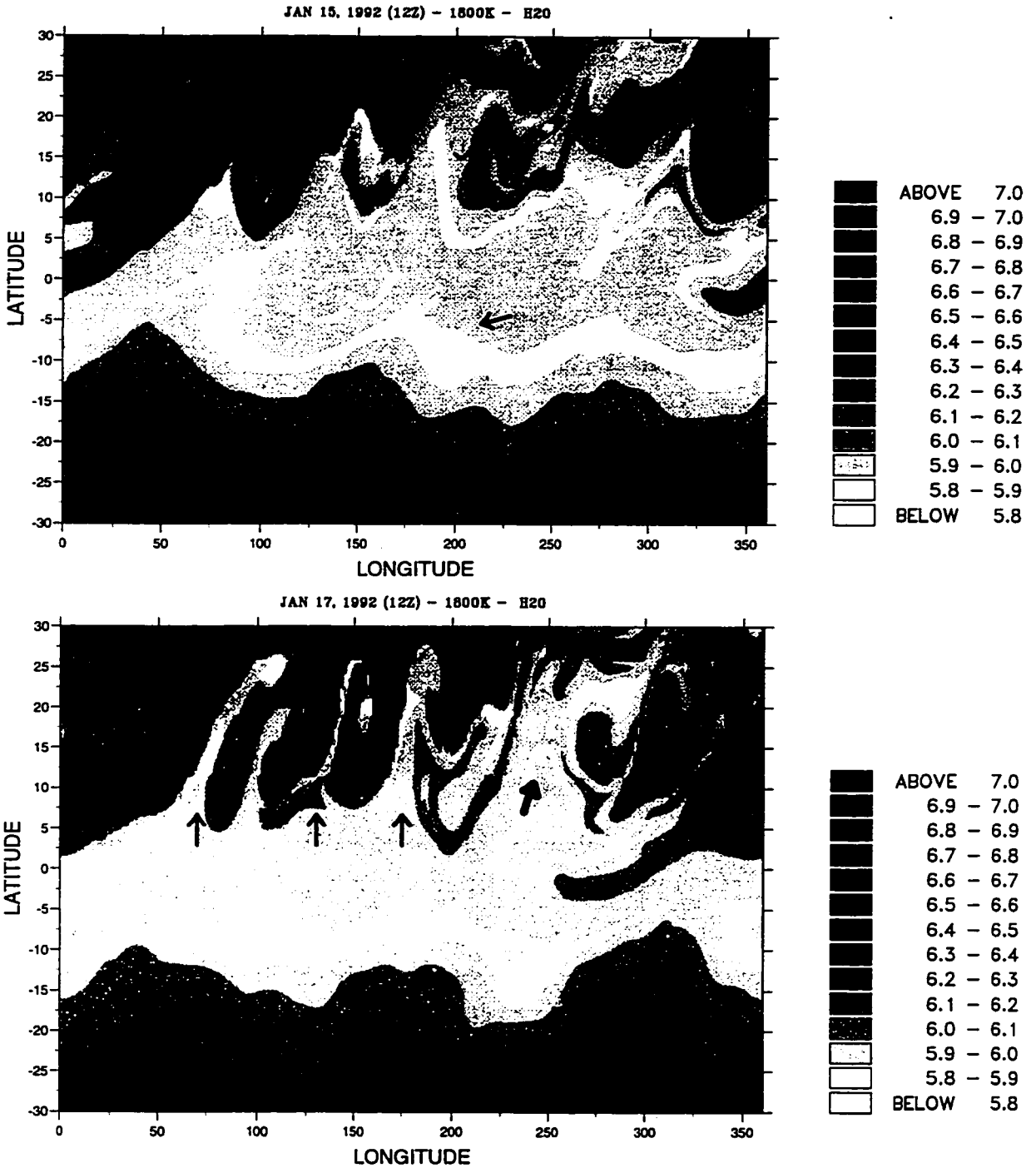

Figure 2.14: The water vapor mixing ratio structure from an off-line transport model using the UKMO winds at 1800 K (~1 hPa). The arrow in the top panel indicates the two-day wave. The arrows in the bottom panel indicate the overturning cells possibly attributed to inertial instability. The bold arrow shows region where large scale planetary wave breaking is occurring. [Adapted from Orsolini et al. (1997).].

attributed the signals to large energy dispersion from winter-time planetary waves breaking in the surf zone regions. They claimed that this cross-equatorial leakage can provide near-resonant (i.e. near the neutral normal mode) forcing in the summer hemisphere and can easily be enhanced by forcing due to mean flow instability of the easterly jet.

The Extended U.K. Universities Global Atmospheric Modeling Program Global Circulation Model (EUGCM) run of Norton and Thuburn (1996 and 1997) also simulated the two-day wave. Both components of the two-day wave were identified. In middle and upper mesosphere, the wave 3 mode was consistently stronger than the wave 4 mode and appeared equally dominant during the austral and boreal summer. Transition between the two modes was readily seen as their amplitudes often anticorrelated in time. Note that satellite observations generally found the wave 3 component to be considerably stronger during the austral summer than during boreal summer (see Figure 2.1). However, these observations mainly accounted for the two-day wave up to the lower mesosphere (~65 km). It may be that at higher levels the wavenumber 3 mode is equally strong during both summer seasons as suggested by the EUGCM model.

The simulated wavenumber 3 two-day wave was determined to have characteristics of both a neutral normal mode and an unstable wave (Figure 2.15). The temperature phase structure was baroclinic in nature with rapid phase transition near 0.1 hPa. Above this level, the temperature structure was reminiscent of the third Rossby-gravity normal mode (see Figure 2.9). The temperature amplitude peaked in both hemispheres with a node near the equator. The winter peak was nearly out of phase with the summer peak. Below 0.1 hPa, the temperature structure was remarkably similar to that found by Burks and Leovy (1987) shown in Figure 2.2. The meridional wind peaked near the equator with a slight bias toward the summer hemisphere. This structure also concurred with the structure observed by Wu et al. (1993) in Figure 2.5.

Importantly, Norton and Thuburn (1997) suggested that, in order for the two-day wave to exist, unstable summer easterlies (within which the wave flourished) must be gen-

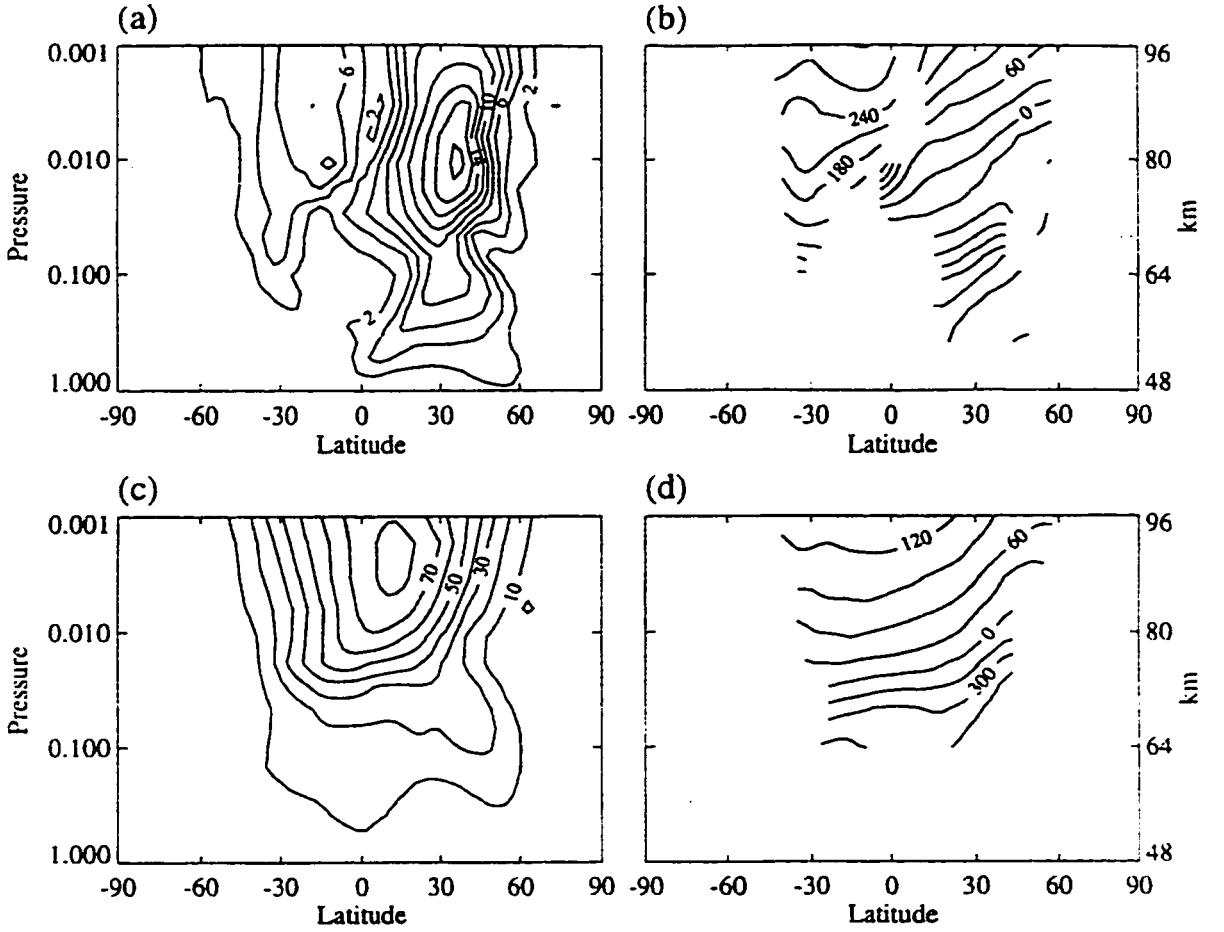

Figure 2.15: The EUGCM wavenumber 3 two-day wave amplitude and phase structure for temperature (a,b) and meridional wind (c,d) for 23-24 June. Temperature and meridional wind amplitude contour interval is 2 K and 10 ms^{-1}, respectively. Phase contours are given every 30°. [Adapted from Norton and Thuburn (1997).].

erated and maintained. Strong gravity wave drag was essential in producing the necessary wind shear and subsequently the reversal of potential vorticity gradient. In the case where the shear was weak due to weak drag or the gravity wave parametrization replaced by Rayleigh friction, the two-day wave was absent or appeared at higher latitude in the summer hemisphere. In addition, as the instability waves grow, they tend to stabilize the mean flow through heat and/or momentum transport. For these waves to be long-lived (as demonstrated in the observations), gravity wave drag must continually maintain the necessary wind shear.

Using a 5-year National Meteorological Center (NMC) analyses, Randel (1992) also observed the dual nature of the two-day wave in the upper stratosphere. Although his results made no distinction between the different modes of the two-day wave (he computed the wave variance by band-passing over zonal wavenumber 3 and 4), the wave 3 signal is assumed to be dominant. This assumption is supported by the fact that the NMC data he used was given every 24 hrs, so signals faster than a 2.0 day period were likely unresolved in the data set (although some aliasing may also be possible).

Randel (1992) found strong spatial and temporal correlation between the two-day wave peak amplitude and regions of instability where the meridional gradient of potential vorticity is negative (Figure 2.16). The two-day wave variance rapidly grew as multiple episodes on the equatorward side of easterly jet where the shear is substantially strong enough for mean flow instability to occur. The wave rapidly decayed when the flow was stabilized as seen by the removal of the negative PV gradient regions. The wave signature also had a structure reminiscent of the third Rossby-gravity mode in agreement with the observed structure of Wu et al.(1996) and the simulated structure of Norton and Thuburn (1997).

2.4 RELATED PHENOMENA

The two-day wave is observed mainly equatorward of 45° latitude near the upper

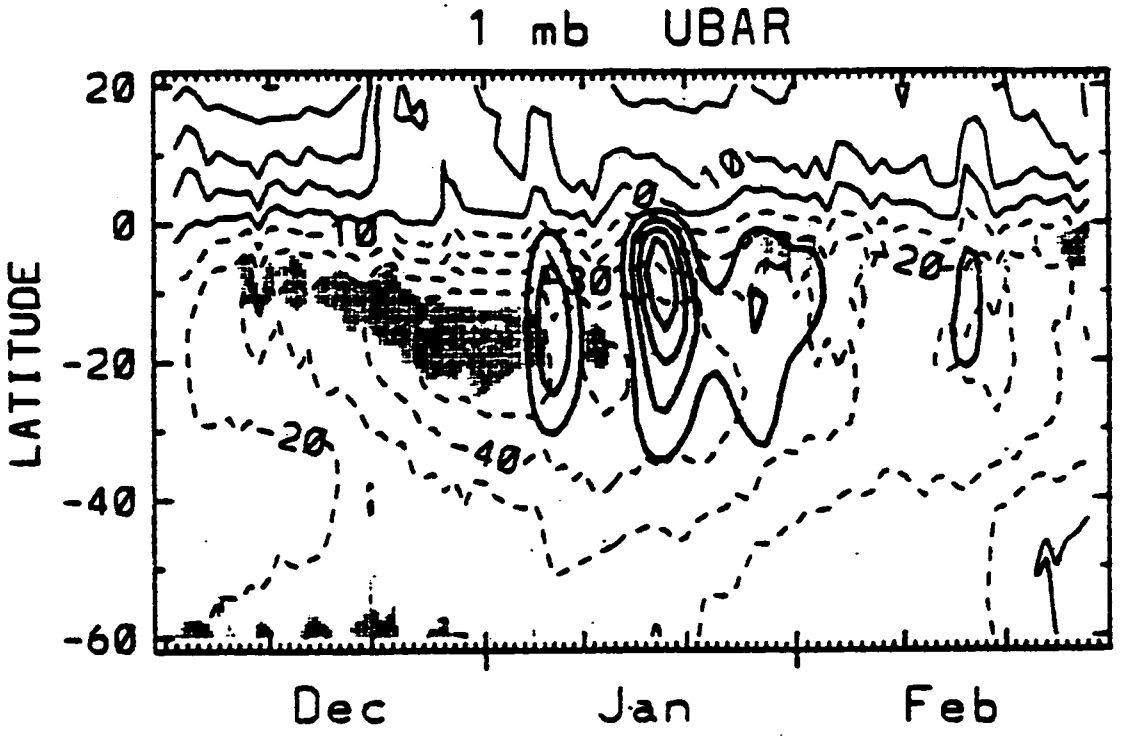

Figure 2.16: The NMC 1985-1986 latitude-time 1 hPa structure of the two-day wave variance given in solid bold contours of 0.5 K^2 intervals. Thin contours show the zonal mean zonal wind with the easterlies shown as dashed contours. Shading marks the regions where the meridional PV gradient is negative. [Adapted from Randel (1992).].

stratosphere and lower mesosphere. (At higher altitudes, the observed two-day wave may appear at higher latitudes). In this region, the seasonal cycle is dominated by the annual reversal of the zonal and meridional winds between summer and winter of each hemisphere. Winter planetary waves are primarily responsible for driving the annual oscillation. This seasonal cycle is strongly modulated by a pronounced equatorial semiannual oscillation (SAO). Convectively generated internal gravity waves and Kelvin waves as well as planetary Rossby waves are believed to be the main driving agents for the SAO.

The monthly-mean equatorial zonal mean zonal wind calculated from the UARS MLS temperature by Ray (1997) is shown in Figure 2.17. The calculation is based on the thermal wind relationship discussed in Section 3.2.2. The wind field is dominated by the SAO above 35 km (~5 hPa) and the quasi-biennial oscillation (QBO) below. The solstices are marked by the bold vertical lines, and the 5 hPa level is denoted by the thin horizontal line. Large amplitudes near the beginning of 1995 are attributed to the lack of data as result of power failures aboard UARS (Ray, 1997). Near the stratopause, the wind pattern is characterized by a descending westerly shear zone (wind increasing with height) in switching from the easterly to westerly SAO phase. This descending pattern is considerably weaker during the second easterly SAO cycle (near June).

Just after the solstice when the two-day wave is prominent, the SAO is in its easterly phase near the stratopause. Tropical zonal wind is easterly in the upper stratosphere and westerly aloft. Subtropical zonal wind is easterly in the summer hemisphere and westerly in the winter hemisphere. A sketch of the wind structure equatorward of 60° latitude is shown in Figure 2.18. Numerous wave activities are evident at this time. Mid-latitude planetary waves propagate upward and equatorward from the winter hemisphere and impart easterly momentum in the low winter latitudes. Vertically propagating equatorial Kelvin waves and gravity waves are damped near the lower mesosphere where they deposit westerly momentum. Other gravity waves are also present.

The meridional circulation driven by these various waves shown in the schematic is

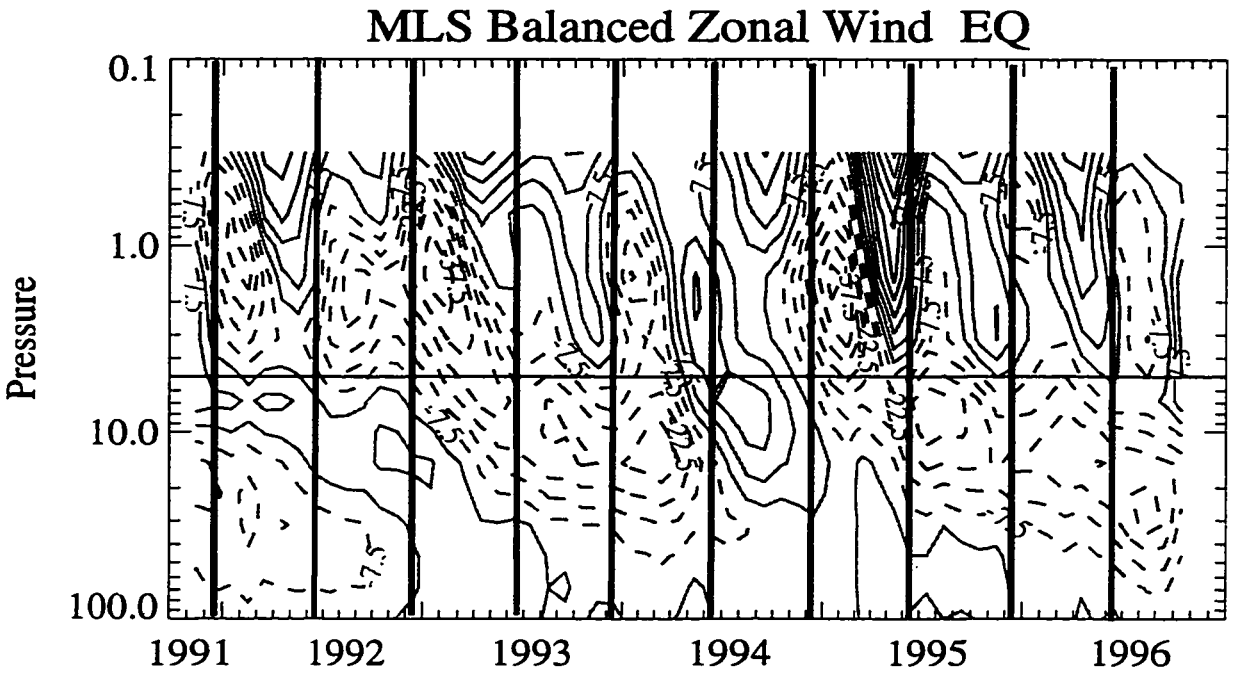

Figure 2.17: Time-height evolution of the MLS equatorial zonal wind as calculated from the MLS temperature. Dashed contours indicate easterly wind. Line contours indicate westerly wind and the zero wind line. Bold vertical lines mark the solstice. Thin horizontal black line denotes the 5 hPa (~35 km) level. [Adapted from Ray (1997).].

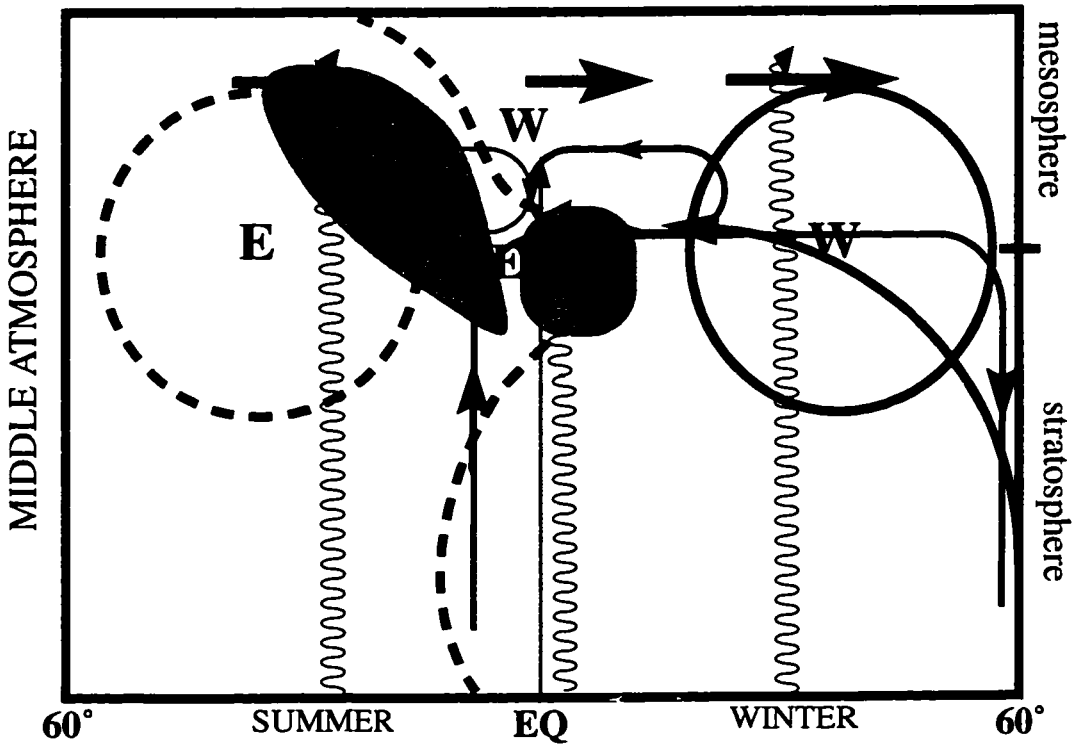

Figure 2.18: Schematic view of the wave activity and circulation in the middle atmosphere around the solstice The solid and dashed lines indicate, respectively, the westerly and easterly jet structure. The straight red line shows the propagation of the Kelvin waves while the wavy red lines indicate the vertically propagating gravity waves. The curved red line in the winter hemisphere shows the propagation of stationary planetary wave. The blues lines indicate the various wave-driven circulation. Shaded regions correspond to where instability regions may occur.

also important. Circulation from the summer hemisphere tends to increase easterly momentum in the tropics and subtropics through angular momentum conservation. This circulation also directly advects subtropical easterlies equatorward and the subtropical westerly winds poleward. The relatively weaker downward circulation superimposed over the equatorial regions causes the westerly wind shear zone aloft to descend. This descending signature is seen in Figure 2.17.

Given the various wave-related forcing mechanisms around the solstice, the mean wind configuration can be barotropically-baroclinically unstable. Near the low summer latitude regions of stratopause, meridional (and possibly vertical) wind curvature can be quite large. As result, the corresponding potential vorticity gradient may be reversed, satisfying the necessary condition of mean flow instability. This region is denoted as a shaded area on the equatorward side of the summer easterly jet shown in Figure 2.18. It is near this region that the two-day wave structure has been observed.

Up to the lower mesosphere, inertial instability can also be present as discussed in Section 2.3. The regions where such instability may occur is shown in Figure 2.18 as a shaded area in the equatorial region. As discussed, cross-equatorial mean circulation near the stratopause tends to advect the summer easterlies toward the winter hemisphere. The advected easterlies are strengthened by angular momentum conservation as air parcels move equatorward. As a result, a strong cross-equatorial shear can occur, producing regions of anomalous vorticity. Inertial eddies can develop as vertically stacked structures. Possible relationships between inertial instability, winter planetary waves, and the two-day wave are discussed in the previous section and will be explored in more detail in Chapters 4 and 5.

CHAPTER 3

DATA AND ANALYSIS

The primary data used in this thesis are temperature and water vapor (H_2O) measured from the Microwave Limb Sounder (MLS) instrument aboard NASA's Upper Atmospheric Research Satellite (UARS). The asynoptic mapping method (Salby, 1982ab) is applied to the data to produce twice-daily maps from which the two-day wave is identified. Additional data are taken from the stratospheric analyses of the United Kingdom Meteorological Office (UKMO) model developed in the conjunction with the UARS mission. The UKMO data set supplements the MLS data and facilitates further analysis. Both data sets can be obtained from the UARS CD-ROM set distributed to the scientific community. A description of the data and the analytical methods are presented in this chapter.

3.1 THE MLS DATA

The UARS began orbiting the Earth on September 12, 1991 at the altitude of 600 km and a 57° inclination to the equator. Each orbit takes about 96 minutes to complete, and successive orbits are 24° longitude apart. The orbital plane precesses slowly with respect to the Earth-Sun line. As a result, the satellite must perform a 180° yaw-around maneuver every 30-40 days to keep some of the onboard instruments pointing directly at the Sun and others away.

The MLS is one of UARS' limb viewing instruments. Its latitudinal coverage alternates every 30-40 days, a consequence of the yaw-around maneuver performed by the satellite. Prior to a maneuver, the global coverage of the sounder ranges from 80° latitude in the northern hemisphere to 32° latitude of the southern hemisphere. After the maneuver, the hemispheric coverage is reversed. Thus, regions equatorward of 32° latitude are continuously observed while regions at higher latitudes are intermittently sampled.

The MLS takes approximately 65 seconds to vertically scan the atmosphere. During this time, the satellite travels along its orbit approximately 500 km which is the limit of the instrument's horizontal resolution. As it scans, the MLS measures atmospheric thermal emission from molecular spectral lines near 3 microwave frequency channels: 63, 183, and 205 GHz. The MLS temperatures are retrieved from the 63 GHz radiance emitted by molecular oxygen (O_2) while the H_2O mixing ratios are retrieved from the 183 GHz radiance. The latter channel failed in April 1993 resulting in a short time series of the H_2O data.

The MLS data used in this study are version 3 of the unbinned along-track vertical profiles (Level 3AT). The profiles are presented on the standard 43 UARS levels that are evenly spaced in log pressure. The pressure levels are governed by the formula $1000\times10^{-\frac{n}{6}}$ where $n = 0, \cdots, 42$. For the temperature profile, useful vertical coverage is from 22 hPa to 0.46 hPa. For the water vapor profile, useful coverage ranges from 46 hPa to 0.22 hPa. Within these ranges, only data on the even surfaces (with even index n) contain actual retrieved values. Data at other levels are averages of data on adjacent even surfaces, and data outside the useful ranges are climatological values. The effective MLS vertical resolution is then about 6 km. Estimations of the retrieved profile precision and accuracy are given in Table 3.1 (Lahoz et al., 1996; Fishbein et al., 1996).

Six even levels are used for the analysis of both temperature and water vapor: 22, 10, 4.6, 2.2, 1.0, and 0.46 hPa. The latitudinal coverage is limited to between 28° latitude in one hemisphere and 68° latitude in the opposite hemisphere during a yaw period. Reasons for this latitudinal band are given in Section 3.2.2. The spatial and temporal coverage of the analyzed data is shown in Figure 3.1.Three austral and two boreal summers are available for analysis. The 1994 boreal summer is not analyzed due to numerous dates with missing data in the archive. In each summer season, however, only five time periods are amenable for detailed examination of the two-day wave structure in the summer hemisphere. As marked in Figure 3.1, these periods consist of the time when the instrument is scanning mainly the summer hemisphere (from 28° in the winter hemisphere to 68° in the

Table 3.1: Estimated Precision and Accuracy of the MLS data

	H_2O		Temperature	
Pressure (hPa)	Precision (ppmv)	Accuracy (%)	Precision (K)	Accuracy (K)
0.22	0.4	15-30	---	---
0.46	0.4	15-30	3	7
1.0	0.3	15-30	2.5	5
2.2	0.2	15-30	1.5	5
4.6	0.2	15-30	1.5	5
10	0.1	15-20	1.5	4
22	0.2	15-20	1.5	4
46	0.2	15-20	---	---

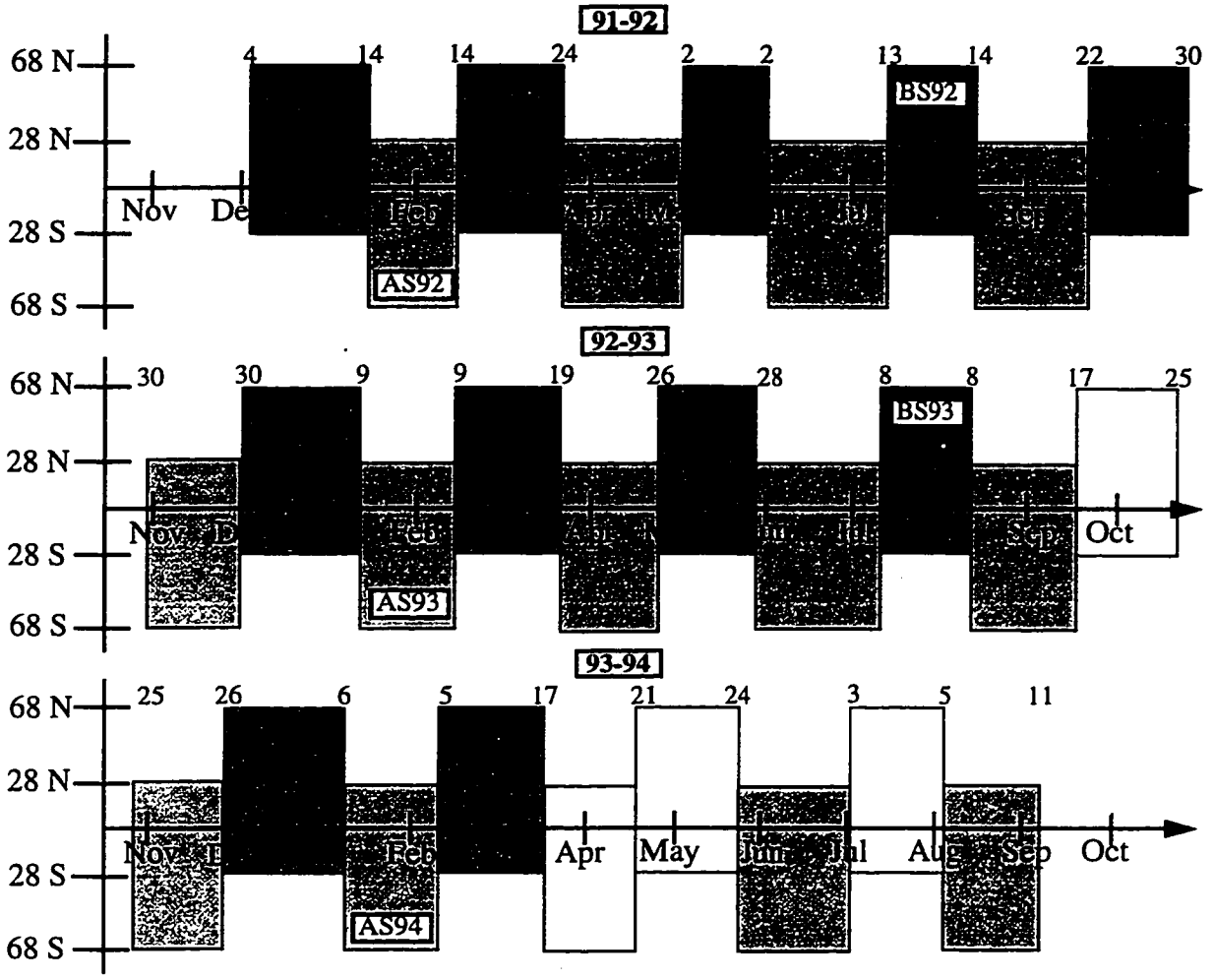

Figure 3.1: Latitudinal-time coverage of the analyzed MLS data. Each tick on the horizontal axis denotes a beginning of each month. The numbers immediately above the rectangles denote the day of the month. Dark (light) shaded rectangles designate the coverage when the instrument is looking North (South). Unfilled rectangles represent unused data due to numerous missing dates. Periods covering extratropical summer latitudes are marked with "AS" for "austral summer" and "BS" for "boreal summer" and the year.

summer hemisphere). As mentioned, the MLS 183 GHz radiometer failed completely on April 1993. Consequently, only two austral summers and one boreal summer are examined for H_2O.

3.2 THE UKMO DATA

Additional data used in this study are generated by the UKMO unified model in assimilation mode. The model has horizontal resolution of 2.5° in the meridional direction and 3.75° in the zonal direction. There are 42 levels in the model's hybrid vertical coordinate system with the top level at 0.28 hPa. In the stratosphere, the vertical resolution is about 1.6 km. The model uses a full radiative scheme. Multiple sets of observational data (primarily operational satellite temperature soundings and radiosonde ascents) are assimilated in the model run by using an analysis correction scheme. Observed data are incorporated repeatedly, and the model is continually adjusted to each data set while maintaining dynamical balance. Swinbank and O'Neill (1994) discuss the assimilation process in detail. The assimilated winds, temperature, and geopotential height are interpolated onto the UARS standard levels (1000 to 0.32 hPa) and distributed along with other UARS measurements. In the future, data measured by the UARS will be assimilated into the model. The UKMO data are used for diagnostic studies and to help validate UARS measurements.

3.3 ANALYSIS

The main objective of the data analysis is to identify wave signals and examine their structures and evolution. The wave's presence can be elucidated through standard space-time spectral analysis (Blackman and Tukey, 1958; Hayashi, 1971). Before such analysis can be done, twice-daily maps of the MLS temperature and H_2O fields must first be constructed using the asynoptic mapping method (Salby, 1982 ab). The UKMO data is then used to facilitate the computation of some useful zonal mean diagnostics from the MLS temperature data.

3.3.1 ASYNOPTIC MAPPING METHOD

Polar orbiting satellites, such as the UARS, have provided valuable observational soundings of temperature and trace constituents for the past two decades. These observations are important in the understanding of the atmosphere's behavior as well as in the initialization of forecast models. With certain exceptions (see Section 3.1), they provide nearly uniform global coverage and are extremely useful over areas lacking conventional radiosonde stations.

The analysis and interpretation of these satellite data can, however, be complicated. This is because polar orbiting satellites obtain their data asynoptically. A polar orbiting satellite transverses over the entire globe in a day by performing a number of orbits. In the process, measurements are taken at a single, local position at a given time. The resulting non-Eulerian view of the atmosphere is not directly amenable to analysis since most equations that govern the atmosphere are formulated in an Eulerian framework. An ideal observational scheme would provide synoptic (simultaneous) "snapshots" of the entire globe in a uniform time interval. In addition, the satellite encircles the globe in a non-integral number of orbits in a day. This results in a day-to-day drift of the coverage and adds to the complexity of the asynoptic measurement.

The asynoptically observed field cannot be easily described by an independent time-longitude coordinate. Figure 3.2 illustrates a schematic pattern of a polar orbiting satellite at a latitude circle. As the satellite transverses the globe the sampled longitude position is dependent on time. Assuming an orbital period of τ_0 days and the satellite's zonal speed of c_0 radians per day, the observational longitudes and times for ascending (a) and descending (d) branches of an orbit j can be written as (see Figure 3.2):

$$\left.\begin{aligned} \lambda_{dj} &= \lambda_{d0} - c_0\tau_0 j \;; \quad \lambda_{aj} = \lambda_{a0} - c_0\tau_0 j \\ t_{dj} &= t_{d0} + \tau_0 j \quad ; \quad t_{aj} = t_{a0} + \tau_0 j \end{aligned}\right\} \quad (3.1)$$

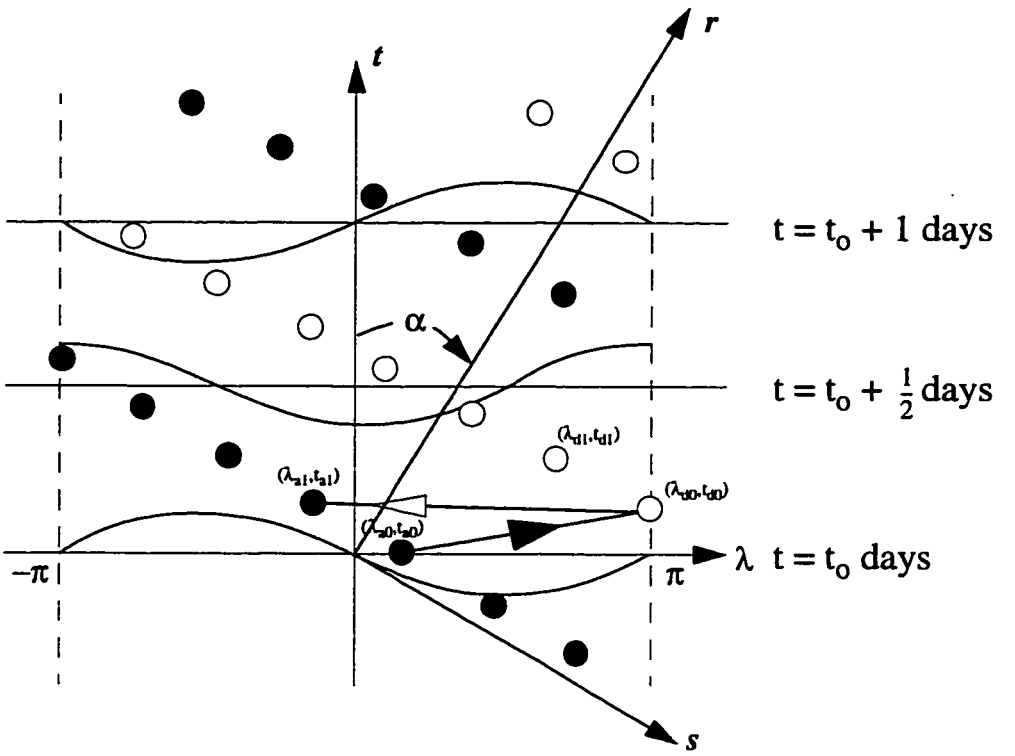

Figure 3.2: Schematic of polar orbiting satellite sampling at a latitude circle. The ordinate is time (t) and the abscissa longitude (λ). Each circle represents the location where the measurements are made. The filled circle indicates that the satellite is heading North (ascending node) and open circle indicates that the satellite is heading South (descending node). The circles can be independently described by the rotated (s-r) axes. The curves represent the evolution of a wave that may be sampled by the satellite.

A common (but crude) way to deal with the asynoptic nature of the observation is to simply *ignore* it. The measurements are assumed to be taken simultaneously during a one day cycle and the data are interpolated in space and time onto an evenly spaced grid. This procedure adequately resolves waves moving at period of 5 days or slower but significantly distorts faster moving signals. Unfortunately, some disturbances found in the middle atmosphere have temporal variation faster than 5 days (e.g. the two-day wave).

Kalman filtering technique offers an objective way of interpolating asynoptic data to the synoptic framework. This technique applies a sequential estimation method to combine the currently measured asynoptic field with its statistical properties at previous times to optimally produce the synoptic field (Salby, 1982b). While better than the crude binning method discussed above, Kalman filtering requires an *a priori* knowledge of the field and its statistical properties and, thus, makes assumptions about the data space-time variability. The method also inherently smooths higher wave frequencies of less than a few days.

A far more successful method for analyzing higher frequency variability applies direct spectral analysis of the asynoptic data (Chapman et al., 1974). This method will be referred to as the "Chapman method". Soundings taken during the ascending (northward heading) and descending (southward heading) portion of the orbits are arranged into two time series of fixed altitude and latitude. The series are then Fourier transformed, and the wave signals are inferred from the resulting spectra. A spectral peak at an integral frequency represents a stationary signal with zonal wavenumber equaling the frequency. A spectral peak at a non-integral frequency corresponds to two possible moving wave signals (Doppler-shifted twins). The satellite's motion relative to the Earth causes a pair of signals (identifiable by zonal wavenumber and frequency) to be Doppler-shifted to the same observed frequency. The wavenumbers of the twins always differ by one, but they can be moving at considerably different speeds in the same direction or at comparable speeds in the opposite zonal directions.

Comparison of ascending and descending spectral peaks ultimately determine which

of the two signals is present. Due to the spatial difference in the crossing of the ascending and descending path at a given latitude, the spectral peaks in both series will be roughly in phase if the disturbance has an even zonal wavenumber or out-of-phase for an odd zonal wavenumber. Although this method does not distort fast moving waves, it does have difficulty resolving both Doppler-shifted twins if they are indeed present in the data (Lait and Stanford, 1988). Burks and Leovy (1986) and Rodgers and Prata (1981) successfully employed the Chapman method to study the two-day wave in the middle atmosphere as mentioned in Chapter 2.

The asynoptic mapping method is a more robust way to systematically resolve the exact longitude-time spectra from data sampled asynoptically than the Chapman method. This method is now outlined. Details are given in Salby (1981ab), Lait and Stanford (1988), and Elson and Froidevaux (1993). As introduced by Salby (1981a), the central idea is that, although orbital track mixes time and position, a new coordinate system can be introduced to independently describe the sampled data. The new coordinate (s, r) is satellite-relative and is simply the (λ, t) coordinate rotated clockwise by an angle α (see Figure 3.2). This angle is related to c_0 by the relationship $\tan\alpha = 1/c_0$. In (λ, t) coordinates, the corresponding spectral coordinate is (m, σ) where m is the zonal wavenumber and σ is the frequency in cycles per day (cpd). The analogy to (m, σ) in (s, r) coordinate is (k_s, k_r). The relationships between these coordinates are given by:

$$\left.\begin{aligned} s &\equiv \lambda\cos\alpha - t\sin\alpha \quad ; \quad r \equiv \lambda\sin\alpha + t\cos\alpha \\ m &\equiv k_s\cos\alpha + k_r\sin\alpha \quad ; \quad \sigma \equiv -k_s\sin\alpha + k_r\cos\alpha \end{aligned}\right\} \quad (3.2)$$

Note that the series of ascending and descending nodes are parallel to the s-axis and perpendicular to the r-axis. Hence, the sampled data can be expressed as the k_s-k_r Fourier transform with the Nyquist limits defined in terms of the orbital parameters (Salby,

1982a):

$$k_{rNyquist} = \pm\sqrt{1+c_0^2} \quad ; \quad k_{sNyquist} = \pm\frac{\pi}{\tau_0\sqrt{1+c_0^2}} \tag{3.3}$$

Since λ is periodic, by shifting the appropriate longitude position of each sounding by -2π, only two straight lines (for ascending and descending nodes) can be formed to represent all the data series. Each position now retrogrades with time (Figure 3.3). In (s, r) coordinates, the two lines are parallel to the s-axis and are located at r_a and r_d. Their initial position on the s-axis will be designated as s_{d0} and s_{a0}. These parameters are given as:

$$\left.\begin{aligned} s_{d0} &= \lambda_{d0}\cos\alpha - t_{d0}\sin\alpha - \frac{\tau_0(N-1)}{\sin\alpha} & r_d &= (\lambda_{d0} + c_0 t_{d0})\sin\alpha \\ s_{a0} &= s_{d0} + (-\Delta\lambda_{ad}c_0 + \Delta t_{ad})\sin\alpha & r_a &= r_d - \Delta\lambda'_{ad}\sin\alpha \end{aligned}\right\} \tag{3.4}$$

where $\Delta\lambda_{ad} \equiv \langle\lambda_{dj} - \lambda_{aj}\rangle$, $\Delta t_{ad} \equiv \langle t_{dj} - t_{aj}\rangle$, $\Delta\lambda'_{ad} \equiv \Delta\lambda_{ad} + c_0\Delta t_{ad}$, and N is the length of the data series. The brackets denote an average over the entire data series.

Figure 3.4 shows the spectral regions of the resolved signals. Within the rectangular area defined by the Nyquist limits (Equation 3.3), there are exactly two integral zonal wavenumber (m and m+1) intersecting a line of constant k_s, say k_{sj}. These are the Doppler twin spectral pair resolved by the asynoptic data (Salby, 1981a). In (k_s, k_r) coordinate, the pair is located at (k_{sj}, k_{rpos}) and (k_{sj}, k_{rneg}) corresponding to m+1 and m, respectively. The ascending and descending node spectra, $\Psi(k_{sj}, r_a)$ and $\Psi(k_{sj}, r_d)$, have Fourier expansion in k_r consisting only of the summed contribution from the resolved pair (Salby, 1982a):

$$\left.\begin{aligned} \Psi(k_{sj}, r_d) &= \Psi(k_{sj}, k_{rneg})\exp(ik_{rneg}r_d) + \Psi(k_{sj}, k_{rpos})\exp(ik_{rpos}r_d) \\ \Psi(k_{sj}, r_a) &= \Psi(k_{sj}, k_{rneg})\exp(ik_{rneg}r_a) + \Psi(k_{sj}, k_{rpos})\exp(ik_{rpos}r_a) \end{aligned}\right\} \tag{3.5}$$

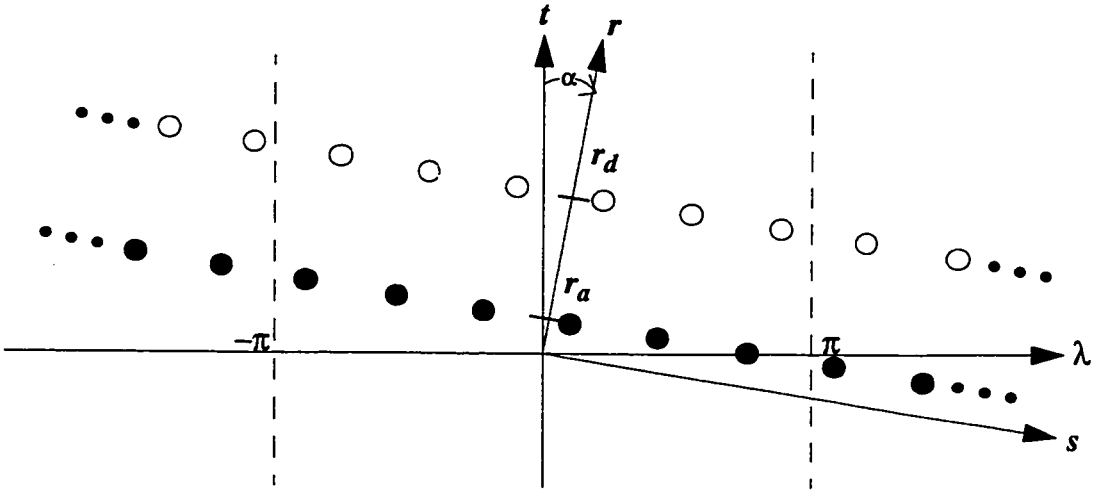

Figure 3.3: Schematic of the translated polar orbiting satellite sampling at a latitude. This the same as Figure 3.2 except now the longitude positions of the ascending and descending nodes that reappear in the interval [-π, +π] are shifted by -2π. Note that this describes the same sampled region since longitude positions are periodic.

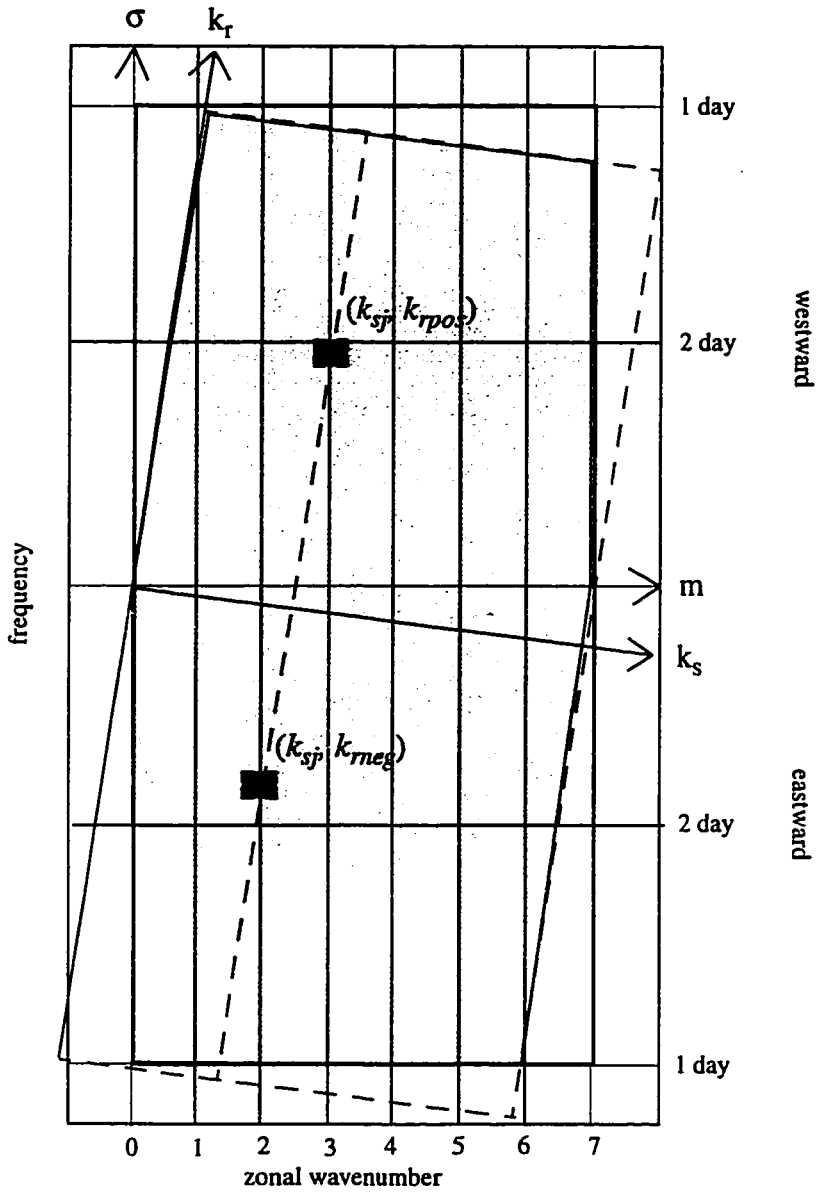

Figure 3.4: Schematic of the spectral signals resolved by the asynoptic mapping method. Boundaries of the dashed box are marked by the Nyquist limits given in Equation 3.3. Boundaries of the bold box are marked by the Nyquist limits of a corresponding transform of twice-daily synoptic data. Shaded region shows the resolved signal with the Doppler twin indicated by filled squares.[After Lait and Stanford (1988).].

The location of the pair is defined by the orbital parameters:

$$\left.\begin{aligned} k_{sj} &= 2\pi j \frac{\sin\alpha}{N\tau_0}, j = -N/2, \cdots, 0, \cdots, N/2 \\ k_{rpos} &= -k_{sj}c_0 + (m+1)\sqrt{1+c_0^2} \\ k_{rneg} &= -k_{sj}c_0 + m\sqrt{1+c_0^2} \end{aligned}\right\} \quad (3.6)$$

Equations 3.5 can be solved for the Doppler twin spectra. The result is:

$$\left.\begin{aligned} \Psi(k_{sj}, k_{rneg}) &= \frac{\Psi(k_{sj}, r_d)\exp(ik_{rpos}r_a) - \Psi(k_{sj}, r_a)\exp(ik_{rpos}r_d)}{\exp[i(k_{rneg}r_d + k_{rpos}r_a)] - \exp[i(k_{rneg}r_a + k_{rpos}r_d)]} \\ \Psi(k_{sj}, k_{rpos}) &= \frac{\Psi(k_{sj}, r_a)\exp(ik_{rneg}r_d) - \Psi(k_{sj}, r_d)\exp(ik_{rneg}r_a)}{\exp[i(k_{rneg}r_d + k_{rpos}r_a)] - \exp[i(k_{rneg}r_a + k_{rpos}r_d)]} \end{aligned}\right\} \quad (3.7)$$

The above set of equations can be simplified using Equations 3.4 and 3.6 to yield

$$\left.\begin{aligned} \Psi(k_{sj}, k_{rneg}) &= \frac{\Psi'_a - \Psi'_d\exp(-i\Delta\lambda'_{ad})}{1 - \exp(-i\Delta\lambda'_{ad})} \\ \Psi(k_{sj}, k_{rpos}) &= \frac{(\Psi'_d - \Psi'_a)\exp\left(-i\frac{r_d}{\sin\alpha}\right)}{1 - \exp(-i\Delta\lambda'_{ad})} \end{aligned}\right\} \quad (3.8)$$

where,

$$\left.\begin{aligned} \Psi'_d &\equiv \hat{\Psi}(k_{sj}, r_d)\exp[-i(k_{rneg}r_d + ik_{sj}s_{d0})] \\ \Psi'_a &\equiv \hat{\Psi}(k_{sj}, r_a)\exp[-i(k_{rneg}r_a + ik_{sj}s_{a0})] \end{aligned}\right\} \quad (3.9)$$

The quantities with the hat symbols are the Fourier transforms of the ascending and

descending data along the *s*-axis.

Interpretation of the method is straightforward. The resolved Doppler twin pair given in Equation 3.8 is just the linear complex combination of the Fourier transforms of the ascending and descending data along the *s*-axis that are phase shifted by the exponential factor in Equation 3.9. The relative strength of the pair will depend upon the signal that is actually present, generally the weaker signal of the pair being the aliased component. With the transformation given by Equation 3.2, the resolved spectra can be described in the usual (m, σ) coordinates. Note that the method is similar to the Chapman method in that both ascending and descending data are compared to resolve the signal. However, unlike the Chapman method, the power of each signal in the twin pair is quantitatively resolved.

To implement the asynoptic mapping method, the procedure of Canziani et al. (1994) is used to organize the along-track MLS data. At each level, data are divided into ascending and descending nodes and interpolated, in space and time, onto an evenly spaced latitudinal grid of 4° interval. Missing data are linearly interpolated, and the resulting data series are smoothed with a 0.25-0.50-0.25 filter. Hence, at a given level and latitude, ascending data and descending data time series are obtained. Both series are first time-reversed and then tapered 10% on each end with a split cosine window. The time-reversing procedure is important since time- and *s*- coordinates are inversely related and the Fourier transforms of the ascending and descending data taken along *s*-direction are required in Equation 3.9. The Fourier transform is done via an FFT routine.

The MLS data is analyzed for the entire yaw period, starting from a day after the yaw maneuver to one day before the subsequent yaw maneuver. Each data segment has variable length ranging from 26 to 34 days, resulting in variable frequency resolutions. It will be assumed that these variations have no bearing on the resolved wave signatures and in their comparison.

Although the actual data coverage switches between [30°S,80°N] and [80°S,30°N]

between yaw maneuver, only the data between 28° latitude in one hemisphere and 68° latitude of the other are used in the method. Data poleward of 68° latitude is avoided because the ascending and descending nodes become less distinct in going nearer the pole. This implies that $\Delta\lambda'_{ad} \equiv \Delta\lambda_{ad} + c_0\Delta t_{ad}$ is closer to zero and the Doppler twin solutions tend to be large (Equation 3.8). Other limitations of the method are explored by Lait and Stanford (1988).

Twice-daily global maps of temperature and H_2O are made by summing the Fourier coefficients. Signals with frequencies greater than 0.8 cycles per day (period less that 1.23 days) are removed from the maps. Analyzing the mapped fields with a conventional spectral analysis method yields nearly identical spectral signal as presented directly by the asynoptic mapping method.

3.3.2 ZONAL MEAN DIAGNOSTICS

Two useful diagnostics are derived from the observed data: the zonal mean zonal wind ($\bar{u}$) and the quasi-geostrophic potential vorticity meridional gradient ($\bar{q}_\varphi$). The former quantity gives an indication of the basic flow structure, in which possible wave disturbances reside. The latter quantity provides a measure of the basic flow stability and may suggest the origin of the observed waves.

Computation of the zonal mean zonal wind uses the zonal mean balance equations in log-pressure coordinates that make up the thermal wind relation (Andrews et al., 1987):

$$\left(2\Omega\sin\varphi + \frac{\bar{u}\tan\varphi}{a}\right)\bar{u} = -\frac{1}{a}\frac{\partial\bar{\Phi}}{\partial\varphi} \tag{3.10}$$

$$\frac{\partial\bar{\Phi}}{\partial z} = \frac{R\bar{T}}{H} \tag{3.11}$$

where φ is the latitude, a is the radius of the Earth, Ω is the rotation rate of the Earth, H is

the scale height (assumed to be 7km), R is the dry gas constant, and $z \equiv -H\ln(p/p_o)$. Also, $\overline{\Phi}$ is the zonal mean geopotential, and $\overline{T}$ is the zonal mean temperature.

First, the zonal mean geopotential field is calculated from the twice-daily MLS temperature maps by integrating the hypsometric relation given in Equation 3.11. The UKMO geopotential field, with signals that have zonal scales smaller than zonal wavenumber 7 removed, serves as the boundary condition at 22 hPa. Then, the zonal mean zonal wind poleward of 8° latitude is computed from the zonal mean geopotential field using Equation 3.10. Equatorial winds are attained by linear interpolation.

The quasi-geostrophic potential vorticity meridional gradient is computed from $\bar{u}$. The relationship in log-pressure coordinate is given in Randel (1994):

$$\bar{q}_\varphi = A + B + C \tag{3.12}$$

where,

$$A \equiv \frac{2\Omega}{a}\cos\varphi$$

$$B \equiv -\frac{1}{a^2}\frac{1}{\cos\varphi}\frac{\partial}{\partial\varphi}\left[\frac{1}{\cos\varphi}\frac{\partial}{\partial\varphi}(\bar{u}\cos\varphi)\right]$$

$$C \equiv -(2\Omega\sin\varphi)^2 e^{\frac{z}{H}}\frac{\partial}{\partial z}\left[e^{-\frac{z}{H}}\frac{1}{N^2}\frac{\partial\bar{u}}{\partial z}\right]$$

Here, N^2 is the zonal mean log-pressure buoyancy frequency. Other notations are identical to those used in Equations 3.10 and 3.11. Regions where $\bar{q}_\varphi$ is less than zero satisfy the necessary condition for inflection instability of the basic flow (Charney and Stern, 1962; Andrews el al., 1987). Barotropic instability can occur when the horizontal curvature of

the mean flow is large (as represented by term *B*), while baroclinic instability can occur when the vertical curvature is large (as represented by term *C*). In the summer easterly jet, both term *B* and *C* can be large and negative so that combined barotropic-baroclinic instability is possible (Pfister, 1985).

CHAPTER 4

OBSERVATIONAL RESULTS

The two-day wave is readily seen in the MLS temperature and H_2O fields. Both modes of the two-day wave are identified on an *a priori* basis as they are found to appear after the solstice with spectral and structural characteristics similar to past observations (see Chapter 2). The observed wave event of 1993 presented here coincides with the observation of Wu et al. (1996). They applied the least square fitting method of Wu et al. (1995) to a different version of the MLS temperature data. The purpose of this chapter is to first present clear evidence of the two-day wave and examine the wave's interannual and intra-annual variability. The wave's possible origin is then explored using derived zonal mean zonal wind. Possible connection with the recently observed inertial instabilities in the UARS CLAES (Hayashi et al., 1998) is discussed.

4.1 TEMPERATURE FIELD

Twice-daily temperature maps during each observed austral summer (mainly January-February) show a clear two-day period, westward propagating oscillation above 1 hPa. In these maps, no band-pass filtering has been performed although possible tidal signals have been removed. The wave motion is confined mainly in the summer hemisphere and can persist for over two weeks. During early 1992 and 1993, the disturbance is clearly dominated by a wavenumber 3 component; however, during early 1994, both wavenumber 3 and 4 features are present with apparent zonal scale transition during the active period. Figure 4.1 shows the two-day wave evolution around the summer anticyclonic vortex of 1992. Three revolving cold air "pools" are centered near 30°S. Synoptic maps of this wavenumber 3 disturbance are remarkably similar to that of Rodgers and Prata (1981) who observed the wavenumber 3 two-day brightness temperature wave using the Selective Chopper Radiometer (SCR) on the Nimbus 5 satellite.

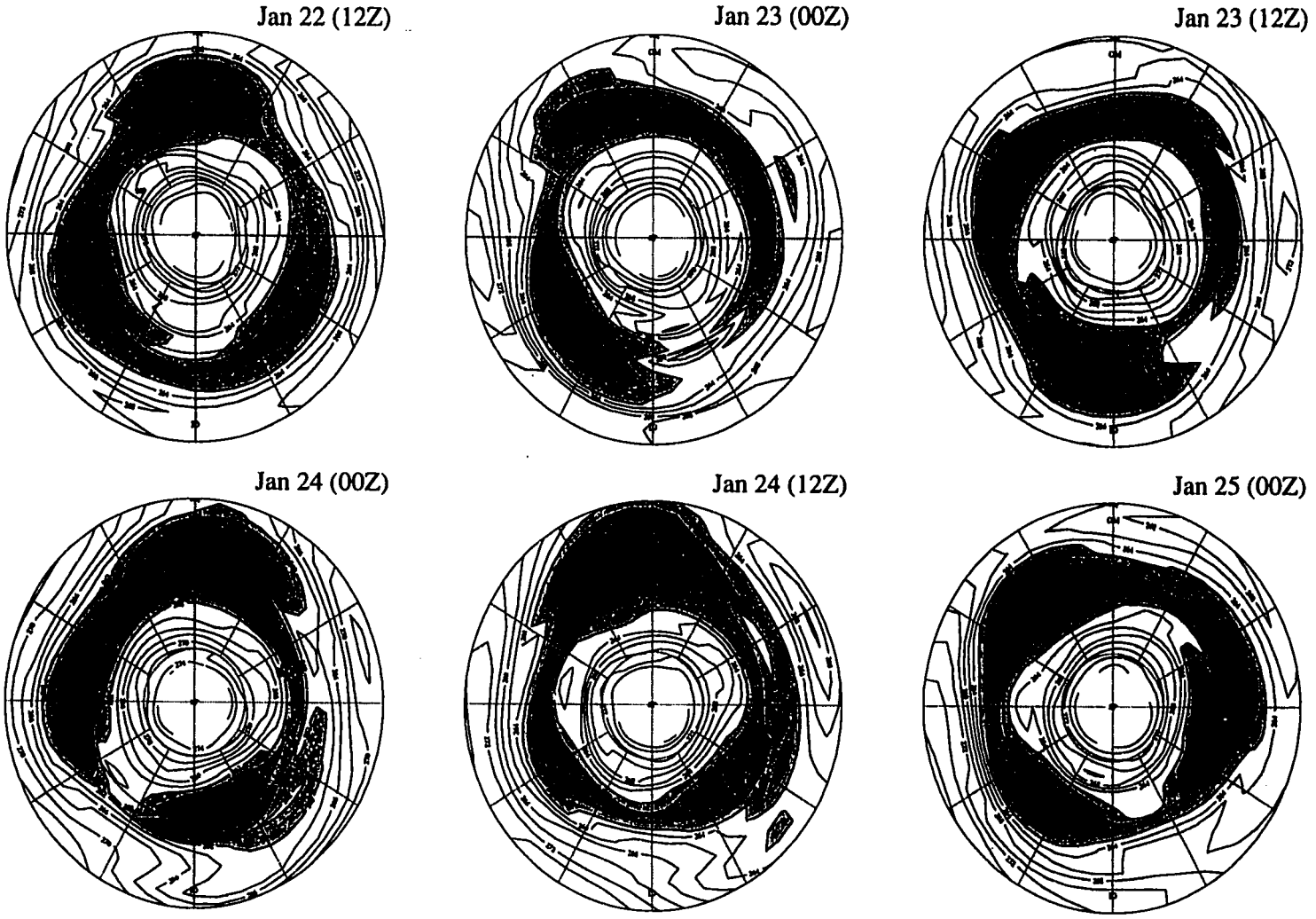

Figure 4.1: Southern hemisphere stereographic plots of unfiltered temperature 12 hour daily maps from 12Z Jan. 22, 1992 to 00Z Jan. 25, 1992 (during data period AS92). The latitude circles are in increments of 30° from the equator. The temperature contours are displayed every 2 K with values less than 256 K shaded.

The two-day wave is also prominent in the constructed temperature maps during both boreal summers (mainly July-August). The disturbance again appears above 1 hPa and in the summer hemisphere. Figure 4.2 shows the maps during 1992 boreal summer when a strong wave event occurs. Cold anomalies are seen to concentrate near 30°N. Unlike the two-day wave event in the austral summer, this wave feature is dominated by a wavenumber 4 disturbance and propagates westward with a slightly lower period.

Spectral analysis is used to isolate the two-day wave from other atmospheric phenomena that are present. Since the wave is a post-solstitial phenomenon, preliminary analysis is performed for 5 periods of data amenable for detailed examination of the two-day wave. These periods (marked with the labels "AS" or "BS" in Figure 3.1 for austral and boreal summer) consist of the time shortly after the solstice when the MLS instrument is scanning mainly in the summer hemisphere. For the analysis, a 28-day time series is used. The "raw" power spectra is defined as $0.5(A^2+B^2)$, where A and B are the Fourier coefficients. Cross-spectral calculations are computed using the formulation of Hayashi (1971). The spectra are smoothed with a normalized Gaussian filter as in Randel (1993). The method of Blackman and Tukey (1958, p.24) is used to evaluate the number of degrees of freedom (DOF) of the individual spectra at each latitude. Approximately five DOF are attained, and the corresponding 95% confidence level for the coherence squared (COH^2) is about 0.55.

The zonal wavenumber-frequency power spectra for these 5 data segments clearly identify the repeating two-day wave signal observed in summer hemisphere maps. As an illustration, the spectra for AS92 and BS92 are shown in Figure 4.3 and Figure 4.4, respectively. The spectra are averaged over the entire observed latitudinal domain: 28° in the winter hemisphere to 68° in the summer hemisphere. Generally, a dominant westward propagating signal appears each summer at the top data levels. During the austral summer, that signal corresponds to a wavenumber 3 disturbance with a period of nearly 2 days. During the boreal summer, the repeating signal is a wavenumber 4 disturbance with period slightly faster than 2 days. During the 1994 austral summer, both modes are prominent in the spectra although the wavenumber 3 signal is weaker (see Figure 4.5).

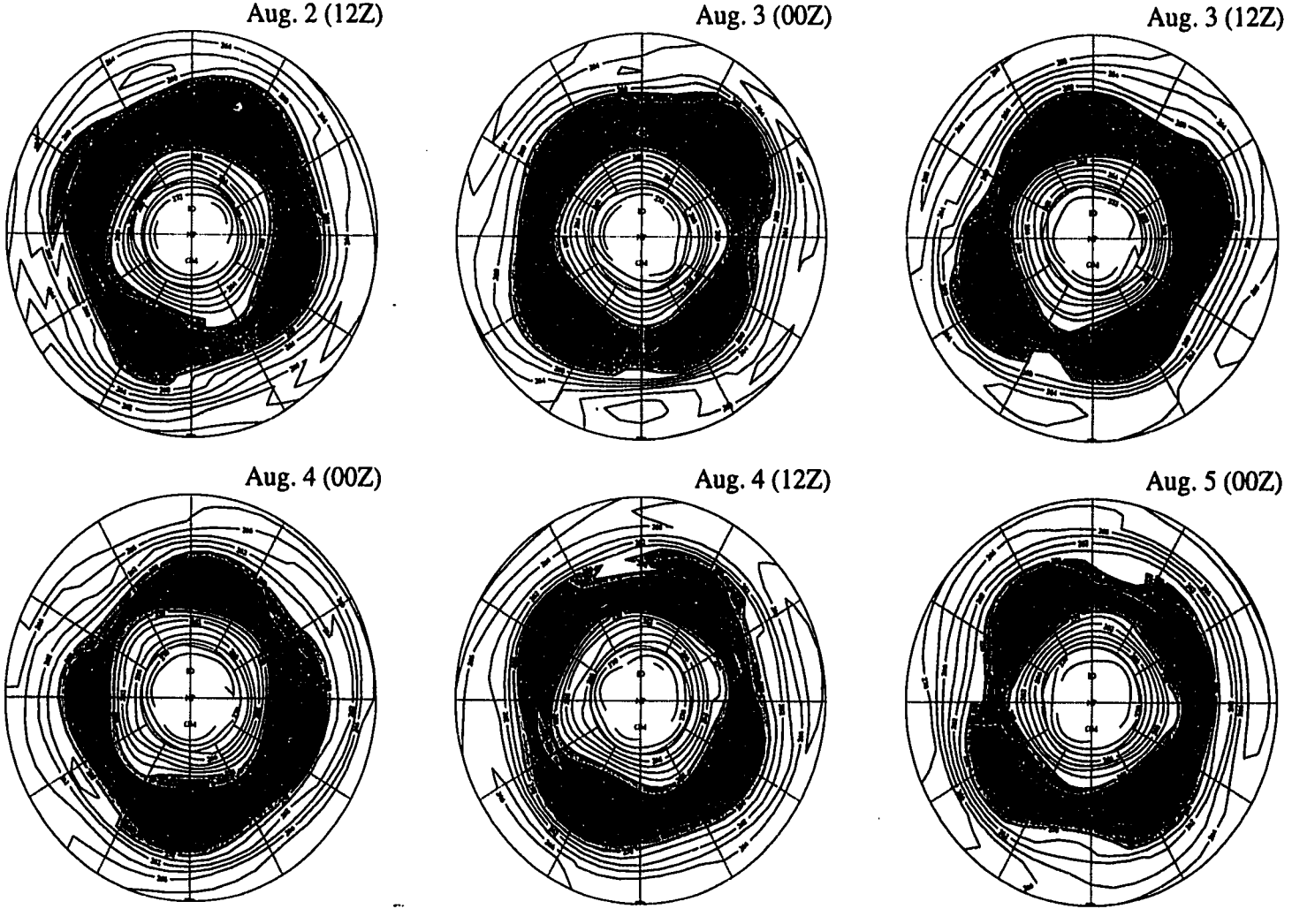

Figure 4.2: Northern hemisphere stereographic plots of unfiltered temperature 12 hour daily maps from 12Z Aug. 2, 1992 to 00Z Aug. 5, 1992 (during data period BS92). The latitude circles are in increments of 30° from the equator. The temperature contours are displayed every 2 K with values less than 256 K shaded.

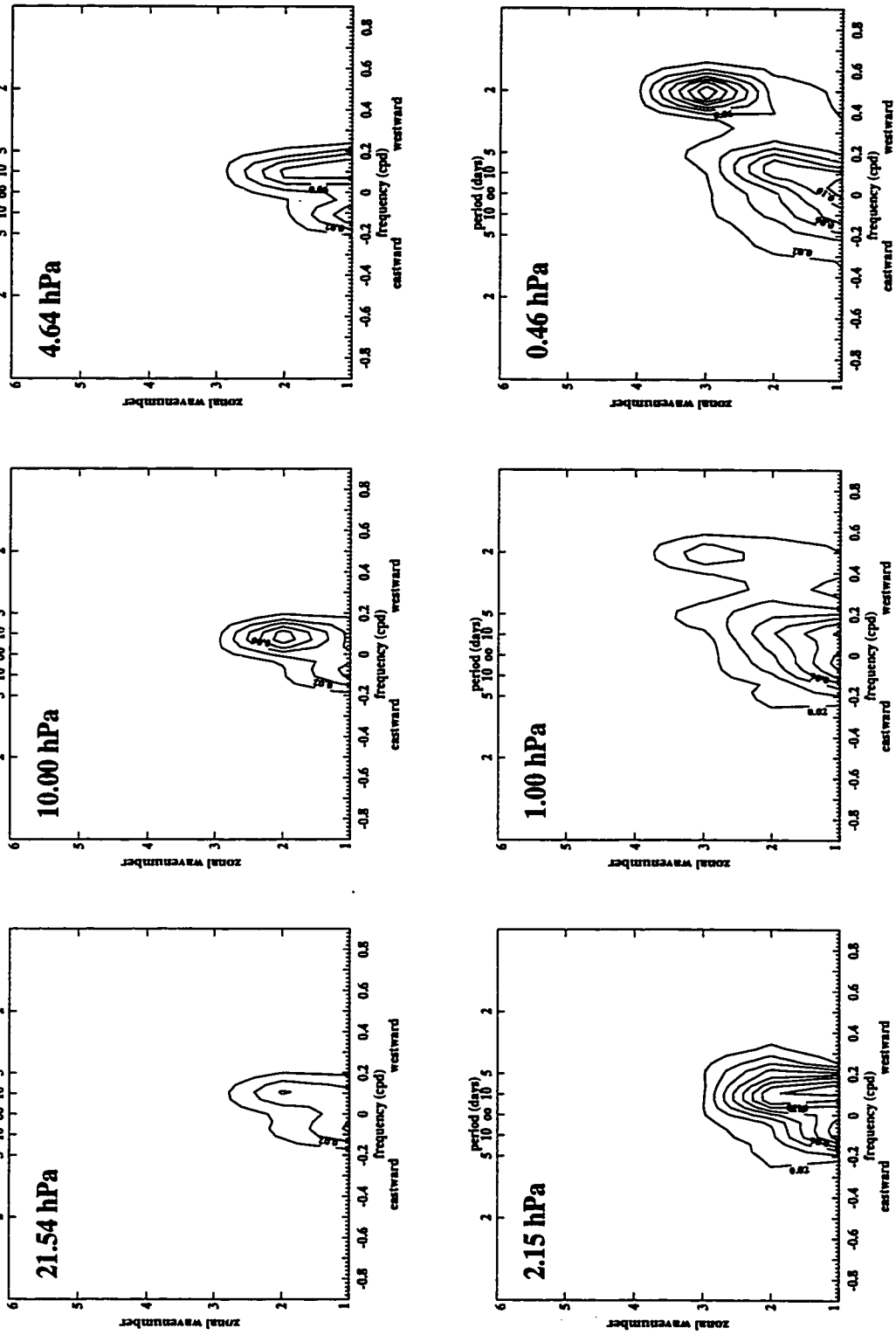

Figure 4.3: Latitudinally averaged [68°S, 28°N] temperature spectra during AS92 (January 14 to February 14, 1992) at each observational level.

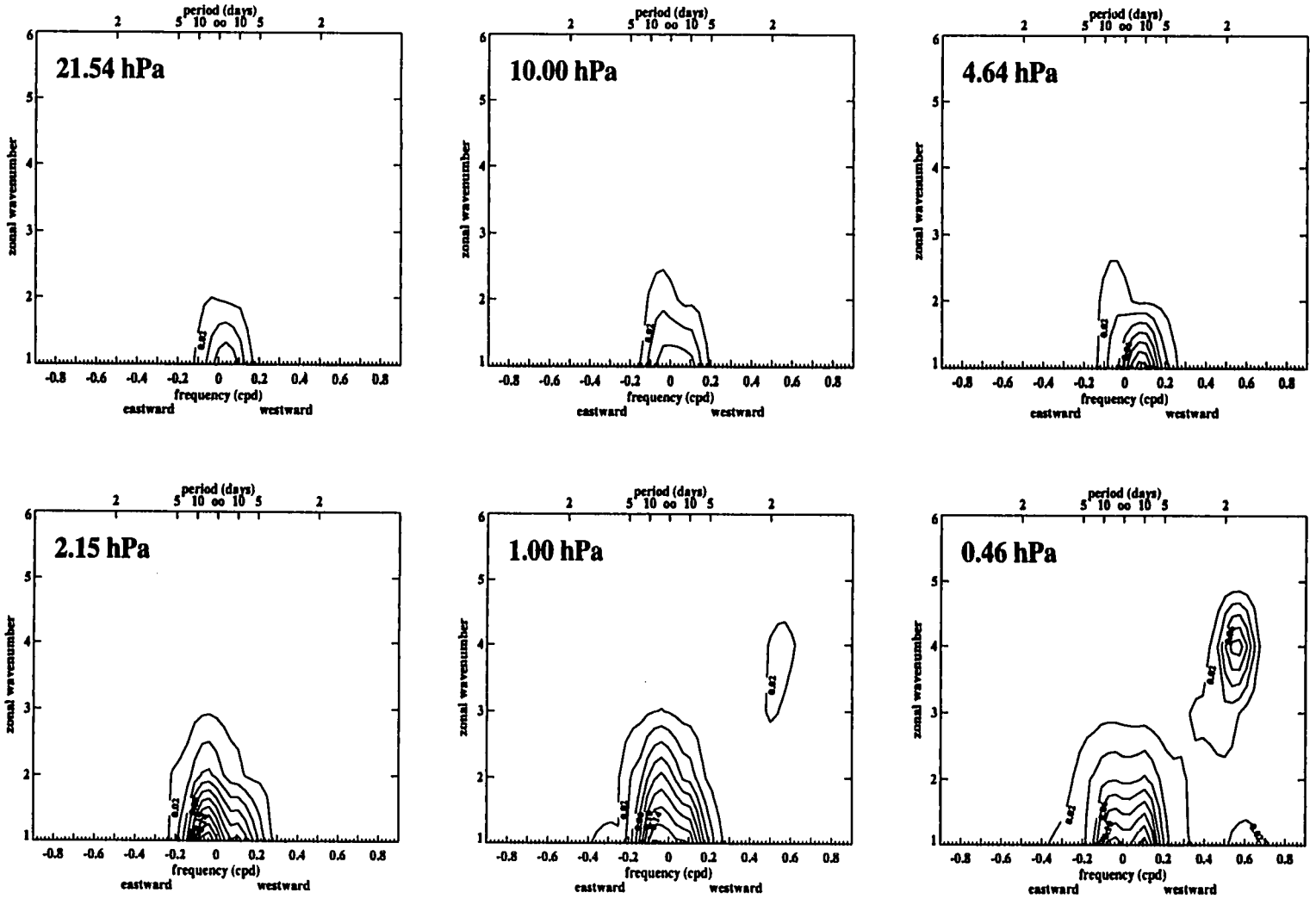

Figure 4.4: Latitudinally averaged [28°S, 68°N] temperature spectra during BS92 (July 13. to August 14, 1992) at each observational level.

Other wave signals are also evident. Namely, wavenumber 1 signals are seen at all data levels. Latitude-frequency spectral diagrams (not shown) find these signals to be comprised of an eastward propagating wave centered near the equator, a stationary wave in the winter subtropics, and a westward propagating wave near the middle summer latitudes. The propagating signals have central period that varies from year to year between 5-15 days. A dominant wavenumber 2 signal is only seen near 10 hPa during the AS92 (see Figure 4.3). It has a westward period close to 10 days and resides in a mid summer latitude band.

The latitudinal coverage of the repeating two-day signals is illustrated in the latitude-frequency spectra diagrams. The signals are vertically averaged between 1.0 and 0.46 hPa where they are found to be dominant. In three AS data segments, the westward propagating signals are confined in the summer hemisphere (Figure 4.5). The spectra are focused between 20°S and the equator. As noted earlier, the wavenumber 3 component is dominant during these times (with the exception of 1994) and is consistently focused at the period of 2 days (~0.5 cycles per day or cpd). For the two BS data segments, the dominant westward signals correspond to a zonal wavenumber 4 component and are also confined in the low summer latitudes (Figure 4.6). The mode period is consistently near 1.8 days (~0.56 cpd).

The spectral peaks show the dominant wave signal in the analyzed time series. Computation of the corresponding red noise (background) spectra reveals that these peaks are generally well above the 99% *a priori* confidence level as determined by the F-statistic. In fact, the entire wave signal confined within the frequency band drawn on Figure 4.5 and Figure 4.6 is statistically significant above the 95% confidence level. Thus, to elucidate the wave's spatio-temporal structure, the wave signal at a given wavenumber will either be integrated or band-passed over the denoted frequency band. The band boundaries span from 0.35 cpd (2.9 days) to 0.65 cpd (1.5 days) for wavenumber 3 signal and 0.40 cpd (2.5 days) to 0.7 cpd (1.4 days) for wavenumber 4. By convention, the integrated wavenumber 3 and 4 two-day wave signal will be referred to as the (3, 2.0) mode and (4, 1.8) mode, respectively. The first number in the parenthesis denotes the signal's wavenumber while

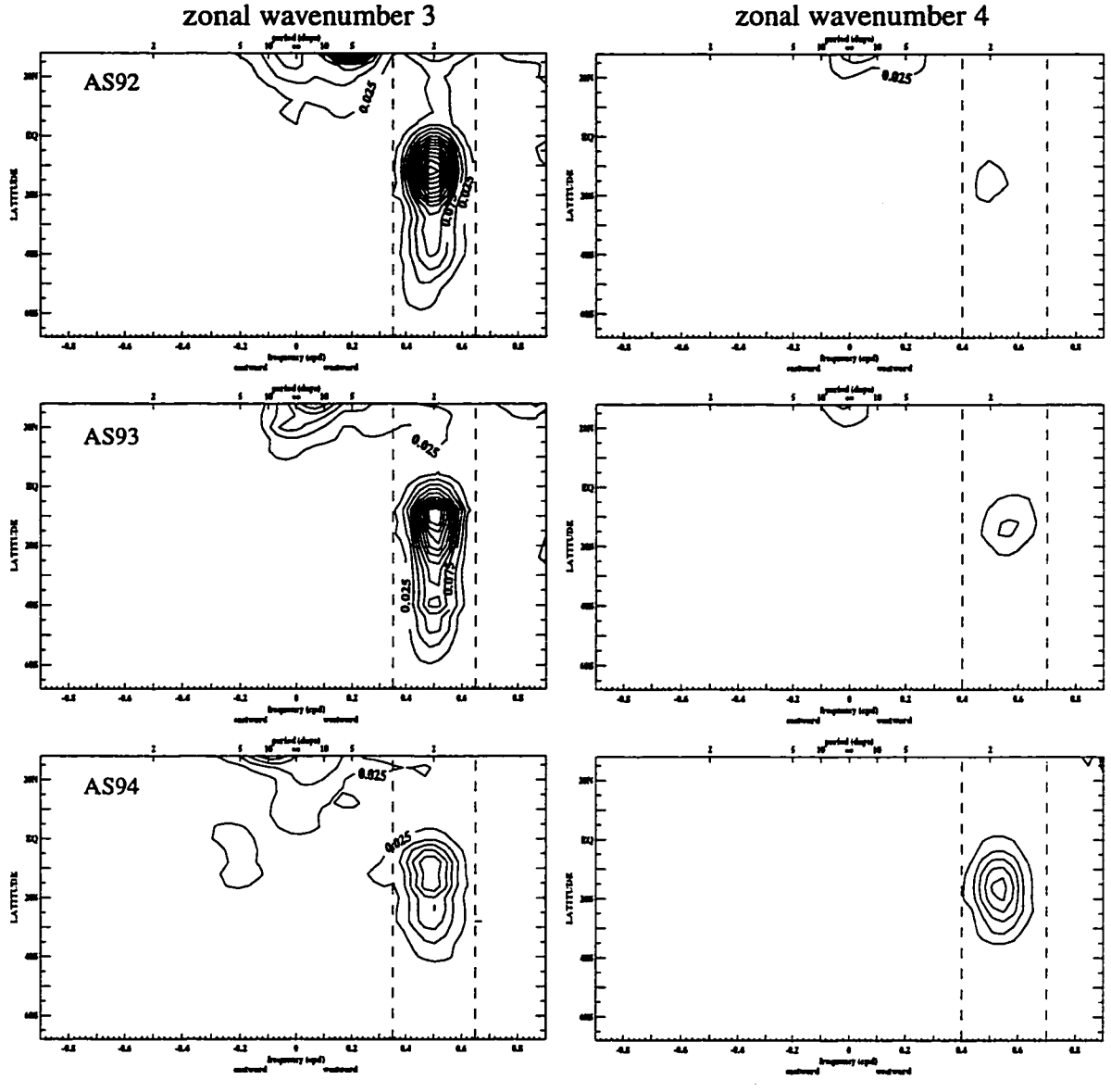

Figure 4.5: Zonal wavenumber 3 and 4 temperature power spectra averaged between 1.0 hPa and 0.46 hPa for three boreal summer data segments. The contours are displayed every 0.025 K^2 starting from 0.025 K^2. Signals enclosed by the frequency bands marked by the dashed lines are used to compute the variance. For zonal wavenumber 3, the band is between 0.35 and 0.65 cycles per day. For zonal wavenumber 4, the band is between 0.40 and 0.70 cycles per day.

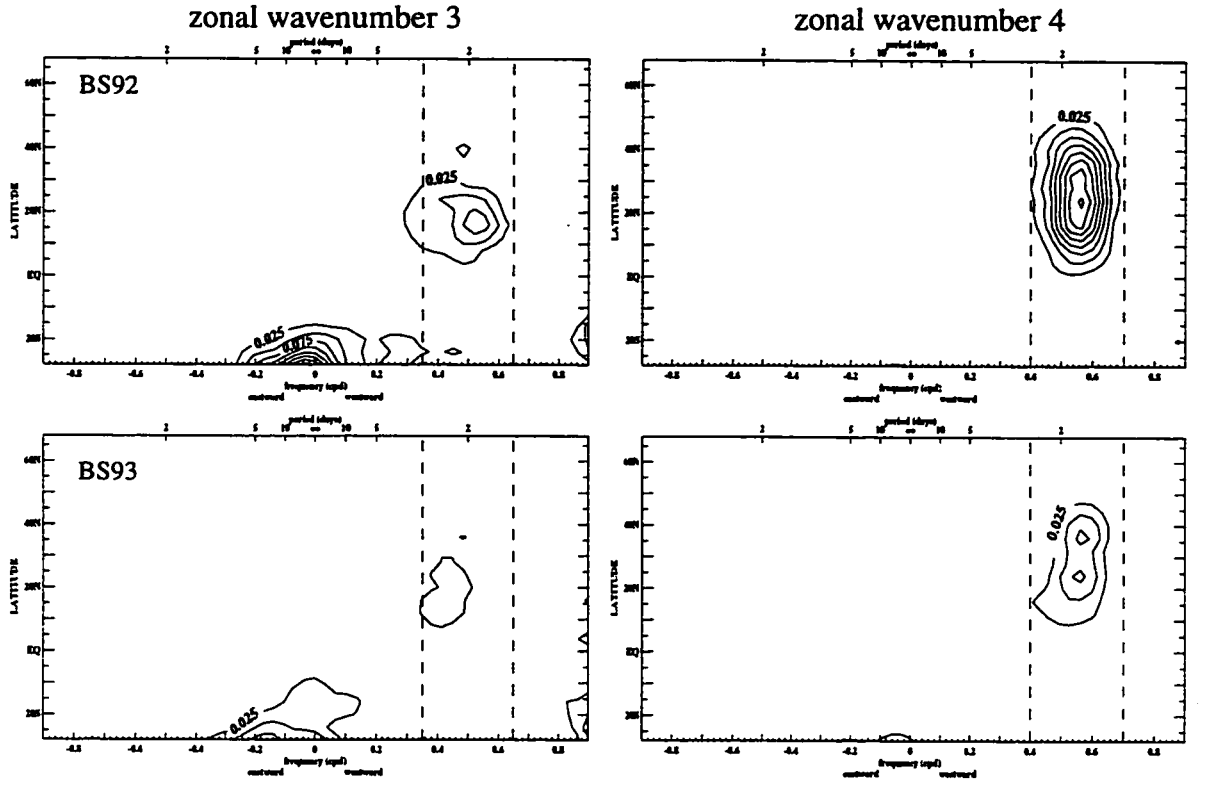

Figure 4.6: Zonal wavenumber 3 and 4 temperature power spectra averaged between 1.0 hPa and 0.46 hPa for the Boreal summers. The contours are displayed every 0.025 K^2. Signals enclosed by the frequency bands marked by the dashed lines are used to compute the variance. The bands are identical to those in Figure 4.5.

the second number roughly indicates the period of the spectral peak in the analysis

The amplitude structure of the two-day wave is calculated by taking the square root of twice the power spectra integrated over the frequency band. Using cross-spectral analysis, the accompanying wave phases are computed with respect to the spatial location of the spectral peak. The amplitude-phase meridional structure of the (3, 2.0) and (4, 1.8) modes are shown in Figure 4.7 for AS92 and BS92, respectively. The phase lines are computed with respect to 12° summer latitude and 0.464 hPa. Only regions where COH^2 is statistically significant above the 95% level are shown.

Both modes are similar in structure. The striking feature of the wave amplitude is the growth in latitudinal extent with height (a "wedge-like" shape). The tip of the wedge extends downward to near 2.1 hPa. The axis of maximum amplitude tilts slightly poleward with height. Overall, the structure is focused in the low summer latitudes. At a given latitude, an increase (decrease) in phase line with height indicates an eastward (westward) phase tilt with height. At a given height, an increase (decrease) in the phase line to the north indicates eastward (westward) tilt to the north. The zonal wavenumber is assumed to be positive. For both modes throughout much of the summer hemisphere, the phase tilts slightly eastward with altitude above 1.0 hPa.

The overall amplitude structures compare favorably with those identified by Burks and Leovy (1986) using the LIMS temperature data (see Figure 2.2). Both analyses find the shape of the two-day wave amplitude to point downward and equatorward and suggest that larger amplitude may occur higher up in the mesosphere. The wave phase generally tilts very weakly with height. The amplitude presented here is, however, slightly larger. This may be attributed to the wave's interannual differences although the difference can also be due to the differences between UARS MLS and LIMS data and retrievals.

During AS92, a significant portion of the (3, 2.0) amplitude shown in Figure 4.7 appears in the low winter latitudes. North of 20°N at 0.464 hPa, the winter signal is nearly

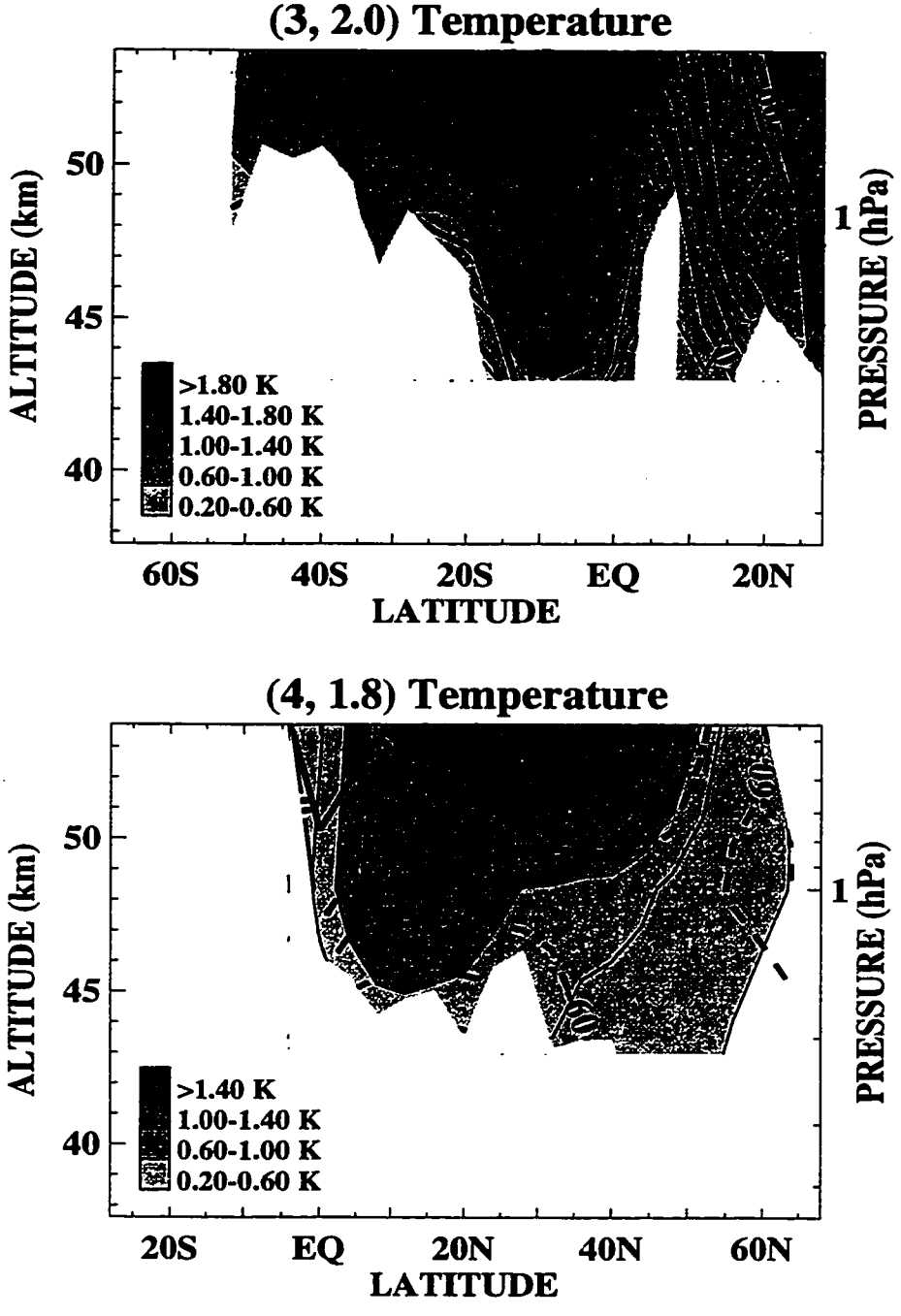

Figure 4.7: The meridional cross-section structure of the MLS temperature two-day wave. The wave amplitude is represented by shaded contours given in intervals of 0.2 K. The phase lines are shown as heavy solid and dashed contours, in increments of 30°. The top and bottom panels represent dominant modes during AS92 and BS92, respectively.

180° out of phase with respect to the reference point at 12°S. This vertically growing structure is suggestive of the temperature Rossby-gravity normal mode in theory and as observed by Wu et al.(1996) and Randel (1994). However, the (3, 2.0) meridional structure at other times *does not* exhibit this behavior.

To observe the wave's evolution in time, the wave variance is computed. The wave variance is defined as the square of the zonally averaged band-pass filtered field. For each mode of the two-day wave, the filtering is done for a given wavenumber band-passed over the appropriate frequency bands shown in Figure 4.5 and Figure 4.6. For completeness, the wave variance is determined for the entire data series from winter 1991 to fall 1994 (see Figure 3.1). Figure 4.8 and Figure 4.9 show the variance for (3, 2.0) and (4, 1.8) at 0.464 hPa where the wave signals are the strongest. The two-day wave activities are observed mainly during the available AS and BS data segments. Relatively strong wave signals are also present prior to these time periods when the data is available mainly in the winter hemisphere. Clearly, the observed temperature two-day wave surfaces semiannually after the solstice. The disturbance mainly resides in the summer hemisphere as confirmed by previous diagrams. The (4, 1.8) mode generally appears in the northern hemisphere during the boreal summer. The (3, 2.0) mode is observed mainly in the southern hemisphere during the austral summer. Detailed look at the wave variance will be deferred until next section when it will be discussed in conjunction with the basic wind evolution.

To examine the temperature wave variability, the latitudinally averaged two-day wave variances are shown in Figure 4.10 and Figure 4.11 for all available austral and boreal summers at 0.46 hPa. The latitudinal averaging is done from 28° in the winter hemisphere to 28° in the summer hemisphere. This latitudinal range is common for all data segments. Year-to-year variations are obvious in the modal amplitudes and peak time. Intra-annually, the austral (3, 2.0) mode is at least twice as strong as the boreal (3, 2.0) mode while the (4, 1.8) mode can be equally strong in both austral and boreal summer. The (3, 2.0) mode tends to dominate over the (4, 1.8) mode in austral summer (except during the 1993-94

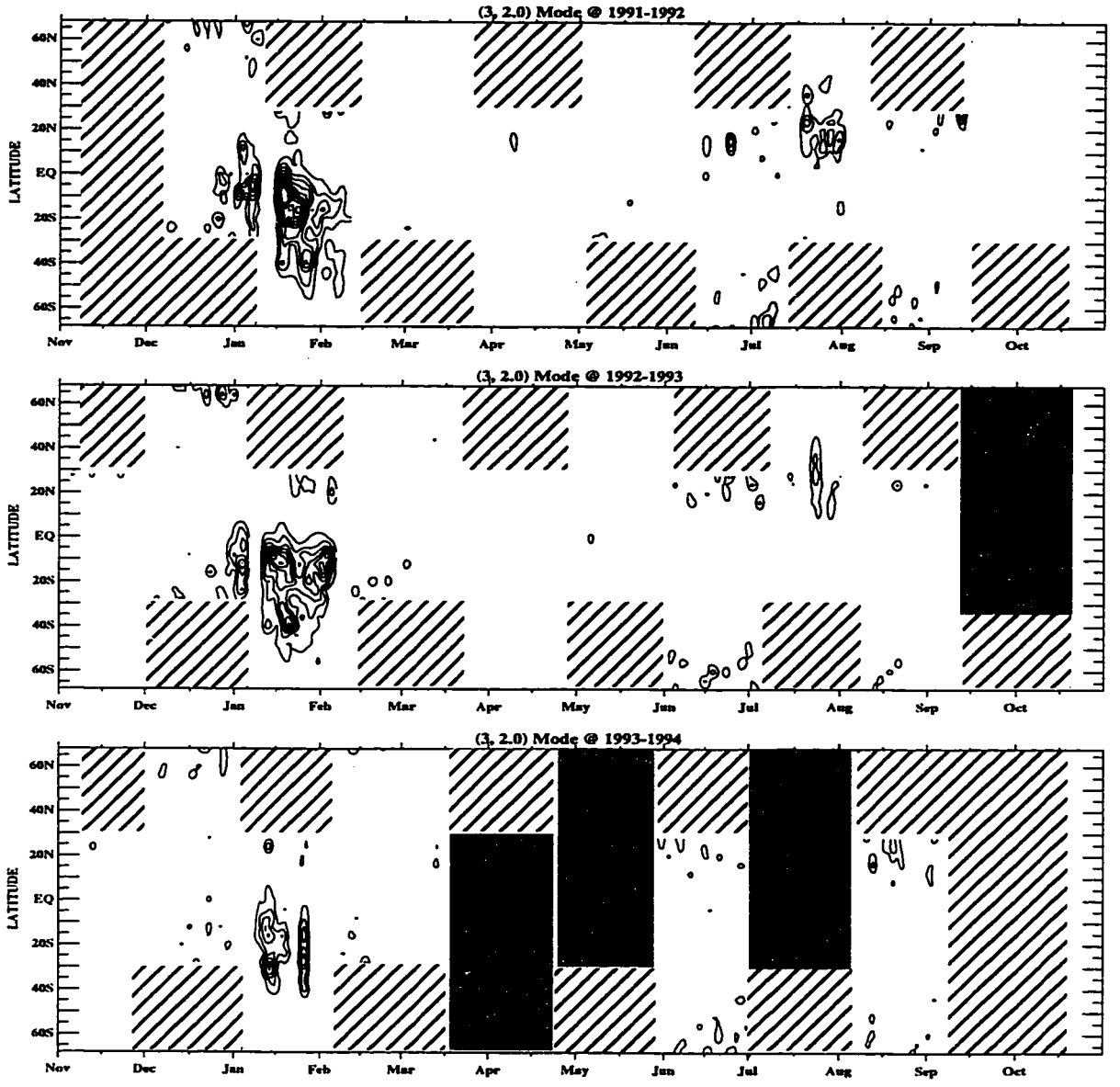

Figure 4.8: The (3, 2.0) mode variance at 0.46 hPa. This mode is synthesized from zonal wavenumber 3 disturbances over the westward frequency range of 0.35 to 0.65 cycles per day (between periods of 2.86-1.54 days). The contour interval is 1.0 K^2, starting at the 1.0 K^2 contour line. Hatched regions indicate times when no data are available and filled regions indicate times when no analysis is done.

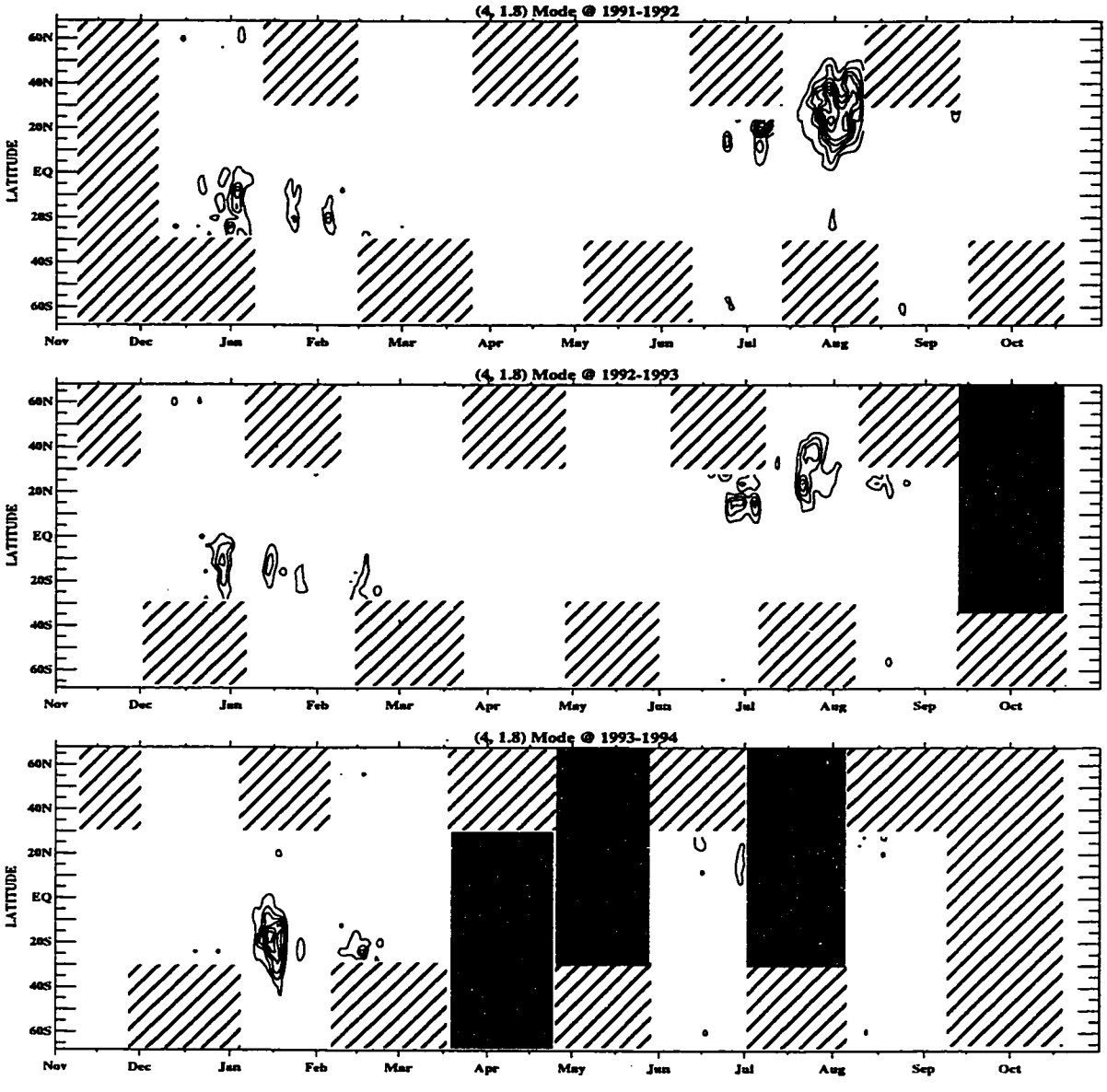

Figure 4.9: The (4, 1.8) mode variance at 0.46 hPa. The mode is synthesized from zonal wavenumber 4 disturbances over the westward frequency range of 0.40 to 0.70 cycles per day (between periods of 2.50-1.43 days). Other descriptions are identical to Figure 4.8.

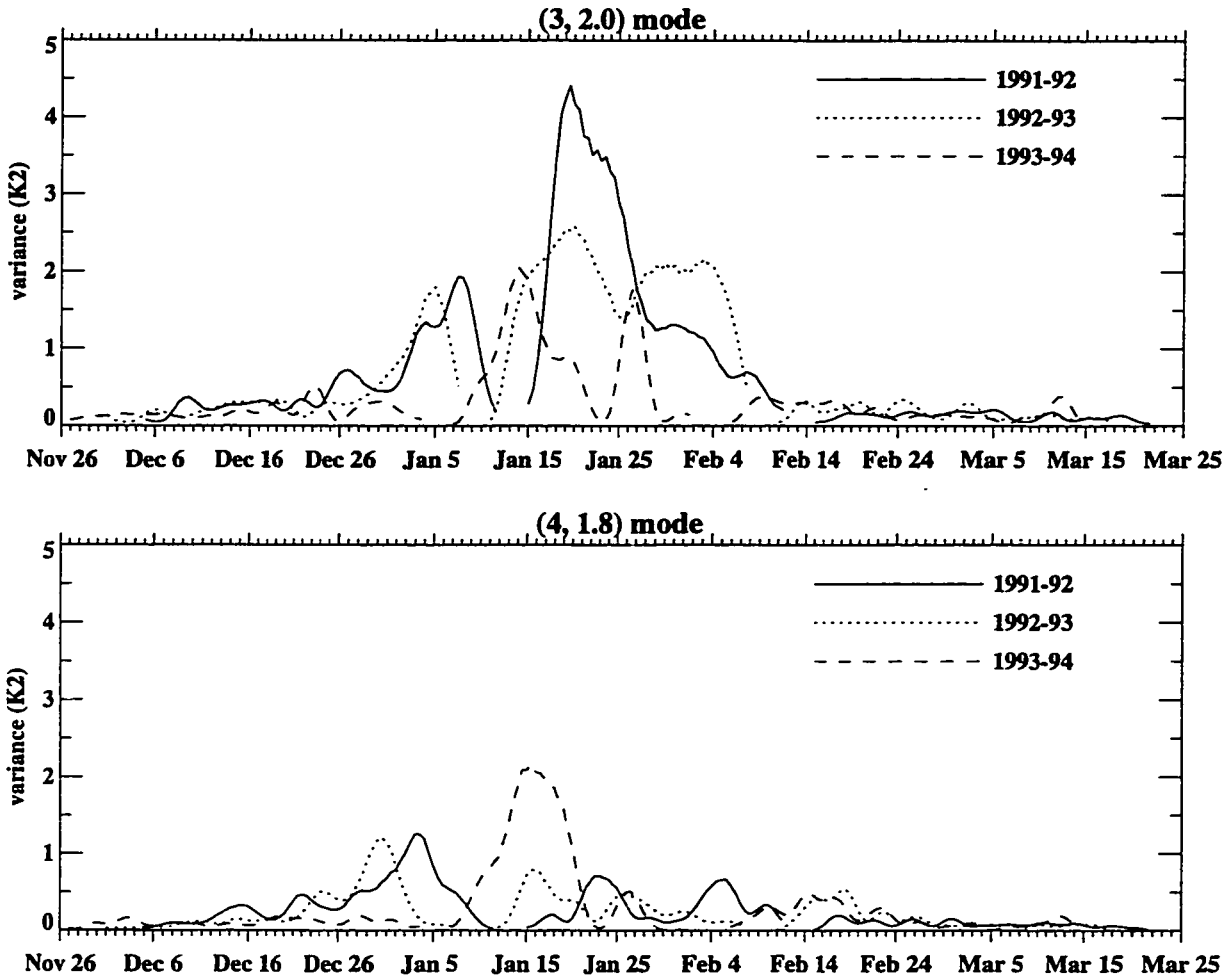

Figure 4.10: Two-day temperature wave variability at 0.46 hPa. The variance is averaged between 28° latitude of the winter hemisphere to 28° latitude of the summer hemisphere.

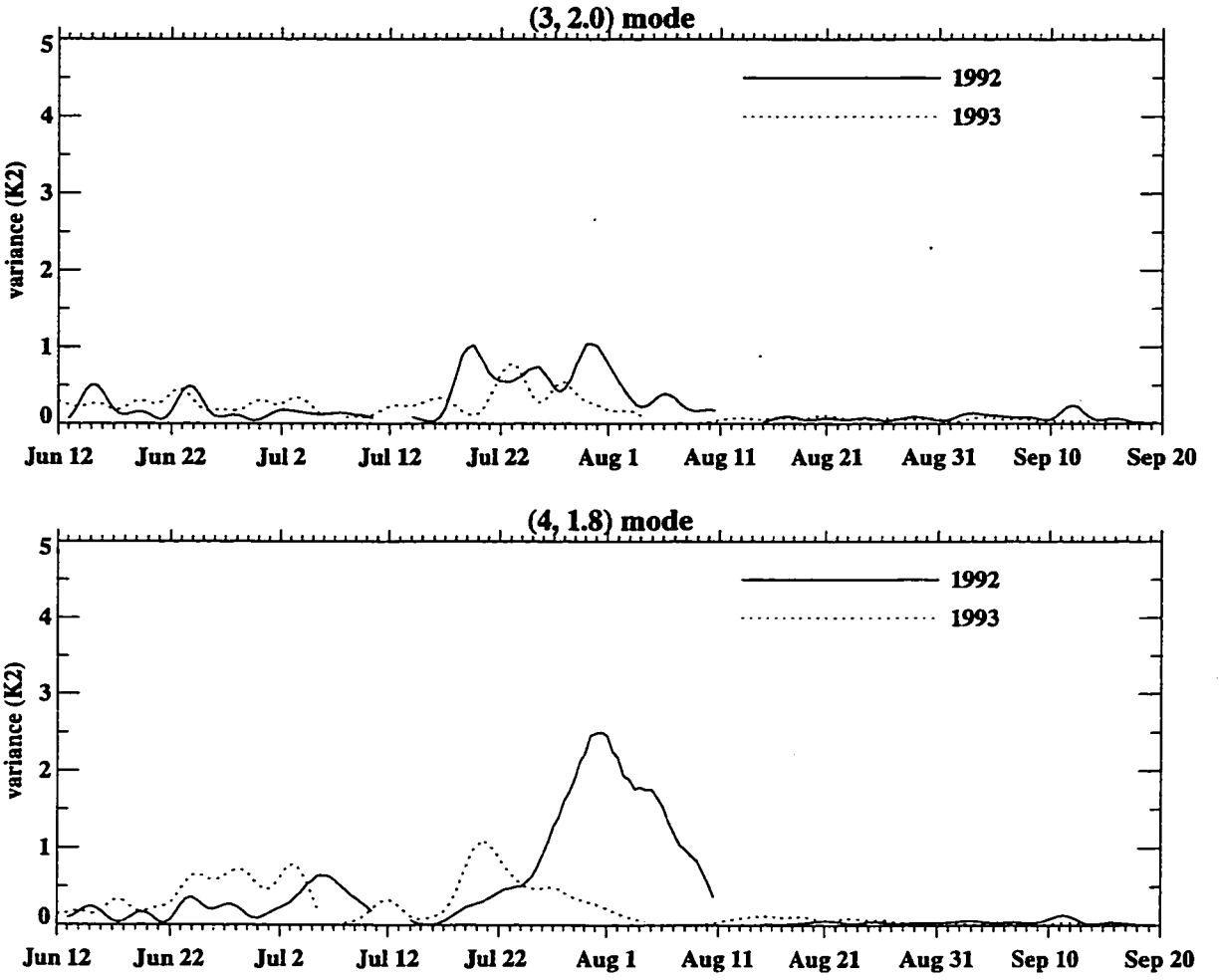

Figure 4.11: Two-day temperature wave variability at 0.46 hPa. The variance is averaged between 28° latitude of the winter hemisphere to 28° latitude of the summer hemisphere.

case). However, during the boreal summer, the (4, 1.8) mode can have considerably larger amplitude than the (3, 2.0) mode. This pattern of modal dominance agrees with the finding of Wu et al. (1996) who observed the two-day wave using a different version of the 1993 MLS temperature data (see Figure 2.3 and Figure 2.4). The times when these modes maximize also concur with their study. At these altitudes and for disturbances with vertical wavelength larger than 5 km, the radiative time scale is likely to be less than 5 days (Fels, 1982). Despite strong radiative damping, the dominant mode is observed to grow steadily over time on the order of 5-10 days and persists, in some instances, well into mid summer.

4.2 EVOLUTION OF MEAN WIND AND WAVE

The two-day wave temperature structure in relation to the zonal wind is now examined. Regions of reversed quasi-geostrophic potential vorticity (QGPV) gradient ($\bar{q}_\varphi \leq 0$, where $\bar{q}_\varphi$ is defined in Equation 3.12) and the wave critical surfaces (where the waves' zonal phase speed is Doppler-shifted to zero by the zonal wind) will also be examined. For the (3, 2.0) mode, the wave period of 2.0 days is used to determine the wave phase speed. For the (4, 1.8) mode, the wave period of 1.8 days is used. The zonal phase speed (c_r) is given by the relation $c_r \equiv \omega/k$, where ω is the wave frequency in radians per second and k is the wavenumber in m^{-1}. Since the wavenumber can be expressed in terms of the (nondimensional) planetary zonal wavenumber (s): $k = s(a\cos\varphi)^{-1}$, the zonal phase speed can be written as:

$$c_r = \xi\left(\frac{\cos\varphi}{sP}\right) \tag{4.1}$$

where $\xi \cong -463$ $ms^{-1}day$ and P is the wave period in days. The zonal wavenumber (s) is always taken to be positive and the period is positive for westward (ground relative) moving waves.

4.2.1 AUSTRAL SUMMERS

The bottom panels of Figure 4.12, Figure 4.13, and Figure 4.14 show a detailed examination of the background wind evolution for austral summer of 1991-92, 1992-93, and 1993-94, respectively, at 0.464 hPa. Easterly wind persists over much of the season in the low winter latitudes. Superimposed on this equatorial wind pattern are brief episodes of easterly intrusion that can displace the zero wind further into the winter hemisphere. The summer easterly jet core has a magnitude of about 70-80 ms^{-1} and resides near 20°S. On the equatorward flank of the easterly core, meridional wind shear is quite strong and, in the equatorial region, the wind shear can exceed *f*, the Coriolis parameter. This latter region is marked by the enclosure of the bold black line and indicates that the atmospheric flow is inertially unstable.

After the solstice, notable regions of negative $\bar{q}_\varphi$ appear in the low summer latitudes. In the 1991-92 and 1992-93 case, these regions coincide with the tendency of the adjacent easterly contours to "bunch up" just north of the easterly jet core. A good example of this behavior is seen around Dec. 29, 1992 (Figure 4.13) around 5°S. This implies that the increased horizontal wind curvature in the low summer latitudes is mainly responsible for the QGPV gradient reversal. Examination of the terms (B, C) that make up $\bar{q}_\varphi$ in Equation 3.12 reveals that term B (which essentially represents the horizontal curvature of the mean wind) is the major contributor to the negative region in each case. That is, the term A+B generally accounts for nearly all of the negative $\bar{q}_\varphi$ region where strong meridional wind shear is observed. Similar mean flow evolution and the location of negative $\bar{q}_\varphi$ regions near the easterly jet core are also observed at 1.0 hPa (not shown). In the 1993-94 case, negative $\bar{q}_\varphi$ regions are evident closer to the jet core and depend significantly on the vertical wind curvature contribution (i.e. term A+B+C accounts for the negative $\bar{q}_\varphi$).

The two-day wave variances are presented in the top panels of Figures 4.12-4.14. The (3, 2.0) mode and (4, 1.8) mode are shown in blue and red contours. A common feature in all three cases is the proximity of the temperature variances to regions of $\bar{q}_\varphi \leq 0$ on the equatorward flank of the easterly jet. Within the vicinity, the critical lines of both the (3, 2.0) mode and the (4, 1.8) mode are also present as shown by the thick blue and red lines.

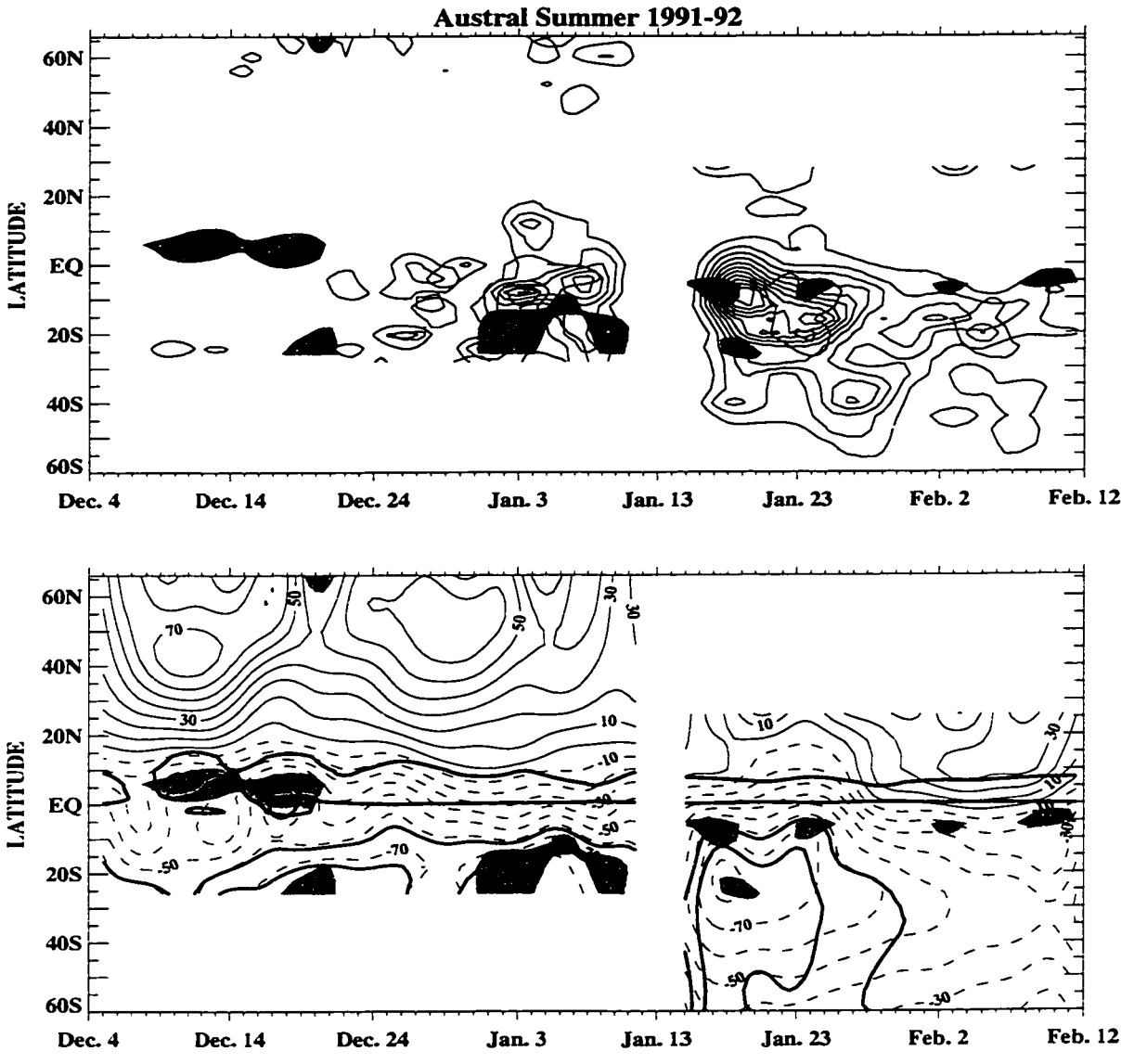

Figure 4.12: Close-up of the two-day temperature wave variances (top) and mean wind evolution (bottom) at 0.46 hPa during the austral summer of 1991-92. Thin blue contours represent the (3, 2.0) variance and the thin red contours represent the (4, 1.8) variance. Both are given in increments of 1.0 K^2 starting at 1.0 K^2. The zonal mean zonal wind is shown as thin black contours in the bottom figure with dashed contours denoting easterly wind. The bold blue and red lines are the critical surfaces of the (3, 2.0) mode and (4, 1.8) mode, respectively. The shaded regions are areas where the gradient of the quasi-geostrophic potential vorticity is less than or equal to zero. The black bold line encloses region of inertial instability.

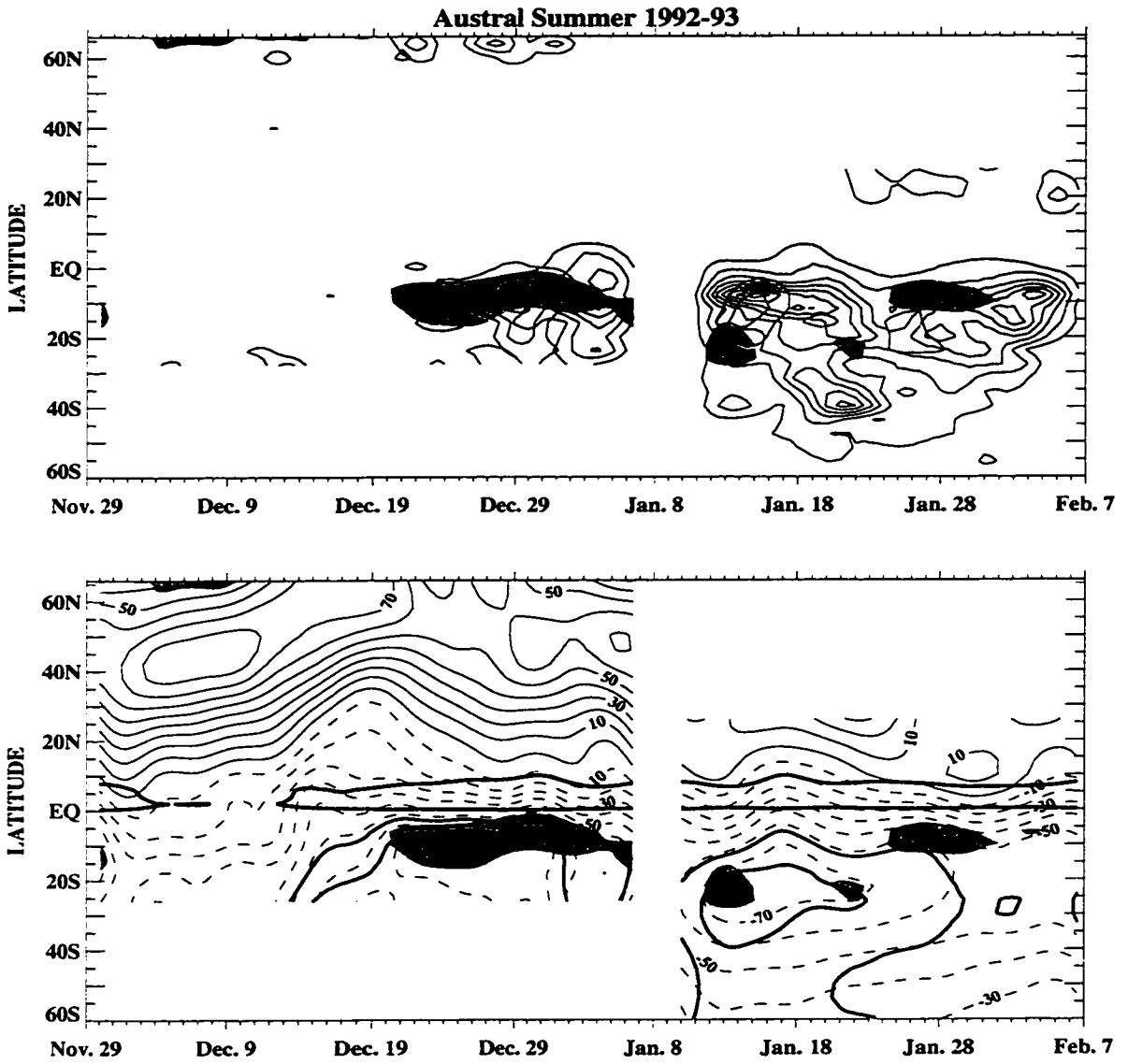

Figure 4.13: Same as Figure 4.12 except for austral summer of 1992-93. Note that the dates are also different.

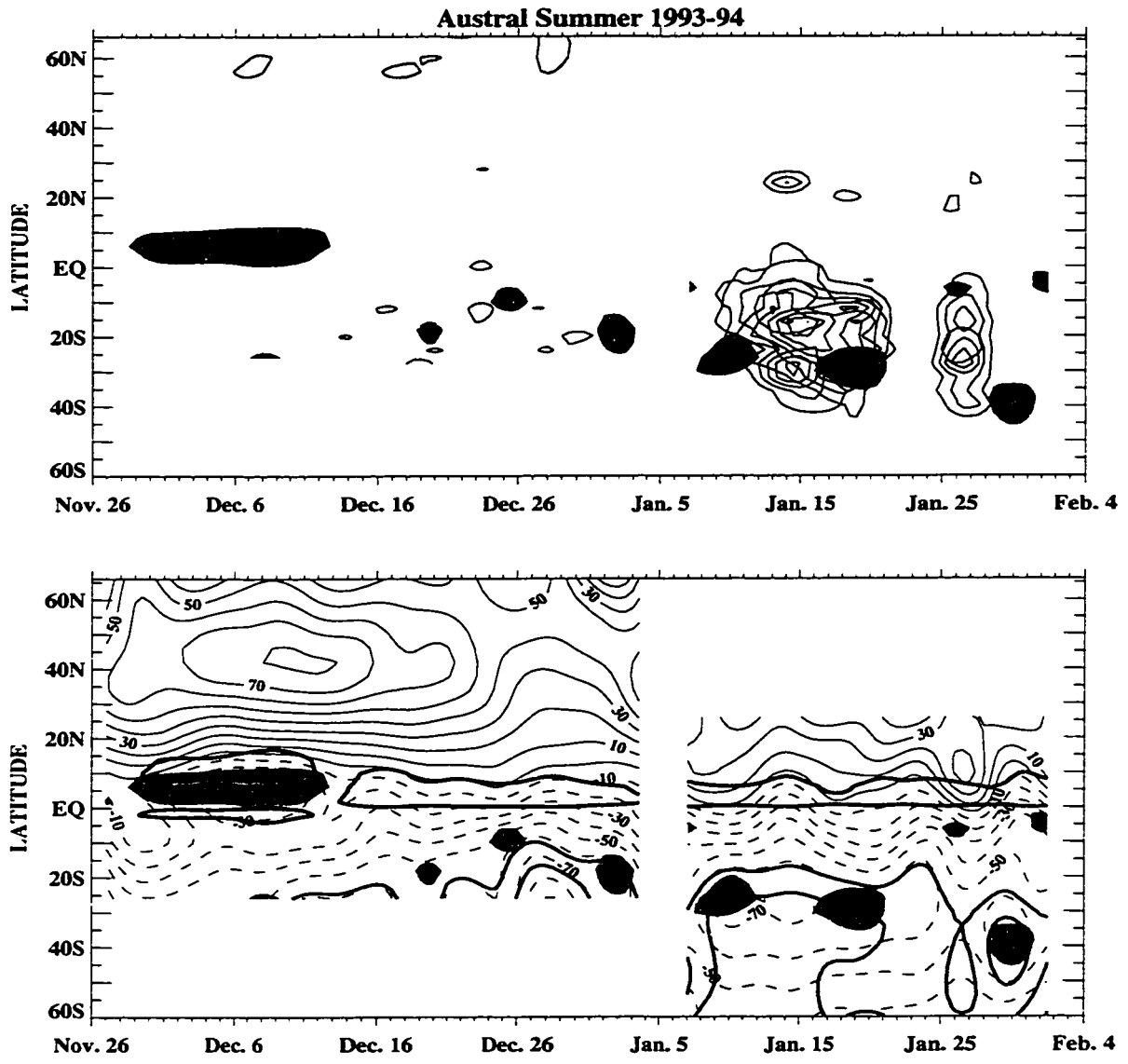

Figure 4.14: Same as Figure 4.12 except for austral summer of 1993-94. Note that the dates are also different.

Note that during each austral summer, the easterlies are strong enough to support both critical lines. These lines tend to intersect the $\bar{q}_\varphi \leq 0$ region when significant wave variances are observed.

From a wave instability point of view, the presence of the critical surface with negative $\bar{q}_\varphi$ regions suggests that the observed modes are manifested from mean flow inflection instability. The growth is quite rapid for the dominant mode in the highly dissipative lower mesosphere. The mode amplitude equilibration (peaking of the variance) appears to coincide with the removal of the $\bar{q}_\varphi \leq 0$ region and a possible mean flow alteration. Similar instability interpretation of the two-day wave has been used by Randel (1992) as illustrated in Figure 2.16 and Orsolini et al. (1997). As a barotropic instability, the wave tends to flux westerly momentum from the equatorial region toward the easterly jet core, reducing the strength of the easterly jet core while increasing the easterly strength of the equatorial winds. Baroclinic instability may also be possible, especially in the 1993-94 austral summer case. Consistent with this instability picture would be an emanation of wave Eliassen-Palm (EP) flux vectors from the wave critical surface during the growth of modal disturbances. The wave's effects on the mean flow over the equatorial region is not quite obvious due to probable mean wind driving effects of other planetary waves. However, some indication exists that the easterly jet core may be accelerating as the two-day wave saturates.

Quasi-stationary, mid-latitude winter planetary waves are known to propagate meridionally toward the equatorial regions. Figure 4.15 shows the variance associated with these waves in the low winter latitudes during the same time segments shown in the above diagrams. The variance is computed from zonal wavenumber 1 and 2 disturbances that have been low-pass filtered to retain only signals slower than 5 day period. The variance is then latitudinally averaged from 20°N-28°N and vertically averaged from 2.2-0.464 hPa.

The observed persistence of the easterlies in the low winter latitudes appears to be associated in part with the prolonged presence (and damping) of these waves throughout

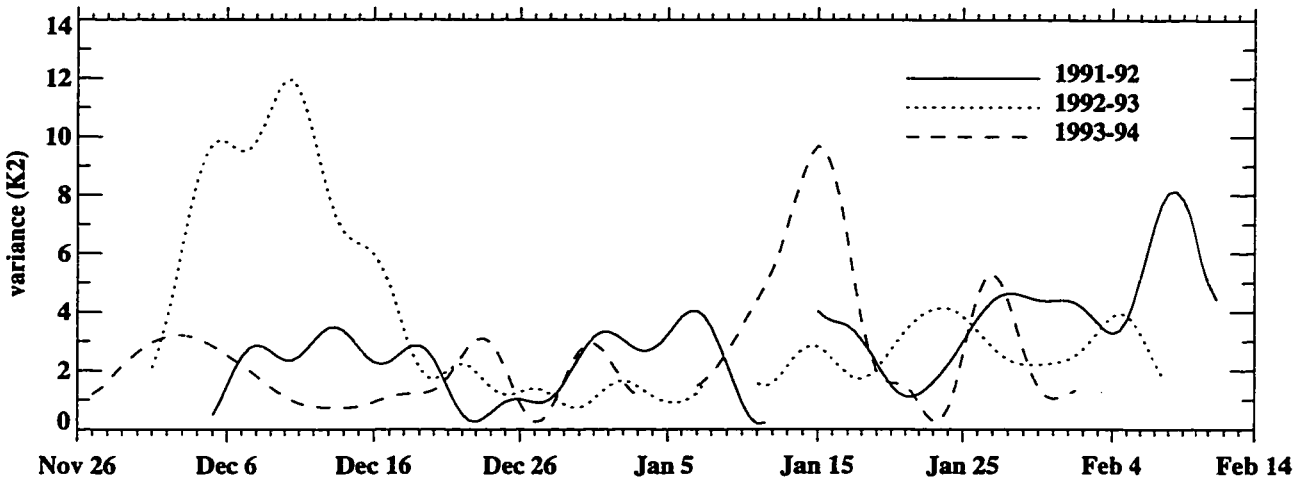

Figure 4.15: Variance of mid-latitude winter planetary waves (zonal wavenumber 1-2). The variance is computed from disturbances that have been low-pass filtered to retain signals slower than 5 days. The variance is latitudinally averaged between 20°N-28°N and vertically averaged between 2.2-0.46 hPa. Gaps indicate yaw periods and regions not analyzed.

much of the season. Wave damping can locally affect the mean flow directly or drive a residual mean circulation that advects easterlies across the equator. In the 1992-93 case (dotted line), a strong amplification of the mid-latitude waves around Dec. 6, 1992 is seen to precede the pronounced easterly intrusion around Dec. 19, 1992 (see Figure 4.13). Another notable mid-latitude wave peak happens around Jan. 15, 1994, but the possible corresponding easterly intrusion is not dramatic.

Near the stratopause (~1 hPa), cross-equatorial advection by residual mean circulation tends to produce strong cross-equatorial wind shear. By angular momentum conservation, the advected easterlies are strengthened as parcels move equatorward while the advected westerlies are also strengthened as parcels move away from the equator. As a result, a strong cross-equatorial shear can occur, and the normal gradient of angular momentum can be reversed. The region where $f(f-a^{-1}\overline{u}_{\varphi}) < 0$ is said to be inertially unstable. Here, $a^{-1}\overline{u}_{\varphi}$ represents the horizontal shear of the mean wind. Areas where this condition holds are also shown in Figure 4.12-Figure 4.14. The regions are focused mainly over the equatorial region where the Coriolis parameter is small.

Observational evidence of inertial instability during the same time period as this study has been recently presented by Hayashi et al. (1998). They use UARS Cryogenic Limb Array Etalon Spectrometer (CLAES) temperatures to elucidate the vertically stacked disturbance structure associated with inertial waves. Unlike the MLS data, this particular data product has a finer vertical resolution of about 2.5 km, so it is amenable for the examination of the disturbance's small vertical scale (~5-14 km). Figure 4.16 and Figure 4.17 summarize the results of Hayashi et al. (1998). Their study covers the early winter 1992 to early spring 1993. Inertial wave activities are readily observed over the equatorial band after the solstice as episodic pulses confined in various longitudinal bands. The strongest mid-latitude planetary waves are observed to peak nearly in coincidence with the initial inertial wave pulses. Their results largely confirm the earlier observation of Hitchman et al. (1987) using the 1979 LIMS temperature. Both studies find inertial instability ("pancake") structure to occur when the atmosphere flow is inertially unstable and in conjunc-

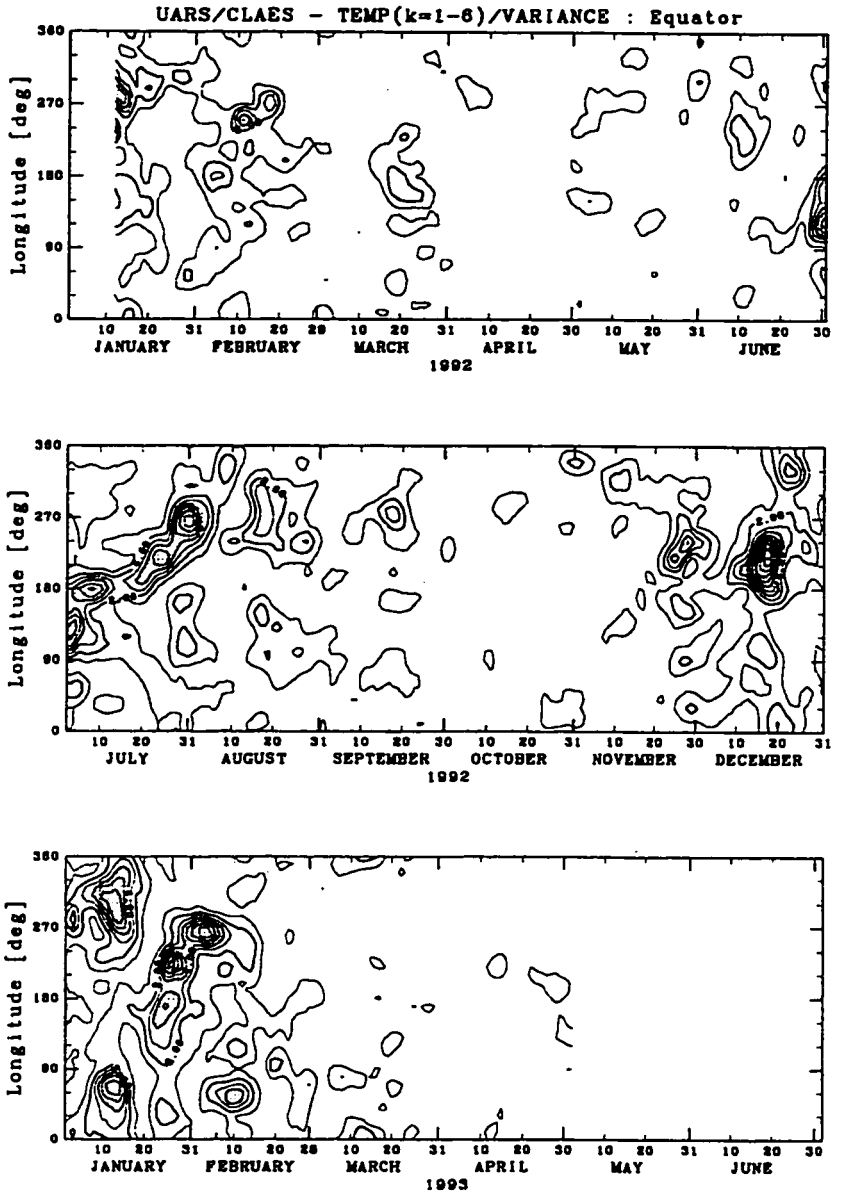

Figure 4.16: Inertial instability wave index. Time-longitude plot of the UARS CLAES temperature disturbance (zonal wavenumber 1-6) is averaged between 4.6 hPa and 0.2 hPa and [4°S, 4°N] latitudinal band. Before computing the variance, the data have been smoothed by a 7-day running mean and filtered vertically by a high-pass filter to remove the influence of winter planetary waves. Contour interval is 1 K. Shaded regions (> 4K) indicate the appearance of temperature pancake structures. [Taken from Hayashi et al. (1998).].

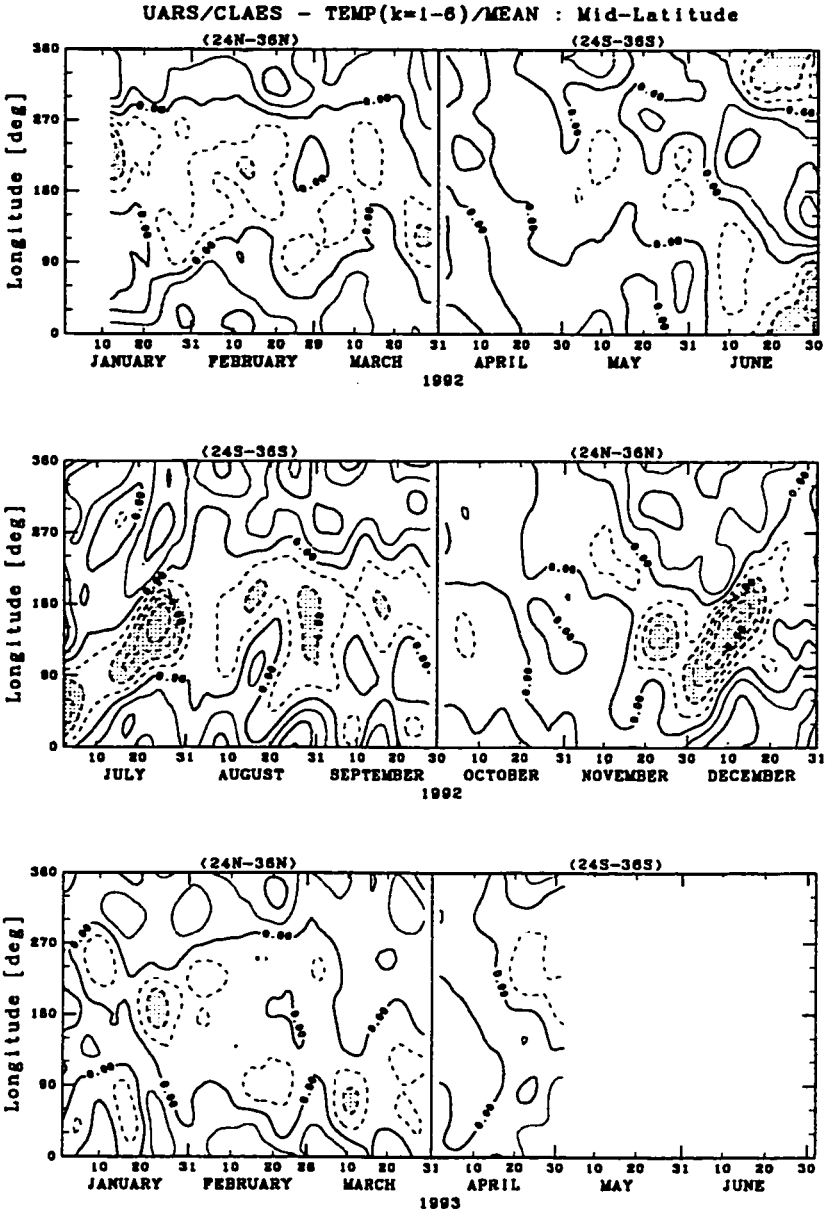

Figure 4.17: Mid-latitude winter planetary wave index. Time-longitude evolution of the UARS CLAES temperature disturbance (zonal wavenumber 1-6) is averaged between 4.6 hPa and 0.2 hPa and between [24°N, 36°N] if during October-March or between [24°S, 36°S] if during April-September. Before computing the disturbance, the data have been smoothed by a 7-day running mean. Contour interval is 2 K. Shaded regions (< -4K) indicate the appearance of strong mid-latitude winter planetary wave. [Taken from Hayashi et al. (1998).].

tion with strong mid-latitude planetary wave activity.

Comparison of Figure 4.16 and Figure 4.17 to Figure 4.13 suggests a possible connection among mid-latitude winter planetary wave, inertial wave, and the two-day wave during 1992-93 austral summer. This connection is discussed by Orsolini et al. (1997). First, strong mid-latitude planetary wave activity in late November to late December 1992 organizes inertial instability by locally advecting anomalous PV across the equator. Note that the strong mid-latitude wave disturbance in Figure 4.17 coincides in time with the wave variance peak presented in Figure 4.15 (dotted line). Momentum redistribution associated with inertial instability circulation tends to flux westerly momentum across the equator and, in the process, increases horizontal wind curvature in the easterlies as shown schematically in Figure 2.13(b). The increased curvature is responsible for the negative $\bar{q}_\varphi$ regions near 10°S (around Dec. 29, 1992) and the destabilization of the easterly wind as made evident by the subsequent appearance of the observed two-day wave. The overall picture can be viewed as a consecutive sequence of wave events initiated by a strong mid-latitude planetary wave, followed by inertial waves, and concluding with the two-day wave. The latter two wave events transfer momentum from the low winter latitude band across the equator and into the easterly jet core. Similar wave events may also be occurring in the 1991-92 austral summer as the $\bar{q}_\varphi$ negative regions are largely associated with strong horizontal wind curvature (see Figure 4.12). Hints of inertial waves and mid-latitude planetary waves are seen around Jan. 10, 1992 in Figure 4.16 and Figure 4.17.

4.2.2 BOREAL SUMMERS

Figure 4.18 and Figure 4.19 show a detailed examination of the background wind evolution for the boreal summers of 1992 and 1993, respectively, at 0.464 hPa. Unlike the austral summer, persistent easterly winds are noticeably lacking in the low winter latitudes. Brief episodes of easterly intrusion are nonetheless observed. The boreal summer easterly jet core has a magnitude of only about 50-55 ms^{-1} which is considerably weaker than the austral easterly jet at the same level. The jet core also resides at slightly higher lat-

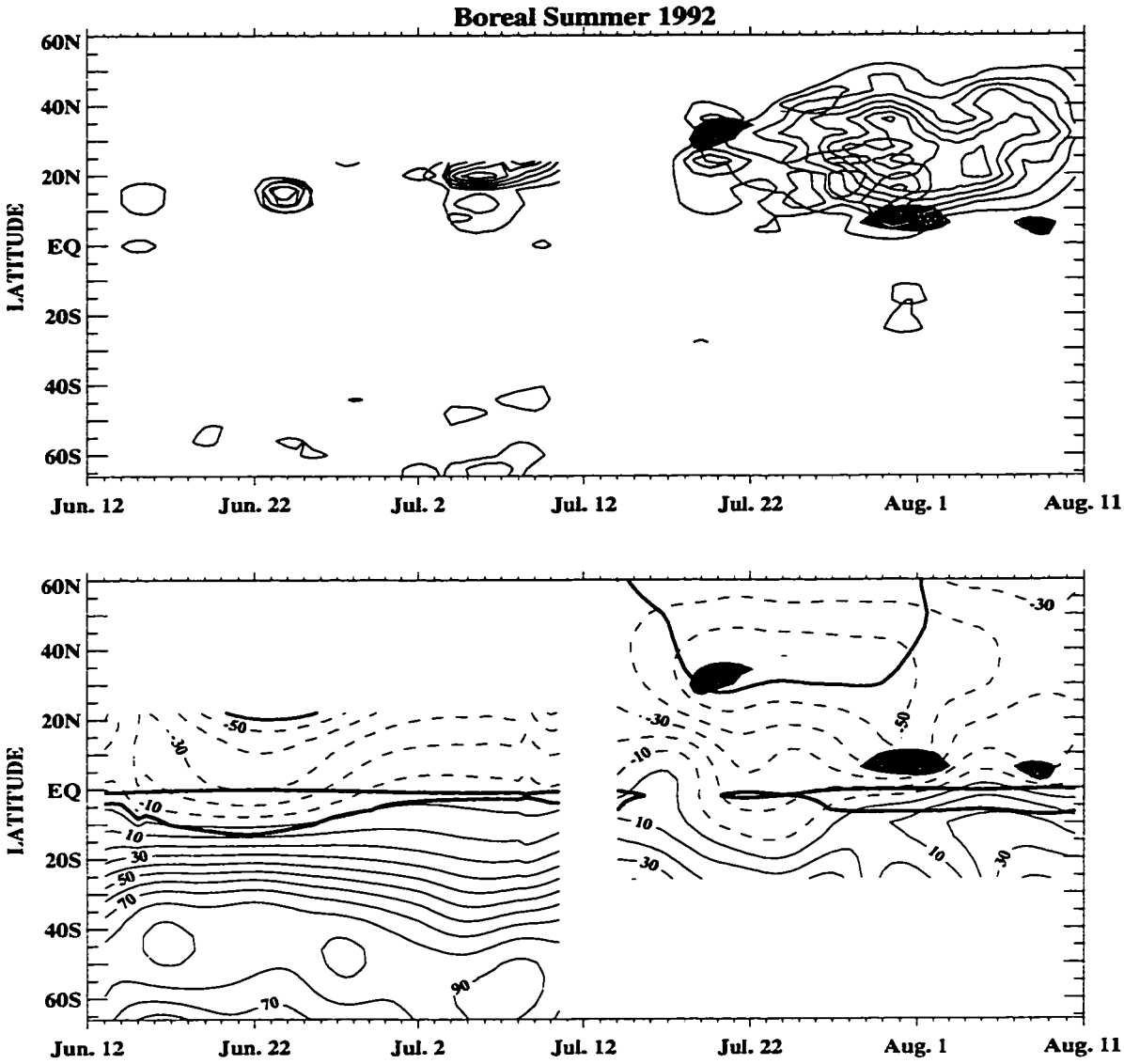

Figure 4.18: Close-up of the two-day temperature wave variances (top) and mean wind evolution (bottom) at 0.46 hPa during the boreal summer of 1992. Thin blue contours represent the (3, 2.0) variance and the thin red contours represent the (4, 1.8) variance. Both are given in increments of 1.0 K^2 starting at 1.0 K^2. The zonal mean zonal wind is shown as thin black contours in the bottom figure with dashed contours denoting easterly wind. The bold blue and red lines are the critical surfaces of the (3, 2.0) mode and (4, 1.8) mode, respectively. The shaded regions are areas where the gradient of the quasi-geostrophic potential vorticity is less than or equal to zero.

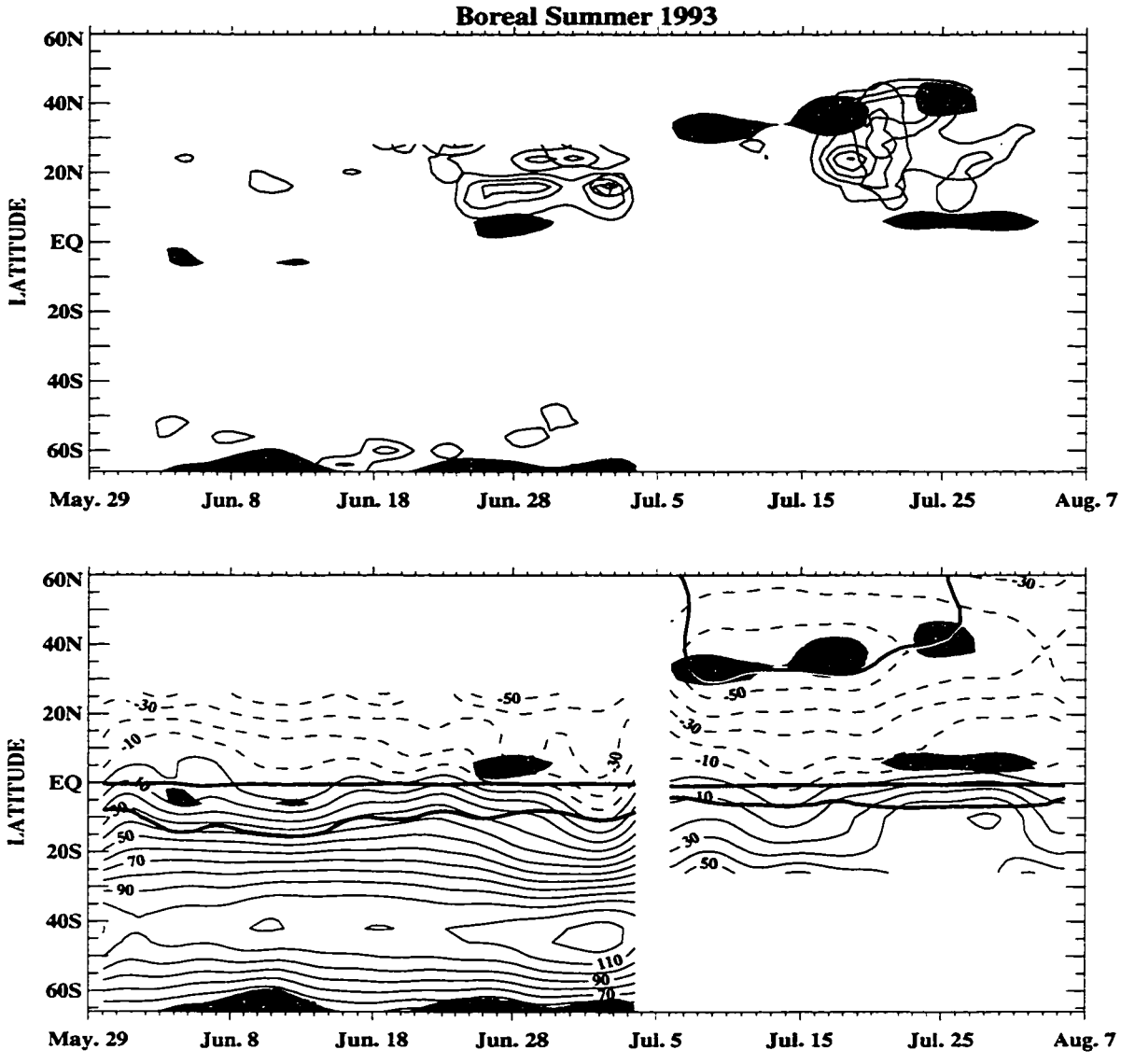

Figure 4.19: Same as Figure 4.18 except for boreal summer of 1993. Note that the dates are also different.

itude near 30°S. The weaker wind condition is only able to support a critical line of the (4, 1.8) mode. On the equatorward flank of the easterly core, the meridional wind shear is noticeably weaker than in austral summer. As a result, the negative $\overline{q}_{\varphi}$ regions that intersect the critical line are mainly in the easterly jet core where the vertical wind curvature contributes significantly to the sign of $\overline{q}_{\varphi}$. Note that this scenario is somewhat analogous to the 1994 austral summer case. In lower winter latitudes, the wind flow is inertially unstable over much of the season as shown by the areas enclosed by the bold black line, especially during 1993. The inertially unstable regions occur despite the failure of easterlies to significantly intrude across the equator at this level.

Similar to the austral summers, the two-day wave variances are observed near regions where the critical line intersects areas of $\overline{q}_{\varphi} \leq 0$. Inflection instability appears to explain the appearance of the (4, 1.8) mode. As the mode grows, there is indication of the removal of instability which is baroclinic as well as barotropic. Around July 5, 1992 and Jun. 28, 1993, some variance is seen and may be associated with mean flow instability north of the data coverage. Interestingly, the (3, 2.0) variance is also apparent albeit very weak. Given the weak easterly condition during the boreal summer, the observed (3, 2.0) mode does not appear to be an instability phenomenon although wave-wave interaction with the (4, 2.0) may be possible. The strength and longevity of the (3, 2.0) mode seems to parallel that of the (4, 1.8) mode.

Figure 4.20 shows the variance associated with the quasi-stationary mid-latitude winter waves in the low winter latitudes during the same time segments. The variance is computed in the same manner discussed in the previous section except the latitudinally averaging band is from 20°S-28°S. The observed variance at these latitudes can be comparable or even larger than observed during the austral summer (see Figure 4.15). The variance peak at different times may account for the brief easterly acceleration in the low winter southern latitudes.

The 1992 mid-latitude wave variance (solid line) agrees fairly well with the planetary

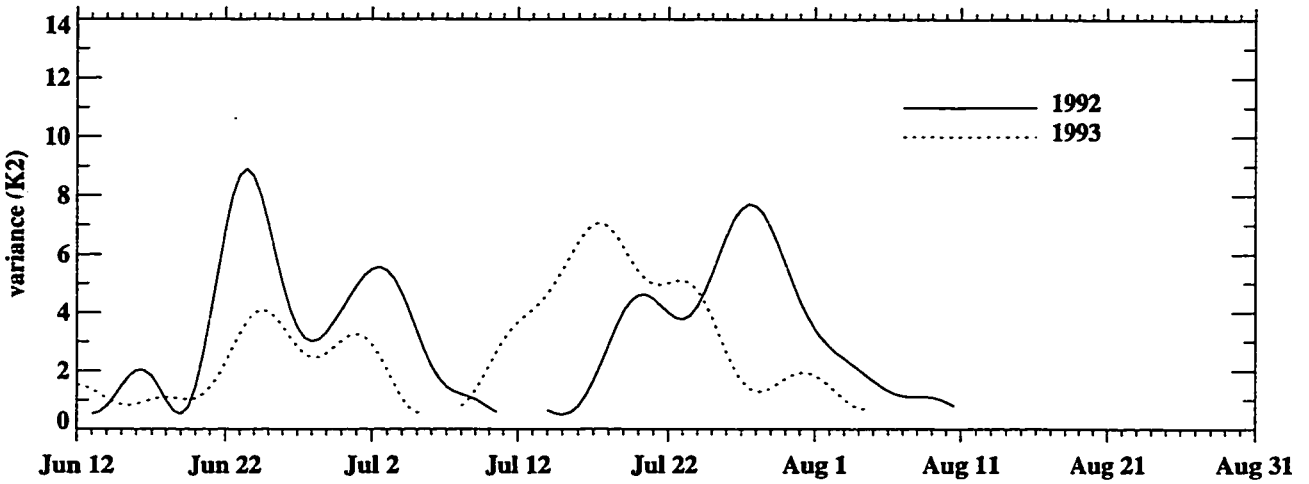

Figure 4.20: Variance of mid-latitude winter planetary waves (zonal wavenumber 1-2). The variance is computed from disturbances that have been low-pass filtered to retain signals slower than 5 days. The variance is latitudinally averaged between 20°S-28°S and vertically averaged between 2.2-0.46 hPa. Gaps indicate yaw periods and regions not analyzed.

wave indices of Hayashi et al. (1998) shown in Figure 4.17. In conjunction with this wave activity, inertially unstable structure is observed in the CLAES data (Figure 4.16). The momentum redistribution by inertial wave activity should increase the horizontal curvature of the easterlies. The negative $\overline{q}_{\varphi}$ region around August 1, 1992 may be attributed to the inertial wave activity ending in late July. This region is however well removed from the critical line. Hence, inertial instability does not appear to set up favorable mean flow for the instability growth of the two-day wave as discussed in the 1992 and 1993 austral summer. The two-day wave during the 1993 case is likewise not related to the inertial wave activity. On the other hand, strong wind shear set up by gravity wave drag can also destabilize the easterly jet and may be responsible for the two-day wave during the observed boreal summers (and possibly the 1994 austral summer case too). The role of gravity wave drag in relation to the two-day wave has been noted by Norton and Thuburn (1996, 1997).

4.3 WATER VAPOR FIELD

As discussed in Chapter 2, the meridional wind variations associated with the two-day wave can be quite large, with amplitude as big as 65 ms^{-1} near 95 km (Wu et al., 1993; Harris, 1994). Latitudinal transport of long-lived tracer by the two-day wave may then perhaps be the most effective mixing process in the summer middle atmosphere. Plumb et al. (1987) estimate the meridional parcel displacement associated with a two-day event to be on the order of a 1000 km in the mesosphere. For this reason, one may expect a two-day wave behavior to appear in a passive tracer distribution each summer.

The MLS observations of the H_2O field unfortunately ceased in April 1993. This limits the number of observed summers to three: two austral summers and one boreal summer. Moreover, the MLS measured levels for H_2O only extend up to 0.22 hPa (~59 km) where the wave meridional wind amplitude may not be quite as large. Despite these limitations, two-day wave signals are nevertheless observed. During 1992 austral summer, the two-day wave signature is most dominant in relation to other existing wave signals and has a coherent wave structure. In this section, most emphasis will be placed on the wave event

in AS92. During other times, only weak two-day signals are found.

Figure 4.21 shows the unfiltered synoptic maps of the H_2O distribution on the 1800 K potential temperature surface (approximately 1 hPa) for AS92. Near 20°S, a prominent zonal wavenumber 3 signal repeats about every two days. Half-daily maps and spectral analysis (discussed below) confirm that this signal propagates westward in time. Other waves detected by the satellite are also seen. In particular, a disturbance of zonal wavenumber one with westward propagating period between 5-10 days is observed in conjunction with the wavenumber 3 two-day wave. Tongues of dry low latitude air can be seen to perturb the transport "barrier" region where the tracer distribution shows a strong latitudinal gradient between 20°S and 40°S. Strong mixing may be occurring across the gradient near 60° longitude on February 2 as result of meridional folding of the isopleths.

Globally averaged spectral signals for AS92 are displayed in Figure 4.22. A well defined wavenumber 3 signal is observed at 0.47 cpd (~2.12 days). The signal peaks at 1.0 hPa and extends weakly upward. The mode is absent at other observed levels. A vertically growing wavenumber one power is also found to peak at the same level as the (3, 2.0) mode. Latitude versus frequency spectral diagrams (not shown) reveal that the wavenumber one power is made up of a stationary component in the winter subtropics and slow westward moving component in the low summer latitudes. The appearance of westward moving wavenumber 1 signal and the two-day wave 3 are clearly evident in the H_2O distribution maps shown in Figure 4.21. Weak wavenumber 2 spectral signal (~3 day period) also exists along with a weak signature of the wavenumber 4 (near 2 day period) at the two highest observed levels. The synoptic sequence in Figure 4.21 and the approximate tendency for constant phase speed in the propagating wavenumber 1-4 signals at 1.0 and 0.46 hPa (Figure 4.22) suggest that the wave 1, 2, and 4 components appear as a constant phase speed modulation of the basic wave 3 disturbance.

Figure 4.23 displays the globally averaged spectral signals for AS93. Contour values of Figure 4.22 are used, so direct interannual comparison is possible. The striking differ-

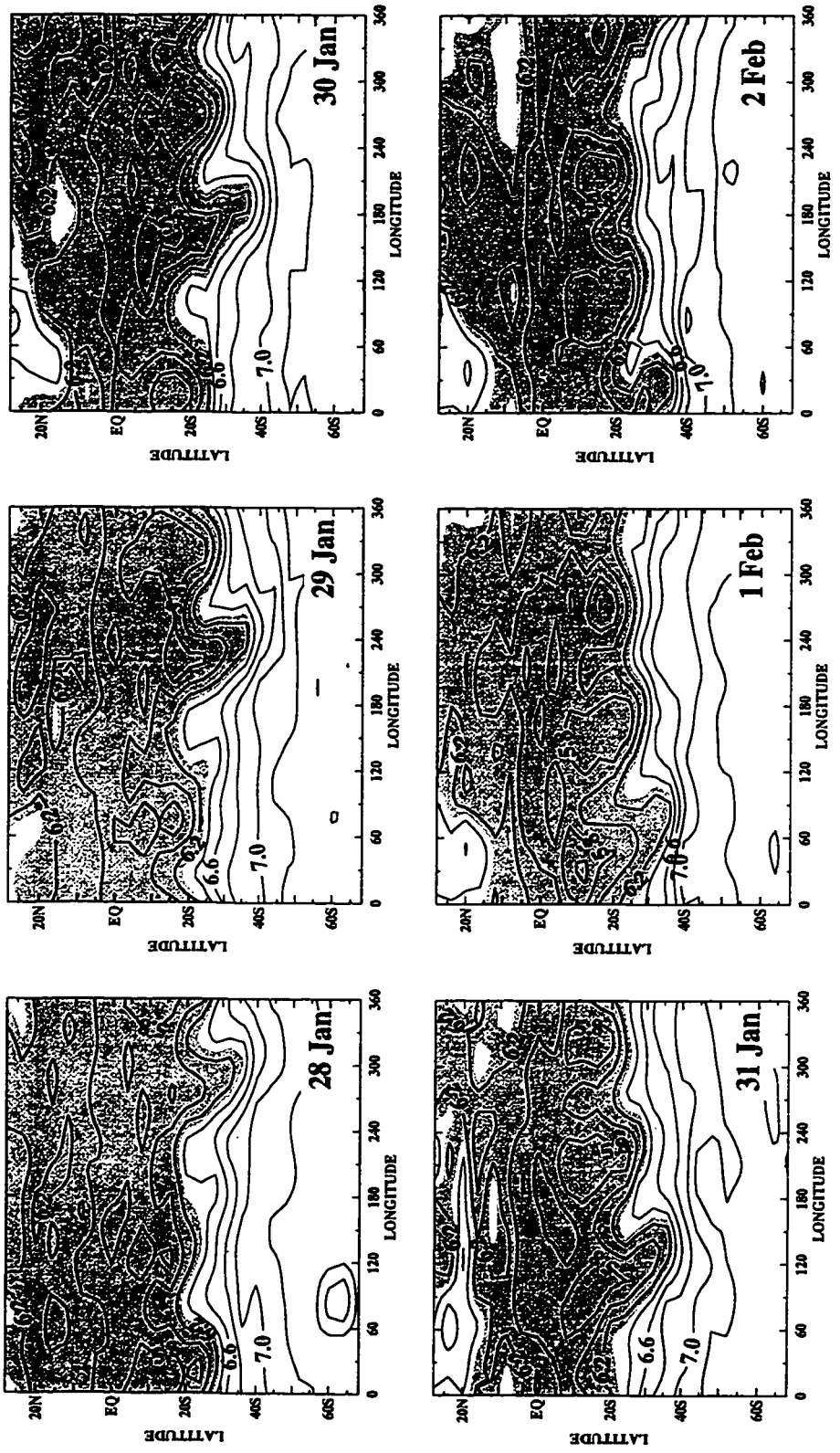

Figure 4.21: Synoptic maps of H_2O on 1800 K isentropic surface (approximately 1 hPa) during AS92. Contours are given in increments of 0.2 ppmv with values less than or equal to 6.3 ppmv shaded.

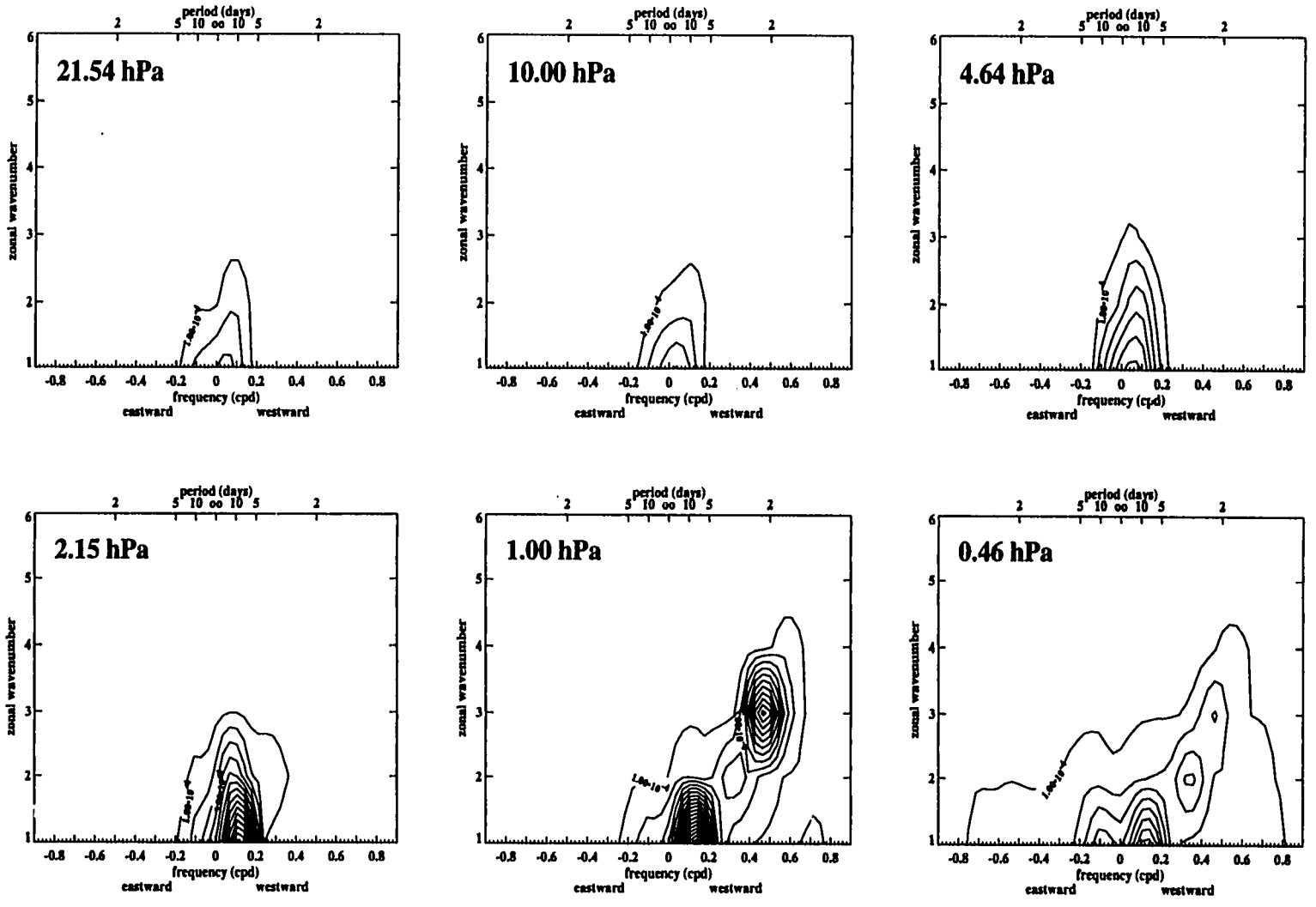

Figure 4.22: Latitudinally averaged H_2O spectra for AS92 at each observational level. Contour intervals are given every 0.0001 ppmv^2 starting at 0.0001 ppmv^2.

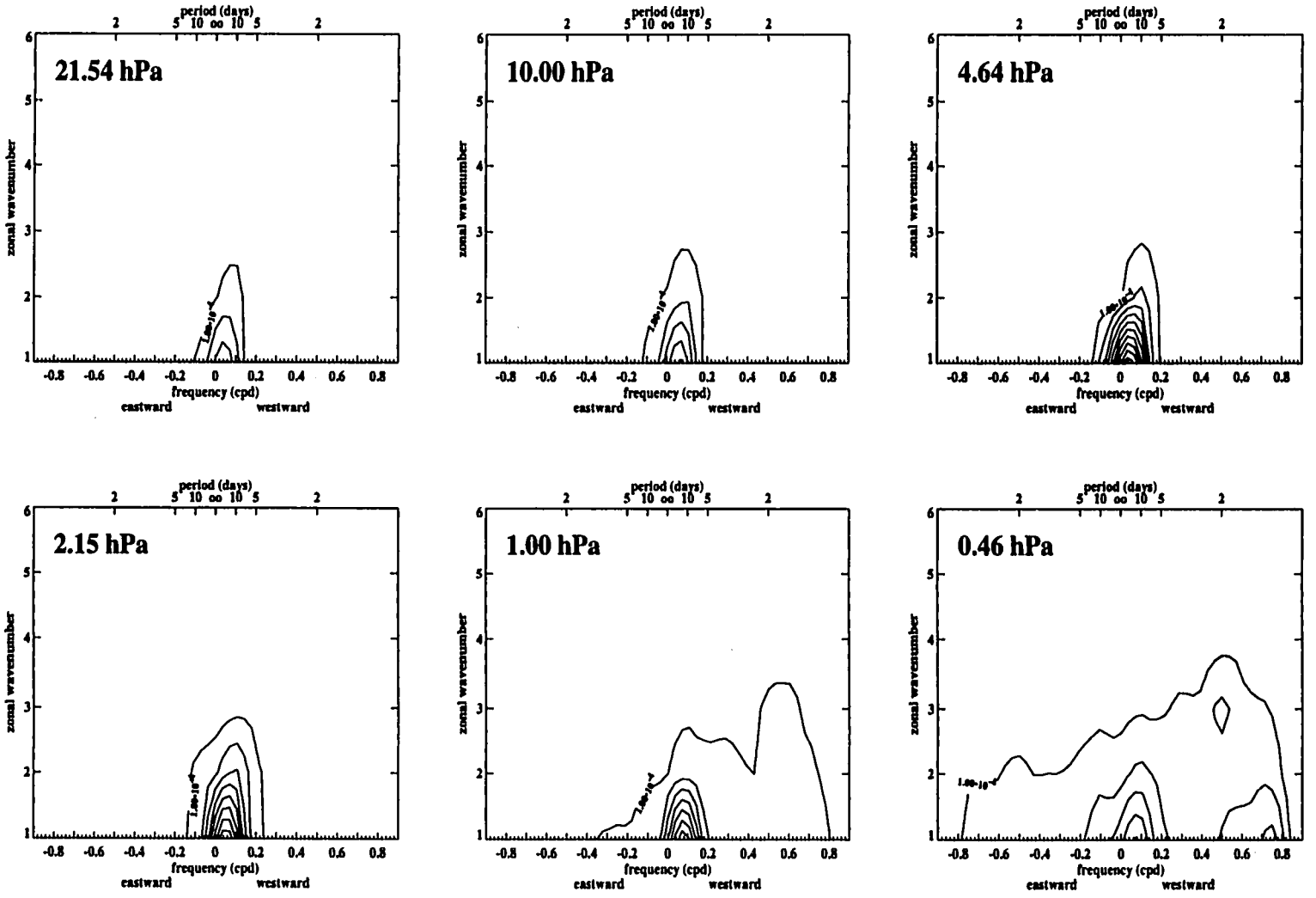

Figure 4.23: Latitudinally averaged H_2O spectra for AS93 at each observational level. Same contour intervals as Figure 4.22.

ence in 1993 is that the signal of the wavenumber 3 two-day wave is not clearly defined and is relatively much weaker compared to other wave signals. As a result, the wave evolution does not readily show up in the twice-daily synoptic maps. Nevertheless, a weak spectral peak near a two-day period and zonal wavenumber 3 is evident at the highest level (0.46 hPa). The two-day wavenumber 4 signal is absent. A wavenumber 1 disturbance is again observed and is composed of a stationary component in the winter subtropics and a slow westward moving component in the low summer latitudes.

The zonal wavenumber 3 and 4 latitude-frequency H_2O power spectra for the austral summers can be seen in Figure 4.24. The spectra are vertically averaged between 1.0 hPa and 0.46 hPa where the signals are strongest. The frequency bands used in the temperature data are indicated in the diagrams (see Figure 4.5). For AS92, both wavenumber 3 and 4 peaks are focused near 20°S and confined exclusively to the summer hemisphere. During AS93, these signals are noticeably much weaker despite the fact that the temperature signature in wavenumber 3 is similar in AS92 and AS93 (see Figure 4.5). Note that the H_2O two-day wave signal is slightly slower and maximizes at a slightly higher southern latitude than the temperature two-day wave in the austral summer.

Globally averaged power spectra for BS92 are presented in Figure 4.25. Most of the spectral power is associated with the wavenumber 1 disturbance. As with the austral summer, the components that make up the wavenumber 1 energy are stationary waves in the winter subtropics and slow westward propagating waves in the low summer latitudes. A weak spectral peak at wavenumber 4 is evident at 0.464 hPa and has a period of about 1.9 days (0.53 cpd). Latitude-frequency spectral diagrams (not shown) illustrate that this signal is confined to the summer hemisphere and is focused in the mid summer latitude band near 40°N. As expected, synoptic H_2O maps do not show the evolution of the observed wavenumber 4 two-day disturbance. Like Figure 4.22, Figure 4.25 shows that the signal associated with the four lowest wavenumbers (1-4) are "phase-locked" together (i.e. they propagate with nearly the same phase speed).

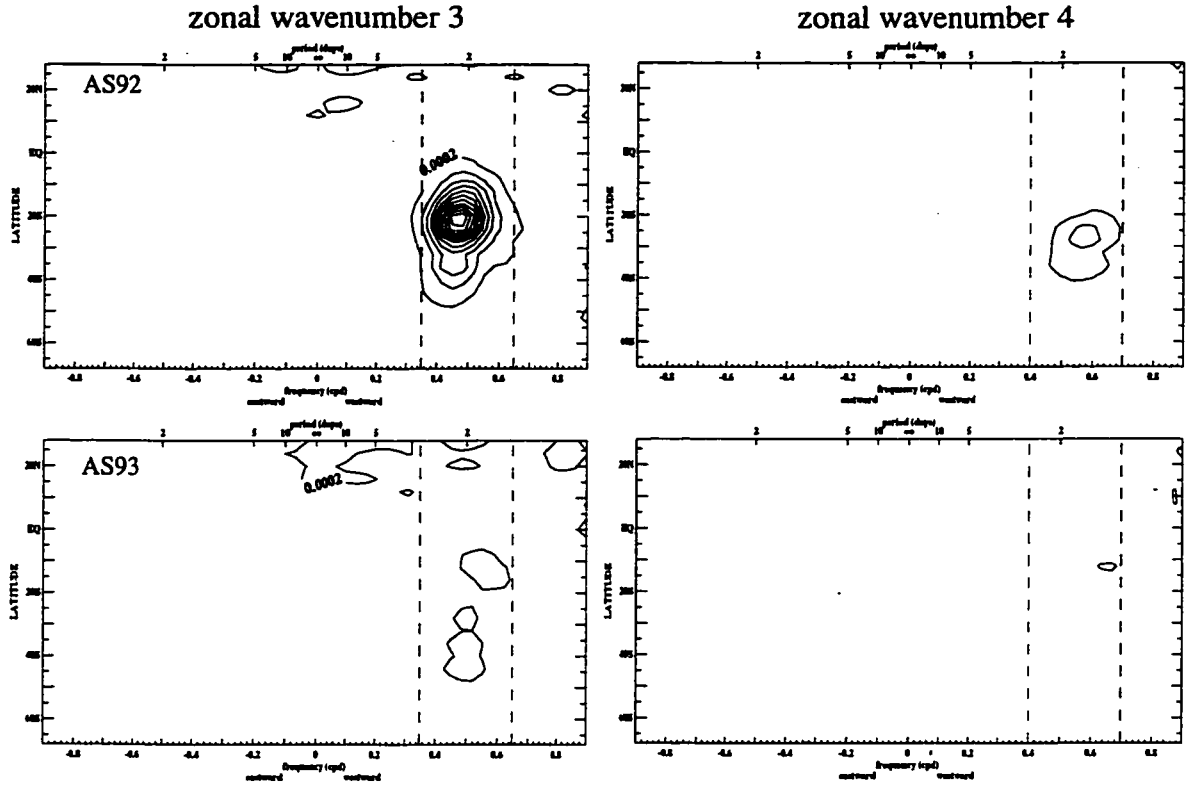

Figure 4.24: Zonal wavenumber 3 and 4 H_2O power spectra averaged between 1.0 hPa and 0.46 hPa for the austral summers. The contours are displayed every 0.0003 ppmv^2 starting from 0.0002 ppmv^2. Signals enclosed by the frequency bands marked by the dashed lines are used to compute the variance. For zonal wavenumber 3, the band is between 0.35 and 0.65 cycles per day. For zonal wavenumber 4, the band is between 0.40 and 0.70 cycles per day. These frequency band are identical to the ones defined in Figure

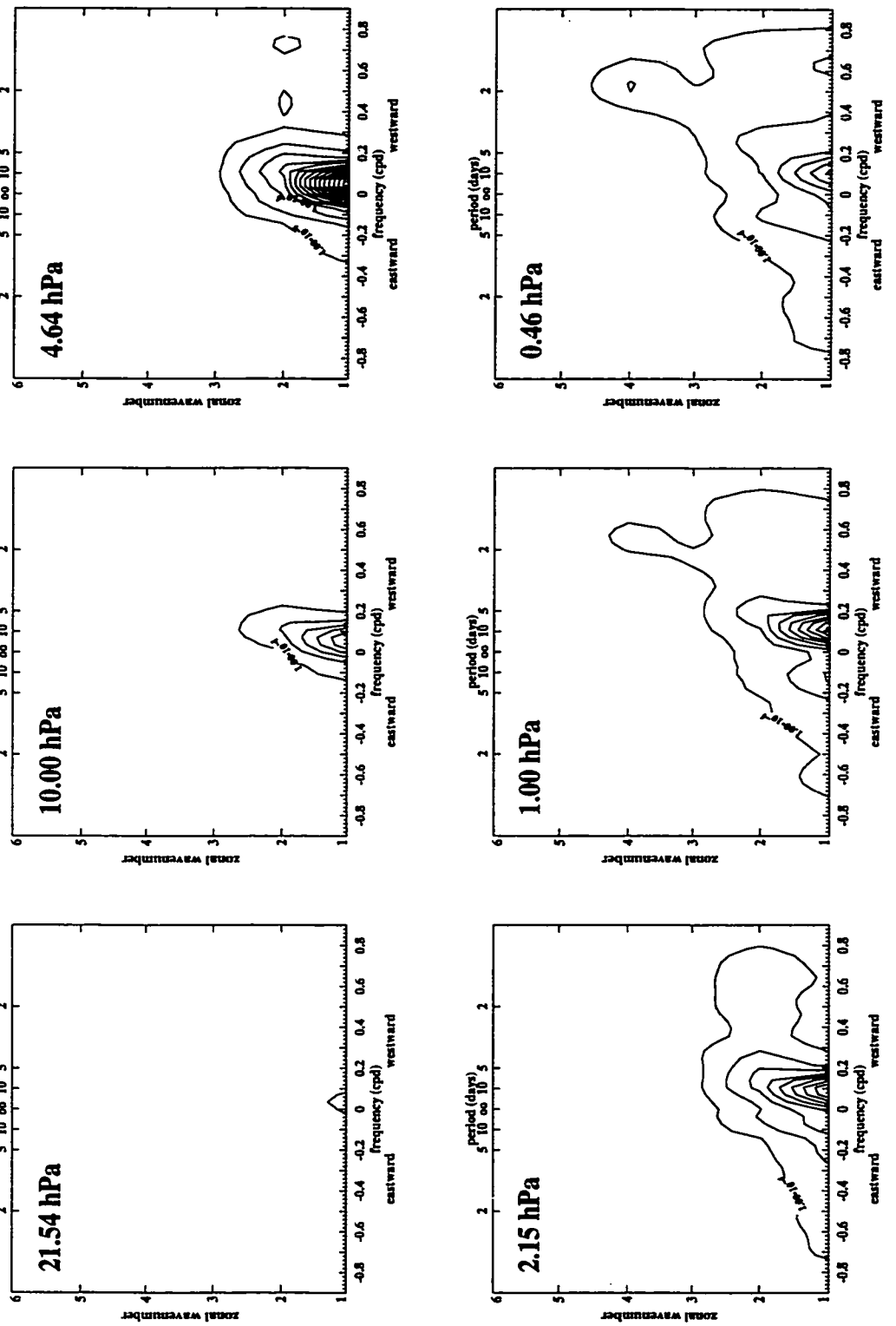

Figure 4.25: Latitudinally averaged H_2O spectra for BS92 at each observational level. Same contour intervals as Figure 4.22.

Although only one strong two-day H_2O wave event is observed, there is an indication of the dominant two-day mode in each hemisphere. During the austral summer, the two-day wave is dominated by the wavenumber 3 mode although some evidence of wavenumber 4 is observed when wavenumber 3 mode is strong. During the boreal summer, the two-day wave is identified by the weak wavenumber 4 mode. With the exception of the 1994 austral summer, this trend agrees with the two-day wave observation in the MLS temperature field shown in Section 4.1.

To examine the spatio-temporal structure of the H_2O two-day wave, the (3, 2.1) and (4, 1.9) modes will be defined as in Section 4.1. The frequency bands for spectral integration or band-pass filtering are the same as those used in the temperature analysis. Each mode's amplitude will be calculated by taking the square root of twice the integrated power spectra. Figure 4.26 shows the meridional structure of the (3, 2.1) and (4, 1.9) amplitudes in AS92 and BS92, respectively. The phase lines are computed with respect to 20°S and 1 hPa for the (3, 2.1) mode and 40°N and 0.464 hPa for (4, 1.9). The phase structure and wave amplitude are shown approximately where the COH^2 is statistically significant above the 95% level.

For the (3, 2.1) mode, the wave phase generally tilts slightly westward with height to about 1 hPa and then eastward above 1 hPa. The wave also tilts slightly westward toward the north at all heights. The H_2O amplitude spread is nearly concentric about the amplitude peak at 1 hPa and 20°S. This wave structure is quite different from the (3, 2.0) temperature which exhibits a wedge-like structure with the greatest amplitude at lower latitude (12°S) and altitude (0.464 hPa) as shown in Figure 4.7. The wave phase structures are however similar.

The structure of the (4, 1.9) mode shows almost no phase tilt in the horizontal or vertical direction. The wave amplitude grows in latitudinal extent with height (a "wedge-like" shape). The tip of the wedge extends downward to near 1.0 hPa. The axis of maximum amplitude tilts slightly poleward with height. The strongest amplitude is observed at 0.464

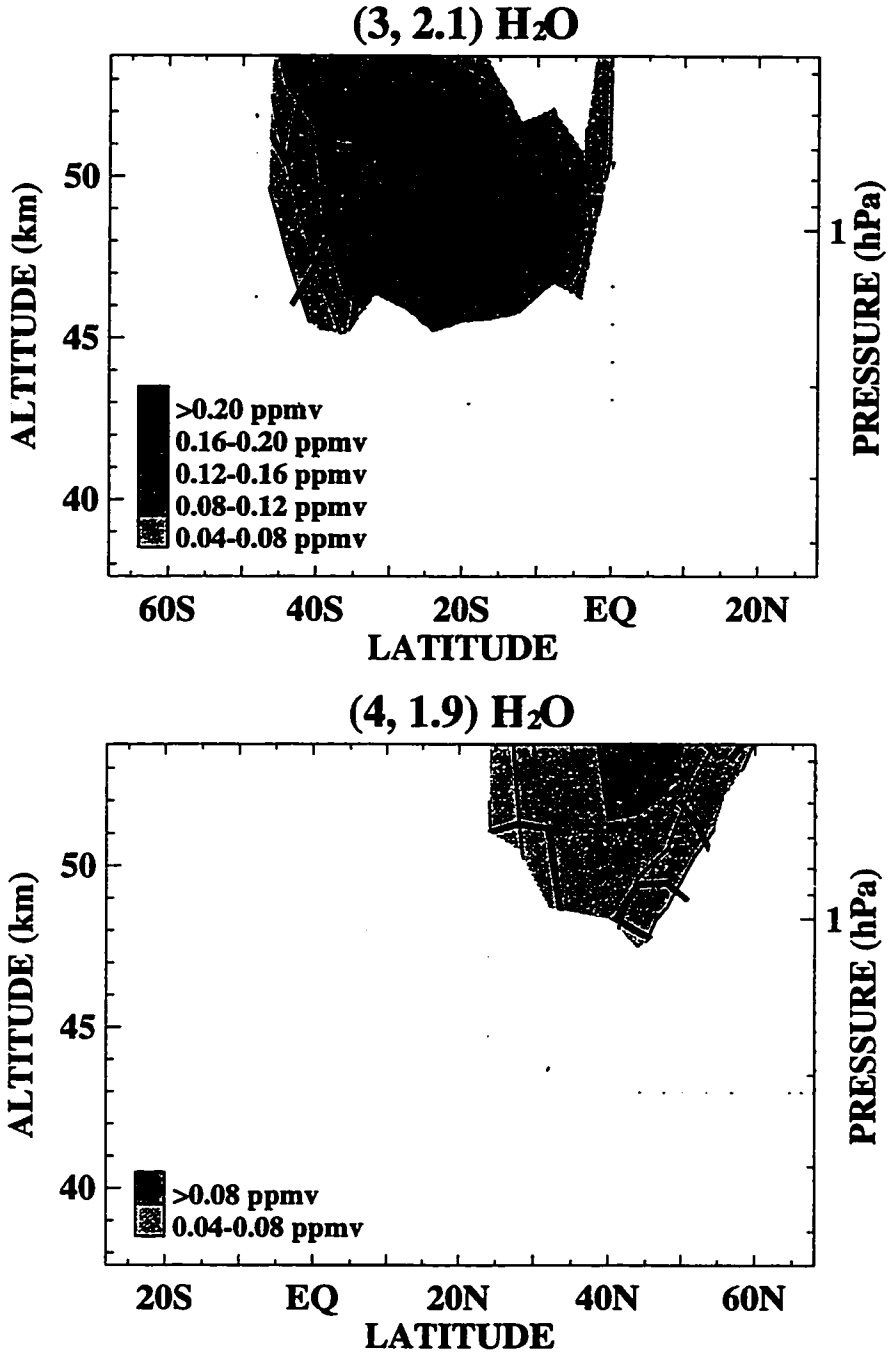

Figure 4.26: The meridional cross-section structure of the H_2O (3, 2.1) mode during AS92 (top) and the H_2O (4, 1.9) mode during BS92 (top). The wave amplitude is represented by shaded contours given in intervals of 0.02 ppmv. The phase lines are shown as heavy solid and dashed contours, in increments of 30°.

hPa in the mid summer latitudes. The shape of the wave structure is similar to the (4, 1.8) temperature shown in Figure 4.7. Both structures peak at the highest observed level, but the temperature structure is equatorward of the H_2O structure.

The evolution of the (3, 2.1) H_2O mode at 1.0 hPa is shown in Figure 4.27 for the 1992 austral summer. The evolution of the (3, 2.0) temperature mode is also shown at the same level as a reference. Note that the temperature signal is actually strongest at 0.464 hPa. The variance evolution indicates two separate pulses of the H_2O two-day wave. The first events lasts from January 17-24, 1992 and reaches a maximum of 0.07 $ppmv^2$ around January 20. This pulse coincides with a weak temperature wave pulse. A longer-lasting, stronger event starts around January 25 and peaks at the around 0.11 $ppmv^2$ around January 29, 2-3 days after the time that the temperature variance had peaked. The selected H_2O synoptic maps shown in Figure 4.21 corresponds to the beginning of this strong second two-day wave event. The appearance of the (3, 2.1) H_2O mode dies out by February 7. For both pulses, the H_2O wave variance is mainly confined between 36°S and 4°S and is generally poleward of the temperature disturbance as revealed by the amplitude-phase structure.

The evolution of the (4, 1.9) H_2O and temperature at 0.464 hPa is shown in Figure 4.28 for 1992 boreal Summer. This level locates where both the H_2O and temperature (4, 1.8) signals are the strongest. The variance evolution shows a weak and short-lived double pulse of the H_2O two-day wave. The first pulse peaks around August 3. A second pulse of lesser strength peaks about five days later. These events consistently remain poleward of the temperature disturbance and appear after the temperature signal had reached its maxima.

From a few observations of coherent H_2O two-day wave structures, it is observed that the H_2O disturbance is generally located poleward of the temperature disturbance at the same level. The times when these disturbances maximize lag the temperature peaks by a few days. The levels where the two-day signals peak in each field do not necessarily coin-

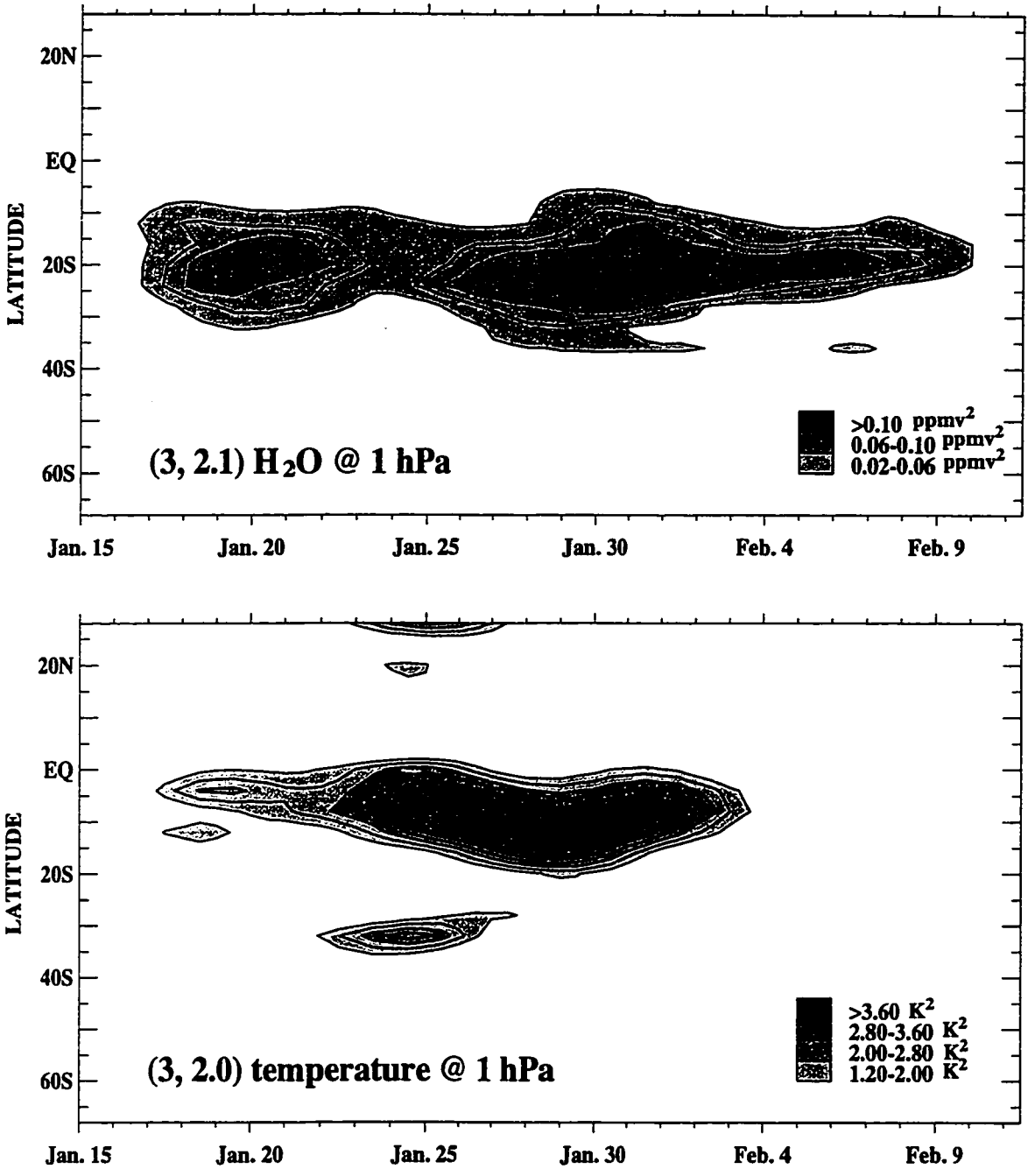

Figure 4.27: Latitude-time plot of the H_2O (3, 2.1) and temperature (3, 2.0) mode variance at 1.0 hPa during austral summer 1992. The variance contours are given in increments of 0.02 ppmv^2 and 0.4 K^2 for H_2O and temperature, respectively.

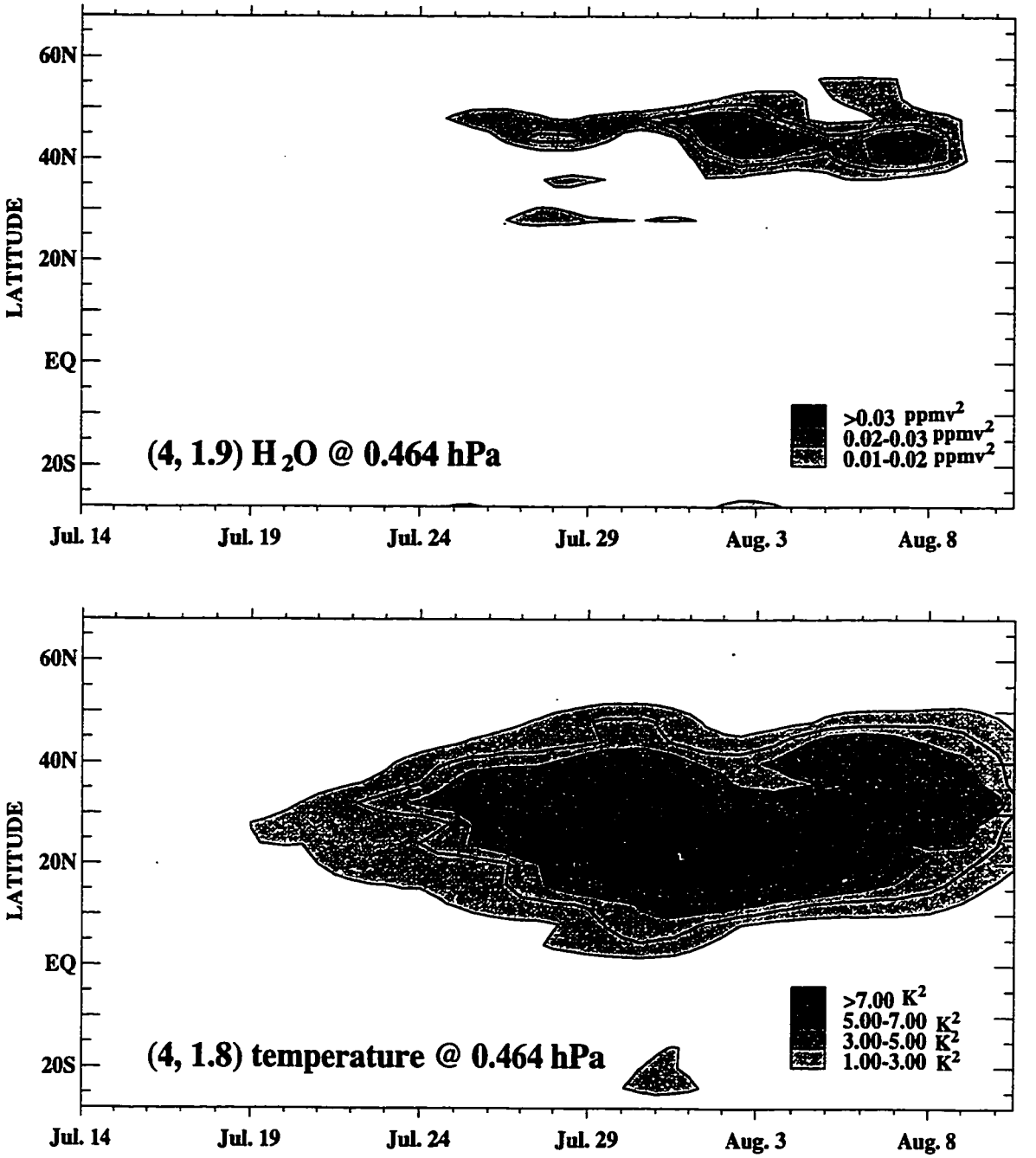

Figure 4.28: Latitude-time plot of the H_2O (4, 1.9) and temperature (4, 1.8) mode variance at 0.464 hPa during 1992 boreal summer. The variance contours are given in increments of 0.005 ppmv^2 and 1 K^2 for H_2O and temperature, respectively.

cide. During the 1991-92 austral summer, the H_2O signal peaks at 1.0 hPa while the temperature signal peaks at 0.464 hPa. During the 1992-93 austral summer, both signals peak at 0.464 hPa. The appearance of a strong temperature signal also does not always correlate with strong H_2O signal as illustrated in 1992-93 austral summer.

The meridional cross-sections of the zonal mean water vapor distribution are shown in Figure 4.29, Figure 4.30, and Figure 4.31 for each available summer season. In general, the H_2O distribution has a Gaussian shape with a minimum mixing ratio near the equator. Largest H_2O mixing ratios of greater than 7.0 ppmv are consistently observed in the high summer latitudes. The equatorial bulge in the distribution is consistent with a rising motion in the tropics. As a result, relatively strong meridional gradient of the water vapor is evident in the subtropics. However, some flattening of the tracer meridional gradient can be seen in the winter subtropics, presumably due to winter wave breaking in the subtropical edge of the surf zone. During the 1991-92 austral summer, strongest rising motion is evident by the overshooting of the 5-6 ppmv band to 1 hPa from mid-January to early February. During the same period, the smallest mixing ratios are also observed near 20 hPa. Subsequently, considerable meridional tracer gradient in the low summer latitudes is evident near the stratopause. During other summers, the tracer gradient is noticeably much weaker around 1.0 hPa.

The importance of background tracer gradient can be seen by considering the linearized continuity equation for a conservative tracer (χ) in Cartesian coordinate (x, y, z):

$$\left(\frac{\partial}{\partial t} + \bar{u}\frac{\partial}{\partial x}\right)\chi' + v'\bar{\chi}_y + w'\bar{\chi}_z = 0 \qquad (4.1)$$

Here, the overbar denotes zonal average, and the subscript indicates partial derivative. Neglecting advection by vertical wind perturbation (w'), multiply Equation (4.1) by χ'

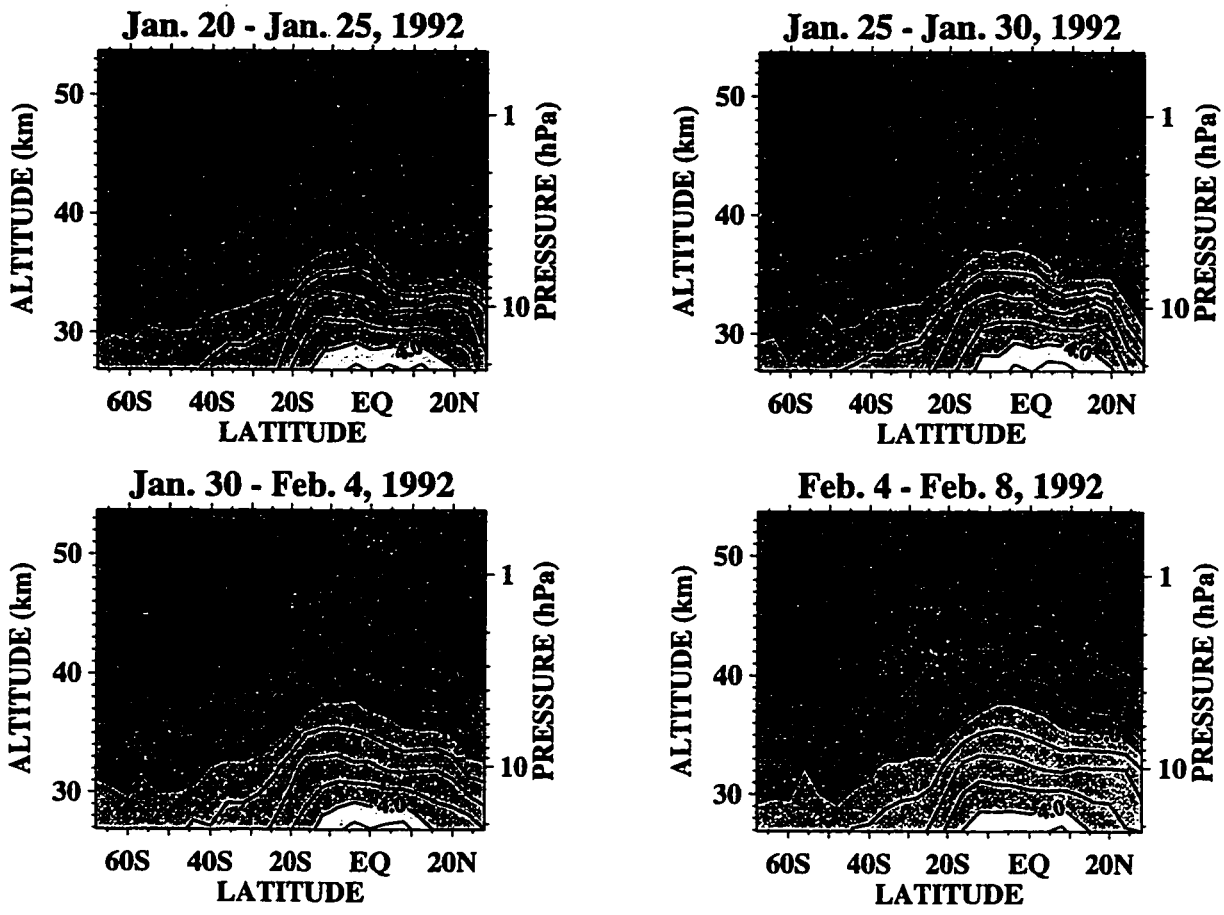

Figure 4.29: Latitude-height cross-sections of the 5-day averaged zonal mean H_2O for 1991-92 austral summer. The contours are given in increments of 0.25 ppmv.

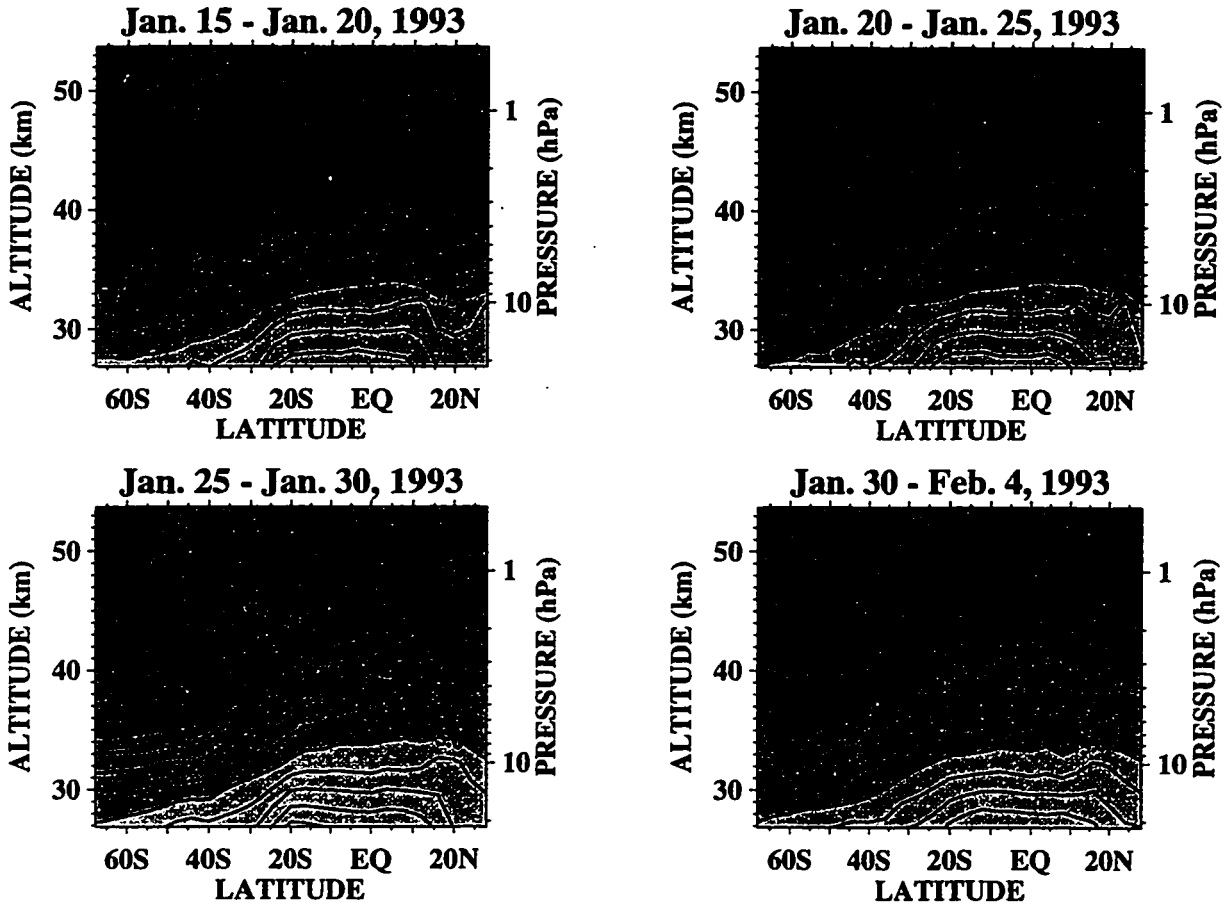

Figure 4.30: Latitude-height cross-sections of the 5-day averaged zonal mean H_2O for 1992-93 austral summer. The contours are given in increments of 0.25 ppmv.

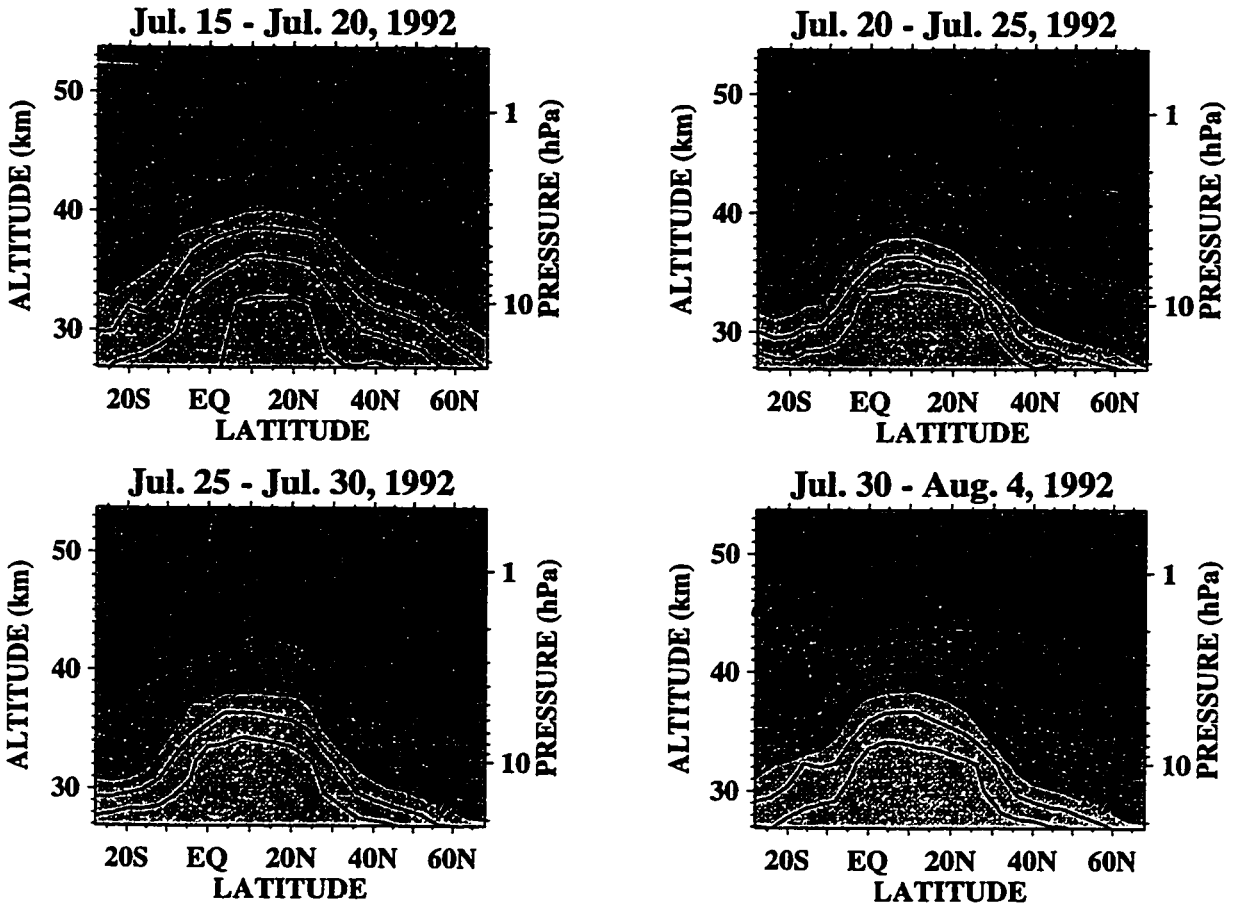

Figure 4.31: Latitude-height cross-sections of the 5-day averaged zonal mean H_2O for 1992 boreal summer. The contours are given in increments of 0.25 ppmv.

and take the zonally average to get:

$$\frac{\partial}{\partial t}\overline{\chi'^2} = -2(\overline{v'\chi'})(\bar{\chi}_y) \qquad (4.2)$$

This equation states the dependence of the local time change of the tracer variance on the tracer meridional flux ($\overline{v'\chi'}$) and the mean tracer meridional gradient ($\bar{\chi}_y$). The product of the terms in the parentheses is always positive for a growing wave perturbation since wave stirring tends to flux tracer down the mean tracer gradient. This is shown schematically in Figure 4.32 for water vapor which has a minimum mixing ratio near the equator.

Given a strong two-day wave event as observed during each summer in the MLS temperature, a large disturbance in a passive tracer field will be observed near the region of strong wave fluxes and large meridional gradient of the mean tracer field. Thus, for the 1991-92 austral summer, strong wave signatures are readily seen in the latitude band (20°S-40°S) just south of the temperature two-day wave maxima (Figure 4.21). Of course, other wave activities, besides the two-day wave, are evident in same region. For the 1992-93 austral summer and 1992 boreal summer, the low summer latitude meridional tracer gradient is weaker near the stratopause, and, subsequently, the H_2O wave signals are weakly resolved despite the presence of strong two-day wave seen in the temperature field. Thus, if the background tracer field is more or less homogeneous, dynamical wave disturbance are not readily observable in the passive tracer response.

4.4 SUMMARY OF THE OBSERVATIONAL RESULTS

The 3-year UARS MLS temperature observations clearly show the presence of the two-day wave near the stratopause. The phenomenon is evident semiannually several weeks after the solstice. The maximum temperature two-day wave amplitude consistently resides in the summer subtropics and on the equatorward flank of the summer easterly jet. Both modes (zonal wavenumber 3 and 4) of the two-day wave are observed. The wave-

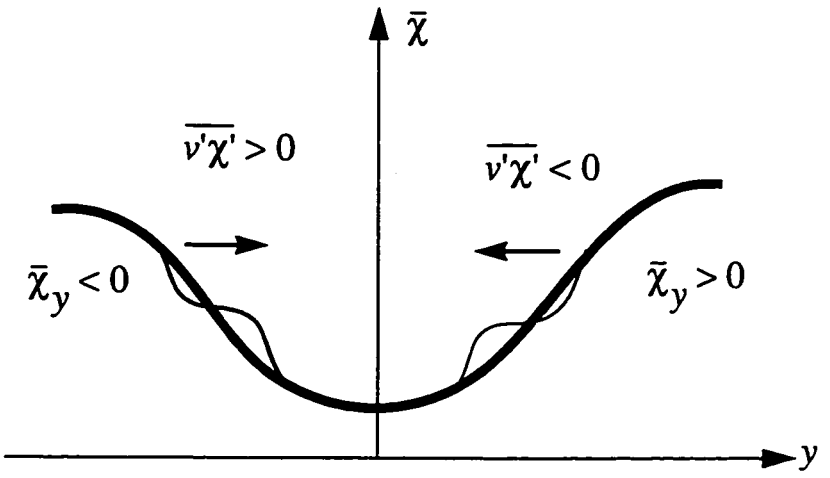

Figure 4.32: A schematic of the latitudinal profile of the zonal mean H_2O tracer ($\bar{\chi}$) during wave mixing. The thick line is the background tracer profile. The superimposed thin line is the profile as result of wave mixing. Wave stirring tends to flatten the meridional gradient through equatorward flux of tracer.

number 3 mode dominates over the wavenumber 4 mode during the austral summer. The opposite is true during the boreal summer. The mode dominance is reflected in its strong spectral signal and the long duration of its variance in relation to the other mode during the summer season. In a given year, the austral summer wavenumber 3 mode amplitude can be more than twice as large as the boreal summer amplitude. However, for the wavenumber 4 mode, its amplitude can be equally strong during both summers.

An examination of the wave variance and the ambient wind strongly suggests that, during the austral summer, both modes of the two-day wave grow from barotropic-baroclinic instability mechanism. Each mode's variance appears near the regions of reversed potential vorticity gradient. These regions are crossed by the critical lines of both modes implying that the critical lines serve as the instability wave source. On the other hand, during the boreal summer, the easterly jet is considerably weaker than its austral summer counterpart and can only support the wavenumber 4 mode critical line. Thus, only the wavenumber 4 mode can be attributed to wave instability as its critical line is seen to intersect with the regions of reversed potential vorticity gradient. Weak wavenumber 3 mode variance is nonetheless seen during the boreal summer.

Overall, the instability of the summer easterly is governed mainly by the barotropic component. That is, the horizontal curvature of the mean wind largely accounts for the observed regions of potential vorticity gradient reversal. This is especially true during the seasons when these regions are observed on the equatorward flank of the easterly jet. In these cases, momentum redistribution by inertial instability in the winter subtropics may be responsible for the required strong horizontal wind curvature. Concurring UARS CLAES observations by Hayashi et al. (1998) show evidence for the "pancake" temperature structures associated with inertial instability to precede the observed regions of strong horizontal wind curvature that locally causes the reversal of the potential vorticity gradient. Since the two-day wave appears to grow from the unstable regions, inertial instability may, in effect, trigger the growth of the two-day wave. The possible connection between inertial instability and the two-day wave is illustrated numerically in Chapter 6.

Finally, the MLS H_2O observations reveal a strong two-day wave signal where and when the zonal mean H_2O meridional gradient is strong. In the available data, clear evidence for the two-day wave oscillation in the H_2O data is found only during the 1991-92 austral summer. The synoptic maps near 1 hPa clearly show the two-day wave perturbing the region of strong meridional tracer gradient. Interestingly, a prominent wavenumber 1 signature is observed to be phase-locked with the two-day wave. Their coupled evolution provides evidence for wave breaking and mixing of H_2O across the mean tracer gradient.

CHAPTER 5

MECHANISTIC MODEL AND ITS IMPLEMENTATION

An intriguing result from the MLS observations is the possible connection between inertial wave activity and the two-day wave, at least in some summers. This connection has been first proposed by Hitchman (1985) and discussed by Orsolini et al. (1997). Interestingly, such a relationship would form a global connection between the winter wave activity (which is believed to organize inertial activity) and the summer wave disturbances near the stratopause. This scenario connecting winter planetary waves, inertial activity, and the two-day wave is explored numerically in the remainder of this thesis using a mechanistic model. A brief account of the model is first presented in this chapter. Design of the model experiments is then given. The primary goal of the experiments is to numerically simulate the two-day wave. A successful simulation allows for the examination of the two-day wave propagation, its effect on the mean flow, and perhaps its triggering mechanism as related to inertial instability. Two-day wave variability can be also examined through variation of the model forcing, initial conditions, and damping mechanisms. The model set up is crucial in allowing such waves to be generated. Several important assumptions must be made based on previous observations and full general circulation model simulations.

5.1 MODEL DESCRIPTION

The model is adapted from the National Center for Atmospheric Research (NCAR) Middle Atmosphere version of the Community Climate Model 2 (MACCM2). Takahashi and Boville (1992) presented a study of the quasi-biennial oscillation (QBO) using a similar mechanistic model based on a preliminary version of the NCAR Community Climate Model 2 (CCM2). Details of the CCM2 and MACCM2 are discussed in Hack et al. (1993) and Boville (1995), respectively.

The model is three dimensional and solves the primitive equations by invoking the spectral transform method in the horizontal and a finite-difference scheme in the vertical. To save computational resources, a "T21×10" trapezoidal truncation scheme is used. This scheme has the same meridional resolution as the T21 scheme but the zonal resolution is reduced by half (see Boville, 1995). Thus, there are 32 Gaussian grid points in the meridional direction and 32 evenly spaced grid points in the zonal direction. Hence, the zonal resolution is 11.75° while the meridional resolution is roughly ~6°. In the vertical, a pressure coordinate is used, with 47 model levels ranging from 234.57 to 0.004 hPa (about 10-87 km). For a scale height of 7 km, the level separation in log pressure coordinate is 1.4 km at the lower boundary and 1.7 km at the model's top. The model integration time step is 24 minutes.

The model performs a dry adiabatic adjustment to remove instabilities in the temperature profiles. If the model-predicted temperatures produce lapse rate exceeding the dry adiabatic lapse rate, an energy conserving temperature adjustment is made. At all levels, a biharmonic (∇^4) horizontal diffusion is applied with a constant coefficient value of 1.0×10^{16} m^4 s^{-1}. The vertical diffusion parametrization depends on the local Richardson number, and a minimum diffusivity of 0.01 m^2s^{-1} is assumed for stable conditions in the middle atmosphere.

Cooling-to-space is approximated by Newtonian cooling. The scheme relaxes the model temperature to the zonally symmetric initial condition discussed below. The damping rate of the cooling coefficient (K_n) varies only in height (z) roughly from 23 days at the lower boundary to less than 5 days near the model top. The coefficient profile is given by:

$$K_n = 1.0\times10^{-6}s^{-1}\left[\alpha+\beta\tanh\left(\frac{z-35km}{7km}\right)\right] \qquad (5.1)$$

and is shown in Figure 5.1 for two combinations of (α, β).

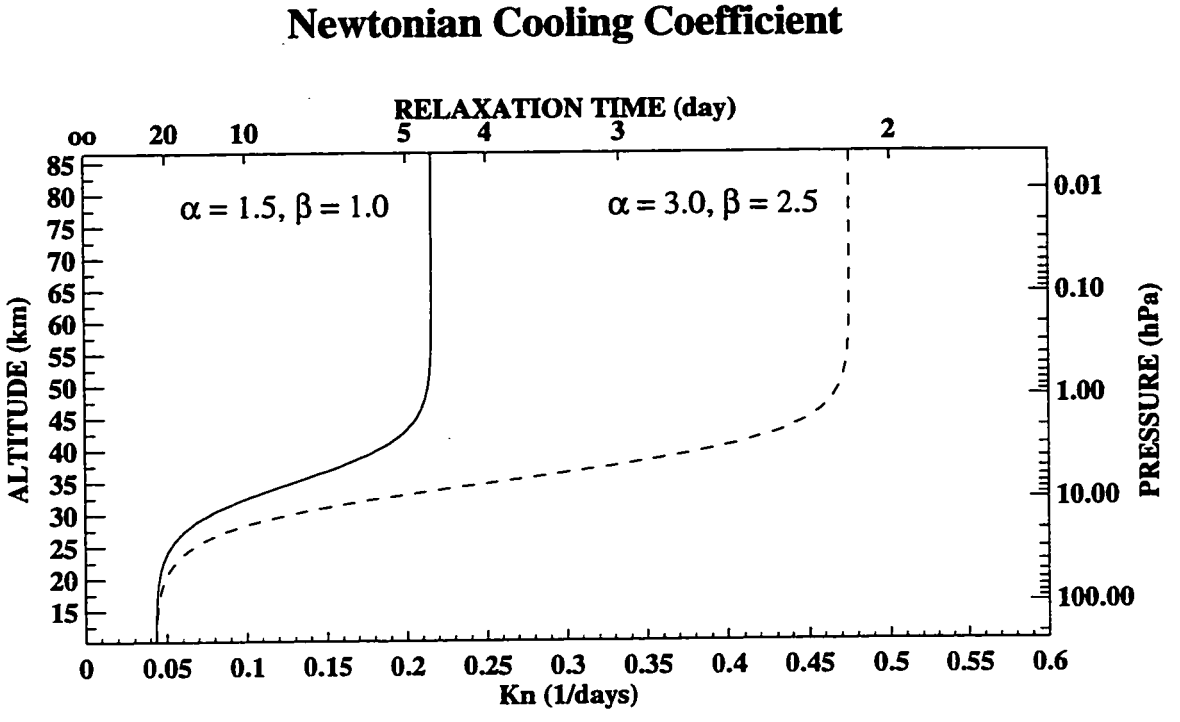

Figure 5.1: Newtonian cooling coefficient profiles used in the model. The vertical coordinate is given over the range covered in the model.

The mean flow effects of gravity waves are approximated by simple Rayleigh friction. The scheme takes on a linear drag form in the momentum equation with the frictional coefficients varying only in height. The coefficient is given as:

$$K_r = \frac{2}{3} s^{-1} \left[1.0 + \tanh\left(\frac{z - 80km}{5km} \right) \right] \tag{5.2}$$

and shown in Figure 5.2. Rayleigh friction crudely emulates the decelerative effect of breaking gravity waves in the mesosphere in closing the jets. Since it is applied to the total wind field, it damps both the mean wind and incipient wave variations. Hence, its presence in the upper model levels also serves as a buffer ("sponge") to prevent reflection of extraneous waves that might appear at these altitudes. Wave reflection can result as a rigid "lid" boundary condition is placed at the top of the model where vertical velocity is set to zero.

The model's initial wind fields are specified analytically. The meridional wind field (v) is taken to be zero, and the zonal wind (u) is zonally symmetric. The initial temperature (T) is also zonally symmetric as it is derived from the initial zonal wind field by using the thermal wind relation obtained by combining Equation (3.10) and (3.11):

$$\left(2\Omega \sin\varphi + \frac{2\bar{u}\tan\varphi}{a} \right) \frac{\partial \bar{u}}{\partial z} = -\frac{R}{aH} \frac{\partial \bar{T}}{\partial \varphi} \tag{5.3}$$

The notations are defined in Chapter 3 (Section 3.2.2). To facilitate the derivation, a vertical temperature profile at the equator is specified according to the U.S. Standard Atmosphere 1976. The profile serves as an integration constant which allows the wind field to be integrated separately in each hemisphere to obtain the temperature field. The design of the initial wind structure is discussed below. The initial fields are first computed in an evenly spaced coordinate system. The latitude coordinate ranges from -90° to 90° in intervals of 1°. In the vertical, log pressure coordinate is used covering heights of 10 km to 90 km in increments of 1 km. The fields are then interpolated onto the model coordinates.

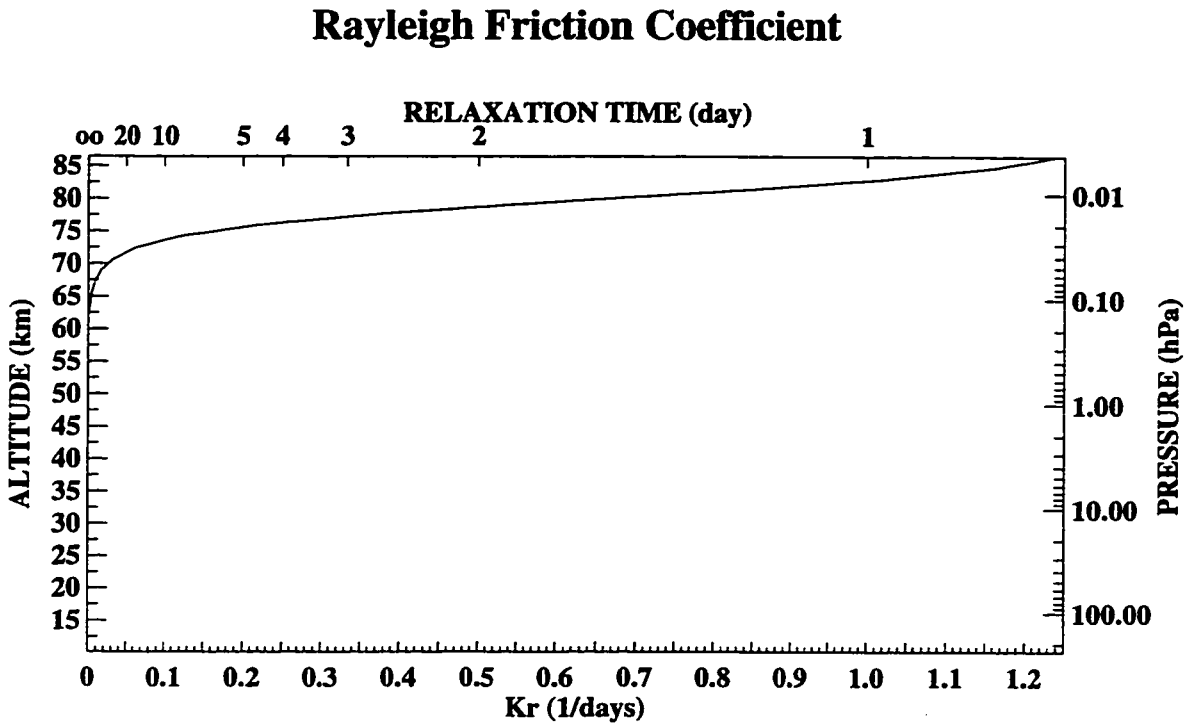

Figure 5.2: Rayleigh friction coefficient profile used in the model. The vertical coordinate is given over the range covered in the model.

The top boundary condition is "rigid" as the vertical velocity is set to zero. This boundary condition is common in general circulation models, but unrealistic reflections of wave activity near the top boundary can occur (Andrews et al., 1987). A large dissipative term must be specified near the top to minimize the spurious reflections that can contaminate model results. In this model, Rayleigh friction provides the needed dissipation as discussed. Usually, the model top is assumed to be far away from the interesting modeled feature.

The bottom boundary condition is specified through the vertical derivatives of the prognostic variables and a geopotential field at the lowest model layer interface. The prognostic variables are divergence (δ) and relative vorticity (ζ) (both computed from zonal and meridional winds) along with temperature (T) and default specific humidity (Q). They are assumed to have zero vertical derivative at the model lowest level. The geopotential distribution at the lowest level is comprised of a stationary (time independent) zonal mean geopotential field plus a time dependent perturbation geopotential field. The stationary component is obtained from the zonally symmetric initial condition. The perturbed component is analytically defined.

5.2 EXPERIMENTAL DESIGN

Observations have shown that pronounced two-day wave signals consistently appear shortly after the solstice near the stratopause region and above. Around this time in the middle atmosphere, the zonal mean wind structure is dominated in the extratropics by strong easterlies and westerlies in the summer and winter hemisphere, respectively. Above 35 km, the equatorial region is characterized by the easterly phase of the semiannual oscillation (SAO) and a descending westerly shear zone. In the equatorial regions below 35 km, the flow is dominated by either westerly or easterly zonal wind depending on the phase of the quasi-biennial oscillation (QBO). Pre-existing thermal and dynamical forcings are responsible for setting up this atmospheric condition.

Sufficiently strong wind shear on the equatorward flank of the summer easterly jet appears to be necessary for the generation of the two-day wave near the stratopause. Strong wind shear can destabilize the summer easterly jet and produce the two-day wave with an instability behavior as shown by Norton and Thuburn (1997), Randel(1993), Orsolini et al. (1997), and Plumb (1983). Norton and Thuburn (1997) find that gravity wave (GW) drag is needed to generate the required wind shear in the EUGCM and use a Lindzen-type GW parametrization with nonstationary components to simulate GW drag. Their one-year integration run shows the summer easterly jet intensifying until around the solstice. Above and equatorward of the jet core, a strong westerly shear zone accompanies the jet intensification as strong GW drag imposes decelerative forcing on the wind near the shear zone. The zonal GW drag region is concentrated in the low summer latitudes near the stratopause and tilts poleward with altitude. Regions of reversed potential vorticity gradient and unstable two-day wave are evident along and poleward of the drag region (see Figure 5.3)

To simulate the two-day wave, the mechanistic model should have an initial state similar to the atmospheric condition under which the wave flourishes. It will be assumed that given a suitably designed initial mean flow configuration, one presumably shaped by preexisting thermal and dynamical forcing, the two-day wave can be generated *in situ* using a model with no tropospheric information. To maintain the favorable atmospheric condition, the model state will be continually "nudged" back to the initial state through strong Newtonian cooling which relaxes the model temperature to its initial zonally symmetric value. The maintenance of the zonal wind structure will break down if the mean wind is strongly affected by wave-mean flow interaction during the course of model run or in a region where the strongly imposed Rayleigh friction acts to decelerate the mean wind at all latitudes. As shown in Figure 5.2, the region affected by Rayleigh friction is above 65 km and presumably far away from the location of the wave generation.

The defined initial condition to be used in the numerical experiments is illustrated in Figure 5.4. The analytical expressions that represent the initial mean wind are given in the

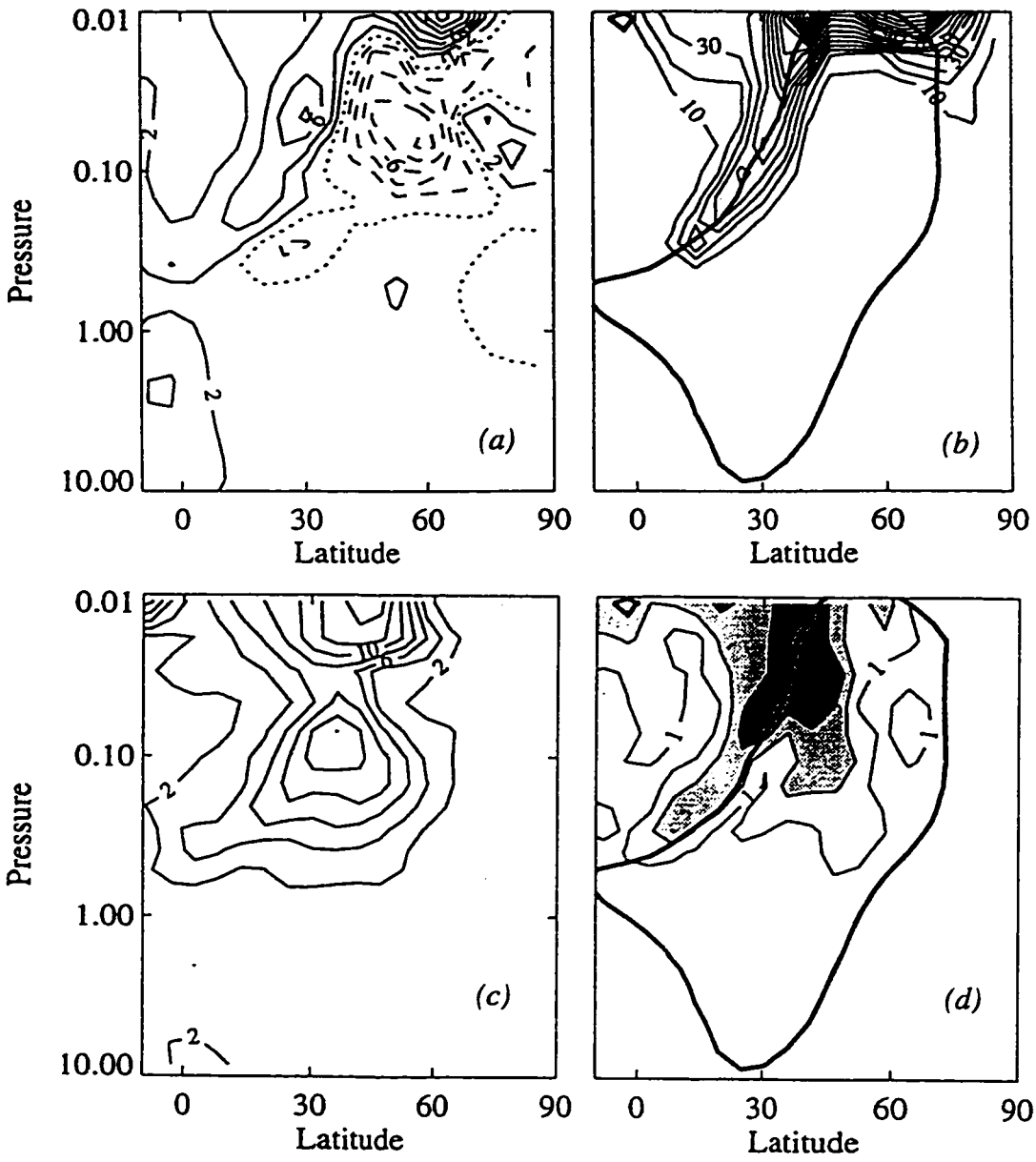

Figure 5.3: July 9th results from a one year T21 integration of the EUGCM model. (a) Meridional gradient of zonal mean quasi-geostrophic potential vorticity ($\bar{q}_\varphi$) in intervals of 2×10^{-11} $m^{-1}s^{-1}$. The dotted (dashed) contour denotes the zero (negative) value. (b) Mean gravity wave drag in the zonal direction in intervals of 10 $ms^{-1}day^{-1}$. (c) Temperature wavenumber 3 two-day wave amplitude structure with contour interval of 2 K. (d) Relative vorticity wavenumber 3 two-day wave amplitude structure with contour interval of 10^{-5} s^{-1}. The -30 ms^{-1} zonal mean wind isopleth is shown as bold line in (b) and (d). [Taken from pre-print of Norton and Thuburn (1996).].

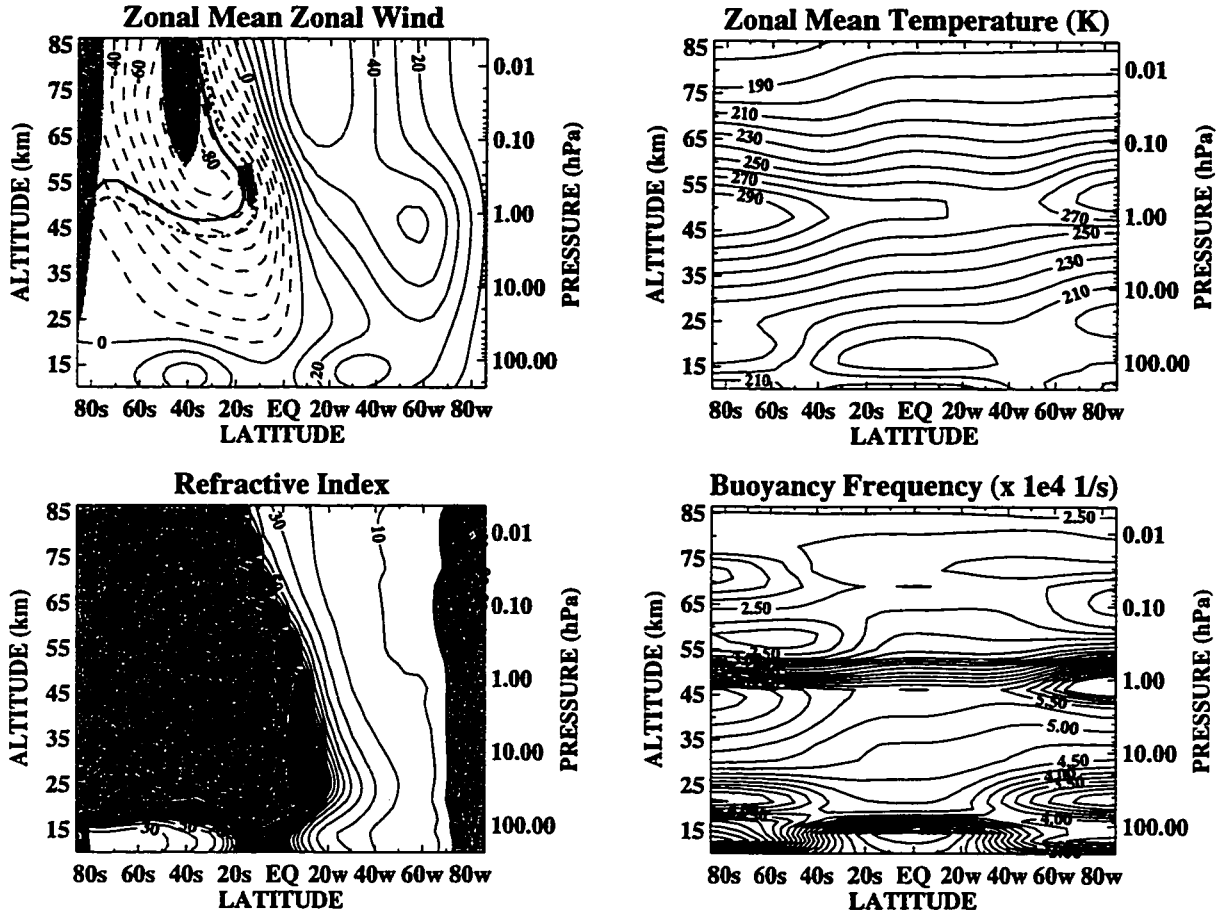

Figure 5.4: Prescribed zonally symmetric initial condition. The letter "s" and "w" designations along the latitude axis denote summer and winter, respectively. Top left panel: zonal wind field, $\bar{u}_{init}$, is contoured in 10 ms^{-1} increments. Regions where the quasi-geostrophic potential vorticity meridional gradient is less than or equal to zero are shaded. For reference, the MLS observed critical surfaces of the (3, 2.0) mode and the (4, 1.8) mode are marked by the bold line and dotted bold line, respectively. Bottom left panel: the nondimensionalized quasi-geostrophic refractive index (a^2n^2) for stationary zonal wavenumber 1. The light-shaded regions show areas of negative values while dark-shaded regions show areas of values exceeding 100. Top right panel: temperature in increments of 10 K. Bottom right panel: the scaled buoyancy frequency in increments of 0.25 s^{-1}.

Appendix. The zonal wind structure shows a strong easterly jet that tilts toward the summer pole with height. The easterly jet has magnitude that surpasses 80 ms^{-1}. Around the stratopause (as marked by the strong buoyancy frequency gradient around 50 km), strong meridional wind shear is evident on the equatorward flank of the easterly jet. Correspondingly, a small region of reversed meridional gradient of the quasi-geostrophic potential vorticity ($\bar{q}_\varphi \leq 0$) is seen in low summer latitudes. Over the equator, the observed vertical westerly shear zone associated with the easterly phase of the SAO is simulated. The westerly winds in the middle atmosphere are moderately strong and the jet core tilts equatorward with height.

The initial condition shown in Figure 5.4 mimics the main characteristics of the observed easterly wind structure derived from the MLS temperature during the austral summer. It was determined that the strong easterly jet allows for the critical lines of both two-day wave components to be present near regions of $\bar{q}_\varphi \leq 0$. For reference, these critical lines are shown on Figure 5.4 as bold solid and dotted lines for mode (3, 2.0) and (4, 1.8) observed in the MLS data, respectively. This is not to say that these modes will necessarily be generated in the experimental runs. The critical lines shown only demonstrate the similarity between the constructed winds and the observed austral summer conditions.

Two important points are raised here. First, the strong equatorial wind shear in the initial condition allows the zonally symmetric condition for inertial instability to be satisfied. This again concurs with the observed MLS wind structure which shows that such a condition is fulfilled for a lengthy period (see also Ray, 1997). O'Sullivan and Hitchman (1992) have used similar wind structure with inertially unstable equatorial flow to simulate inertial instability in their mechanistic model. Second, the phase of the QBO is fixed at easterly. It is assumed that the QBO phase will have negligible effects on the experimental results.

For the specified initial condition, a stationary, zonal wavenumber one forcing is imposed at the model's base (~10 km or 235 hPa) in the winter hemisphere. In reality,

such winter wave forcing is common and is generated near the ground through topographical variations and land-sea thermal contrast. That only the largest zonal scale and the lowest frequency wave can propagate into the middle atmosphere is attributed to the filtering nature of the troposphere (Charney and Drazin, 1961; Andrews et al., 1987). The forced wave is expected to propagate upward through much of the lower stratosphere and then veer equatorward near the stratopause region where it is mechanically and/or thermally damped. The signals of mid-latitude planetary waves in low winter latitude are observed in the MLS observations (e.g. Figure 4.15) and the CLAES observation (Hayashi et al., 1998).

The quasi-geostrophic (QG) refractive index serves as a useful predictor of the forced planetary wave propagation. For stationary, zonal wavenumber one planetary wave forcing, the index is also shown in Figure 5.4. Generally, for a planetary wave of zonal wavenumber (s) and frequency (ω) in radians per second, the QG refractive index (n) is given in Chen and Robinson (1992) as:

$$n^2 = \frac{\bar{q}_\varphi}{\bar{u} - \frac{(a\omega\cos\varphi)}{s}} - \left(\frac{s}{a\cos\varphi}\right)^2 - \left(\frac{f}{2NH}\right)^2 \qquad (5.4)$$

where $\bar{q}_\varphi$ is given in Equation (3.12) and other symbols are defined in Sections 3.2.2. The refractive index is plotted as the nondimensional quantity a^2n^2. The forced stationary wave is expected to propagate in regions of positive n^2, avoid regions of negative n^2, and wave rays in positive n^2 regions are expected to refract toward larger values of n^2.

In the model, the forcing is accomplished through the geopotential field. The total geopotential field at the model's base consists of the wave perturbation forcing in addition to the stationary, zonally symmetric forcing:

$$\Phi_{bc}(\lambda, \varphi, t) = \bar{\Phi}(\varphi) + \Phi'(\lambda, \varphi, t) \qquad (5.5)$$

The field, $\overline{\Phi}(\varphi)$, is derived from the initial temperature input. The wave perturbation is described analytically and is slowly turned on from the model initial time (model day 0) reaching its steady peak amplitude by model day 20. The geopotential perturbation is focused in the winter hemisphere and is given by (summer and winter latitudes are negative and positive, respectively):

$$\Phi' = F(\lambda, \varphi)G(t) \qquad \text{for } 30°w \le \varphi \le 82.5°w$$

$$\Phi' = 0 \qquad \text{for other } \varphi$$

where,

$$F(\lambda, \varphi) = \left\{ \sin\left[\pi \left(\frac{|\varphi| - 30°}{60° - \frac{(|\varphi| - 60°)}{3}} \right) \right] \right\}^2 \cos\left(\frac{\pi}{180°} \lambda \right)$$

$$G(t) = A\left(1.0 - \exp\left(-\frac{t}{\tau}\right)\right)$$

The value of the forcing peak amplitude (A) will be varied but the parameter τ will be fixed at 2.5×10^5 seconds. Figure 5.5 shows the functions that make up the forcing perturbation for various peak amplitudes. Note that by model day 10, the forcing amplitude already exceeds 90% of its constant peak value.

As an instability phenomenon, the two-day wave will be generated even with the weakest forcing amplitude in the model run if the potentially unstable initial condition is properly defined. Only a minute perturbation will spark an instability growth. The amount of winter forcing will have little or no effect on the amplitude of the unstable wave. In that sense, the winter forcing does not directly force the two-day wave. However, near the stratopause when the forced winter planetary wave propagates toward the equator, wave breaking process can perhaps be linked to the 2-day wave as suggested by Orsolini et al.

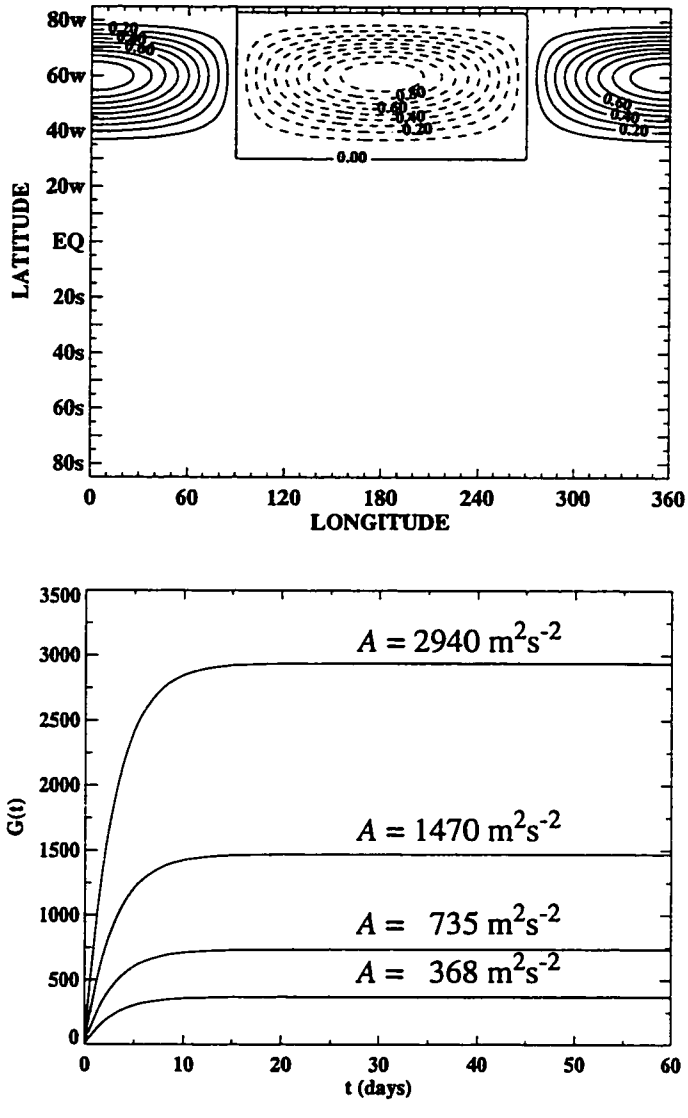

Figure 5.5: The geopotential perturbation at the model's base. The function F(λ, φ), top, and G(t), bottom, of the prescribed perturbation for various peak amplitudes (A).

(1997). Breaking stationary waves tend to organize inertial eddies in the winter subtropics (O'Sullivan and Hitchman, 1992; Sassi et al., 1993). These eddies flux momentum toward the summer hemisphere, tending to increase the meridional curvature on the equatorward side of the easterly jet. The increased curvature adds to the jet's unstable nature and may provide favorable condition for the growth of the unstable two-day wave.

5.3 ANALYSIS

The analytical tools used to diagnose the model results are similar to those used in the observational study. The space-time spectral analysis of Hayashi (1971) is performed to identify wave signals. The mean quasi-geostrophic potential vorticity meridional gradient is also computed using the Equation (3.12). Band-pass filtering will also be employed. The model generated global wind fields also facilitate another important analysis, that of Eliassen-Palm (EP) fluxes.

The zonal momentum equation of the transformed Eulerian mean (TEM) equations is given in Andrews et al. (1987) as:

$$\frac{\partial \bar{u}}{\partial t} = DF + \bar{\eta}\bar{v}^* - \frac{\partial \bar{u}}{\partial z}\bar{w}^* \tag{5.6}$$

where $\bar{v}^*$ and $\bar{w}^*$ are the meridional and vertical components of the residual mean circulation, $\bar{\eta}$ is the absolute vorticity of the zonal mean flow. The term $\overline{\eta v}^*$ represents mean wind acceleration by horizontal advection while the last term on the right ($-\bar{u}_z\bar{w}^*$) represents the mean wind acceleration by vertical advection. The term DF is the zonal forcing per unit mass (i.e. body force) by the resolved waves and is related to the divergence of the EP flux vector (F):

$$DF = \frac{1}{\rho_0 a \cos\varphi}\nabla \bullet F \tag{5.7}$$

where,

$$\nabla \bullet F \equiv \frac{1}{a\cos\varphi}\frac{\partial}{\partial\varphi}(F^{(\varphi)}\cos\varphi) + \frac{\partial F^{(z)}}{\partial z} \tag{5.8}$$

and the horizontal and vertical components of the vector are expressed respectively as:

$$F^{(\varphi)} = \rho_0 a\cos\varphi\left(\frac{\partial\bar{u}}{\partial z}\overline{v'\theta'} - \overline{u'v'}\right) \tag{5.9}$$

and

$$F^{(z)} = \rho_0 a\cos\varphi\left(\frac{\bar{\eta}}{\partial\bar{\theta}/\partial z}\overline{v'\theta'} - \overline{u'w'}\right) \tag{5.10}$$

The quantity $\bar{\theta}$ is the zonal mean potential temperature and the rest of the symbols are identical to ones used in Andrews et al. (1987). The EP flux analysis allows for the examination of wave forcing contribution to the zonal mean momentum budget and the direction of the wave energy propagation. The forcing can affect the zonal mean wind tendency and drive a residual mean circulation.

CHAPTER 6

EXPERIMENTAL RESULTS

Results of the experimental runs are presented in this chapter. The control run results will first be discussed. In this run, the weakest planetary wave forcing amplitude is specified ($A = 368\ m^2s^{-2}$), and the Newtonian cooling profile with the constants (α, β) = (3.0, 2.5) is used. The initial condition is given in Figure 5.4. Variations to the control run are subsequently imposed to examine its sensitivity. The Newtonian cooling profile will be altered, then the winter wave forcing amplitude is incrementally doubled. Finally, the control experiment is redone using a different initial wind condition. For all runs, the model is integrated for 60 days. Overall, the model is able to produce features remarkably similar to the observed two-day wave with evidence of triggering by inertial instability. For the diagrams shown in this chapter, latitudes in the winter (summer) hemisphere are denoted with the letters "w" ("s"); for example, "20w" and "20s" represent 20° latitude in winter and summer hemisphere, respectively.

6.1 CONTROL RUN

The meridional structure of the zonal mean zonal wind is shown in Figure 6.1. By day 10, the structure below 0.10 hPa (~65 km) remains similar to the initial wind. This is due to the strong Newtonian cooling above 1.0 hPa and the weak Rayleigh friction below 0.1 hPa parametrized in the model. The region of negative quasi-geostrophic potential vorticity (QGPV) gradient (the shaded areas indicating $\bar{q}_\varphi \leq 0$) in the low summer latitudes remains small. Above 0.10 hPa, the effects of Rayleigh friction are obvious. The mean wind has experienced the decelerative effects of the parametrization which mimics the role of breaking gravity waves in the mesosphere. The strong meridional wind shear has also diminished above 0.1 hPa as a result of Rayleigh friction. For this reason, to maintain the meridional wind shear condition near the stratopause, the Rayleigh friction parametrization is designed to take effect above 0.1 hPa.

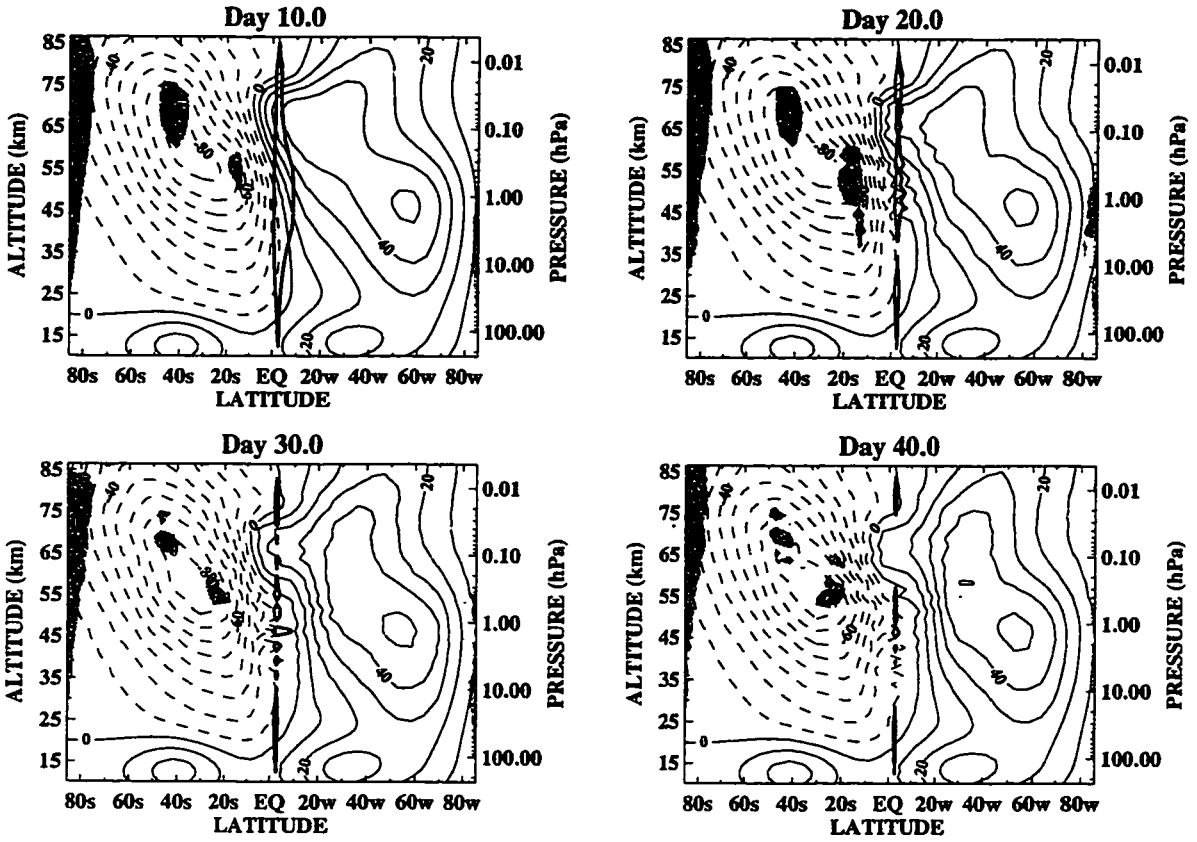

Figure 6.1: The zonal mean zonal wind meridional structure for the control run. The contours are in increments of 10ms^{-1}. The shaded areas show where $\bar{q}_{\varphi} \leq 0$, denoting regions where the necessary condition for barotropic-baroclinic instability is satisfied. The bold line in the equatorial region encloses the region where $f(f - a^{-1}\bar{u}_{\varphi}) < 0$, denoting the region where the necessary condition for inertial instability is fulfilled.

Subsequent zonal mean zonal wind states show changes mainly within 30° latitude of the equator. In low summer latitudes, the region of negative QGPV gradient has expanded by day 20, extending well below 2.0 hPa and growing meridionally. Apparent with this expansion is the increased meridional wind shear on both sides of the equator and equatorial wind shear reduction. As a result, the size of the region where $f(f - a^{-1}\bar{u}_{\varphi}) < 0$ (enclosed by the bold line) has decreased. This condition is a necessary criterion for inertial instability and is dictated by strong meridional wind shear exceeding the local Coriolis parameter. After day 20, the low summer latitude region of negative QGPV gradient is displaced toward higher latitude and closer to the easterly jet core. Around 1.0 hPa, the region completely disappears. The equatorial wind shear is notably weak, consistent with the dwindling regions of potential inertial instability. The easterly wind has also further crossed the equator around the stratopause.

Figure 6.2 illustrates the 5-day averaged Eliassen-Palm (EP) flux vectors for the run. Wave fluxes in the vectors' formulation are computed using fields with zonal wavenumber 1-10 components. The diagram illustrates the path of energy propagation and the local zonal acceleration per unit mass of the mean zonal wind (or zonal wave forcing, *DF*). Each vector component in Equations 5.9 and 5.10 is divided by $\rho_0 a \cos\varphi$. In addition, the vertical vector components are scaled by the ratio of the global distance (in kilometers) between 70° summer and winter latitudes to the displayed vertical distant (~62 km). Upward and poleward energy propagation of the weakly forced planetary (Rossby) wave is present in each panel. The Rossby wave is guided equatorward toward the zero mean wind line by the background wind condition and resulting refractive index gradient. Note that by day 10, the forcing wave amplitude has already exceeded 90% of its steady peak value.

During days 10-15, strong wave activity is evident in the low winter latitudes. The feature is barotropic and is directed away from the equator. The zonal wave forcing imparts an accelerative mean wind tendency over the equator and a decelerative tendency around 10° winter latitude. Hence, the zonal wave forcing tends to transport westerly

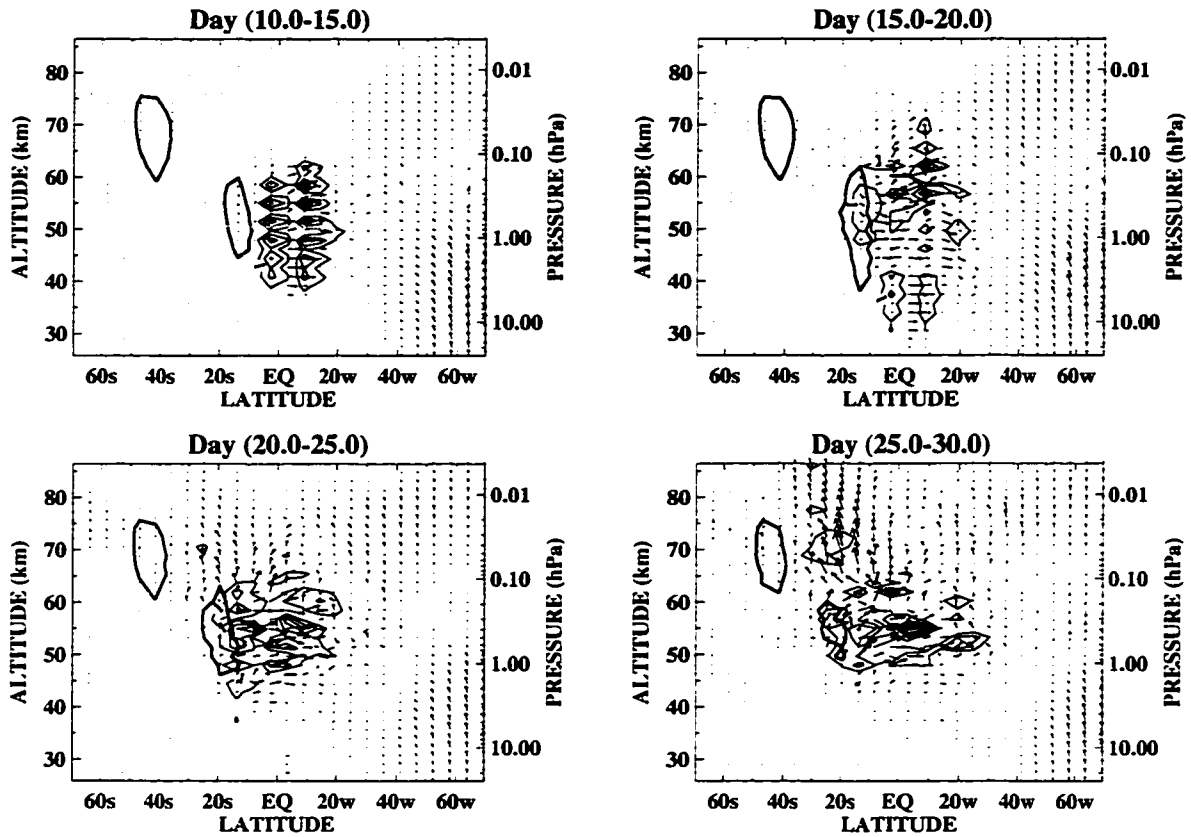

Figure 6.2: Five day time-averaged structure of the Eliassen-Palm flux vector and mean zonal acceleration per unit mass by wave forcing (DF) for the control run. The maximum vector length of each panel is scaled relative to the top left panel. DF is shown as contours in increments of 1.0 $ms^{-1}day^{-1}$ starting from 1.0 $ms^{-1}day^{-1}$. Blue (red) contours denote positive (negative) DF. The bold lines enclose areas where $\bar{q}_{\varphi} \leq 0$, denoting the regions where the necessary condition for barotropic-baroclinic instability is satisfied.

momentum equatorward. The maxima of the forcing have time averaged magnitudes as large as 3 $ms^{-1}day^{-1}$ and are vertically separated by about 3.5 km, nearly twice the model's vertical resolution in this altitude range. The pattern during days 10-15 resembles that shown in Fig. 6B of Hitchman et al.(1987) based on an analysis of estimated balance winds from LIMS data.

The disturbance at later model time is characterized by a gradual shift of wave activity toward the lower summer latitudes. This shift begins with the enlarging of the negative QGPV gradient area near 10° summer latitude during days 15-20. The wave activity remains predominantly barotropic and expands vertically in both direction. By days 20-25, the wave activity in low summer latitudes strengthens. The EP flux vectors now appear to emanate from the negative QGPV gradient area. Equatorward energy propagation is evident near the stratopause and upward energy propagation is notable in the low summer latitudes above 0.2 hPa. The zonal wave forcing shows a decelerative tendency focusing around 10° winter latitude and an accelerative tendency near 10° summer latitude. By days 25-30, similar wave activity persists. Vertical energy propagation is however more pronounced in the summer hemisphere and aligns with the strong meridional wind shear region on the equatorward flank of the easterly jet core (see. Figure 6.1). The low summer latitude negative QGPV gradient area has also diminished and displaced poleward. Despite strong Rayleigh friction damping of both wave and mean flow above 0.10 hPa, significant wave energy propagation is seen in the region.

Disturbances associated with the wave activity in the low summer latitudes are identified using conventional spectral analysis. The computation is performed using a 30-day windowed time series starting from model day 10 to 39, inclusively. The spectral resolution is then ~0.03 cycles per day (cpd). The Nyquist limit is at 1 cpd as the data in the time series is given every half day from the model output. Both meridional wind and the temperature fields are analyzed. Wave activity represented by the vertically stacked EP flux divergence-convergence in the low winter latitude during day 10-15(see Figure 6.2) is likely excluded by the analysis since the disturbance is short-lived and appears near the

beginning of the time series which is tapered. The disturbances related to these features are later examined.

The wavenumber-frequency spectral diagrams for the meridional wind field at 0.3 and 0.01 hPa are given in Figure 6.3 and Figure 6.4. The diagrams reveal that the low summer latitude wave activity shown in Figure 6.2 is dominated by zonal wavenumber 3 and 4 components. At 1.0 hPa (not shown), the strongest signal is located within the equatorial band averaged between 10° summer and winter latitudes. The zonal wavenumber 4 signal peaks at a ground relative westward frequency of about 0.53 cpd, corresponding to a period of 1.89 days. At 0.3 hPa, the similar wavenumber 4 signature remains in the same equatorial band but is more pronounced. However, a significant portion of the energy is now focused at a westward moving zonal wavenumber 3 component with period of about 2.04 days (~0.49 cpd). Away from the equatorial band, the wavenumber 4 peak is prominent in the summer subtropical band while the wavenumber 3 peak is evident in the winter subtropical band. Finally, at 0.01 hPa, where strong damping is present, only the wavenumber 3 peak appears, albeit considerably weaker than at lower altitude.

The latitude-frequency structure of the meridional wind field at 0.3 hPa is given in Figure 6.5 for zonal wavenumbers 3 and 4. The frequency peaks of the spectral signal are as noted previously. Both signals are focused at the equator. While the wavenumber 4 signal is symmetric about the equator, the slightly weaker wavenumber 3 signature is skewed toward the low winter latitudes. These signals are well confined between the frequency band denoted by the dashed lines. This frequency band is used for computing the wave variance shown later.

The spectral analysis of the temperature field finds similar wavenumber 3 and 4 dominance in the resolved spectra. Unlike the meridional field where the strong disturbance signals appear near 0.3 hPa, the temperature spectral peaks are stronger near 1.0 hPa. Figure 6.6 shows the 1.0 hPa temperature wavenumber-frequency spectra averaged in 20 latitude bins. The pronounced spectral peak is smeared over zonal wavenumbers 3 and 4 and

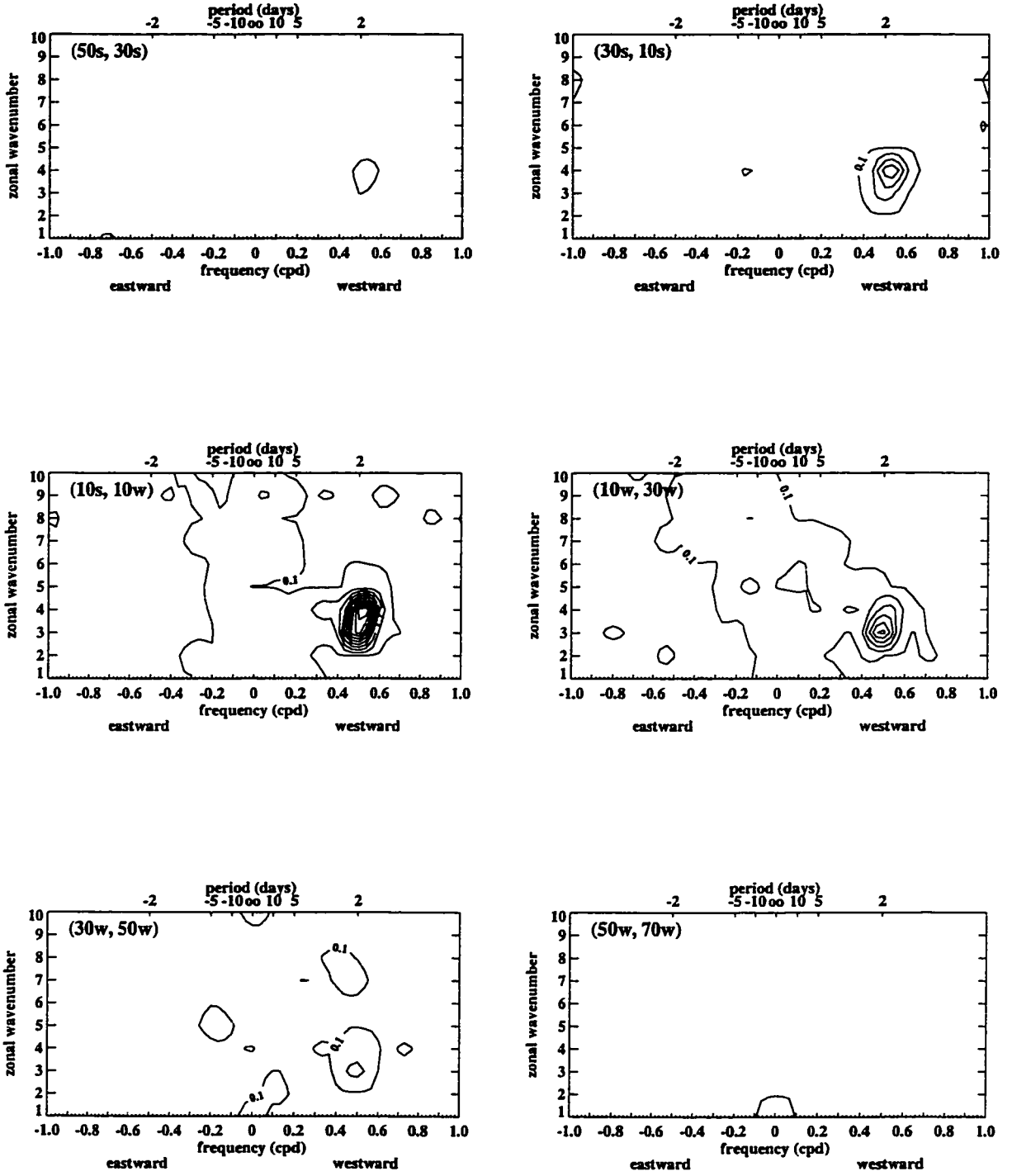

Figure 6.3: The latitudinally averaged meridional wind spectra at 0.3 hPa of the control run. The averaged latitude bands are shown in the top left corners of each panel. The contours are given in increments of 0.1 $ms^{-1}day$.

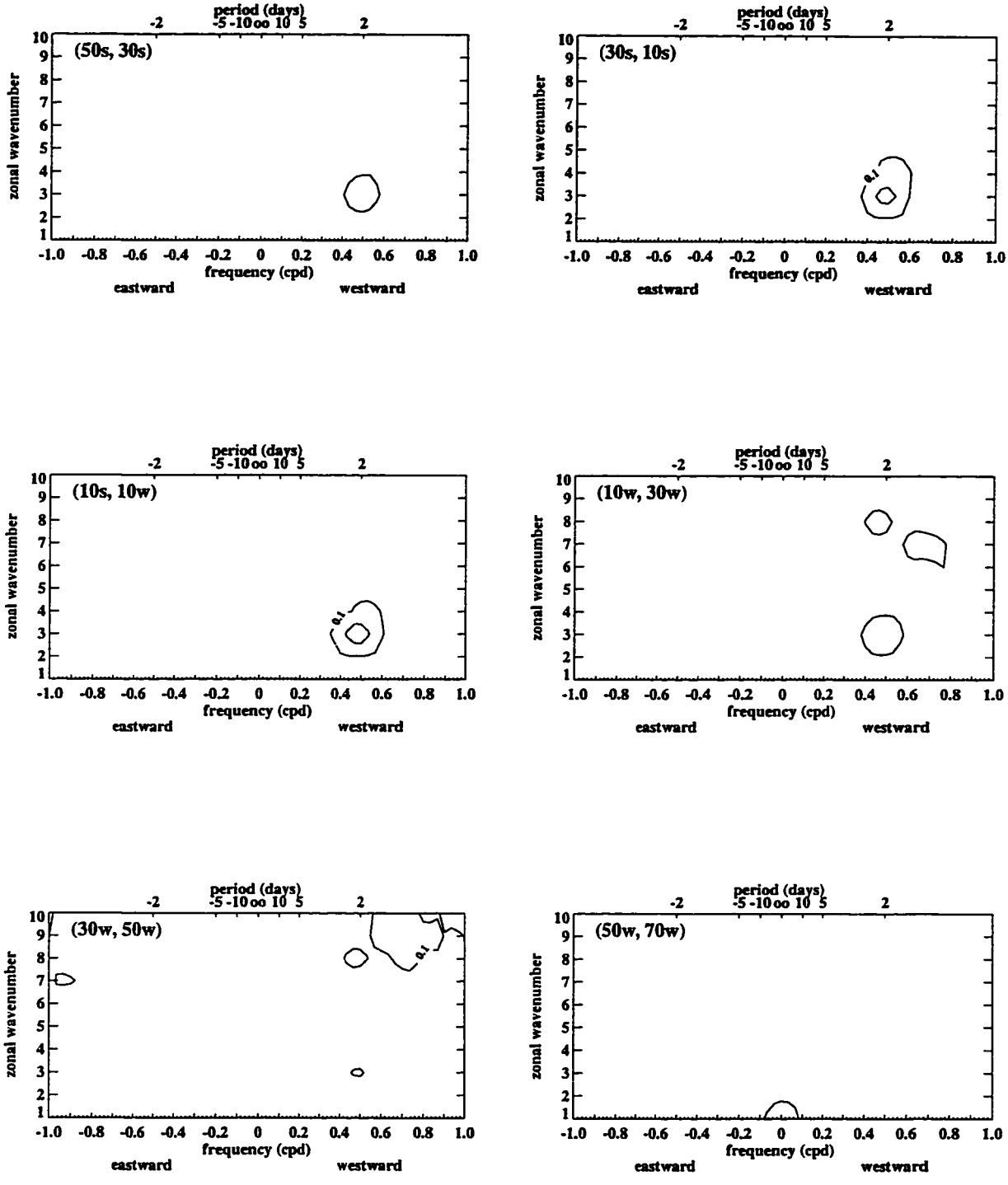

Figure 6.4: The latitudinally averaged meridional wind spectra at 0.01 hPa of the control run. The averaged latitude bands are shown in the top left corners of each panel. The contours are given in increments of 0.1 $ms^{-1}day$.

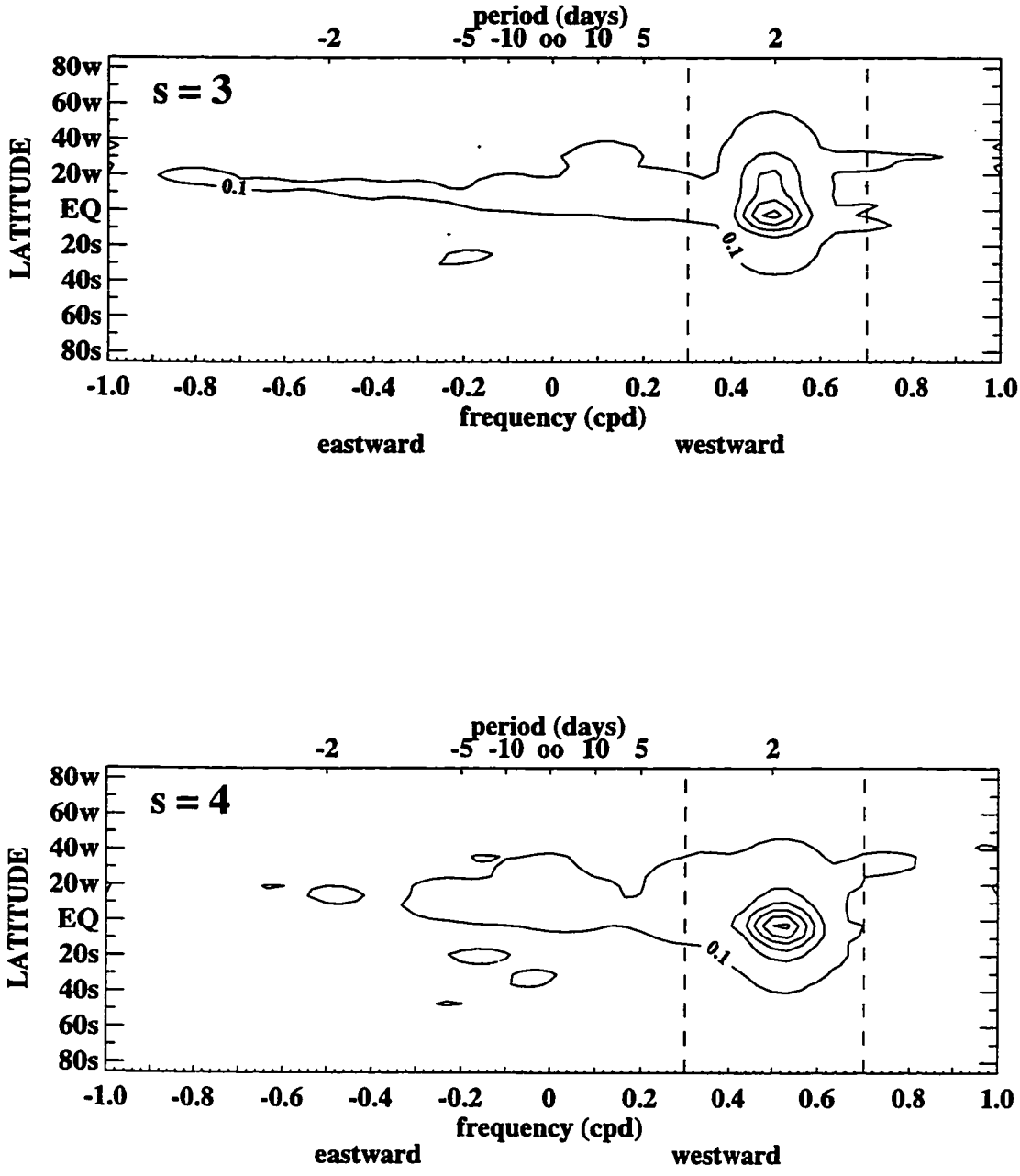

Figure 6.5: The latitude-frequency structure of the meridional wind zonal wavenumber 3 and 4 spectra at 0.3 hPa of the control run. The contours are given in increments of 0.2 ms^{-1}day. The dashed lines define the frequency interval 0.3-0.7 cycles per day (cpd).

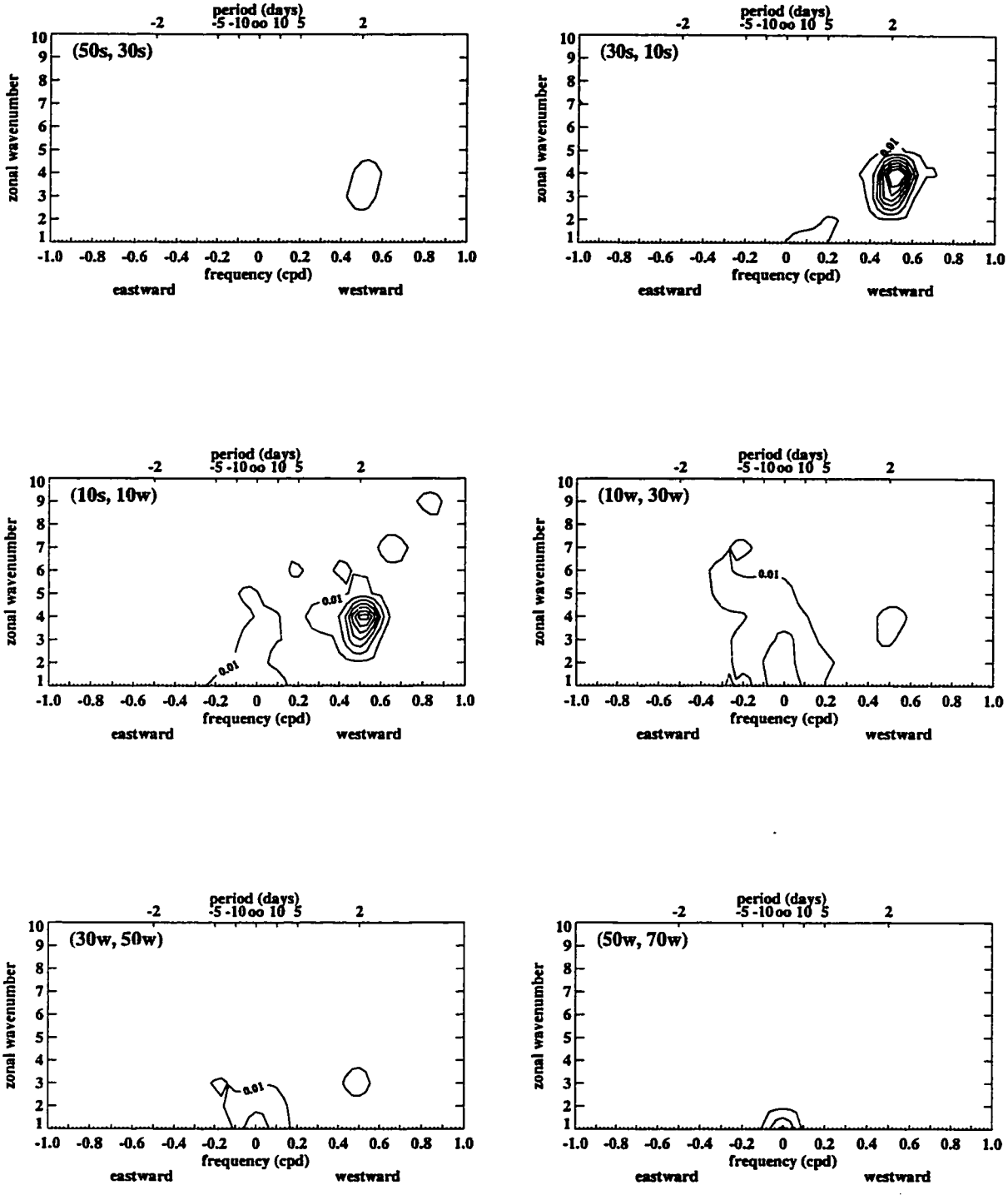

Figure 6.6: The latitudinally averaged temperature spectra at 1.0 hPa of the control run. The averaged latitude bands are shown in the top left corners of each panel. The contours are given in increments of 0.01 Kday.

pronounced in low summer latitudes (10°-30°). This also differs from the meridional wind field in which the strongest wavenumber 3-4 peak is located over the equatorial latitude band. The difference is clearly illustrated in the latitude-frequency temperature spectra diagram at 1.0 hPa (Figure 6.7). The frequency peak is near 0.49 cpd and 0.53 cpd for wavenumber 3 and 4 spectra, respectively, in agreement with the meridional wind spectra at 0.3 hPa. Both temperature spectra are concentrated near 10° summer latitude.

To examine the time evolution of the identified disturbances, band-pass filtering is performed. The zonal wavenumber 3 and 4 perturbations filtered over the westward frequency range of 0.3-0.7 cpd are computed. By definition, the disturbances associated with the filtered zonal wavenumber 3 and 4 signal are referred to as the (3, 2.04) and (4, 1.89), respectively. In the notation, the first number in the parenthesis denotes the zonal wavenumber of the disturbance and the second number represents the central westward period of the disturbance as depicted in the spectral analysis. This nomenclature is identical to that used to define the observed two-day wave and will be used throughout this chapter.

Figure 6.8 illustrates the altitude-time evolution of the meridional wind (3, 2.04) and (4, 1.89) perturbations at the equator. Initial perturbations appear in the model run starting around day 17 and reside near the stratopause and above. The wavenumber 4 disturbance maximizes earlier in the run (around days 20-25) and much of its strength is confined between 0.10 and 1.00 hPa. Little or no phase tilt is apparent in this altitude range. Above 0.10 hPa, some downward phase tilt with time is seen, but the perturbation is extremely weak. After day 40, its signal becomes relatively weak. The wavenumber 3 disturbance maximizes later in the run around day 25-30. Like wavenumber 4, there is minimal vertical phase tilt within the altitude range 0.10 and 1.00 hPa. However, above 0.1 hPa, observable downward phase tilt with time is evident. The perturbation pattern is consistent with the discussed spectral signature in that the wavenumber 3 signature tends to dominate the wind spectra above 0.1 hPa and a mixture of the signals are observed below 0.1 hPa.

The altitude-time evolution of the temperature perturbation at the 10° summer latitude

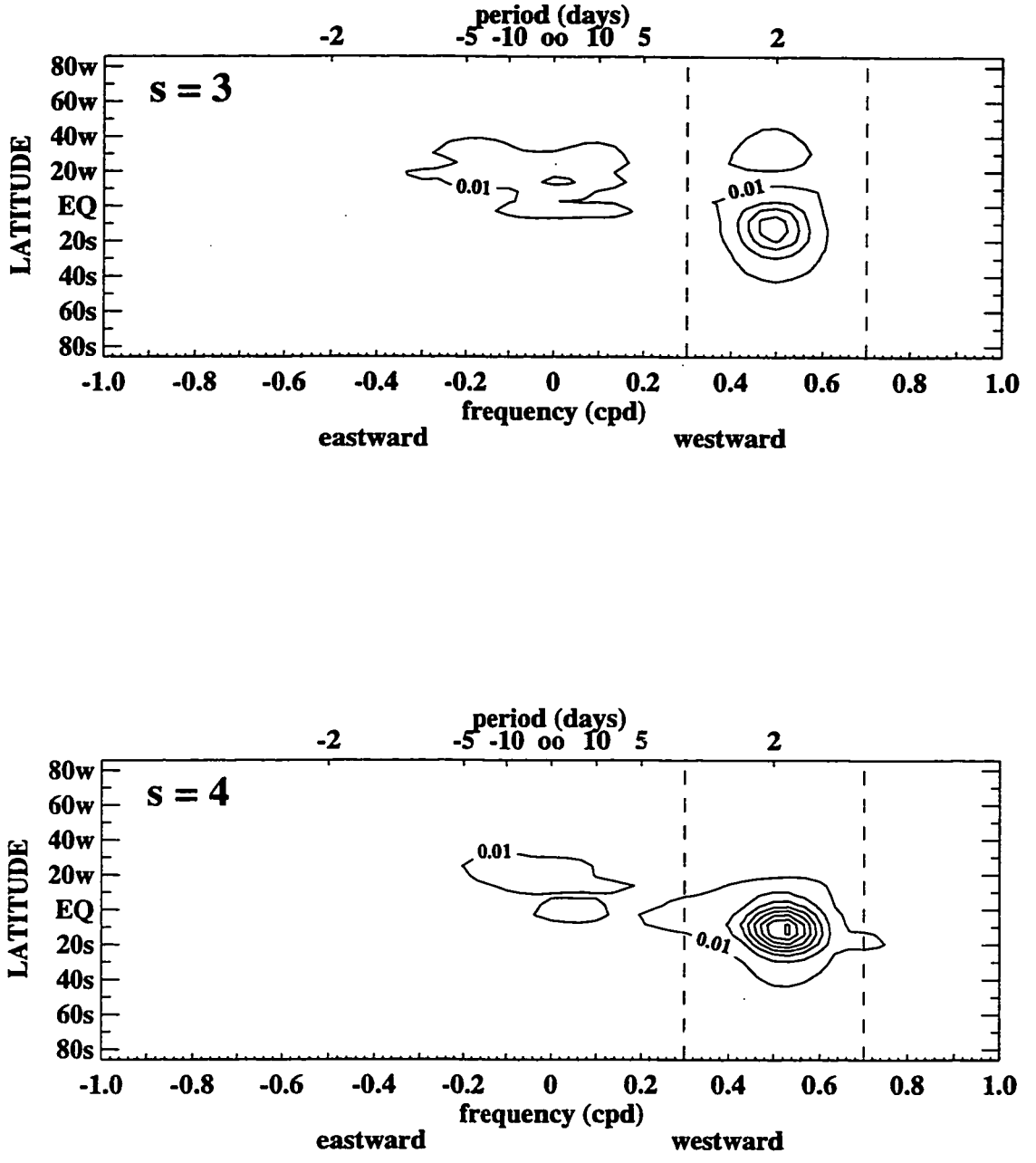

Figure 6.7: The latitude-frequency structure of the temperature zonal wavenumber 3 and 4 spectra at 1.0 hPa of the control run. The contours are given in increments of 0.05 Kday. The dashed lines define the frequency interval 0.3-0.7 cycles per day (cpd).

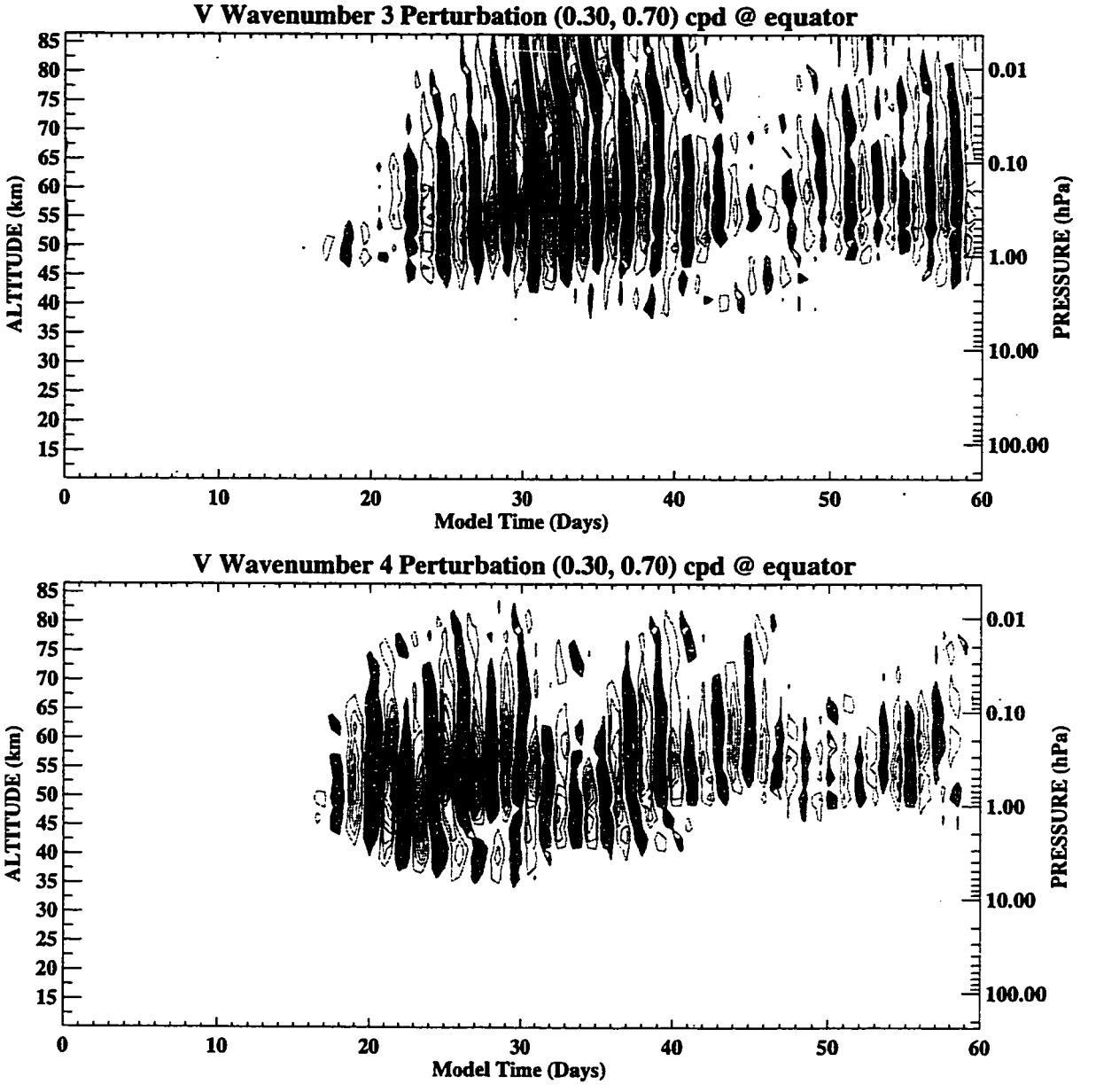

Figure 6.8: The vertical-time evolution of the zonal wavenumber 3 and 4 meridional wind perturbations at the equator of the control run. The perturbation is band-pass filtered in the frequency band 0.30-0.70 cpd. The contour interval is 2 ms^{-1} (starting from 2 ms^{-1}) with the zero contour omitted for clarity. The negative perturbation is shaded.

is provided in Figure 6.9. The temperature perturbation reveals a distinct separation between the disturbance near the stratopause (centered around 1 hPa) and the mesospheric disturbance that is approximately of opposite phase. Incipient perturbations begin around day 17 and peter out after day 40. The wavenumber 4 disturbance is strongest near the stratopause region with minimal vertical phase tilt. The wavenumber 3 perturbation maximizes after the wavenumber 4. Minimal phase tilt is associated with the signal around 1 hPa, but obvious downward phase tilt with time is observed above 0.10 hPa. The spatial and temporal characteristics of the temperature waves are qualitatively similar to the meridional wind perturbation at the equator.

A time sequence of the synoptic (planar) maps shows observable westward phase tilt with latitude in the perturbations. Figure 6.10 shows the temperature (3, 2.04) perturbation at 1.0 hPa during the time period when the mode is strong. A southeast-northwest meridional phase tilt is obvious in low summer latitudes. A secondary perturbation is also present in the winter hemisphere around 25° winter latitude with a node around 15° winter latitude. The "winter" perturbation is relatively weaker and is almost completely out of phase with the summer perturbation. This global characteristic in the temperature perturbation field is consistently apparent even at higher altitude whenever the (3, 2.04) mode reaches its peak amplitude. This characteristic is however short-lived lasting only a few days but is suggestive of the third Rossby-gravity mode discussed in Chapter 2. As suggested by Wu et al. (1996), a global mode can perhaps be excited locally by an instability wave of similar spectral characteristics. The meridional wind (3, 2.04) perturbation (not shown) shows similar meridional phase tilt in the summer hemisphere. Its maxima is centered over the equator. The (4, 1.89) perturbation exhibits similar meridional phase tilt as the (3, 2.04) mode. The (4, 1.89) temperature perturbation however does not show an out-of-phase winter perturbation. Figure 6.11 shows the temperature (4, 1.89) mode during its growth peak.

Time-averaged meridional structures of the amplitude and phase are presented in Figure 6.12 and Figure 6.13 for the (4, 1.89) and (3, 2.04) modes, respectively. The averaging

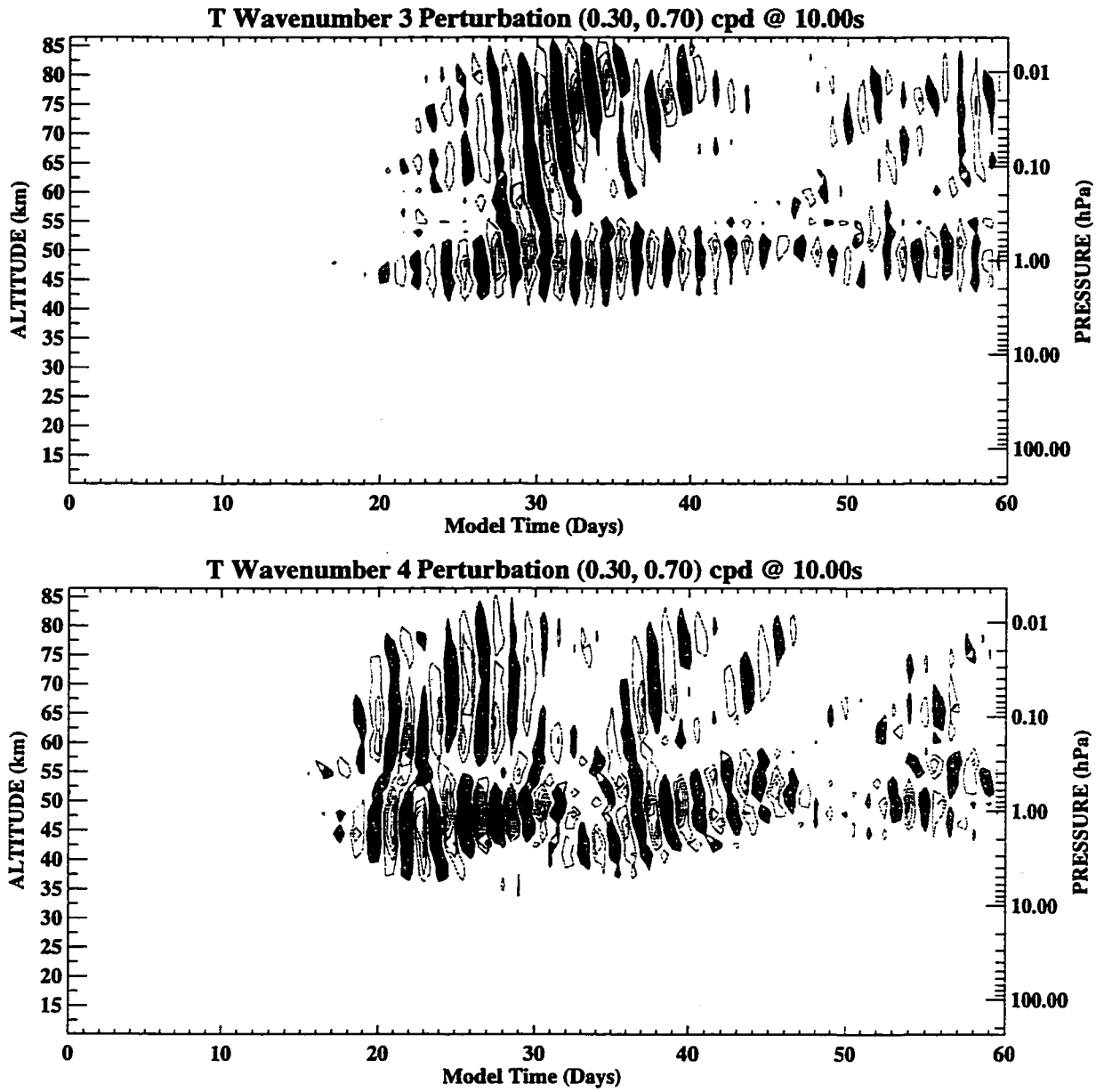

Figure 6.9: The vertical-time evolution of the zonal wavenumber 3 and 4 temperature perturbation at the 10° summer latitude of the control run. The perturbation is band-pass filtered in the frequency band 0.30-0.70 cpd. The contour interval is 0.5 K (starting from 0.5 K) with the zero contour omitted for clarity. The negative perturbation is shaded.

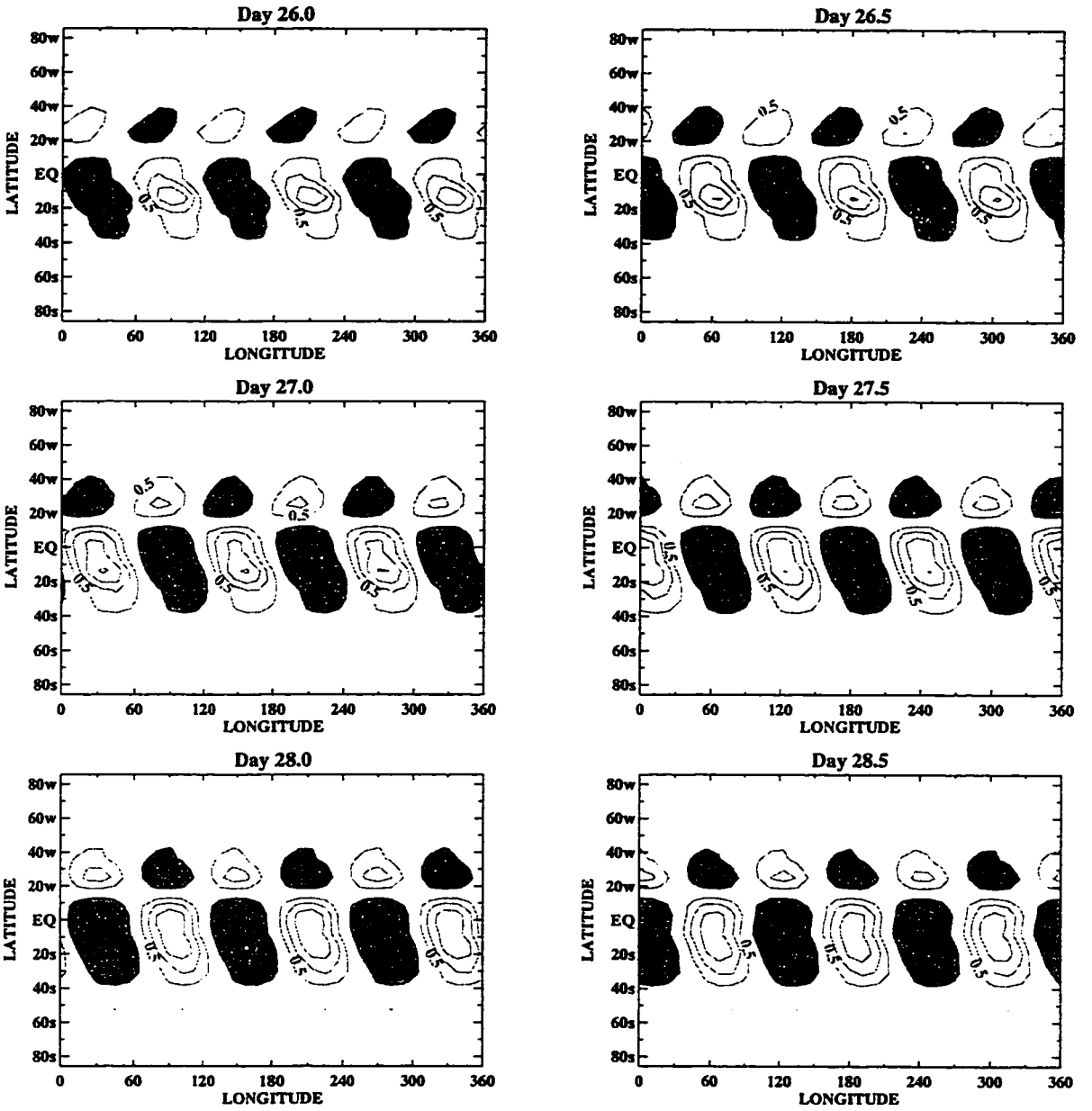

Figure 6.10: A synoptic map sequence for the temperature (3, 2.04) perturbation at 1.0 hPa of the control run. The negative perturbations are shaded. The zero contours are suppressed for clarity. Contour interval is 0.5 K.

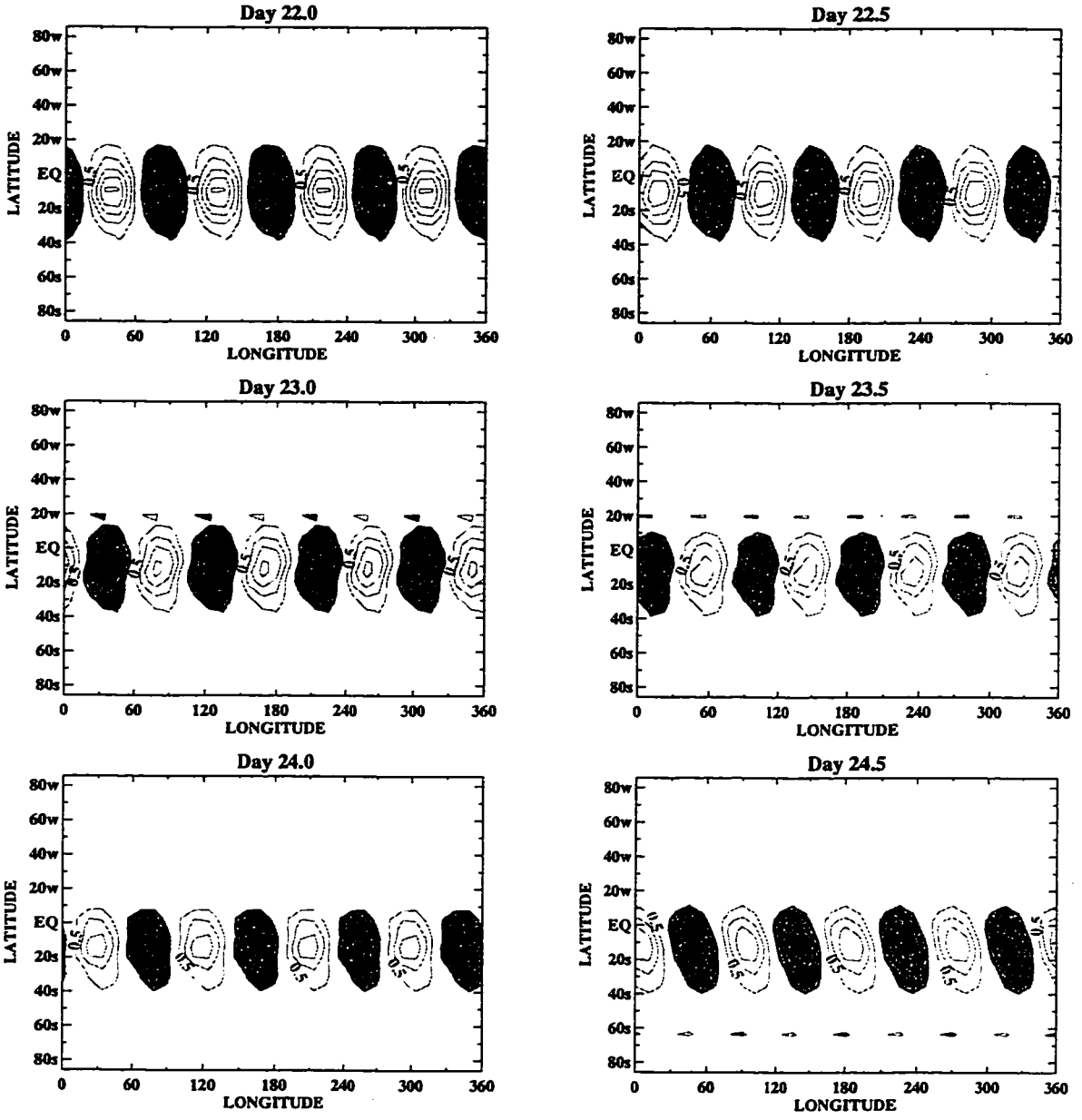

Figure 6.11: A synoptic map sequence for the temperature (4, 1.89) perturbation at 1.0 hPa of the control run. The negative perturbations are shaded. The zero contours are suppressed for clarity. Contour interval is 0.5 K.

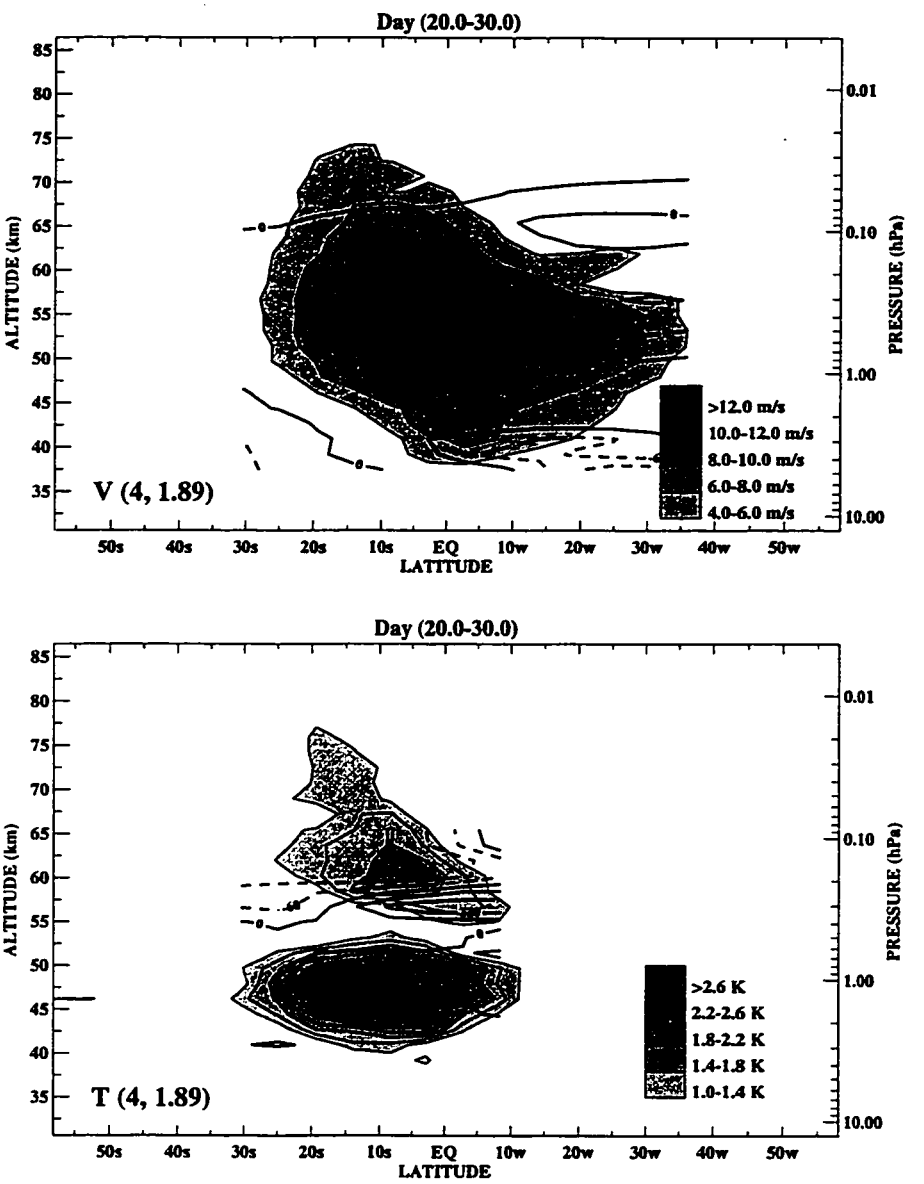

Figure 6.12: The time-averaged meridional structure of the (4, 1.89) amplitude of the control run. The averaging is done for model days 20-30. The meridional wind (top) is contoured every 2 ms^{-1} and the temperature (bottom) is contoured every 0.2 K. The phase lines are shown as the bold contours in increments of 60°.

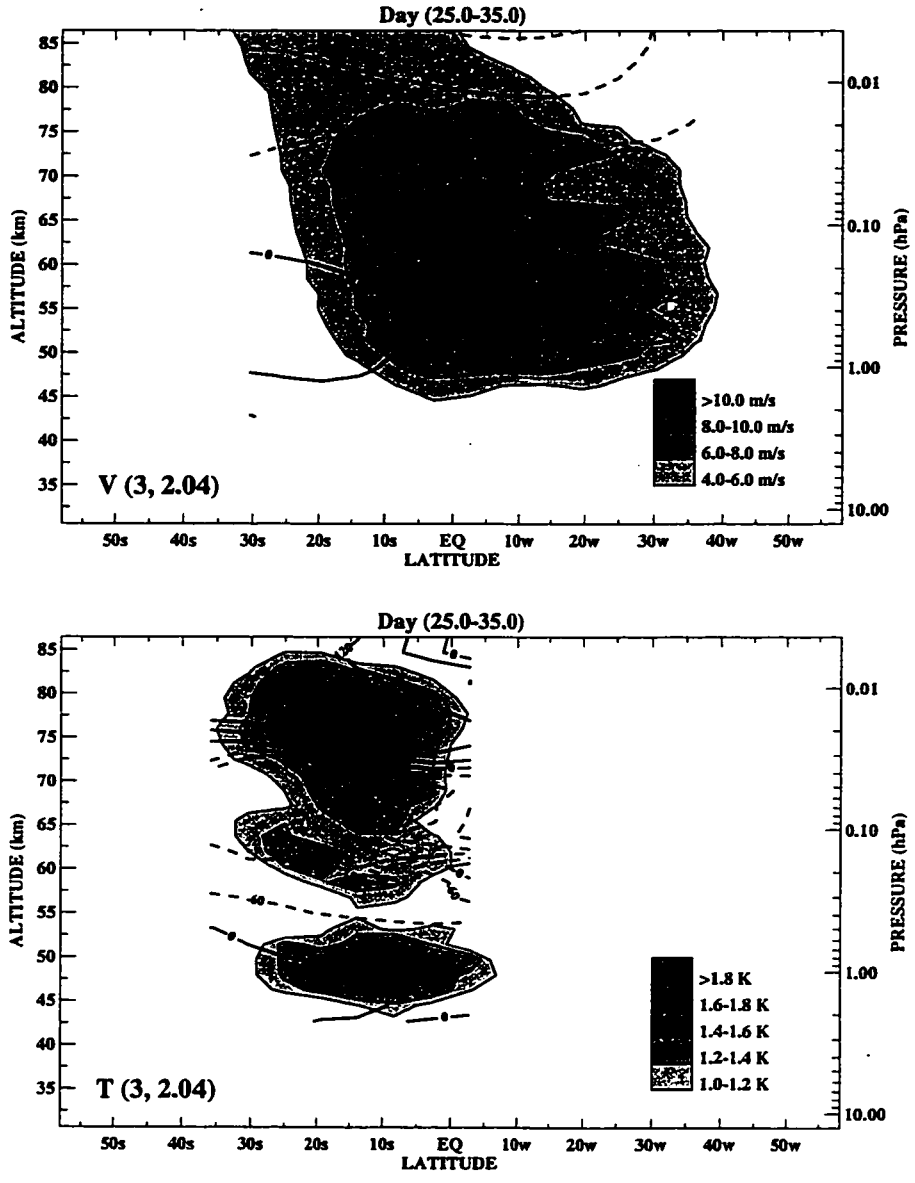

Figure 6.13: The time-averaged meridional structure of the (3, 2.04) amplitude of the control run. The averaging is done for model days 25-35. The meridional wind (top) is contoured every 2 ms^{-1} and the temperature (bottom) is contoured every 0.2 K. The phase lines are shown as the bold contours in increments of 60°.

is performed during the strong perturbation episode indicated by Figure 6.8 and Figure 6.9: days 20-30 for the (4, 1.89) mode and days 25-35 for the (3, 2.04) mode. For the (4, 1.89) mode, the temperature amplitude has a double peak structure in the vertical. The stronger peak has amplitude about 3 K and is centered just below 1.0 hPa. A nearly out-of-phase weaker peak is focused around 0.2 hPa with maximum value of about 1.5 K. The double structure maximizes near 10° summer latitude and is confined mostly in the summer hemisphere. The (4, 1.89) meridional wind amplitude maximum is situated over the equator and at 0.5 hPa, between the temperature amplitude maxima. The meridional wind structure is almost symmetric about the equator and is confined primarily near the stratopause. The maximum wind speed exceeds 14 ms^{-1} at 0.5 hPa. Overall, the phase lines indicate the aforementioned barotropic nature of the (4, 1,89) mode.

The (3, 2.04) temperature structure shows a double peak feature of nearly equal strength (~1.8 K). One peak is in the stratopause region, just below 1 hPa and near 10° summer latitude. The other is in the mesosphere at 0.02 hPa and at slightly higher latitude. This second peak is remarkable since it resides in region of strongly imposed Rayleigh damping. Overall, the temperature structure is located in the summer hemisphere on the equatorward flank of the easterly jet where strong horizontal wind shear is prevalent (see Figure 6.1). The meridional wind structure maximum is located over the equator and near 0.3 hPa, between the temperature maxima. The maximum wind is slightly above 10 ms^{-1}. Latitudinally, the structure is skewed toward the winter hemisphere. Vertically, the amplitude extends well above 0.1 hPa and tilts slightly poleward. The meridional wind phase lines show the lack of vertical tilt between 1.0 and 0.1 hPa. Above 0.1 hPa, the wind amplitude tilts slightly westward with height. The temperature phase picture is less clear possibly because of the weak and short-lived nature of the temperature perturbation averaged over 10 days.

The time-averaged, filtered EP flux vectors for (3, 2.04) and (4, 1.89) disturbance modes are shown in Figure 6.14. The fluxes contributing to the vector components are computed from band-pass filtered (between 0.30-0.70 cpd) variables for each zonal wave-

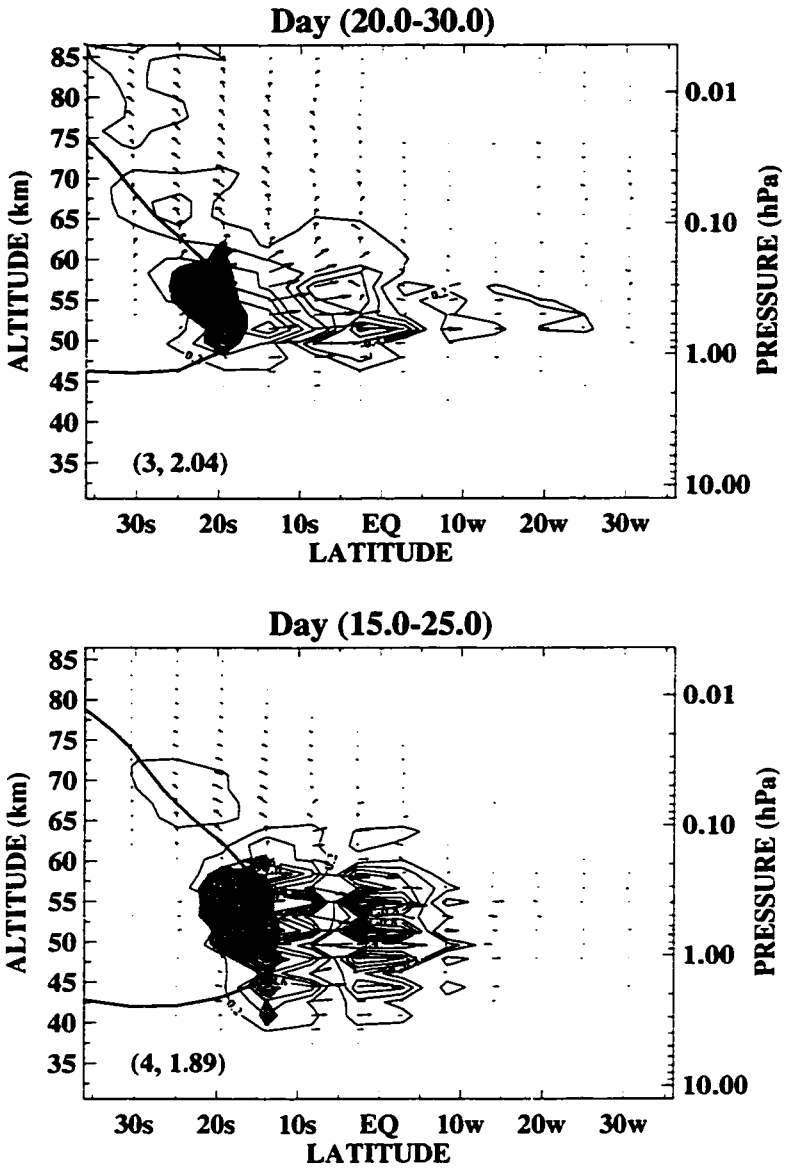

Figure 6.14: The 10-day averaged EP flux vectors diagrams for (3, 2.04) mode, top, and (4, 1.89) mode, bottom, of the control run. The maximum vector length of each panel is relative to one another. The wave forcing per unit mass (DF) is shown by the line contours in increments of 0.2 $ms^{-1}day^{-1}$; blue (red) contours denote positive (negative) DF values. The shaded regions shows the averaged area of negative QGPV gradient. The mode critical line is shown in the diagrams as a bold line.

number. The vector components are scaled in the same fashion as those shown in Figure 6.2. The mode critical line (bold line) is also plotted along with the averaged region where QGPV gradient is reversed. The mode phase speed is computed from the its central period (i.e. 2.04 and 1.89 days) as indicated by the spectral analysis. The time averaging is performed over days 20-30 and 15-25 for the (3, 2.04) and (4, 1.89) modes, respectively. These 10 days encompass the time-frame when the modes are growing and beginning to reach their peaks.

The EP flux vectors reveal that both modes can be attributed to the Charney-Stern inflection instability growth (Charney and Stern, 1962). The (4, 1.89) mode growth appears first in the model. Its greatest energy propagation occurs between 0.10 and 1.0 hPa and is mainly directed horizontally toward the winter hemisphere. The EP flux vectors emanate from the mode critical line which resides in the region of negative QGPV gradient. This local generation of wave activity is consistent with mainly barotropic instability growth and wave over-reflection near the critical line. In barotropic-baroclinic instability, the most vigorous wave vorticity flux occurs at the critical line. At the critical line, the wave does not drift with the respect to the entraining ambient flow so it can effectively extract energy from the mean wind and grow at its expense. The zonal wave forcing associated with the (4, 1.89) mode tends to weaken the easterly mean wind around 10° summer latitude and strengthen the easterly mean wind over the equator. The forcing is as large as 1 $ms^{-1}day^{-1}$ in the ten day averaged period. The growing mode disturbance has the tendency to flux westerly momentum into the summer easterly jet core. Some upward-poleward energy propagation is evident above 0.1 hPa along the critical line but appears highly attenuated.

The (4, 1.89) wave activity is consistent with structure elucidated in the previous subsection. The vigorous horizontal wave activity near the stratopause produces an amplitude maximum in the same region at subsequent time period. The barotropic nature of the wave activity and its tendency to transport westerly momentum down gradient agrees with the observed southeast-northwest meridional phase tilt of the perturbation. The weak upward

and poleward energy propagation results in decreasing amplitude structure above 0.1 hPa and weak downward vertical phase tilt in the perturbation.

The energy propagation of the (3, 2.04) also stems from the intersection of its critical line with the negative QGPV gradient region (see bottom panel of Figure 6.14). This region is now centered near 20° summer latitude during day 20-30. Near the stratopause, the strength of the activity is comparable to the (4, 1.89) mode. The zonal wave forcing tends to flux westerly momentum further toward the easterly jet core. The forcing magnitude is roughly 0.8 $ms^{-1}day^{-1}$ near the stratopause. Unlike the (4, 1.89) mode, the (3, 2.04) energy propagation penetrates higher in the mesosphere where the model is highly damped. The upward-poleward propagation parallels the critical line and is mainly in regions where the wave phase speed is westward relative to the mean zonal wind, characteristic of Rossby waves. The strong vertical propagation pattern produces noticeable (3, 2.04) disturbance amplitude in Figure 6.13 above 0.1 hPa. The downward vertical phase tilt in time (and westward vertical tilt) of the westward propagating perturbation is consistent with the upward energy propagation. Near the stratopause, the horizontally directed wave activity agrees with the southeast-northwest meridional phase tilt of the perturbation and the westerly momentum transport tendency associated with the wave.

To further examine the wave growth and the changing mean flow condition, the latitude-time evolution of each mode and the zonal mean wind is investigated. The (4, 1.89) amplitude evolution is plotted in Figure 6.15 and Figure 6.16 for meridional wind and temperature, respectively. These plots are at different altitudes since each variable maximizes at different levels: near 0.3 hPa for the meridional wind and 1.0 hPa for the temperature. Despite the different heights, the wind and temperature amplitude peaks coincide in time. As illustrated in the spectral analysis, the temperature amplitude is focused in low summer latitudes while the wind amplitude is concentrated at the equator.

Around days 13-20, the (4, 1.89) critical line crosses (over a deep layer) the negative QGPV gradient region and acts as a wave source for (4, 1.89) growth. Initially, the mode

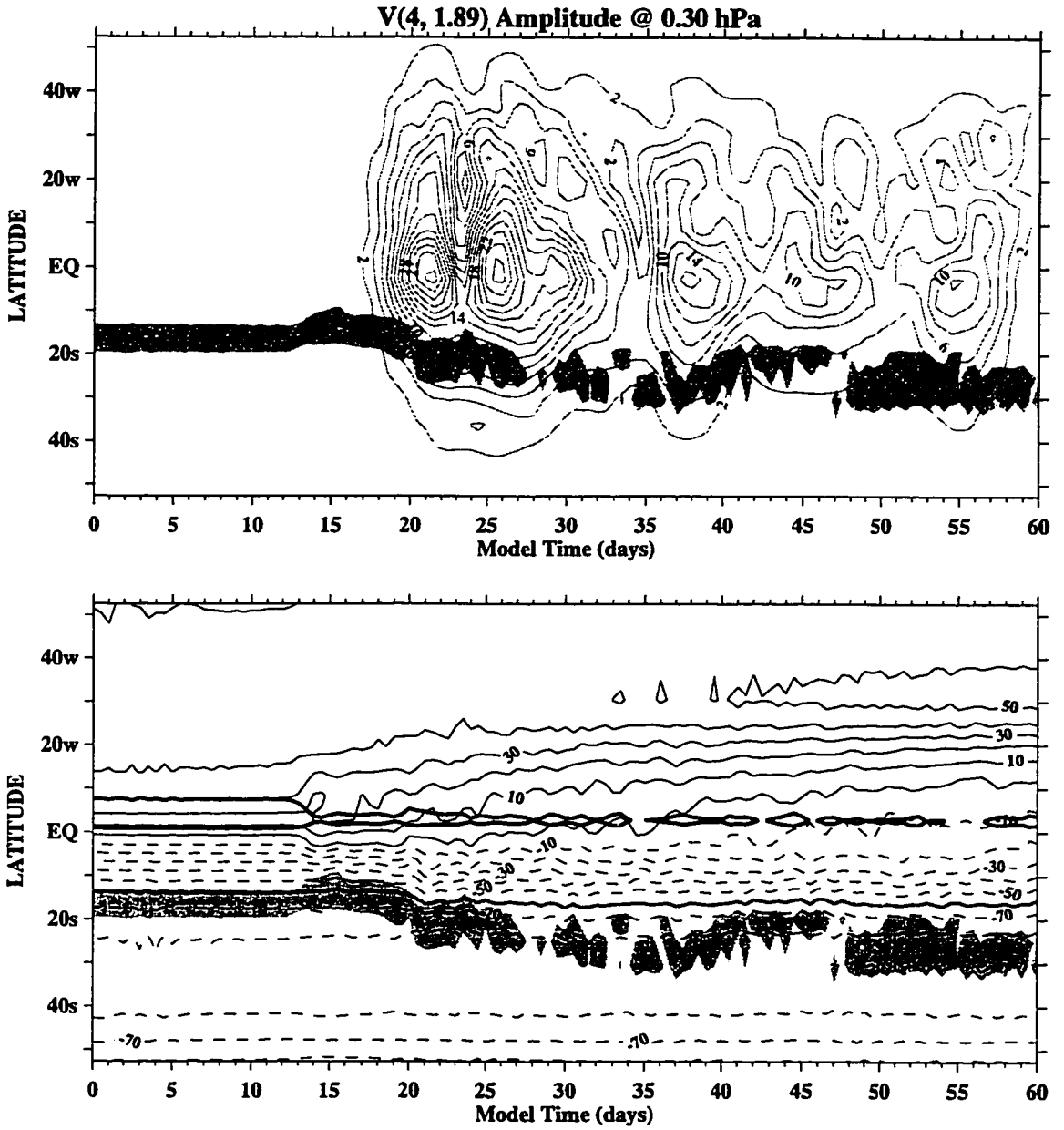

Figure 6.15: The meridional wind (4, 1.89) amplitude (top) and the zonal wind (bottom) evolution at 0.3 hPa of the control run. The wind amplitude and the zonal wind are contoured every 2 ms^{-1} and 10 ms^{-1}, respectively. The region of negative QGPV gradient is represented in both panels as shaded areas. In the bottom panel, the bold gray line indicates the mode critical line and the bold black line encloses areas of possible inertial instability.

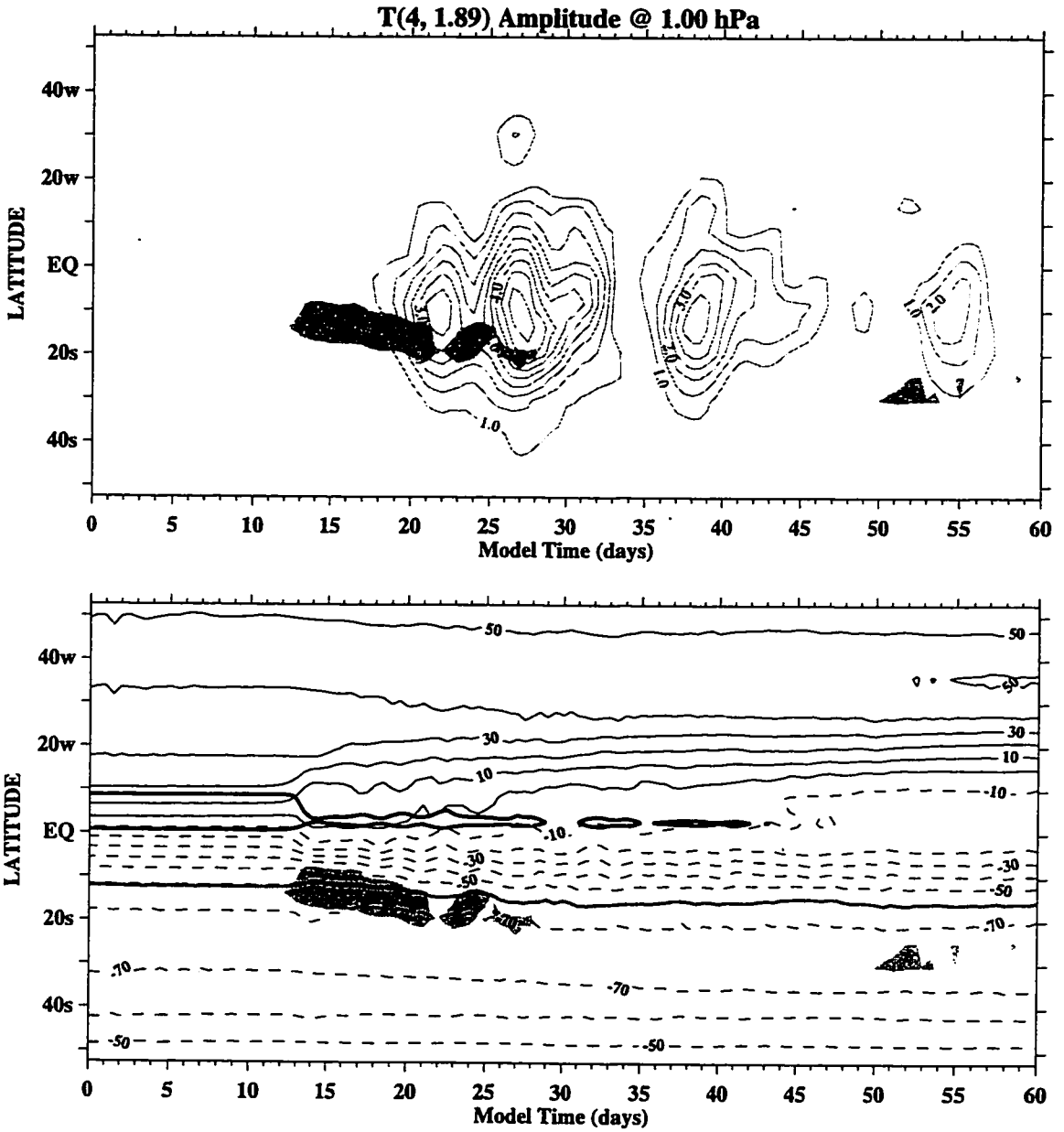

Figure 6.16: The temperature (4, 1.89) amplitude (top) and the zonal wind (bottom) evolution at 1.0 hPa of the control run. The temperature amplitude and the zonal wind are contoured every 0.5 K and 10 ms^{-1}, respectively. The region of negative QGPV gradient is represented in both panels as shaded areas. In the bottom panel, the bold gray line indicates the mode critical line and the bold black line encloses areas of possible inertial instability.

grows linearly as indicated by the gradual increase in amplitude. By day 20, the amplitude of the mode becomes large and begins to alter the mean flow, limiting further wave growth. The mean wind undergoes a pronounced change as the wave amplitude maximizes initially around day 22. The critical line shifts southward while the zero zonal wind line shifts northward. This broadening and weakening of the equatorward flank of the easterly jet is consistent with the wave forcing exerted on the zonal flow shown in Figure 6.14. The altered mean flow displaces the negative QGPV gradient region to higher latitude after day 20. The second growth episode peaking around day 27 may be related to the continued intersection of the critical line source region with the displaced negative QGPV gradient region. The amplitude saturation of the secondary wave episode coincides with further poleward shift of the negative QGPV gradient region. Subsequent growth after day 35 may be the result of nonlinear wave-wave interaction with the (3, 2.04) mode.

The (3, 2.04) amplitudes are plotted in Figure 6.17 and Figure 6.18 for meridional wind and temperature, respectively. As with the (4, 1.89) mode, the temperature and wind amplitudes peak at different altitudes (see Figure 6.13) but at a nearly identical time. After day 20, the generation of the (3, 2.04) mode coincides with the intersection (over a deep layer) of its critical line with the poleward displaced region of the negative QGPV gradient after day 20. The gradual amplitude growth maximizes after day 25 as the wave saturates. The zonal wave forcing is consistent with the zonal wind evolution. After day 25, gradual poleward migration of the zero and -70 ms^{-1} isopleths is readily observed and is indicative of westerly momentum flux into the easterly jet core by wave activity (see Figure 6.14). Since the (3, 2.04) and (4, 1.8) modes show significant amplitudes between days 25-30, the combined mean flow effect of both modes may also be occurring along with possible nonlinear interaction between them.

The above diagrams show that the (4, 1.89) amplitude growth is preceded by the intersection of its critical line with the negative QGPV gradient around days 13 to 20. This region of negative QGPV gradient is not the initial negative QGPV gradient region defined in the initial condition. The initial region is located at slightly higher latitude and above

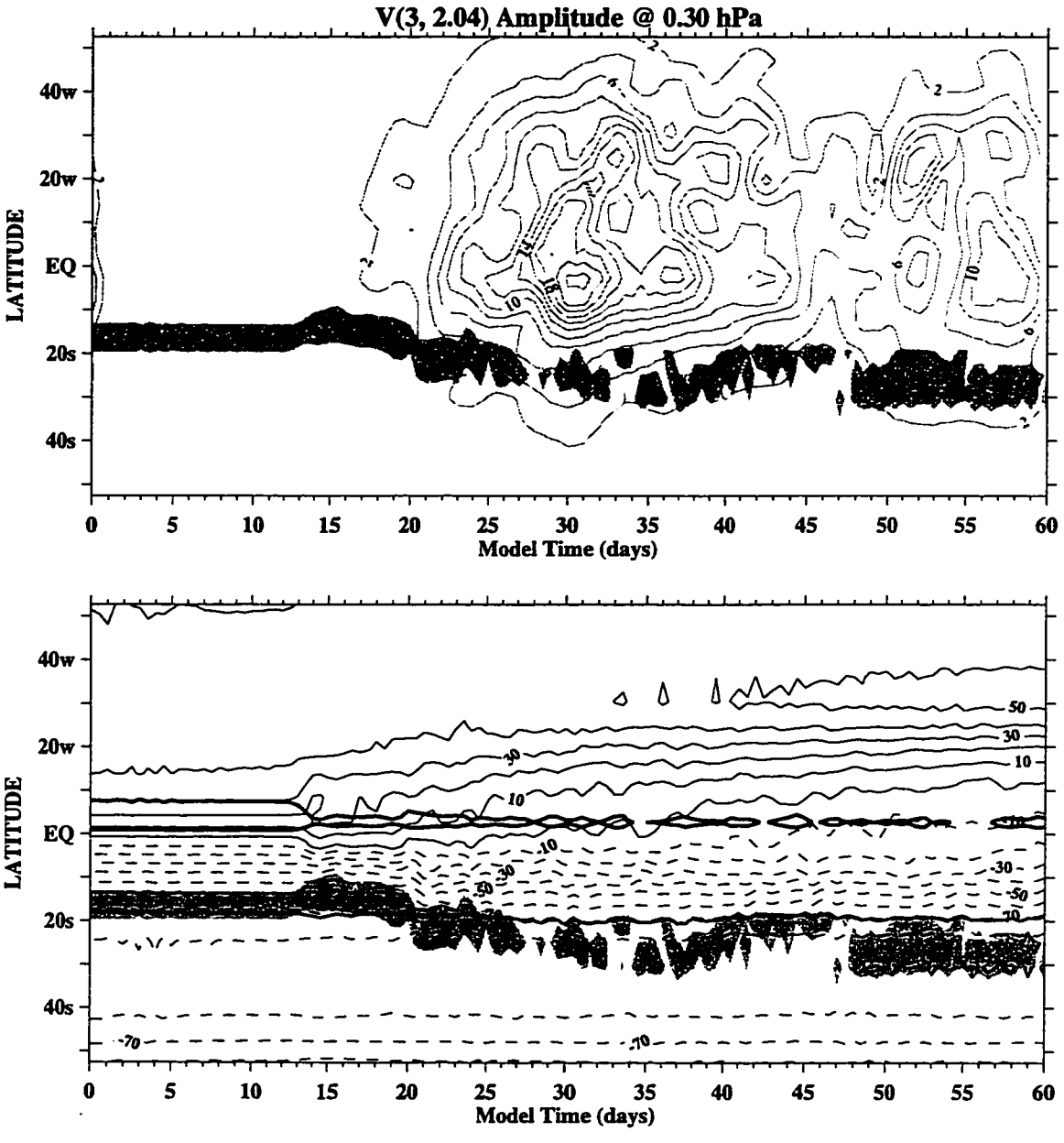

Figure 6.17: The meridional wind (3, 2.04) amplitude evolution (top) and the zonal wind evolution (bottom) at 0.3 hPa of the control run. The wind amplitude and the zonal wind are contoured every 2 ms^{-1} and 10 ms^{-1}, respectively. The region of negative QGPV gradient is represented in both panels as shaded areas. In the bottom panel, the bold gray line indicates the mode critical line and the bold black line encloses areas of possible inertial instability.

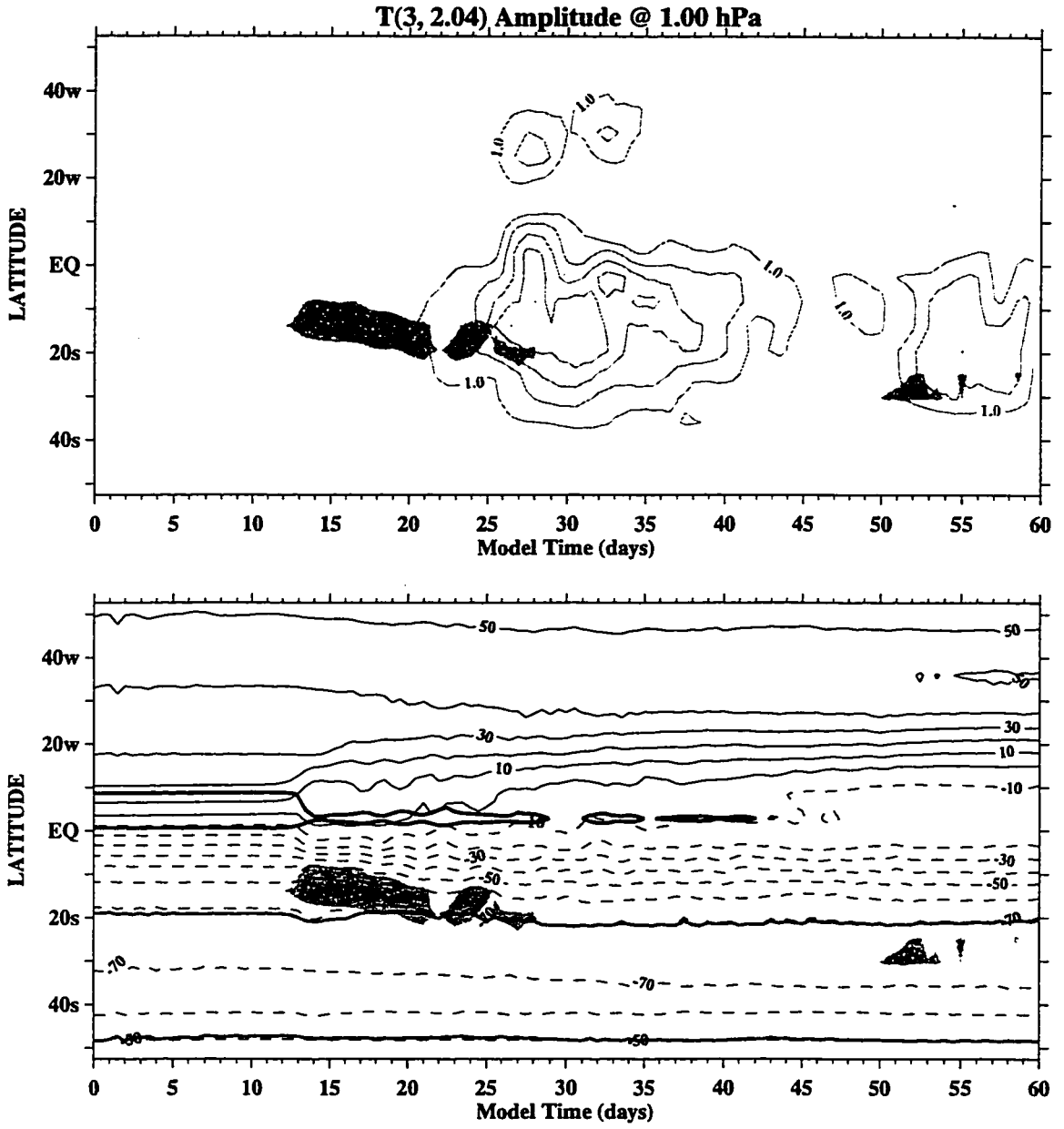

Figure 6.18: The temperature (3, 2.04) amplitude evolution (top) and the zonal wind evolution (bottom) at 1.0 hPa of the control run. The temperature amplitude and the zonal wind are contoured every 0.5 K and 10 ms^{-1}, respectively. The region of negative QGPV gradient is represented in both panels as shaded areas. In the bottom panel, the bold gray line indicates the mode critical line and the bold black line encloses areas of possible inertial instability.

1.0 hPa (see Figure 5.4). Rather, the tightening of the easterly wind contours near 5° summer latitude (beginning around day 13) is responsible for the region of negative QGPV gradient related to wave growth.

The contour tightening, observed over the deep layer, reflects an increase in positive wind curvature. As an illustration, the zonal mean wind latitudinal profiles at 1.0 hPa and 0.3 hPa are given in Figure 6.19 and Figure 6.20, respectively. Increased wind curvature commences around day 13 near 10° summer latitude and is facilitated by the zonal momentum changes near the equator. The westerly momentum is translated toward the summer hemisphere as represented by the wind deceleration near 10° winter latitude and acceleration near the equator. The increased wind curvature causes the mean PV gradient to be reversed locally where the critical line is present.

Earlier occurrence of inertial instabilities appears responsible for this contour tightening. Momentum redistribution associated with inertial instability activity schematically shown in Figure 2.13 is remarkably similar to the momentum changes noted in the zonal wind profiles. The mean wind evolution also shows that during the period of increased wind curvature, the region of $f(f - a^{-1}\overline{u}_{\varphi}) < 0$ (possible inertial instability) simultaneously diminishes in size as shown in Figure 6.15 and Figure 6.16. This suggests the removal of inertial instability by the momentum redistribution. Time-averaged (day 10-15) EP flux vectors shown in Figure 6.2 indeed reveal low winter latitude wave activity prior to any evidence of the (3, 2.04) or (4, 1.89) modes. The associated zonal wave forcing tends to flux westerly momentum toward the summer hemisphere consistent with the momentum redistribution by inertial waves.

During days 10-14, anomaly features reminiscent of inertial waves are observed in the model. In planar maps, temperature and meridional wind anomalies have vertically alternating maxima at consecutive model levels near the equatorial stratopause (Figure 6.21 and Figure 6.22). The model level vertical separation in this altitude range is about 1.7 km. The observed features thus have a vertical wavelength of twice the model's vertical resolu-

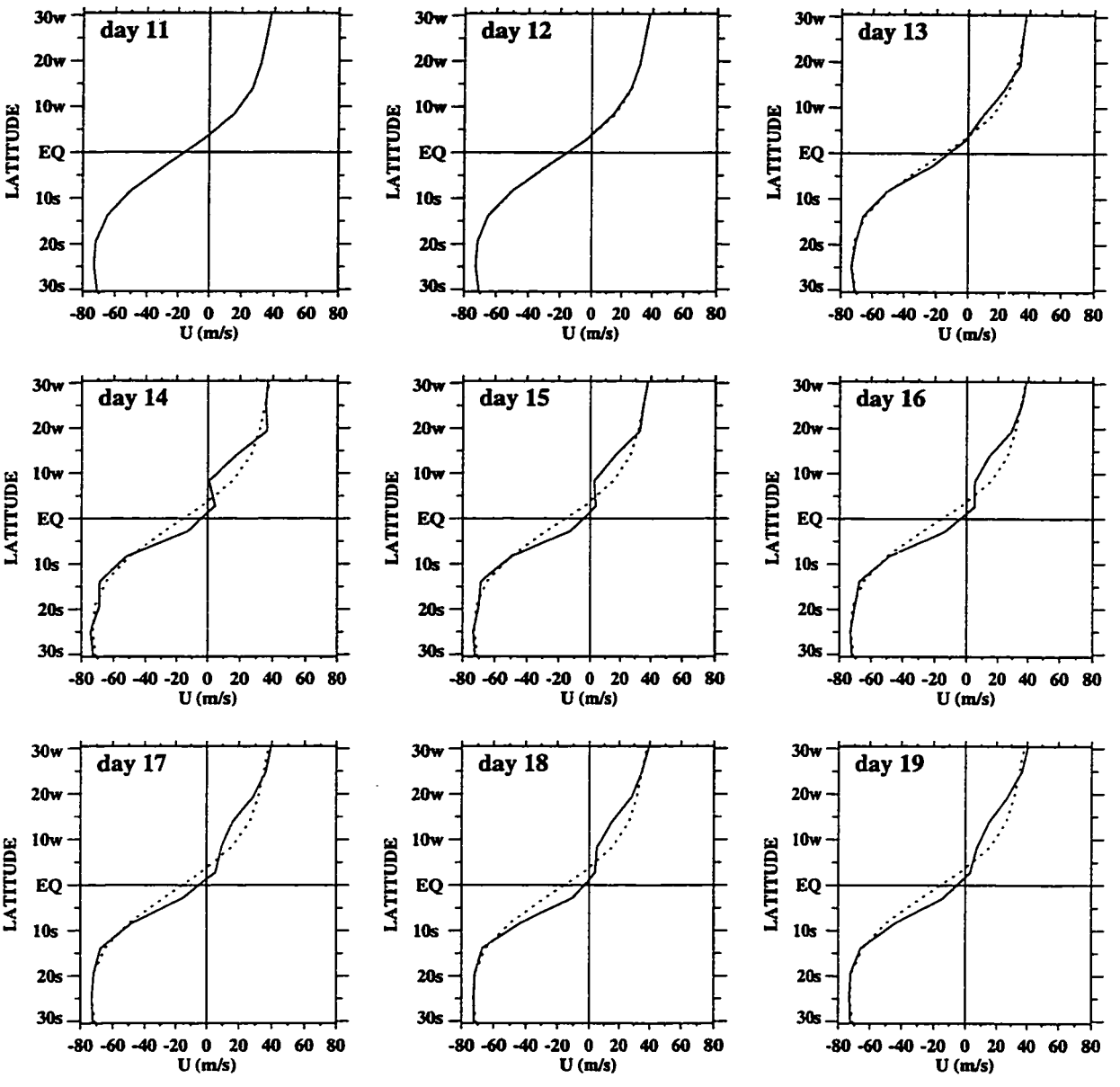

Figure 6.19: The daily zonal mean zonal wind profile at 1.0 hPa of the control run. The dashed line shows the profile for day 11. The solid line shows the profile of the indicated day.

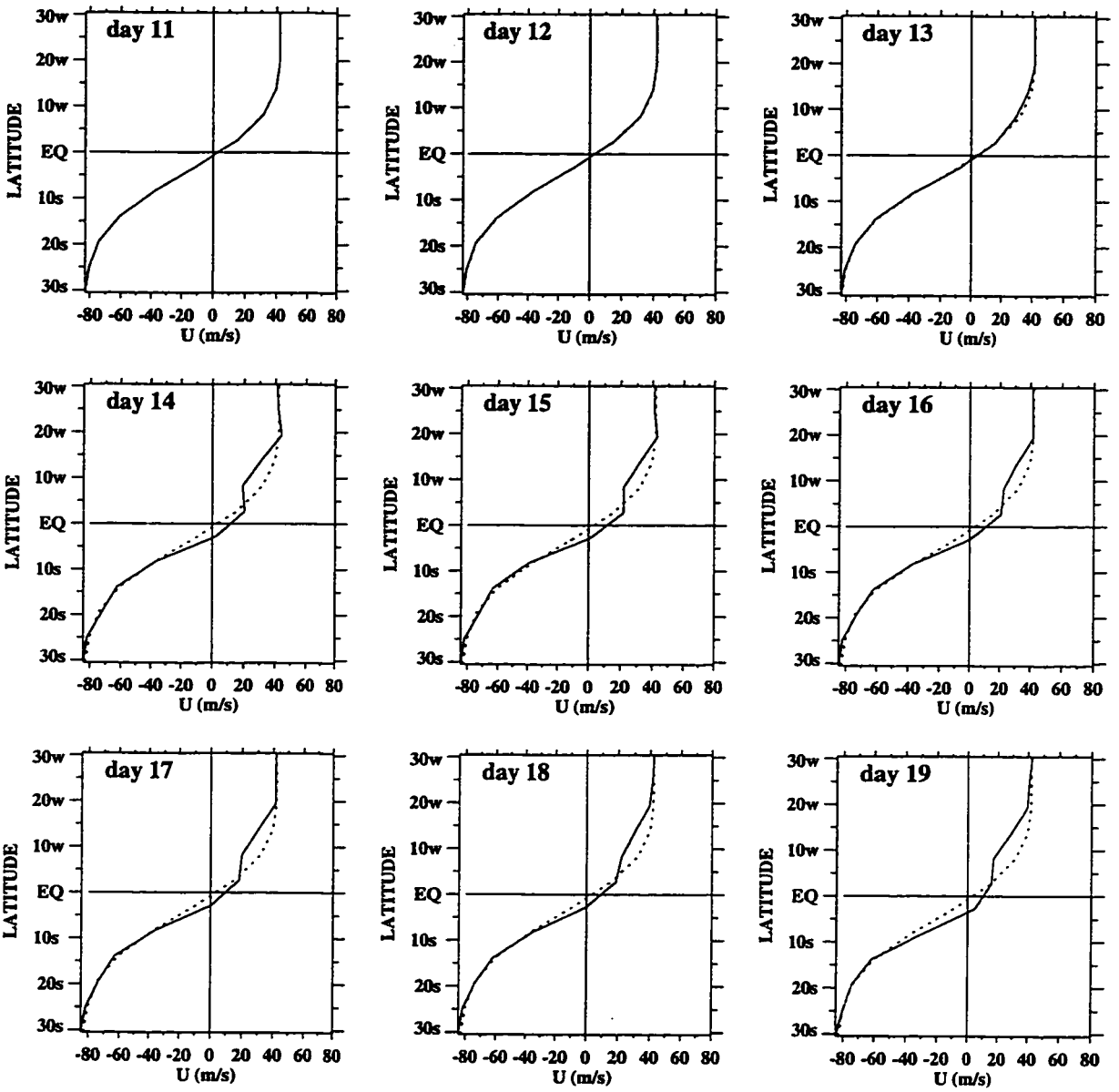

Figure 6.20: The daily zonal mean zonal wind profile at 0.30 hPa of the control run. The dashed line shows the profile for day 11. The solid line shows the profile of the indicated day.

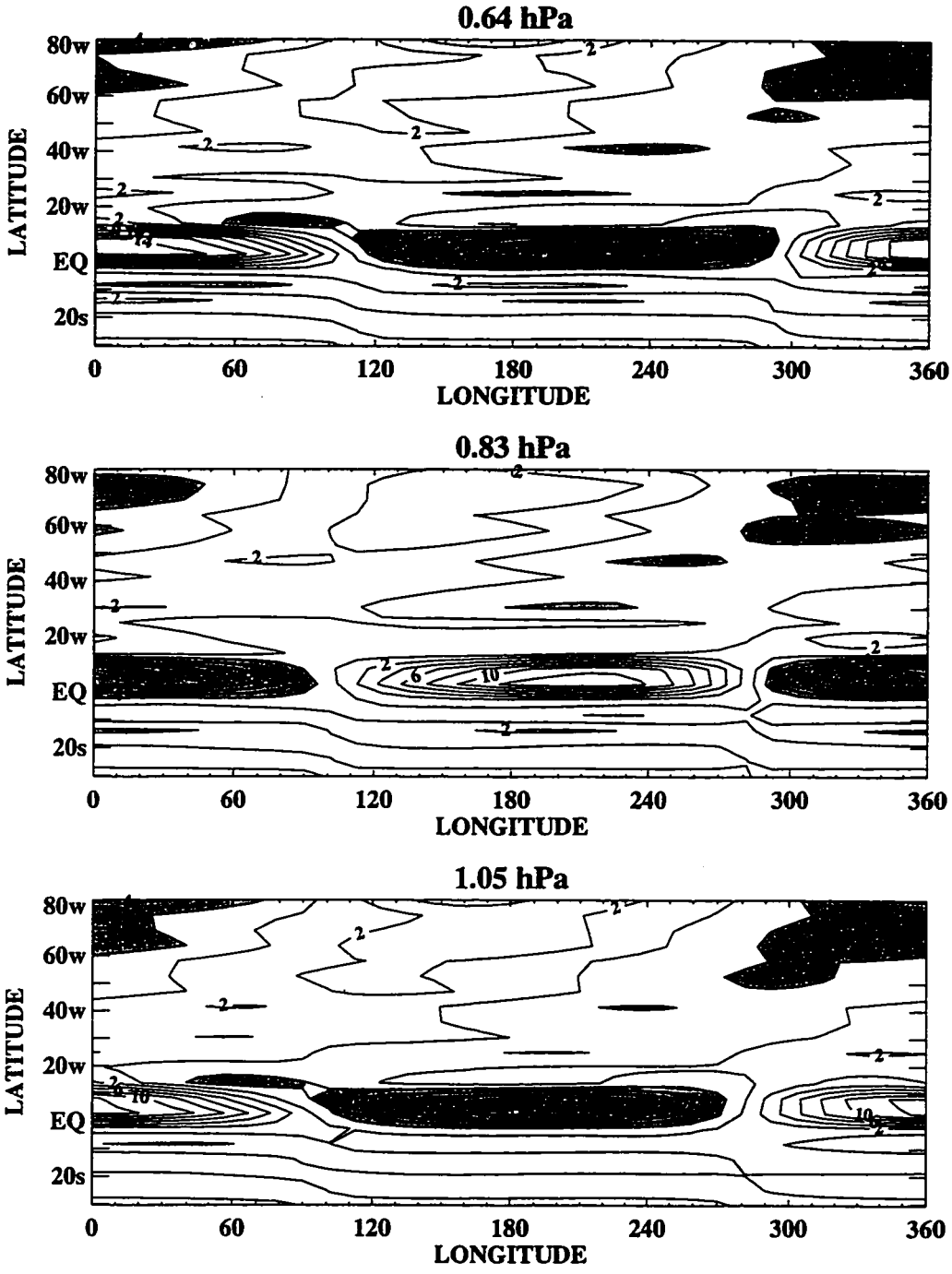

Figure 6.21: Maps of meridional wind anomalies (zonal wavenumber 1-10) at day 13 of the control run. The levels shown correspond to three consecutive model levels. The wind contours are in intervals of 2 ms^{-1} with anomalies less than -2 ms^{-1} shaded.

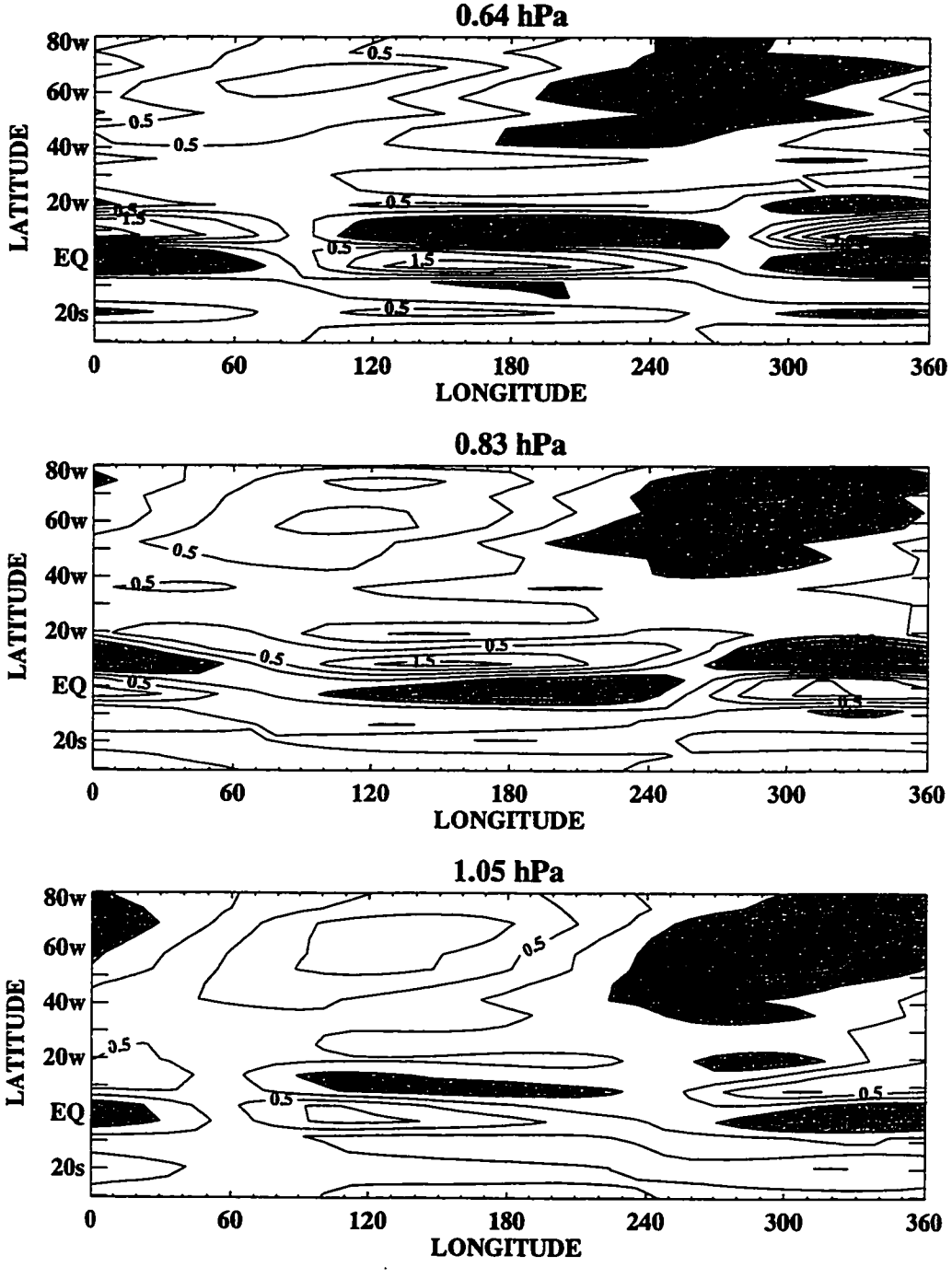

Figure 6.22: Maps of temperature anomalies (zonal wavenumber 1-10) at day 13 of the control run. The levels shown correspond to three consecutive model levels. The temperature contours are in intervals of 0.5 K with anomalies less than -0.5 K shaded.

tion. The pattern is stationary in time and shows a zonal wavenumber 1 structure. The wind perturbation magnitude can be as large as 12 ms^{-1} while the maximum temperature anomaly can exceed 3 K. The temperature and meridional wind maxima are vertically displaced with respect to one another (Figure 6.23). Consistent with the schematic structure shown in Figure 2.12, the winterward flow anomaly (positive meridional wind anomaly) is just below the level where warming appears over the equator. Meridionally, the temperature maxima are centered at 7° winter latitude and near the equator, implying a horizontal half-width of ~778 km. The meridional extent is roughly bordered by the region where $f(f - a^{-1}\overline{u}_{\varphi}) = 0$ shown by the bold black line in Figure 6.15 and Figure 6.16.

The vertically stacked stationary wavenumber 1 pattern is readily seen prior to day 14. As the region of inertial instability diminishes due to inertial readjustment of the mean wind, the coherent wavenumber 1 structure quickly evolves into higher wavenumber features and the coherent stacking characteristic disappears. By day 18, a different kind of anomaly pattern emerges. The latter feature has larger vertical extent and corresponds to the identified (4, 1.89) disturbance (Figure 6.24). The vertically deep zonal wavenumber 1 pattern in the winter high latitudes is associated with the forced winter planetary wave which is propagating meridionally into the region.

Using satellite observations, Hitchman et al. (1987) and Hayashi (1998) have reported stacking structure similar to the modeled feature near the equatorial stratopause. They describe the appearance of vertically alternating temperature anomalies in the winter hemisphere. The structure is quasi-stationary and is dominated by zonal wavenumber 1-2 components. The structure is noted when the horizontal wind shear in low latitudes exceeds the local Coriolis parameter, $f(f - a^{-1}\overline{u}_{\varphi}) < 0$, coupled with the presence of a winter Rossby wave.The inertial instability mechanism appears to account for the observed structure. Zonal wavenumber 1-2 Rossby waves are believed to foster inertial waves by meridionally displacing air parcels which are then accelerated in the inertially unstable region. The observed stacking anomaly pattern has larger spatial extent and persists longer than the modeled feature by as long as 1-2 weeks. Its estimated range of vertical wavelength

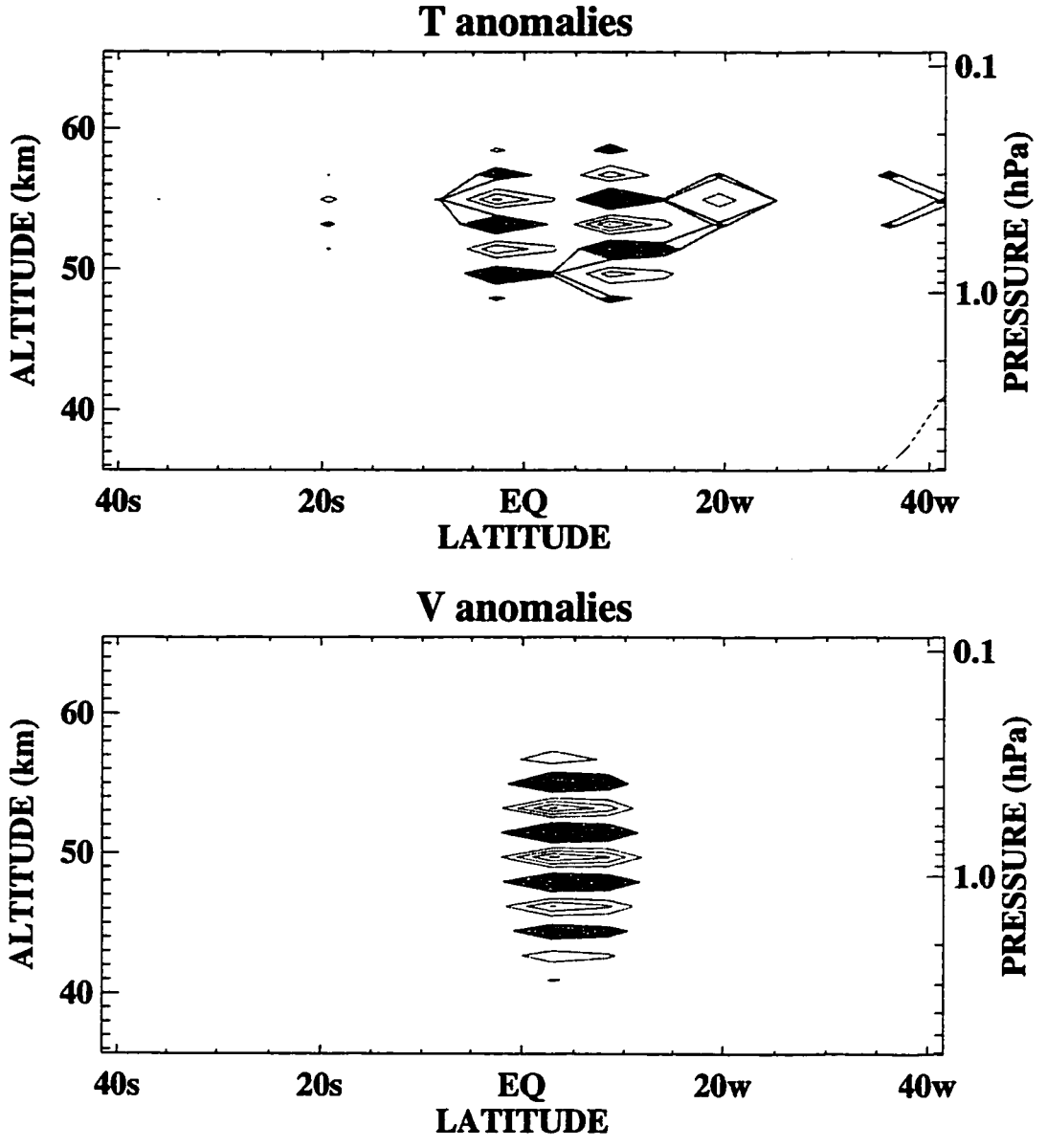

Figure 6.23: Meridional structure of temperature (top) and meridional wind (bottom) anomalies (zonal wavenumber 1-10) at 180° longitude at day 13 of the control run. The temperature (meridional wind) anomalies is contoured every 0.6 K (3 ms^{-1}). Negative anomalies are shaded and the zero contour is removed for clarity.

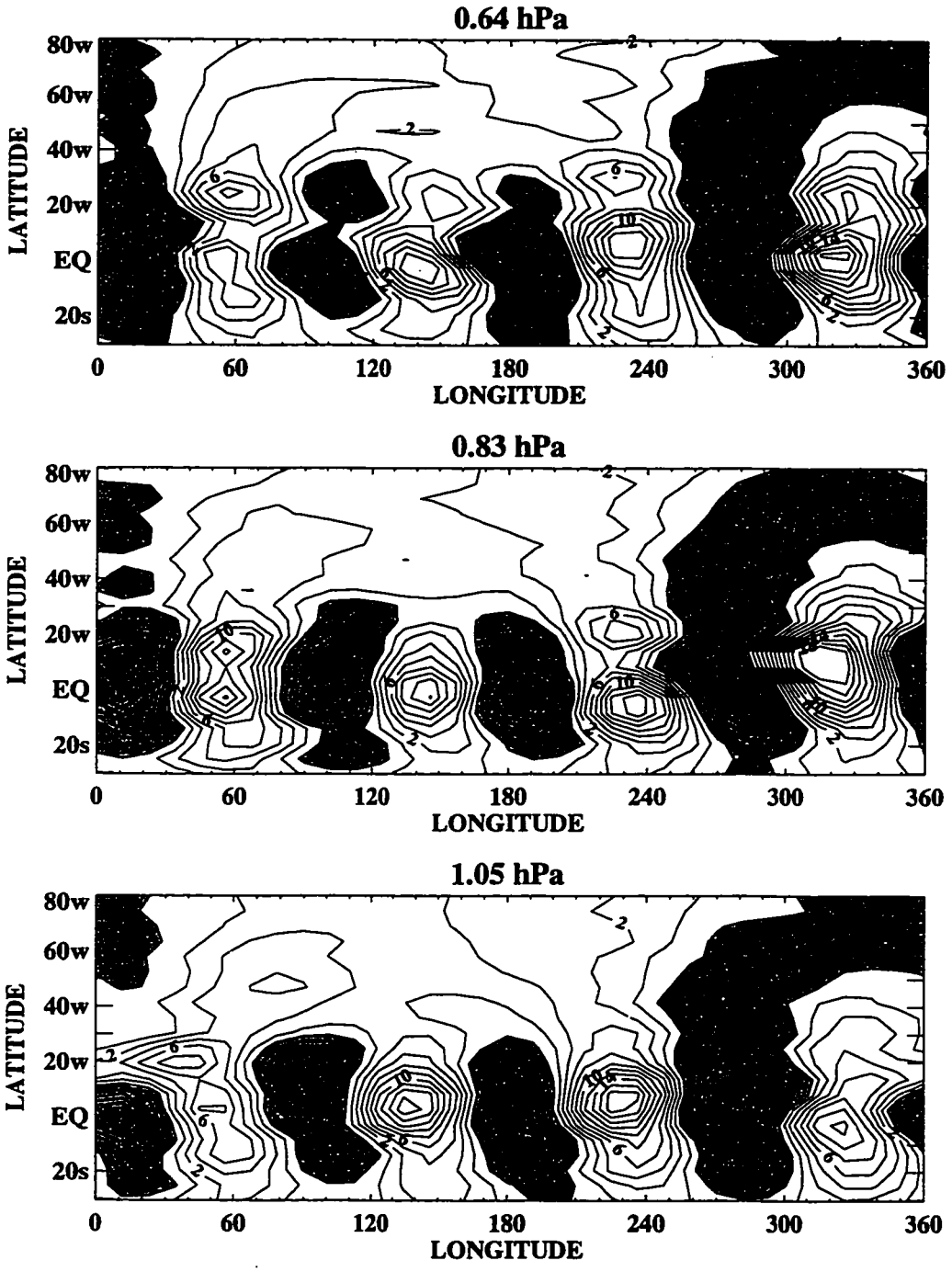

Figure 6.24: Maps of meridional wind anomalies (zonal wavenumber 1-10) at day 20 of the control run. The levels shown correspond to three consecutive model levels. The wind contours are in intervals of 2 ms^{-1} with anomalies less than -2 ms^{-1} shaded.

and meridional half-wavelength are 5-14 km and 3300-4500 km, respectively. In the model, there is only a single time-constrained winter planetary wave radiating into the tropics. In the real atmosphere, there is continual propagation of wave energy whose EP flux drives mean wind shear on the equatorward side of the surf zone and possibly prolongs the observed inertial instability episodes.

Slight alterations of the control experiment find the modeled inertially instability features to be directly related to the meridional motions imposed by the winter forcing. When the forcing amplitude is set to zero, only symmetric inertial instability occurs and is initiated by weak zonal symmetric meridional circulation driven by the imposed Rayleigh friction. In fact, the model evolution remains zonally symmetric past 50 days and no two-day wave is present. The vertically stacked pattern has weaker extrema and persists for a long time before momentum redistribution can alleviate the unstable condition. When the forcing amplitude is kept at the same value but a wavenumber 2 structure is imposed, the zonal wavenumber 2 inertially unstable disturbance is evident. The overturning circulation is weaker than the wave 1 forcing case and lasts until model day 20. As with the wave 1 forcing, the two-day is triggered as the latter inertially unstable feature weakens. However, the (4, 1.89) mode is dominant in this case.

Overall, the simulated quasi two-day wave activity exhibits some similarity to the observed two-day wave in the MLS data during the austral summer. The observation and model show the temperature wave to appear in the stratopause region and on the equatorward flank of the easterly jet. The mode periods and amplitudes are also similar. The mode amplitude-time evolution appears to be associated with the critical line. Large temperature (and meridional wind) amplitudes occur equatorward of the critical lines and near the region where the critical lines intersect with the region of negative QGPV gradient.

However, the simulated two-day wave temperature amplitude structures have nodes near 0.4 hPa which differ significantly from the observations whose amplitudes increase with height near the upper observational limits (compare Figure 4.7 with Figure 6.12 and

Figure 6.13). The model also finds the wavenumber 4 mode to be slightly larger than the wavenumber 3 mode. Comparable amplitude of the modes is only observed during the 1993-94 austral summer case. Interestingly, Burks and Leovy (1986) also found both components of the two-day wave to be equally strong in the LIMS 1979 austral summer temperature.

The modeled results reveal an interesting aspect about the two-day wave that may exist in reality. The model suggests that, as an instability wave, the two-day wave is a part of a sequence of wave events that transports westerly momentum from the low winter latitude across the equator and into the easterly jet core. Two-day wave events are initiated by wave disturbances similar to inertial instability organized by the forced winter planetary wave. The momentum redistribution by the inertial instability destabilizes the mean flow in low summer latitudes where strong meridional wind shear was already present, presumably set up by preexisting radiative and dynamical effects. The asymmetric inertial waves may provide the needed infinitesimal perturbation that grows into the (4, 1.89) mode. This growth is evident from the flux of wave activity away from its critical line as it crosses the negative QGPV gradient region. The mean-flow interaction of the wave 4 mode gradually shifts the negative QGPV gradient region further into the easterly jet core upon which the unstable wave 3 mode can grow. Since the wave 3 mode has longer period, its critical line is always poleward of the wave 4 critical line and the poleward shifting of the negative QGPV gradient region may be necessary for the wave 3 growth. Such a wave triggering scenario is similar to that suggested by Orsolini et al. (1997).

The wave 4 two-day wave is mainly barotropic and its energy propagation is directed equatorward. On the other hand, the wave 3 two-day wave energy is directed upward-poleward and horizontally equatorward. The upward propagation is quite strong and parallels the critical line in the region of strong damping. These characteristics suggest a reason for the absence of wave 4 two-day wave observations in the mesosphere where the wave 3 two-day wave is exclusively reported. *In situ* generation of the wave 3 component is also possible in the mesosphere.

6.2 DECREASED THERMAL DAMPING

The control experiment is repeated in this section except that a Newtonian cooling profile with the constants (α, β) = (1.5, 1.0) is used (see Figure 5.1). With this particular profile, the thermal damping above 1 hPa is less than half the value used in the control experiment. In addition to less damping of the incipient wave perturbation, this weaker profile potentially allows the mean temperature (and consequently mean zonal wind) to deviate to a greater extent from the initial condition. With the winter planetary wave forcing being so weak, the mean zonal wind evolution is found to be nearly identical to the control run even with weak damping. The main results discussed in the preceding section remain true. The sequence of wave events again consists of initial inertial instability, followed by wave 4, then wave 3 components of the barotropically unstable two-day oscillation. Minor deviations from the control experiment are noted here.

Figure 6.25 shows the two-day wave meridional wind amplitude for both the strong (control) and weak Newtonian cooling runs. The amplitude is averaged vertically between 5 hPa and 0.1 hPa and latitudinally between 40° summer latitude and 40° winter latitude. The dominant frequency peaks in the 40-day spectral analysis for the weak damping case differs slightly from the control case. In the first 40 days, the wavenumber 3 mode grows slightly faster and to greater amplitude than the control results. The control wavenumber 4 is slightly stronger but seems to grow at about the same rate. The EP flux vectors are shown in Figure 6.26. The vector lengths are plotted relative to the control result (see Figure 14). The overall structure below is strikingly similar to the control run as suggested by Figure 6.25. However, above 0.1 hPa, greater poleward and upward energy propagation is seen. Since the Rayleigh friction is fixed, the difference is probably attributed to the weaker thermal damping in the present run. The stronger upward and poleward energy flux in this case of weaker (and more realistic) radiative damping is consistent with the observed large amplitude of the wave 3 mode above 0.1 hPa (see Figure 2.5).

6.3 INCREASED WINTER WAVE FORCING

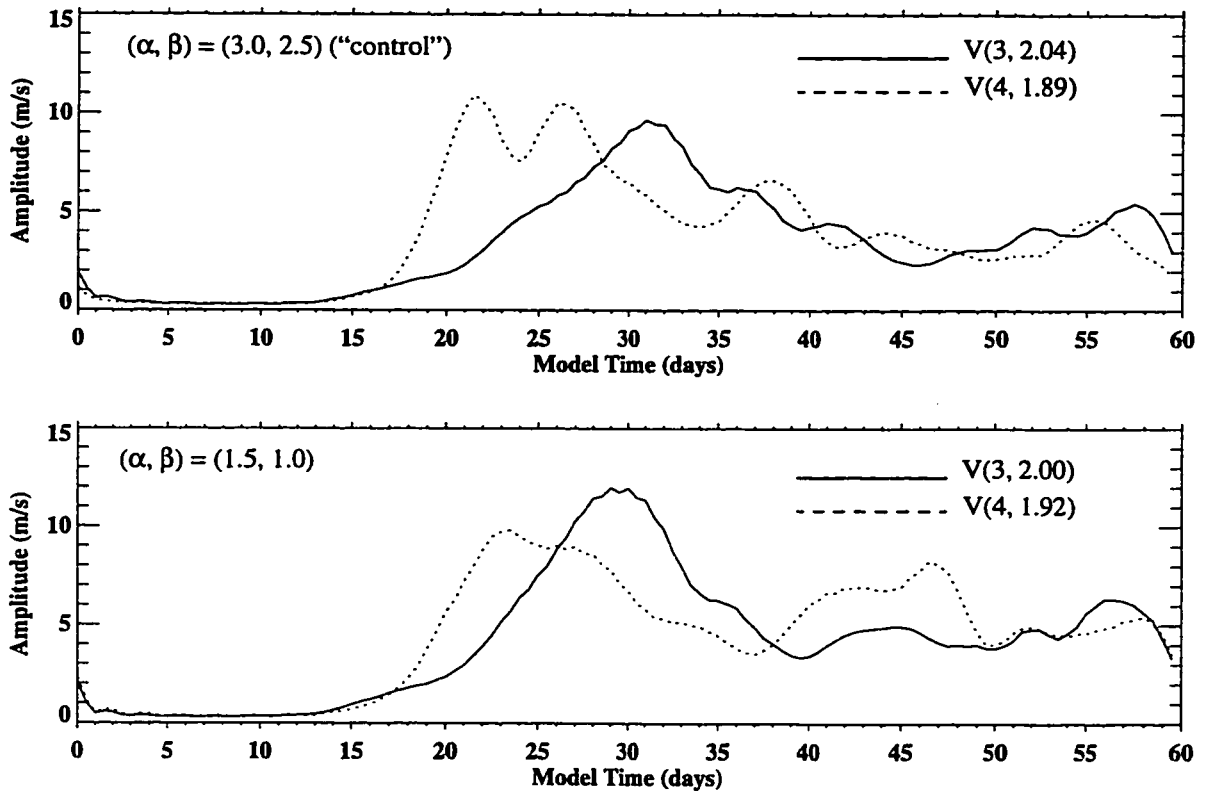

Figure 6.25: The meridional wind two-day wave amplitudes for winter planetary wave forcing of A = 368 m^2s^{-2}. The top (bottom) panel is for the strong (weak) Newtonian cooling. The wave amplitudes are averaged vertically from 5 hPa to 0.1 hPa and latitudinally from 40° summer latitude to 40° winter latitude.

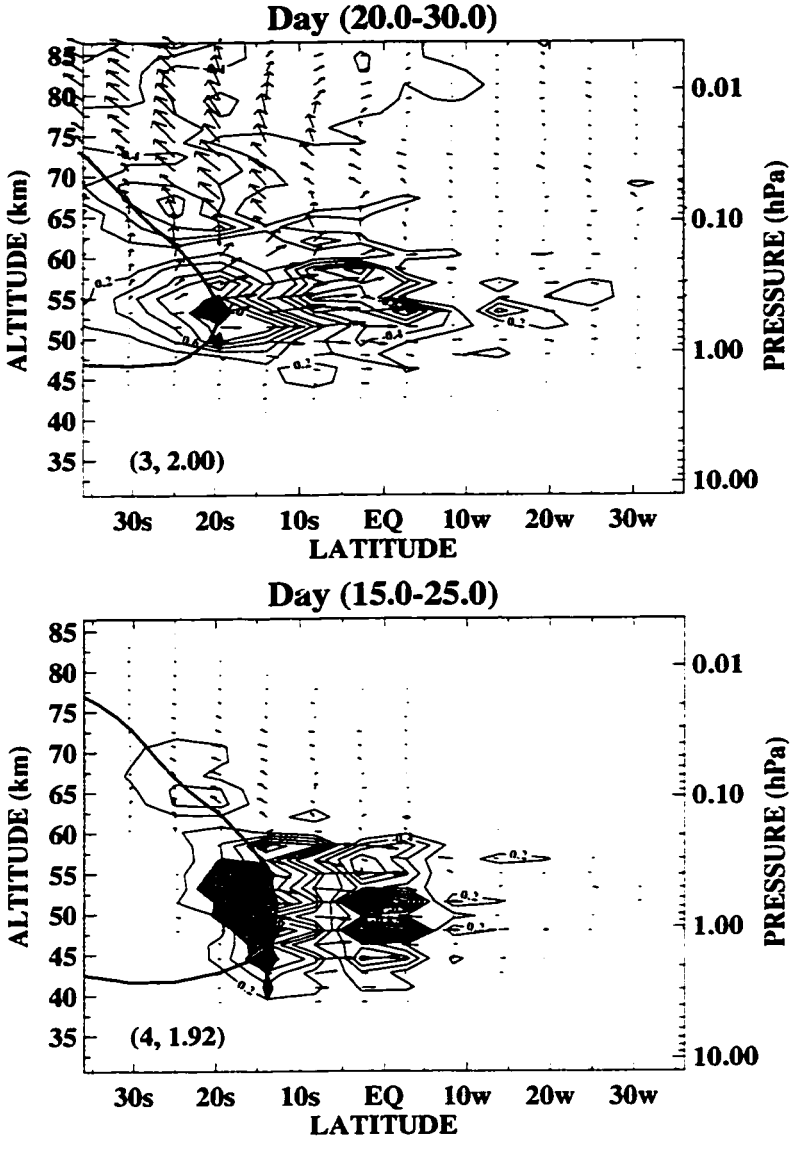

Figure 6.26: The 10-day averaged EP flux vectors diagrams for (3, 2.00) mode, top, and (4, 1.92) mode, bottom, for the weak Newtonian cooling case and the winter planetary wave forcing of A = 368 m^2s^{-2}. The maximum vector length in each panel is relative to maximum length used in the control run (Figure 6.14). The wave forcing per unit mass (DF) is shown by the line contours in increments of 0.2 $ms^{-1}day^{-1}$; blue (red) contours denote positive (negative) DF values. The shaded regions shows the averaged area of negative QGPV gradient. The mode critical line is shown in the diagrams as a bold line.

The control experiment is repeated but now the winter planetary wave forcing is incrementally doubled. As expected, the increased forcing can significantly affect the zonal mean structure, particularly near the low winter latitudes where the winter waves are damped as they approach the zero wind line. The strongly imposed thermal damping tries to keep the mean wind structure near the initial condition. When the forcing amplitude is 735 m^2s^{-2}, plots (not shown) of mean wind difference from the control run show wind structure in the low winter latitude to be 5-10 ms^{-1} slower than the control case between 5-0.1 hPa. Observable wind disparity is noted after day 20 when the forcing amplitude is maximized. Figure 6.27 shows the mean wind differences for the amplitude of 1470 m^2s^{-2} for 10-day increments. The region of weaker winds in the low winter latitudes (~20°w) has grown stronger and larger as the model evolves. Considerable wind difference also permeates into the low summer latitude with time. Finally, Figure 6.28 shows the mean wind differences for the amplitude of 2490 m^2s^{-2}. The area where the mean wind is weaker than the control run enlarges and strengthens with time. The area also expands bilaterally, well into the winter polar regions and into the summer mid-latitude. Consequently, major warming in the winter polar vortex is observed as the polar westerlies are reversed.

The zonal momentum budget is shown in Figure 6.29 for each forcing amplitude. Each term in Equation 5.6 is isolated to identify its relative contribution to the mean wind change. The terms are vertically averaged between 5 hPa to 0.1 hPa and between day 10-40. In each case, the vertical advection term is negligible compared to other terms. As the forcing increases, the net mean wind tendency is increasingly decelerative between 30° summer latitude and 30° winter latitude consistent with the mean difference shown in previous diagrams. In the winter hemisphere, wave forcing (*DF*) by the prescribed winter wave is largely accountable for the wind changes. In the summer hemisphere, horizontal advection ($\overline{\eta v}^*$) is the dominant term. The *DF* in the winter hemisphere and horizontal advection at all latitudes increase in magnitude with the forcing. Clearly, the increased wave forcing is driving stronger meridional circulation ($\bar{v}^*$). According to the zonal momentum equation (Equation 5.6), the advection of easterly wind equatorward intensifies the easterlies. Hence, the difference in easterly jet strength between austral and boreal

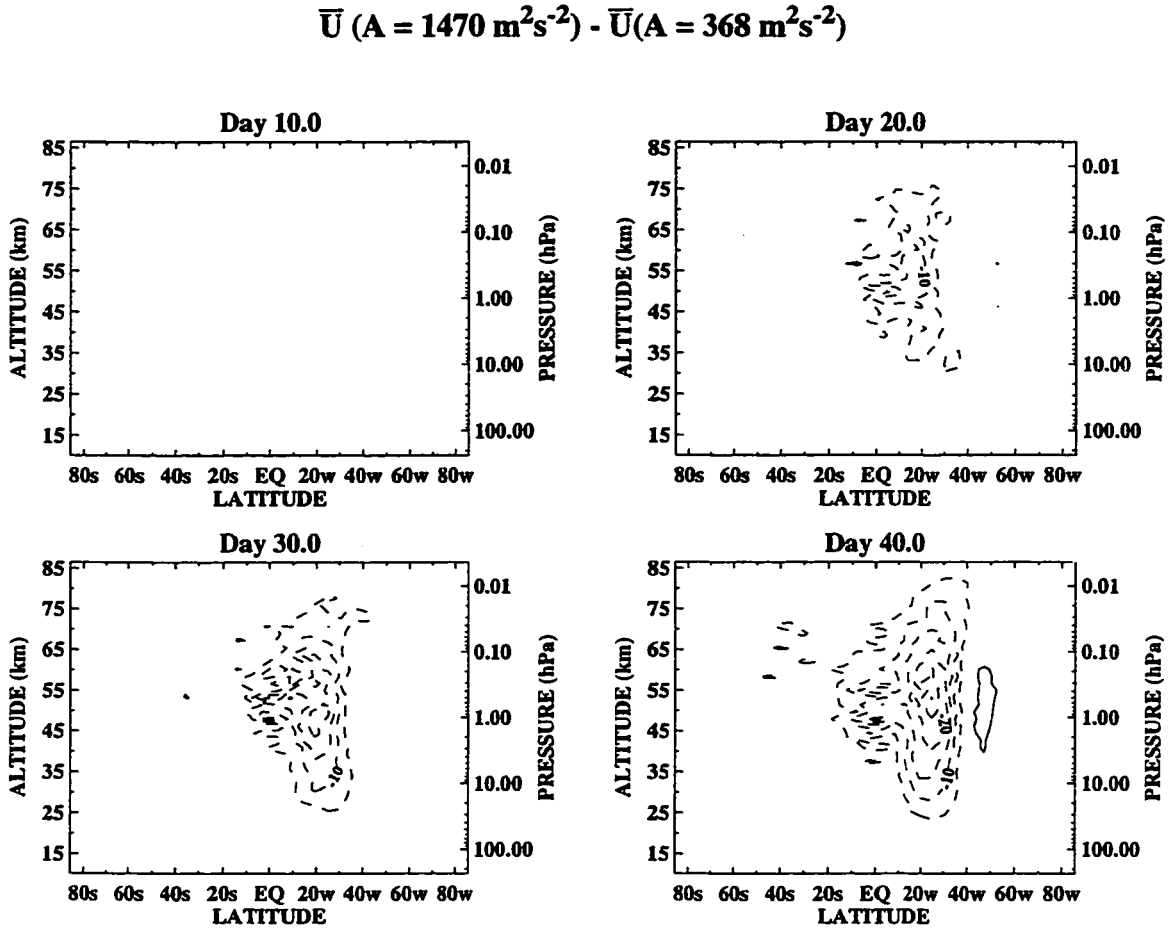

Figure 6.27: Zonal mean zonal wind difference between runs with winter planetary wave forcing amplitude 1470 m^2s^{-2} and 368 m^2s^{-2}. Strong Newtonian case is used. The dashed (solid) contours indicate that the stronger forced case has winds that are slower (faster). The contour interval is every 5 ms^{-1}.

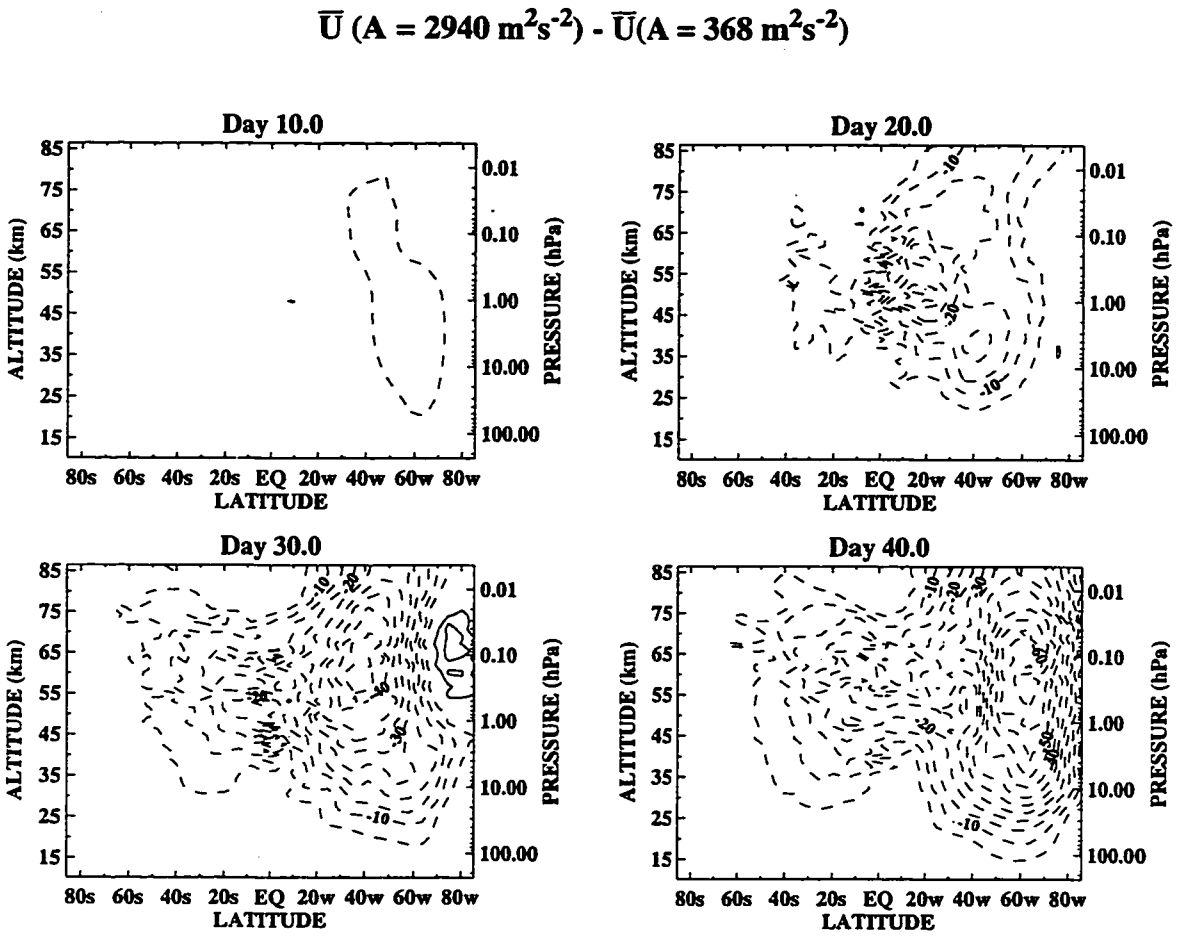

Figure 6.28: Same as in Figure 6.27 but for difference between runs with winter planetary wave forcing amplitude of 2940 m^2s^{-2} and 368 m^2s^{-2}.

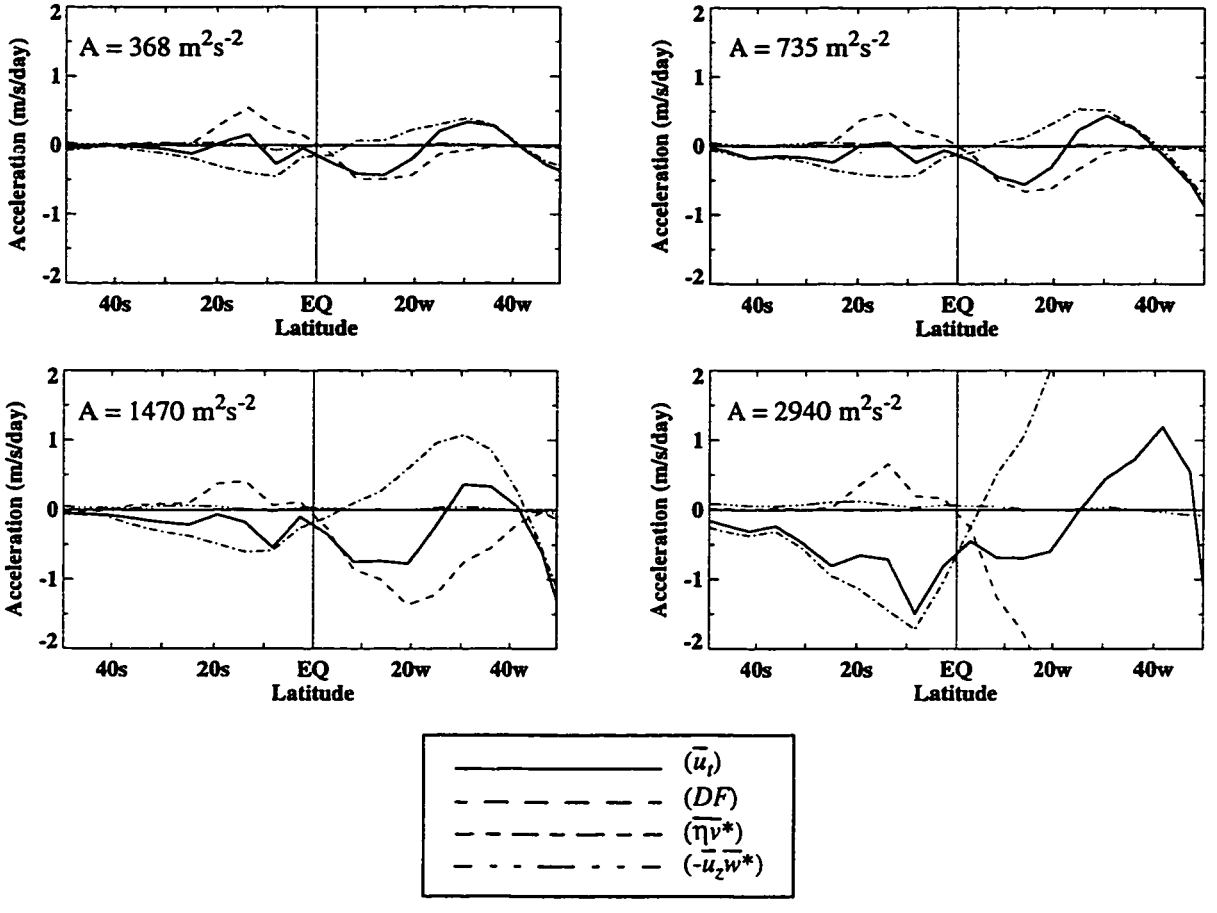

Figure 6.29: The various terms in the Transform Eulerian Mean zonal momentum equation. The values are averaged vertically from 5 hPa to 0.1 hPa and from model day 10-40.

summer noted in the MLS data near the stratopause may be related to the difference in winter wave activity.

The simulated modes of the two-day wave are summarized in Table 6.1. Except for the strongest forcing case, these modes are readily identified in the spectral analysis. The wavenumber 3 modes consistently propagate at slightly lower frequency than the wavenumber 4 modes. With increased forcing, the frequency of the respective mode increases. As a wave instability phenomenon, the frequency of the two-day wave depends on the strengths of the jet in which it resides. Stronger easterlies with larger forcing yield faster modes. When the forcing is too large (e.g. A = 2940 m^2s^{-2}), the easterly wind changes too rapidly to allow for a dominant instability mode to appear in the 40-day spectral analysis. Figure 6.30 shows the two-day wave meridional wind amplitude for each forcing amplitude. The plot shows that the growth of the wavenumber 4 mode is consistently before the wavenumber 3. The wavenumber 4 begins to grow slightly earlier in the run as the forcing is increased. This is due to the slightly earlier occurrence of inertial activity discussed in the control run. The same sequence of wave events seen in the control run is again evident in each case. It is interesting that during austral summer 1992 and 1993 when observational results suggest that inertial instability may be triggering the two-day wave the wavenumber 4 also peaks before the wavenumber 3.

Figure 6.31 shows the two-day wave activity for forcing amplitudes of 735 and 1470 m^2s^{-2}. A critical line instability wave source is always apparent in or near the regions of negative $\bar{q}_\phi$. Below 0.1 hPa, the wave activity of both modes are comparable in strength as seen in Figure 6.30. The wavenumber 4 mode is consistently confined below 0.1 hPa while the wavenumber 3 mode can propagate vertically into the mesosphere. Note that energy propagation into the mesosphere is much stronger in the case of the 735 m^2s^{-2} forcing than in either the 368 or 1470 m^2s^{-2} cases.

6.4 WEAKENED EASTERLY JET

Table 6.1: Central Two-Day Wave Mode Variation

	zonal wavenumber 3		zonal wavenumber 4	
forcing amplitude (m^2s^{-2})	frequency (cpd)	period (days)	frequency (cpd)	period (days)
368	0.50	2.04	0.54	1.80
735	0.50	2.00	0.54	1.85
1470	0.56	1.79	0.60	1.67
2940	---	---	---	---

Note: The westward propagating frequency (and period) correspond to the spectral peak observed in the spectral analysis performed over time series of model day 10-39 (inclusively). The spectral peaks are observed in both the meridional wind and temperature field consistently between 2 hPa and 0.1 hPa. In the 2940 case, no clear peak is observed. The highlighted row corresponds to the "control "run.

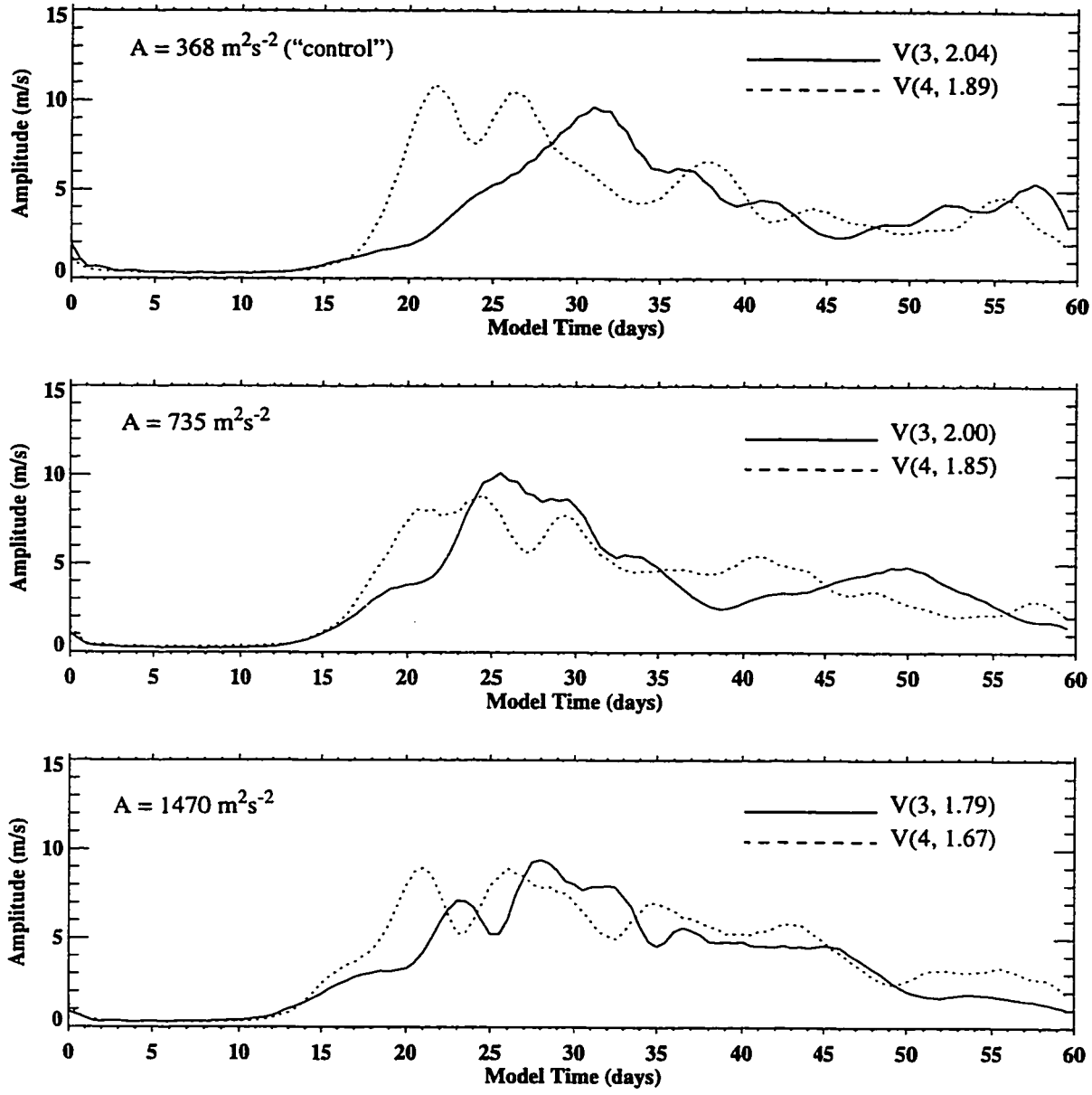

Figure 6.30: The meridional wind two-day wave amplitudes for varied winter planetary wave forcing and strong Newtonian cooling case. The wave amplitudes are averaged vertically from 5 hPa to 0.1 hPa and latitudinally from 40° summer latitude to 40° winter latitude.

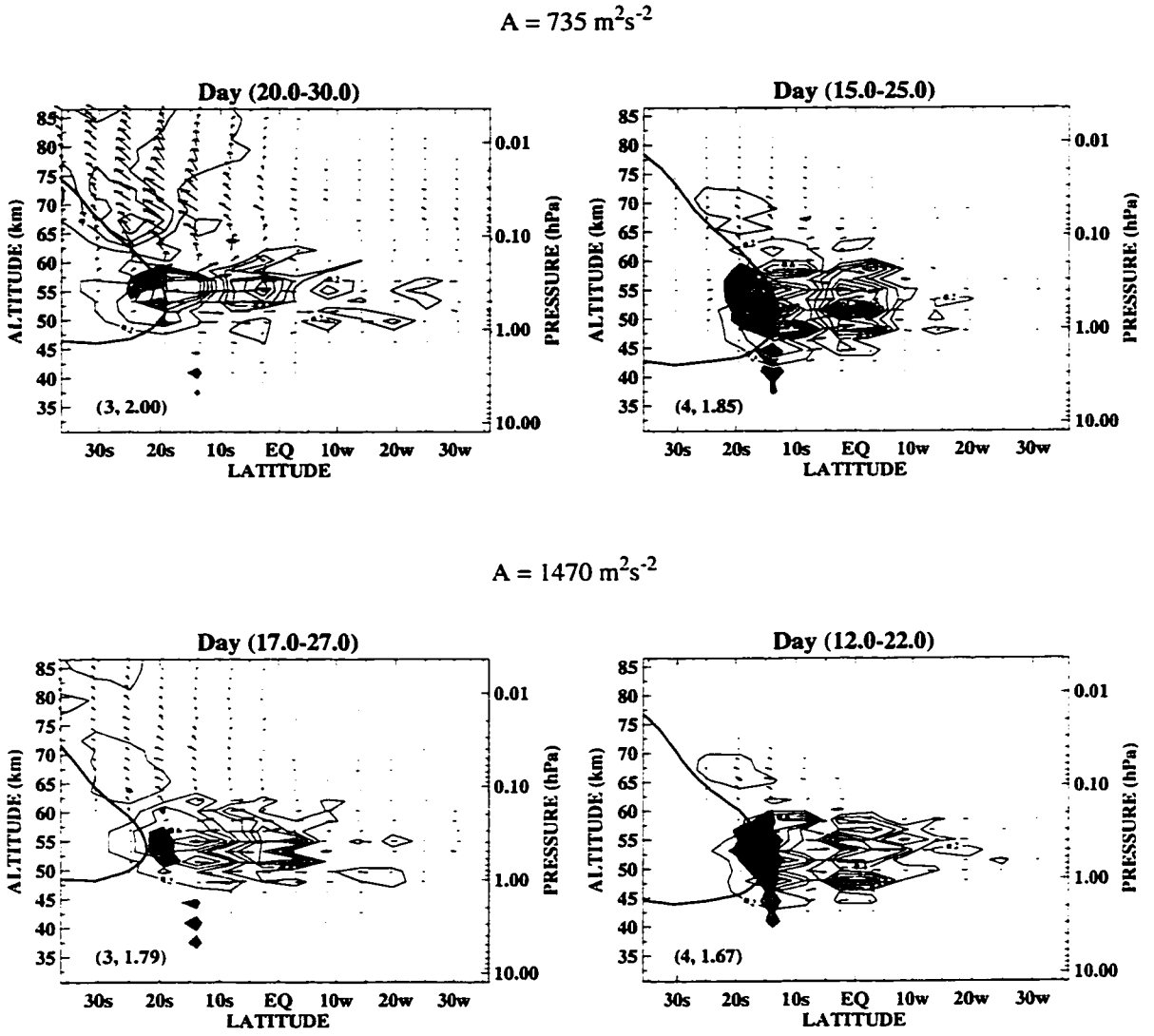

Figure 6.31: The 10-day averaged EP flux vectors diagrams for the two-day wave for the strong Newtonian cooling case and the varied winter planetary wave forcing. The maximum vector length of each panel is relative to the maximum length used in the control run (Figure 6.14). The wave forcing per unit mass (DF) is shown by the line contours in increments of 0.2 $ms^{-1}day^{-1}$; blue (red) contours denote positive (negative) DF values. The shaded regions shows the averaged area of negative QGPV gradient. The mode critical line is shown in the diagrams as a bold line.

The control experiment is now run with a new initial condition shown in Figure 6.32. The analytical expression for the initial wind is given in the Appendix. The easterly jet is weakened considerably so that the observed (3, 2.0) mode critical line is entirely removed and only the observed (4, 1.8) critical surface is supported. Despite the weak easterlies near the stratopause, the strong meridional wind shear is able to produce a region of negative $\bar{q}_\varphi$ in low summer latitudes. The westerly wind structure is identical to the initial condition shown in Figure 5.4 so it effectively guides the forced wave into the subtropical stratopause. The prescribed easterly wind strength is similar to the MLS observed boreal summer conditions (July-August).

The wave activity is similar to the control run (see Figure 6.2). The 5-day averaged EP flux vectors are shown in Figure 6.33. The upward and equatorward propagation of the weakly forced winter planetary wave is evident in the extratropical winter latitude of each displayed panel. Strong wave activity directed away from the equator is evident in the tropical regions of the winter hemisphere in the day 10-15 panel. This feature is barotropic and the associated wave forcing (*DF*) tends to transport westerly momentum equatorward as indicated by the EP flux divergence-convergence pattern centered near 5° winter latitude. The peaks of the coupled pattern nearly are vertically separated by about 3.5 km (2 model grid intervals). The time averaged *DF* of the wave feature has a magnitude as large as 3 $ms^{-1}day^{-1}$.

Later in the model run, wave activity in low summer latitudes appears in the stratopause region. The wave activity is initiated along with the enlarging of the negative QGPV gradient area near 10° summer latitude during days 15-20. The wave activity remains predominantly barotropic and grows largest around days 20-25. The EP flux vectors associated with the wave activity appear to emanate from the negative QGPV gradient area. By days 25-30, the wave activity has greatly diminished, and the area of negative QGPV gradient has translated to 20° summer latitude. One distinct difference from the control result is the lack of vertically propagating wave activity in low summer latitudes above 0.1 hPa (see Figure 6.2).

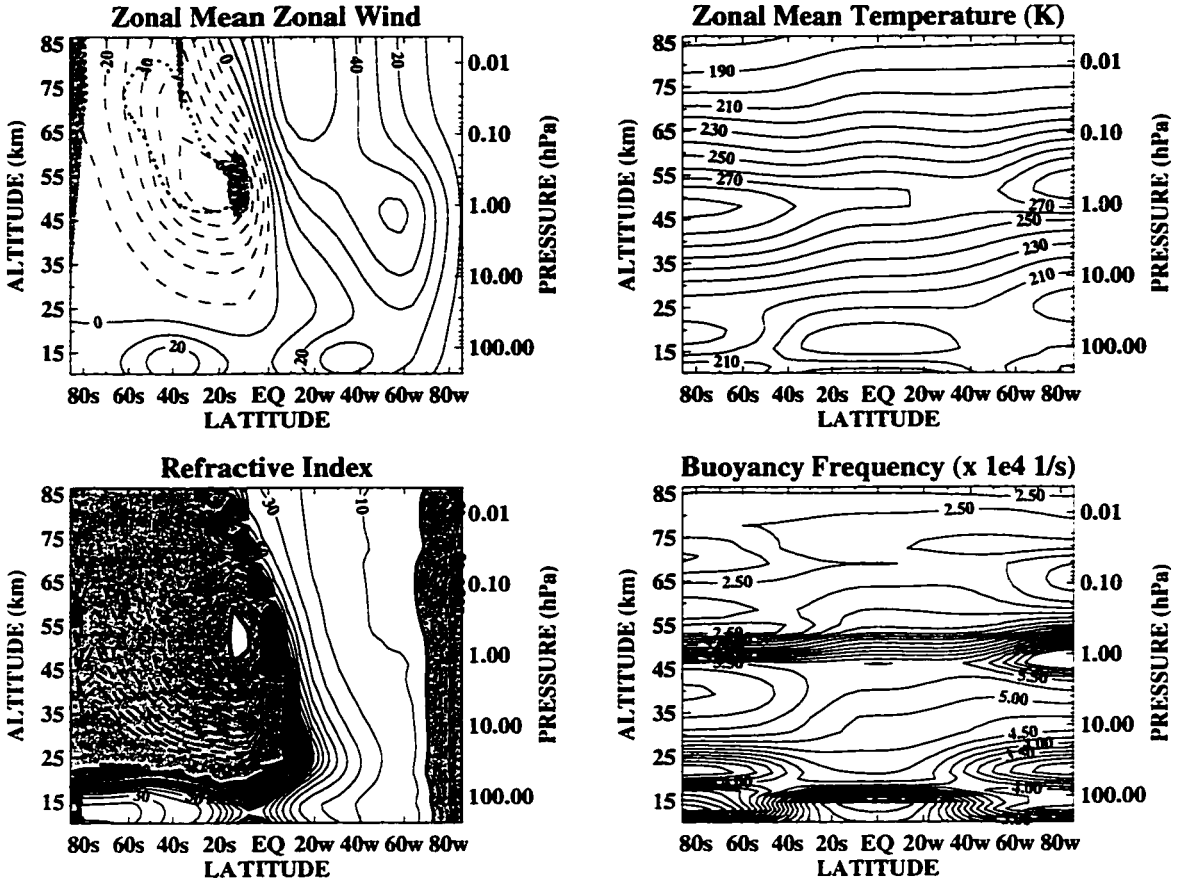

Figure 6.32: Prescribed zonally symmetric initial condition for the weakened easterly jet case. The letter "s" and "w" designation along the latitude denote summer and winter, respectively. Top left panel: zonal wind field, $\bar{u}_{init}$, is contoured in 10 ms^{-1} increments. Regions where the quasi-geostrophic potential vorticity meridional gradient is less than or equal to zero are shaded. For reference, the critical surface of the (4, 1.8) mode is marked by the dotted bold line. Bottom left panel: the nondimensionalized quasi-geostrophic refractive index (a^2n^2) for stationary zonal wavenumber 1. The light-shaded regions show areas of negative values while dark-shaded regions show areas of values exceeding 100. Top right panel: temperature in increments of 10 K. Bottom right panel: the scaled buoyancy frequency in increments of 0.25 s^{-1}.

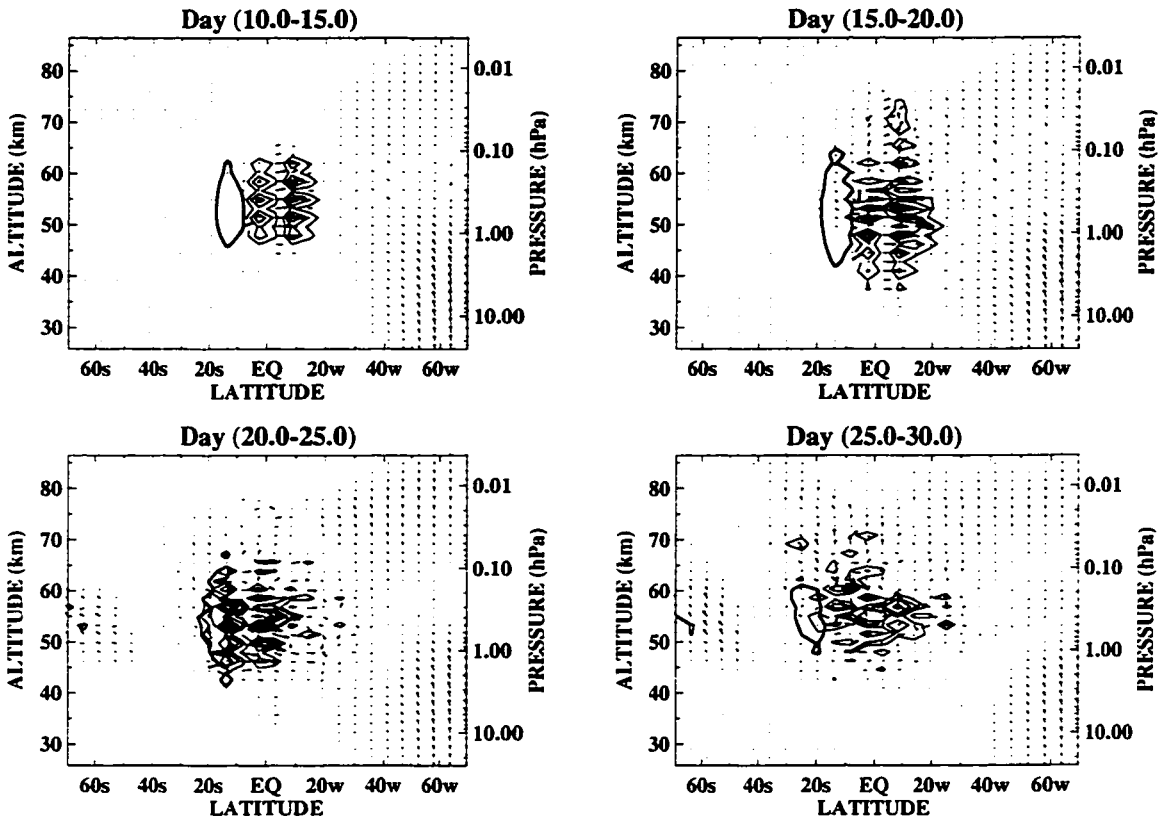

Figure 6.33: Five day time-averaged structure of the Eliassen-Palm flux vector and associated local mean zonal acceleration per unit mass by wave forcing (DF) for the weakened easterly jet case. The maximum vector length of each panel is scaled relative to the top left panel. DF is shown as contours in increments of 1.0 $ms^{-1}day^{-1}$ starting from 1.0 $ms^{-1}day^{-1}$. Blue (red) contours denote positive (negative) DF. The bold lines enclose areas where $\bar{q}_{\varphi} \leq 0$, denoting the regions where the necessary condition for barotropic-baroclinic instability is satisfied.

The spectral analysis finds the disturbances associated with the low summer latitude wave activity to have a dominant zonal wavenumber 4 structure. The latitude-frequency structure of the model temperature field at 1.0 hPa is given in Figure 6.34 for zonal wavenumber 3 and 4. The wavenumber 3 spectral signature is much smaller than the wavenumber 4 signal. The wavenumber 4 temperature disturbance is concentrated primarily near 10° summer latitude although a lower frequency secondary maxima exists at high latitudes. The wavenumber 4 spectral peak is located at westward period of 2.04 days. The wavenumber 3 spectral peak is around 2.22 days.

The amplitude structure computed from band-pass filtering over westward frequency range of 0.3-0.7 cpd bears many resemblances to the control case. Figure 6.35 and Figure 6.36 show the amplitude structure of the (4, 2.04) and (3, 2.22) modes. Both temperature structures show double maxima in low summer latitudes with the (3, 2.22) temperature peaking in the middle mesosphere. Both meridional wind structures are concentrated near 0.5 hPa with the (3, 2.22) amplitude extending well above 0.1 hPa. The phase lines of the meridional wind clearly shows the barotropic nature of these modes between 1.0-0.1 hPa and the slight westward phase tilt with height of the (3, 2.22) mode in the mesosphere. Although not obvious in the phase lines, synoptic maps (not shown) reveal noticeable southeast-northwest tilt where the amplitudes are large. Two main differences from the control case are however obvious. The simulated wavenumber 3 component in this run is considerably weaker than the wavenumber 4. In the control case, the amplitudes are quite comparable. Also, the present two-day wave is slower.

The time-averaged, filtered EP flux vectors for the (3, 2.22) and (4, 2.04) modes are shown in Figure 6.37. A 10-day averaging is performed over the time span when the modes are growing and beginning to reach their peaks. The EP flux vectors suggest that both modes are manifestations of barotropic instability growth. The greatest (4, 2.04) wave activity occurs between 0.10 and 1.0 hPa and is mainly directed horizontally toward the winter hemisphere. The EP flux vectors emanate from the mode critical line where it intersects the region of negative QGPV gradient. The main contributing factor to the

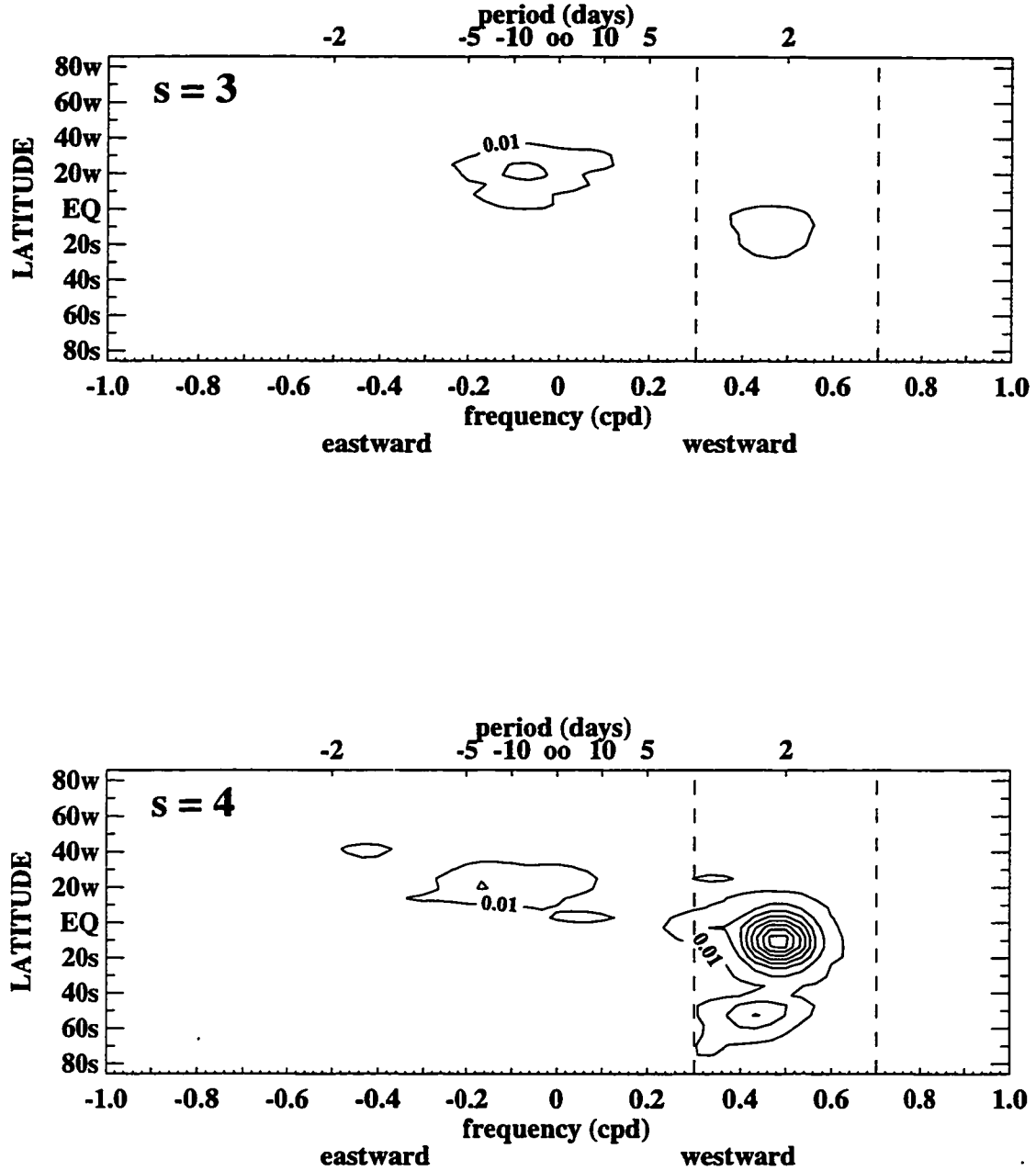

Figure 6.34: The latitude-frequency structure of the temperature zonal wavenumber 3 and 4 spectra at 1.0 hPa for the weakened easterly jet case. The contours are given in increments of 0.05 Kday. The dashed lines define the frequency interval 0.3-0.7 cycles per day (cpd).

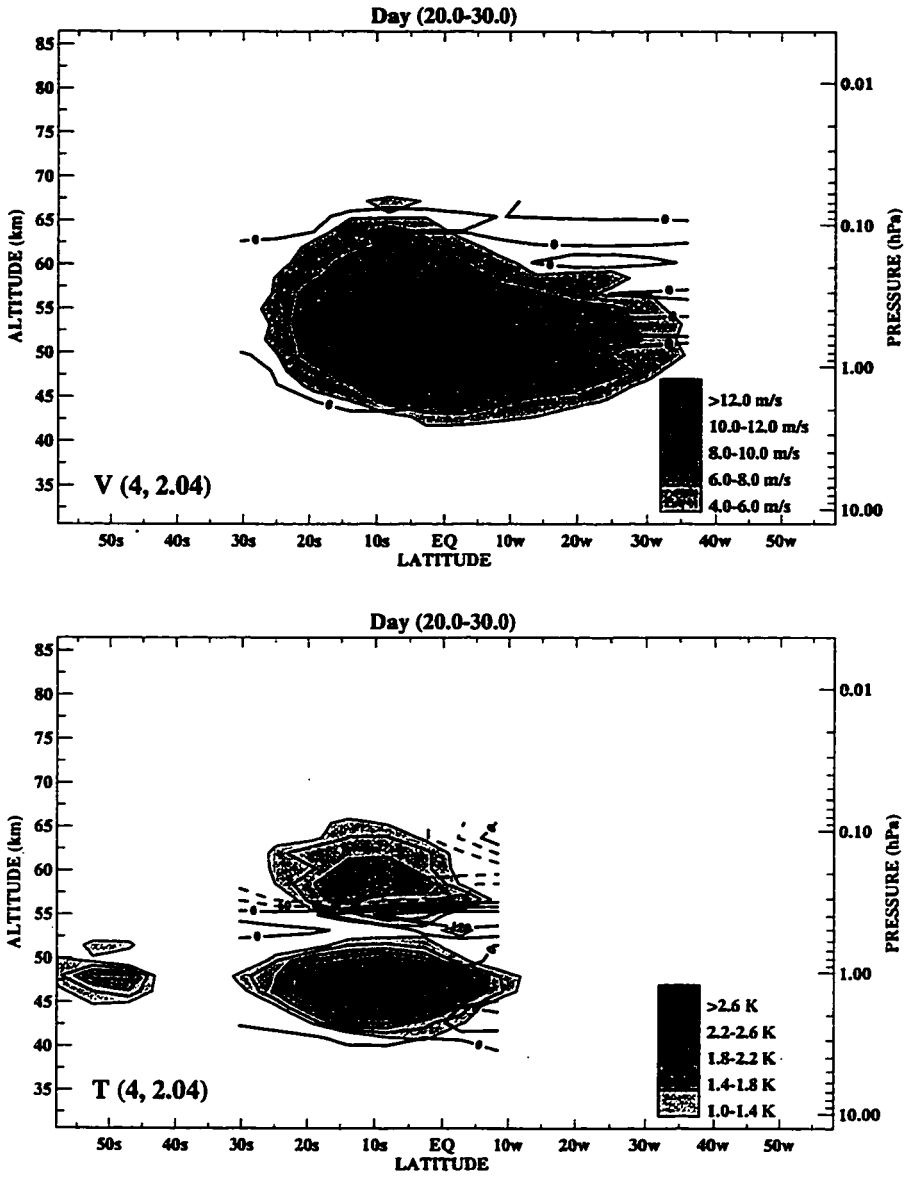

Figure 6.35: The time-averaged meridional structure of the (4, 2.04) amplitude for the weakened easterly jet case. The averaging is done for model days 20-30. The meridional wind (top) is contoured every 2 ms^{-1} and the temperature (bottom) is contoured every 0.2 K. The phase lines are shown as the bold contours in increments of 60°.

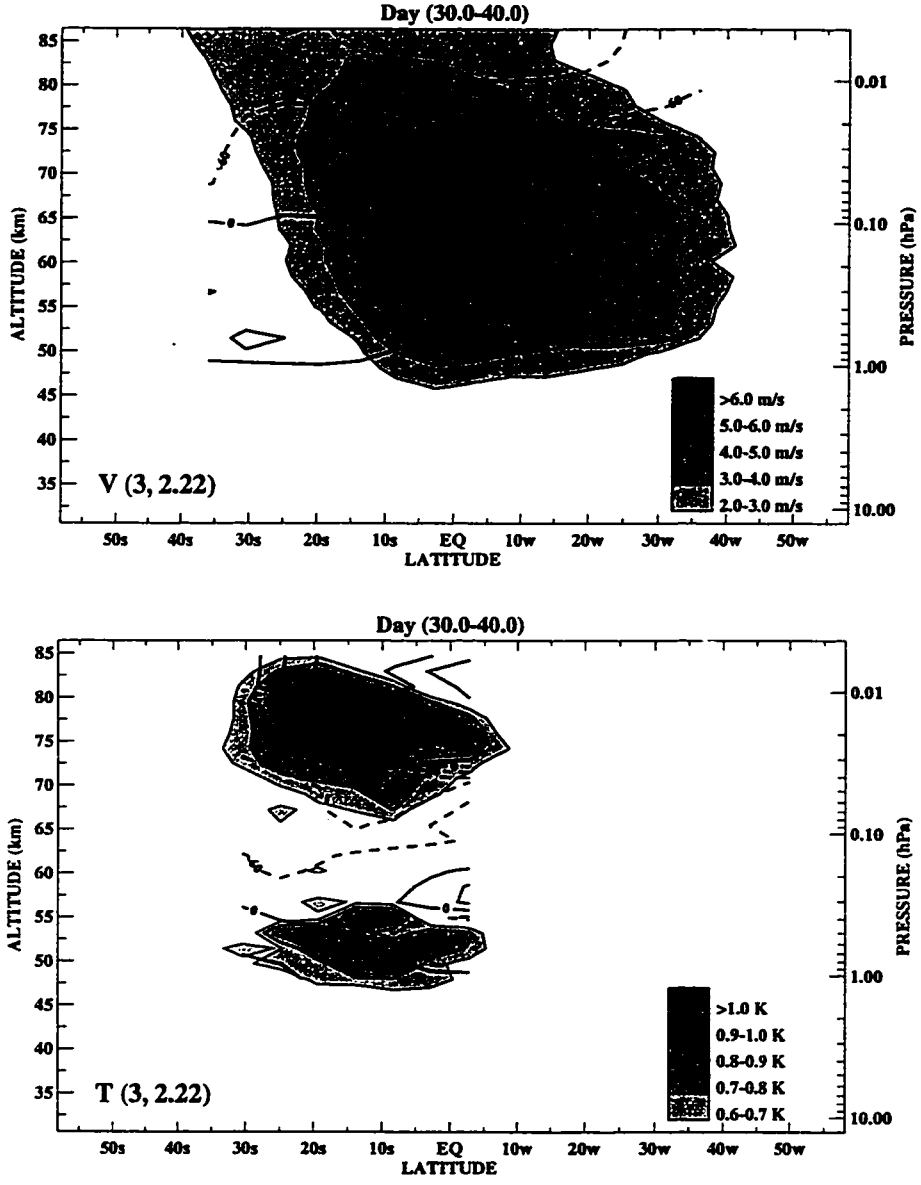

Figure 6.36: The time-averaged meridional structure of the (3, 2.22) amplitude for the weakened easterly jet case. The averaging is done for model days 20-30. The meridional wind (top) is contoured every 2 ms^{-1} and the temperature (bottom) is contoured every 0.2 K. The phase lines are shown as the bold contours in increments of 60°.

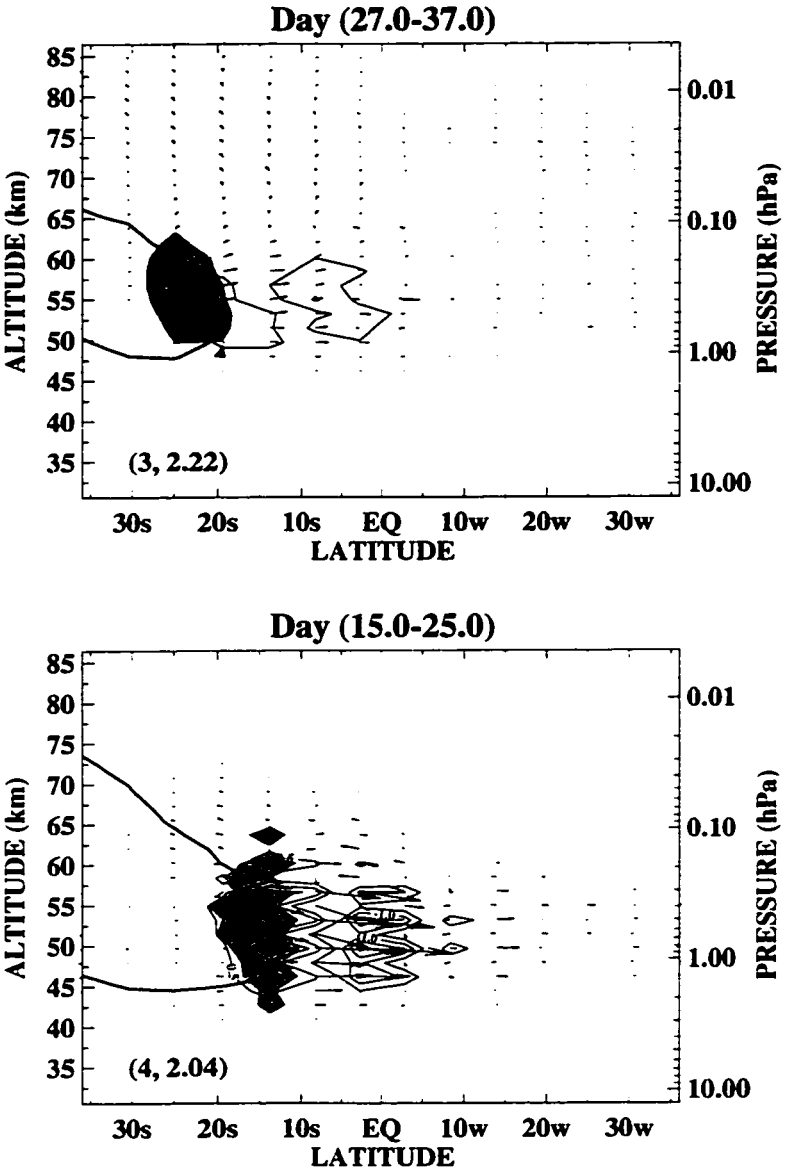

Figure 6.37: The 10-day averaged EP flux vectors diagrams for (3, 2.22) mode, top, and (4, 2.04) mode, bottom for the weakened easterly jet case. The maximum vector length of each panels is relative to the control case. The wave forcing per unit mass (DF) is shown by the line contours in increments of 0.2 $ms^{-1}day^{-1}$ for the top panel and of 0.5 $ms^{-1}day^{-1}$ for the bottom panel. The blue (red) contours denote positive (negative) DF values. The shaded regions shows the averaged area of negative QGPV gradient. The mode critical line is shown in the diagrams as a bold line.

QGPV gradient reversal is the strong meridional wind curvature on the equatorward flank of the easterly jet. The associated wave-mean flow forcing is accelerative around 10° summer latitude and decelerative over the equator. The maximum forcing magnitude is about 1.5 $ms^{-1}day^{-1}$. The growing mode tends to flux westerly momentum into the summer easterly jet core.

The (3, 2.22) activity is considerably weaker as shown in the top panel of Figure 6.37. Nonetheless, the EP vectors appear to emerge from the mode's critical line wave source where it resides in the negative QGPV gradient region. This region is now centered near 20° summer latitude and is also a result of strong meridional wind curvature. The wave energy propagates slightly upward and equatorward in the stratopause region. Poleward and upward migration of the relatively weaker wave activity is evident in the strongly damped region above 0.1 hPa. This latter migration parallels the wave critical line. The associated wave-mean flow forcing magnitude is only about 0.2 $ms^{-1}day^{-1}$ near the stratopause. The tendency of the weakly growing (3, 2.22) mode is to flux westerly momentum deeper into the summer easterly jet.

As with the control run, inertial instability precedes the growth of the wavenumber 4 mode. The same sequence of wave events is again evident and the instability wave growth is predicated on the intersection of the critical line and the negative $\bar{q}_{\varphi}$ region in the equatorward flank of the easterly jet. However, in the boreal summer observations, the MLS two-day wave appears to be related to the instability in the jet core and thus has significant baroclinic contribution (as suggested by Norton and Thuburn, 1996 and 1997). The observed boreal summer instability is seemingly well removed from the effects of momentum redistribution of inertial instability. It remains to be seen whether this is always the case during other boreal summers.

As noted before, one main difference of the weakened easterly jet case results from the control is the slower phase speed of both two-day wave components. This difference ultimately rests on the weaker initial wind field. As momentum redistribution by inertial

instability expands the region of negative QGPV gradient into the low summer latitudes around day 15, the wave 4 grows from the critical line source. In the control case, the easterly wind speed range within the negative QGPV gradient region is 50-70 ms^{-1} over a deep layer around the stratopause (see Figure 6.15 and Figure 6.16). For the weak jet case, this easterly wind speed range is only 40-60 ms^{-1}. To draw energy from the mean wind, the fastest growing mode must be stationary with respect to the background flow in or near the negative QGPV gradient region. That is, a critical line must exist in the domain. The resulting wave phase speed is thus limited by the respective wind speed range of each case. The difference in this range appears to account for the slower wave 4 (longer period) in the present run as opposed to the faster wave 4 in the control case. A similar argument applies to the growth and period of the wave 3 mode in the model.

With the weaker easterly jet, the present run favors the wave 4 two-day wave. Figure 6.38 shows the averaged meridional wind amplitude for the two-day wave. Wave 3 is observed to be considerably weaker in the weakened easterly jet case but nonetheless exhibits some upward-poleward energy propagation into the mesosphere. In this respect, the simulation agrees with the observed MLS boreal two-day wave which is dominated by the wave 4 component. However, the observed wave 4 during the two available boreal summer seasons has significantly higher frequency than the simulated wave. This difference is apparently due to the inability of the defined initial wind to properly emulate the observed boreal summer condition.

6.5 SUMMARY OF THE EXPERIMENTAL RESULTS

The experimental results consistently illustrate triggering of the two-day wave by inertial instability. In the winter subtropical stratopause, the forced winter stationary wave interacts with the inertially unstable regions and organizes inertial instability circulation. Meridional cross-section structure of the simulated circulation resembles the "pancake" structure found in the LIMS and CLAES observations (Hitchman et al, 1987; Hayashi et al, 1998, respectively). The inertial instability circulation fluxes westerly momentum

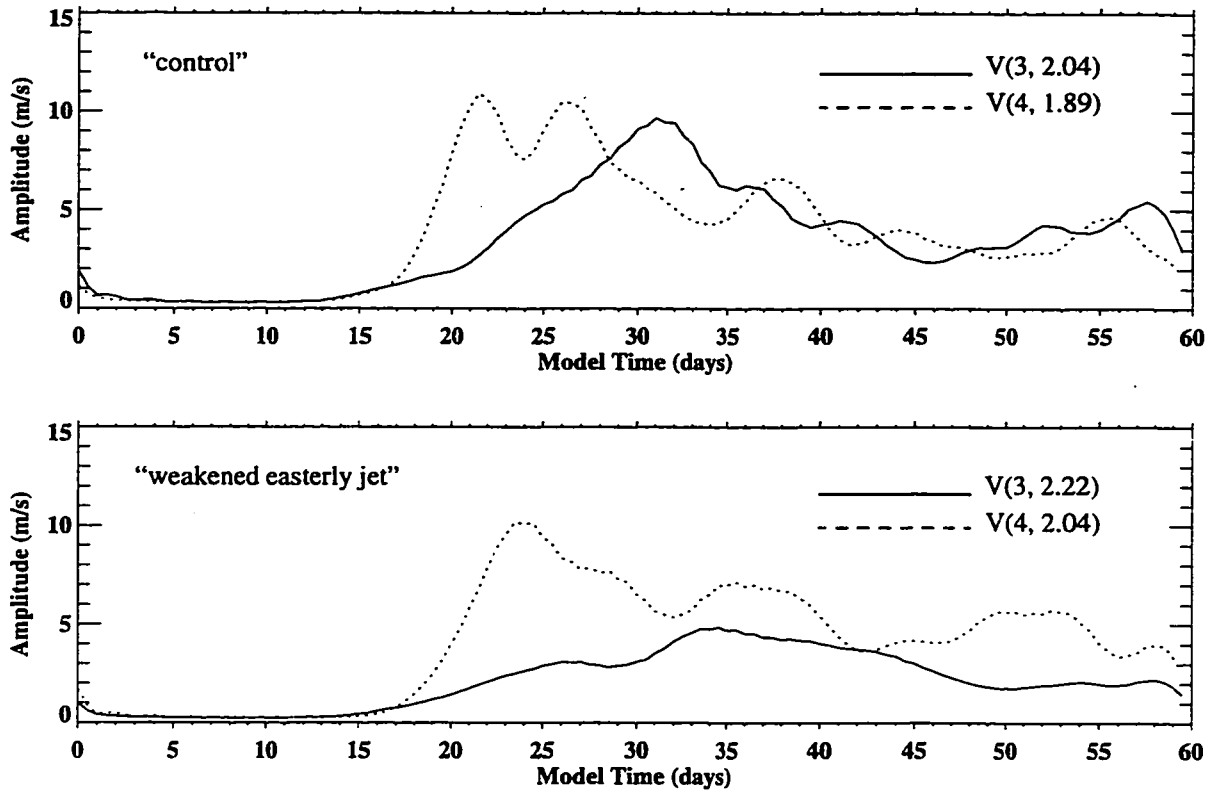

Figure 6.38: Comparison of the meridional wind two-day wave amplitudes for weakened easterly jet case (bottom) and the control case (top). The wave amplitudes are averaged vertically from 5 hPa to 0.1 hPa and latitudinally from 40° summer latitude to 40° winter latitude.

equatorward and, in the process, barotropically destabilizes the easterly jet by increasing the pre-existing horizontal wind curvature in the summer subtropics. Following this event, the wavenumber 4 mode of the two-day wave grows from the barotropically unstable region. As the wavenumber 4 mode saturates, the wavenumber 3 subsequently grows in a similar manner. The critical line in the barotropically unstable region serves as the wave source and is fundamental in the growth of each mode. Overall, the experimental results make plausible the connection between inertial instability and the two-day wave as suggested by the MLS observations in Chapter 4.

In the model results, the lack of observed wavenumber 4 mode in the upper mesosphere is simulated. The wavenumber 4 energy propagation is found to be confined near the stratopause as its upward propagation is greatly attenuated upon encountering strong dissipation in the mesosphere. On the other hand, the simulated wavenumber 3 mode can propagate well into the mesosphere with less attenuation. Decreasing the thermal damping does not alter the wavenumber 4 confinement although more wavenumber 3 energy can propagate upward. The instability growth of the latter mode may excite a normal mode (free oscillation) response in the mesosphere.

Finally, the observed intra-annual asymmetry in the wavenumber 3 mode amplitude is explained by the model. In varying the model forcing and weakening the initial easterly jet, the sensitivity runs suggest that the climatological difference between the northern and southern hemisphere winter Rossby wave activity causes the observed austral summer wavenumber 3 mode to be significantly stronger than its boreal summer counterpart. The easterly jet strength is found to positively correlate with the winter Rossby wave forcing. As the winter forcing increases, equatorward advection of the summer easterly by the induced circulation increases which strengthens the easterly jet in the summer subtropics. Thus, the weaker southern hemisphere Rossby wave activity produces considerably weaker boreal summer easterly jet that can only support the wavenumber 4 mode critical line. The absence of the wavenumber 3 critical line in the barotropically unstable regions greatly suppresses the wave 3 amplitude, observed during the boreal summers.

CHAPTER 7

CONCLUSION

The 3-year UARS MLS data set (Dec. 1991-Sep. 1994) used in this thesis provides considerable insight into the behavior of the two-day wave near the stratopause. The current findings reveal not only the variable nature of the recurrent, post-solstice phenomenon but also clues about its origin. In agreement with the few previous satellite observations, two components of the two-day wave are discovered, corresponding to zonal wavenumbers 3 and 4. The latter component consistently has a slightly higher westward propagating frequency.

Evidence of the two-day wave can be readily seen in twice-daily synoptic maps of the temperature field near the highest observed level. Large scale anomalies are observed to revolve around the summer anticyclonic polar vortex with nearly a two day period. Spectral analyses determine that the wave energy (when strong) consistently peaks at the same zonal wavenumbers and frequencies: zonal wavenumber 3 at 2-day period and zonal wavenumber 4 at 1.8-day period. Intra-annually, the wavenumber 3 component during the austral summer is nearly twice as strong as its boreal summer counterpart. The wavenumber 4 component on the other hand can be equally strong in both summers. In comparing their relative magnitudes, the wavenumber 3 component tends to be larger and of longer duration than wavenumber 4 during the austral summer. The converse is true for the tendency in the boreal summer. An exception occurs during the 1993-94 austral summer when both modes appear equally pronounced and a transition between the modes is readily observed. Observations from the LIMS data for the 1978-79 austral summer by Burks and Leovy (1986) also found both two-day wave components to be equally strong. Overall, the two-day wave components exhibit considerable year-to-year variability. The amplitudes of both modes grow rapidly despite the presence of strong thermal damping near the stratopause region.

Unprecedented evidence of the two-day wave oscillation is seen in the MLS water vapor (H_2O). The strongest signal occurs in the 1991-92 austral summer for the wavenumber 3 component. It is not entirely clear why the H_2O two-day wave signal is not strong at other times, but the strength of the signal is expected to depend on the gradient of the background water vapor distribution (which is strongest in 1991-92 austral summer) as well as on the wave activity. The weak H_2O two-day wave response may also be related to a possible decline in the MLS water vapor data quality. The 183 GHz MLS channel (from which H_2O data is retrieved) ultimately failed in April 1993. Spectral analyses do suggest that the wavenumber 3 mode is dominant during the austral summer and the wavenumber 4 mode is dominant during the boreal summer in agreement with the temperature data. However, the signal of the wavenumber 4 mode is weak even during the boreal summer. The spatial structure of the H_2O wave does not coincide with the temperature wave. For the 1991-92 austral summer, the H_2O amplitude peaks at lower altitude and southward of the temperature wave. Presumably, this behavior reflects differences between the interactions of the two-day wave winds with the passive tracer (H_2O) and the dynamically interactive temperature field. The peak time and frequency of H_2O two-day wave also differ from the temperature two-day wave.

Twice-daily synoptic H_2O maps during the 1991-92 austral summer suggest fluid mixing and strong meridional motion in the summer hemisphere. Tongues of dry low latitude air can be seen to perturb the transport "barrier" region where the tracer distribution shows a strong latitudinal gradient near the summer subtropical regions. In some instances, the meridional folding of the isopleths suggest mixing of dry (low latitude) and moist (high latitude) air. Associated with this apparent mixing is a wavenumber 1 disturbance propagating westward with period between 5-10 days found in conjunction with the wavenumber 3 two-day wave. This wavenumber 1 feature seems to correspond to the wavenumber 1 oscillation identified by Burks and Leovy (1986) in the LIMS temperature. Its origin remains to be further investigated but its presence is suggested in the spectral analysis to be part of non-dispersive wavenumbers 1 and 2 disturbances moving nearly at the same phase speed as the two-day wave. Plumb et al. (1987) suggested that transport by

the two-day wave may be the most effective latitudinal transport process in the summer middle atmosphere. The observed H_2O features support their assertion of strong wave mixing in the region but show that modulation of the wavenumber 3 mode by other waves may also be important.

The observed MLS two-day wave appears to be associated with inflection instability of the easterly jet. The temperature wave variances are consistently found to be surrounded by regions of negative $\bar{q}_\varphi$ and the waves' critical lines exist in close proximity. The wave peak amplitude also coincides with the removal of the unstable region and possible slowing down of the easterly jet. During the 1991-92 and 1992-93 austral summers, the instability appears to be mainly barotropic. The vertically deep, negative regions of $\bar{q}_\varphi$ and intersecting critical lines are located on the equatorward flank of the easterly jet where the horizontal wind curvature is quite large. During the 1993-94 austral summer and each boreal summer, the instability may have a significant baroclinic contribution. In these cases, the negative regions of $\bar{q}_\varphi$ and the intersecting critical lines are located at higher latitude near the center of the easterly jet core where the vertical wind shear can be strong.

The derived easterly wind structure in the boreal summer jet is considerably weaker than the austral summer easterly. The boreal summer easterly jet core is also more poleward. This difference may be related to the climatologically weaker winter planetary wave activity (and associated EP flux divergence) in the southern hemisphere. The mechanistic model experiment in which winter planetary wave forcing is varied shows strong positive dependence of the summer easterly jet strength on the forcing strength. As a result of the weaker easterlies, only the wavenumber 4 two-day wave critical line is supported in the boreal summer mean wind structure. Critical lines of both modes are however present in the austral summer mean wind structure. Hence, while both modes of the two-day wave appear to be instability phenomena in the austral summer, only the wavenumber 4 mode can be attributed to instability in the boreal summer. The reason for the presence of the wavenumber 3 component in the boreal summer is not clear from the instability point of view but may be a consequence of nonlinear wave-wave interaction with the wavenumber

4 mode coupled with the atmosphere's neutral normal mode response to the (3, 2.0) wave.

In general, present discoveries about the wavenumber 3 mode of the two-day wave do not preclude the idea of neutral normal modes. The evanescent nature of a normal mode amplitude is retarded in regions of small Doppler-shifted frequency near the critical line. The normal mode amplitude hence appears amplified near such a region as shown by Salby (1981ab). Indeed, the observed wavenumber 3 mode is found to appear consistently near small Doppler-shifted frequency regions in both summers even when its critical line is absent in the mean wind structure. In that sense, a neutral normal mode behavior is suggested. Also, the mode's meridional structure during the 1991-92 austral summer and generally in the upper mesosphere and lower thermosphere observed by other studies (e.g. Burks and Leovy, 1986; Wu et al., 1993) shows considerable likeness to the third Rossby-gravity mode. Thus, one interpretation is that the wave 3 neutral normal mode in the mesosphere and above is excited and sustained in the face of strong dissipation by instability or, more weakly, by non-linear wave interactions near the stratopause and in the lower mesosphere.

Strong cross-equatorial wind shear is readily seen in the observations. As a result, the mean flow is inertially unstable for much of the time around the solstice. Observational evidence for inertial instability within the time frame of the presented MLS data set is recently reported by Hayashi et al. (1998) using the UARS CLAES temperature data. In the low winter latitude, the observed inertial instability features are slightly preceded by the appearance of a strong winter planetary wave signal encroaching into the region that helps organize the inertial instability. In the 1992-93 austral summer, the horizontal momentum redistribution by inertial instability seems to destabilize the equatorward flank of the summer easterly jet by increasing the horizontal wind curvature. The observed two-day wave (both modes) appears to grow from the flow instability. For this particular case, inertial instability may be creating a mean flow condition favorable for the two-day wave growth as proposed by Orsolini et al. (1997). The derived 1991-92 austral summer mean wind structure and the observed two-day wave likewise suggest the same scenario is at

work. This apparent connection between the two-day wave and inertial instability does not seem to conform with the observed cases of 1993-94 austral summer and the boreal summers. In these cases, the two-day wave appears to grow from instability within the easterly jet core where the negative regions of $\overline{q}_{\varphi}$ have significant baroclinic contributions. This region is well removed from the effects of inertial instability and the zonal flow structure favoring instability is apparently set up instead by gravity wave drag as suggested by Norton and Thuburn (1996, 1997).

The NCAR CCM2 mechanistic model is employed to explore this possible connection between the two-day wave and inertial instability. Indeed, simulation with initial conditions similar to the observed austral summer illustrates the triggering effects of inertial instability for both strong and weak thermal damping scenarios. The model results show that, given a strong horizontal wind shear on the equatorward flank of the easterly jet and across the equator, the amplifying winter planetary wave propagating into low winter latitudes organizes the inertial instability structure. Momentum readjustment associated with the inertial instability circulation then increases the horizontal wind curvature just equatorward of the easterly jet core. As result of the increased curvature, the gradient of potential vorticity is reversed over a deep layer near the stratopause. The wavenumber 4 component of the two-day wave is seen to grow first as result of barotropic instability. As the wave saturates, it fluxes westerly momentum toward the jet core and increases the wind curvature at higher latitude. The reversed gradient of potential vorticity is seen to migrate toward the easterly jet core. The wavenumber 3 component is then observed to grow from barotropic instability.

Diagrams of the filtered EP flux vector dramatically show the emanation of wave activity from the critical line within the region of reversed gradient of potential vorticity. Between 2 hPa and 0.1 hPa, energy of both components of the two-day wave is directed equatorward consistent with the waves' tendency to flux westerly momentum into the jet core. Within this altitude range, the amplitudes of both wave components are comparable. Above 0.1 hPa, only the wavenumber 3 activity show considerable upward and poleward

EP flux along the equatorward flank of the easterly jet. The vertical confinement of the wavenumber 4 component may explain why only the wavenumber 3 two-day wave is reported in the upper mesosphere.

Varying the winter wave forcing does not drastically change the wave propagation pattern, amplitude, or the manner in which it is triggered. However, the two-day wave period is altered because of the mean flow effects of the forcing. Specifically, as the winter forcing is increased, the easterly jet becomes stronger in the model. This is suggested to be the result of stronger meridional advection of zonal momentum by the mean circulation induced by the forcing. As an instability wave, the two-day wave component of higher frequency (lower period) grows from the stronger easterly jet. Nevertheless, the frequency of the wavenumber 4 is always higher than the wavenumber 3. Also, as the forcing increases, the wave is initiated earlier in the model run.

Simulation with initially weaker easterly jet is also performed. The strength of the jet is similar to the observed boreal summer structure. The main model result is the suppression of the wavenumber 3 two-day wave in agreement with the observed tendency during the boreal summers. Given the strong wind shear in the tropics of the initial condition, inertial instability again appears to trigger the two-day wave. However, this model simulation may not emulate reality. In the MLS data, the unstable wave source appears near the jet core and well removed from the destabilizing region of inertial instability. As result, the strong wind speed near the core of the actual jet produces an unstable wavenumber 4 component that has period nearly identical to the austral summer mode (~1.8 days). In the model, the weaker easterly jet wind in the barotropically unstable shear zone, as expected, produces a slower wave period (~2.04 days).

The combined experimental results with weaker initial easterly jet and varied forcing suggest that the diminutive amplitude of the wavenumber 3 two-day wave component observed during the boreal summer is a consequence of the weak winter Rossby wave activity in the southern hemisphere. As the easterly jet strength is found to be positively

correlated with the winter Rossby wave forcing, the weaker southern hemisphere Rossby wave activity would produce considerably slower summer easterly jet that may support only the wavenumber 4 critical line. The absence of the wavenumber 3 critical line in the barotropically unstable regions can greatly suppress its amplitude as noted in the MLS observations during the boreal summers.

In conclusion, the author hopes that, in using both observations and model, the current study provides a better understanding about the two-day wave behavior and its relationship with other atmospheric phenomena near the stratopause. Obviously, further research efforts are necessary to fully understand the two-day wave, especially in the mesosphere and above. At these altitudes, interaction between the two-day wave and atmospheric tides may be relevant. Knowledge of the two-day wave will undoubtedly be important in the refinement of global circulation models (GCMs) as they are continually extended to greater heights. As a recurring phenomenon, the two-day wave provides an ultimate check on the realism of the GCM simulation of the middle atmosphere.

REFERENCES

Andrews, D. G., J. R. Holton, and C. B. Leovy, 1987: *Middle Atmospheric Dynamics*, Academic Press, San Diego, California, 489 pp.

Blackman, R. B., and J. W. Tukey, 1958: *The Measurement of Power Spectra*, Dover Press, 190 pp.

Boville, B. A., 1995: Middle atmosphere version of CCM2 (MACCM2): Annual cycle and interannual variability, *J. Geophys. Res.*, **100**, 9017-9039.

Burks, D., 1986: Observation of traveling planetary-scale waves in the southern summer mesosphere, *Masters Thesis*, University of Washington, Department of Atmospheric Sciences, 57 pp.

Burks, D. and C. B. Leovy, 1986: Planetary waves near the mesospheric easterly jet, *Geophys. Res. Lett.*, **13**, 193-196.

Canziani, P. O., J. R. Holton, E. F. Fishbein, L. Froidevaux, J. W. Waters, 1994: Equatorial Kelvin Waves: a UARS MLS view, *J. Atmos. Sci.*, **51**, 3053-3076.

Chapman, W. A., M. J. Cross, D. A. Flower, G. E. Peckham, and S. D. Smith, 1974: A spectral analysis of global atmospheric temperature fields observed by the selective chopper radiometer on the Nimbus 4 satellite during the year 1970-1, *Proc. R. Soc. London, Ser. A*, **338**, 57-76.

Charney, J. G. and P. G. Drazin, 1961: Propagation of planetary-scale disturbances from the lower into the upper atmosphere, *J. Geophys. Res.*, **66**, 83-109.

Charney, J. G. and M. E. Stern, 1962: On the stability of internal baroclinic jets in a rotating atmosphere, *J. Atmos. Sci.*, **19**, 159-172.

Chen, P. and W. A. Robinson, 1992: Propagation of planetary waves between the troposphere and stratosphere, *J. Atmos. Sci.*, **49**, 2533-2545.

Dickinson, R. E., 1973: Baroclinic instability of an unbounded zonal shear flow in a compressible atmosphere, *J. Atmos. Sci.*, **30**, 1520-1527.

Drazin, P. G. and W. H. Reid, 1981: *Hydrodynamic Stability*, Cambridge University Press, New York, New York, 527 pp.

Dunkerton, T. J., 1981: On the inertial stability of the equatorial middle atmosphere, *J. Atmos. Sci.*, **38**, 2354-2364.

Elson, L. S. and L. Froidevaux, 1993: Use of Fourier transforms for asynoptic mapping: applications to the Upper Atmosphere Research Satellite Microwave Limb Sounder, *J. Geophys. Res.*, **98**, 23,039-23,049.

Fels, S. B., 1982:A parameterization of scale-dependent radiative damping rates in the middle atmosphere, *J. Atmos. Sci.*, **39**, 1141-1152.

Fishbein, E. F., R. E. Cofield, L. Froidevaux, R. F. Jarnot, T. Lungu, W. G. Read, Z. Shippony, J. W. Waters, I. S. McDermid, T. J. McGee, U. Singh, M. Gross, A. Hauchecorne, P. Keckhut, M. E. Gelman, and R. M. Nagatani, 1996: Validation of UARS Microwave Limb Sounder temperature and pressure measurements, *J. Geophys. Res.*, **101**, 9983-10016.

Fritts, D. C., L. Yuan, M. H. Hitchman, L. Coy, E. Kudeki, R. F. Woodman, 1992: Dynamics of the equatorial mesosphere observed using the Jicamarca MST radar during June and August 1987, *J. Atmos. Sci.*, **49**, 2353-2371.

Geisler, J. E. and R. E. Dickinson, 1976: The five-day wave on a sphere with realistic zonal winds, *J. Atmos. Sci.*, **33**, 632-641.

Glass, M., J. L. Fellous, M. Massebeuf, A. Spizzichino, I. A. Lysenko, Yu. I. Portniaghin, 1975: Comparison and interpretation of the results of simultaneous wind measurements in the lower thermosphere at Garchy (France) and Obninsk (U. S. S. R.) by meteor radar technique, *J. Atmos. Terr. Phys.*, **37**, 1077-1087.

Hack, J. J., B. A. Boville, B. P. Briegleb, J. T. Kiehl, P. J. Rasch, and D. L. Williamson, 1993: *Description of the NCAR Community Climate Model (CCM2)*, NCAR Tech. Note, TN-382, National Center for Atmospheric Research, Boulder, Colorado, 108 pp.

Hagan, M. E., J. M. Forbes, and F. Vial, 1993: A numerical investigation of the propagation of the quasi 2-day wave into the lower thermosphere, *J. Geophys. Res.*, **98**, 23193-23205.

Harris, T. J. and R. A. Vincent, 1993: The quasi-two-day wave observed in the equatorial middle atmosphere, *J. Geophys. Res.*, **98**, 10481-10490.

Harris, T. J., 1994: A long-term study of the quasi-two-day wave in the middle atmosphere, *J. Atmos. Terr. Phys.*, **56**, 569-579.

Hayashi, H., M. Shiotani, and J. C. Gille, 1998: Vertically stacked temperature disturbances near the equatorial stratopause as seen in CLAES data, submitted to *J. Geophys. Res.*

Hayashi, Y., 1971: A generalized method of resolving disturbance into progressive and retrogressive waves by space Fourier and time cross-spectral analyses, *J. Meteor. Soc. Japan*, **49**, 125-128.

Hitchman, M. H., 1985: An observational study of wave-mean flow interaction in the equatorial middle atmosphere, *Ph.D. Dissertation*, University of Washington, Department of Atmospheric Sciences, 360 pp.

Hitchman, M. H., C. B. Leovy, J. C. Gille, and P. L. Bailey, 1987: Quasi-stationary zonally asymmetric circulations in the equatorial lower mesosphere, *J. Atmos. Sci.*, **44**, 2219-2236.

Hoskins, B. J., M. E. McIntyre, and A. W. Robertson, 1985: On the use and significance of isentropic potential vorticity maps, *Quart. J. Roy. Meteor. Soc.*, **111**, 877-946.

Hunt, B. G., 1981a: The 2-day wave in the middle atmosphere as simulated in a general circulation model extending from the surface to 100 km, *J. Atmos. Terr. Phys.*, **43**, 1143-1154.

Hunt, B. G., 1981b: The maintenance of the zonal mean state of the upper atmosphere as represented in a three-dimensional general circulation model extending to 100 km, *J. Atmos. Sci.*, **38**, 2172-2186.

Lahoz-W-A., M. R. Suttie, L. Froidevaux, R. S. Harwood, C. L. Lau, T. A. Lungu, G. E. Peckham, H. C. Pumphrey, W. G. Read, Z. Shippony, R. A. Suttie, J. W. Waters, G. E. Nedoluha, S. J. Oltmans, J. M. Russell III, and W. A. Traub, 1996: Validation of UARS Microwave Limb Sounder 183 GHz H_2O measurements, *J. Geophys. Res.*, **101**, 10129-10149.

Lait, L. R. and J. L. Stanford, 1988: Applications of asynoptic space-time Fourier transform methods to scanning satellite measurements, *J. Atmos. Sci.*, **45**, 3784-3799.

Lieberman, R. S., 1991: Nonmigrating tides in the equatorial middle atmosphere, *J. Atmos. Sci.*, **48**, 1112-1123.

Lindzen, R. S. and K. K. Tung, 1978: Wave overreflection and shear instability, *J. Atmos. Sci.*, **35**, 1626-1632.

Lindzen, R. S. and J. W. Barker, 1985: Instability and wave over-reflection in stably strati-

fied shear flow, *J. Fluid Mech.*, **151**, 189-217.

Manney, G. L., T. R. Nathan, and J. L. Stanford, 1988: Barotropic stability of realistic stratospheric jets, *J. Atmos. Sci.*, **45**, 2545-2555.

McLandress, C., G. G. Shepherd, and B. H. Solheim, 1996: Satellite observations of thermospheric tides: Results from the wind imaging interferometer on UARS, *J. Geophys. Res.*, **101**, 4093-4114.

McLandress, C., 1997: Seasonal variability of the diurnal tide: Results from the Canadian middle atmosphere general circulation model, *J. Geophys. Res.*, **102**, 29747-29764.

Muller, H. G. and L. Nelson, 1978: A traveling quasi 2-day wave in the meteor region, *J. Atmos. Terr. Phys.*, **40**, 761-766.

Newman, M., 1991: Model studies of the middle atmosphere of Venus, *Ph.D. Dissertation*, University of Washington, Department of Atmospheric Sciences, 488 pp.

Norton, W. A. and J. Thuburn, 1996: The two-day wave in a middle atmosphere GCM, *Geophys. Res. Lett.*, **23**, 2113-2116, 1996.

Norton, W. A. and J. Thuburn, 1997: The mesosphere in the extended UGAMP GCM, *Gravity Wave Processes and Their Parametrization in Global Climate Models*, vol. 50, K. Hamilton, ed., Springer-Verlag.

Orsolini, Y. J., V. Limpasuvan, and C. B. Leovy, 1997: The tropical stratopause in the UKMO assimilated analyses: Evidence for a 2-day wave and inertial circulations, *Quart. J. Roy. Meteor. Soc.*, **123**, 1707-1724.

O'Sullivan, D. J. and M. H. Hitchman, 1992: Inertial instability and Rossby wave breaking in a numerical model, *J. Atmos. Sci.*, **49**, 991-1002.

Pedlosky, J., 1987: *Geophysical Fluid Dynamics*, Springer-Verlag, New York, New York, 710pp.

Pfister, L., 1985: Baroclinic instability of easterly jets with applications to the Summer Mesosphere, *J. Atmos. Sci.*, **42**, 313-330.

Plumb, R. A., 1983: Baroclinic instability at the Summer Mesosphere: a mechanism for the quasi-two-day wave?, *J. Atmos. Sci.*, **40**, 262-270.

Plumb, R. A., R. A. Vincent, and R. L. Craig, 1987: The quasi-two-day wave event of January 1984 and its impact on the mean mesospheric circulation, *J. Atmos. Sci.*, **44**, 3030-3036.

Randel, W. J., 1993: Global normal-mode Rossby waves observed in stratospheric ozone data, *J. Atmos. Sci.*, **50**, 406-420.

Randel, W. J., 1994: Observations of the 2-day wave in NMC stratospheric analyses, *J. Atmos. Sci.*, **51**, 306-313.

Ray, E. A., 1997: Low frequency variability and mean circulation of the tropical stratosphere from UARS data, *Ph.D. Dissertation*, University of Washington, Department of Atmospheric Sciences, 170 pp.

Rodgers, C. D. and A. J. Prata, 1981: Evidence for a traveling 2-day wave in the middle atmosphere, *J. Geophys. Res.*, **86**, 9661-9664.

Salby, M. L., 1981a: Rossby normal modes in nonuniform background configurations. Part I: simple fields, *J. Atmos. Sci.*, **38**, 1803-1826.

Salby, M. L., 1981b: Rossby normal modes in nonuniform background configurations. Part II: equinox and solstice conditions, *J. Atmos. Sci.*, **38**, 1827-1840.

Salby, M. L., 1981c: The 2-day wave in the middle atmosphere: Observations and theory, *J. Geophys. Res.*, **86**, 9654-9660.

Salby, M. L., 1982a: Sampling theory for asynoptic satellite observations, part I: space-time spectra, resolution, and aliasing, *J. Atmos. Sci.*, **39**, 2577-2600.

Salby, M. L., 1982b: Sampling theory for asynoptic satellite observations, part II: fast Fourier synoptic mapping, *J. Atmos. Sci.*, **39**, 2601-2614.

Sassi, F., R. R. Garcia, B. A. Boville, 1993: The stratopause semiannual oscillation in the NCAR community climate model, *J. Atmos. Sci.*, **50**, 3608-3624.

Swinbank, R. and A. O'Neill, 1994: A stratosphere-troposphere data assimilation system, *Mon. Wea. Rev.*, **122**, 686-702.

Takahashi, M. and B. A. Boville, 1992: A three-dimensional simulation of the equatorial quasi-biennial oscillation, *J. Atmos. Sci.*, **49**, 1020-1035.

Tung, K. K., 1981: Barotropic instability of zonal flows, *J. Atmos. Sci.*, **38**, 308-321.

Vincent, R. A., T. Tsuda, and S. Kato, 1988: A comparative study of mesospheric solar tides observed at Adelaide and Kyoto, *J. Geophys. Res.*, **93**, 699-708.

Walterscheid, R. L. and R. A. Vincent, 1996: Tidal generation of the phase-locked 2-day wave in the southern hemisphere summer by wave-wave interactions, *J. Geophys. Res.*, **101**, 26567-26576.

Wu, D. L., P. B. Hays, W. R. Skinner, A. R. Marshall, M. D. Burrage, R. S. Lieberman, and D.A. Ortland, 1993: Observations of the quasi 2-day wave from the High Resolution Doppler Imager on UARS, *Geophys. Res. Lett.*, **24**, 2853-2856.

Wu, D. L., P. B. Hays, W. R. Skinner, 1995: A least squares method for spectral analysis of space-time series, *J. Atmos. Sci.*, **52**, 3501-3511.

Wu, D. L., E. F. Fishbein, W. G. Read, and J. W. Waters, 1996: Excitation and evolution of the quasi-2-day wave observed in UARS/MLS temperature measurements, *J. Atmos. Sci.*, **53**, 728-738.

APPENDIX

ANALYTICAL INITIAL ZONAL WIND

A.1 "CONTROL" INITIAL WIND

For the "control" experiment, the initial zonal mean zonal wind ($\bar{u}_{init}$) is a sum of the tropospheric wind ($\bar{u}_{trop}$), the stratospheric wind ($\bar{u}_{stra}$), and the mesospheric wind ($\bar{u}_{meso}$). It is prescribed analytically by the expression:

$$\bar{u}_{init} = \bar{u}_{trop} + \bar{u}_{stra} + \bar{u}_{meso}$$

where,

$$\bar{u}_{trop} = 30\frac{m}{s}\left[\operatorname{sech}\left(\frac{\varphi - 30°}{14°}\right) + \operatorname{sech}\left(\frac{\varphi + 40°}{14°}\right)\right]\exp\left[-\left(\frac{z - 13km}{7km}\right)^2\right]$$

$$\bar{u}_{stra} = 55\frac{m}{s}E_{stra}(\varphi)F_{stra}(z) + 45\frac{m}{s}W_{stra}(\varphi)G_{stra}(z)$$

$$\bar{u}_{meso} = 70\frac{m}{s}E_{meso}(\varphi)F_{meso}(z) + 60\frac{m}{s}W_{meso}(\varphi)G_{meso}(z) + 60\frac{m}{s}X_{meso}(\varphi)H_{meso}(z)$$

and,

$$F_{stra}(z) = \exp\left[-\left(\frac{z - 48km}{15km}\right)^2\right] \qquad \text{for } z > 48km$$

$$F_{stra}(z) = \exp\left[-\left(\frac{z - 48km}{25km}\right)^2\right] \qquad \text{for } z \le 48km$$

$$E_{stra}(\varphi) = -\exp\left[-\left(\frac{\varphi + 10°}{15°}\right)^2\right] \qquad \text{for } \varphi \ge -10°$$

$$E_{stra}(\varphi) = -\exp\left[-\left(\frac{\varphi + 10°}{45°}\right)^2\right] \qquad \text{for } \varphi < -10°$$

$$G_{stra}(z) = \exp\left[-\left(\frac{z - 45km}{15km}\right)^2\right] \qquad \text{for } z > 45km$$

$$G_{stra}(z) = \exp\left[-\left(\frac{z - 45km}{30km}\right)^2\right] \qquad \text{for } z \leq 45km$$

$$W_{stra}(\varphi) = \exp\left[-\left(\frac{\varphi - 60°}{30°}\right)^2\right] \qquad \text{for } \varphi \leq 60°$$

$$W_{stra}(\varphi) = \exp\left[-\left(\frac{\varphi - 60°}{20°}\right)^2\right] \qquad \text{for } \varphi > 60°$$

and,

$$F_{meso}(z) = \exp\left[-\left(\frac{z - 75km}{120km}\right)^2\right] \qquad \text{for } z > 75km$$

$$F_{meso}(z) = \exp\left[-\left(\frac{z - 75km}{20km}\right)^2\right] \qquad \text{for } z \leq 75km$$

$$E_{meso}(\varphi) = -\exp\left[-\left(\frac{\varphi + 45°}{15°}\right)^2\right] \qquad \text{for } \varphi \geq -45°$$

$$E_{meso}(\varphi) = -\exp\left[-\left(\frac{\varphi + 45°}{35°}\right)^2\right] \qquad \text{for } \varphi < -45°$$

$$G_{meso}(z) = \exp\left[-\left(\frac{z - 75km}{90km}\right)^2\right] \qquad \text{for } z > 75km$$

$$G_{meso}(z) = \exp\left[-\left(\frac{z - 75km}{30km}\right)^2\right] \qquad \text{for } z \leq 75km$$

$$W_{meso}(\varphi) = \exp\left[-\left(\frac{\varphi - 10°}{35°}\right)^2\right] \qquad \text{for } \varphi \leq 10°$$

$$W_{meso}(\varphi) = \exp\left[-\left(\frac{\varphi - 10°}{45°}\right)^2\right] \qquad \text{for } \varphi > 10°$$

$$X_{meso}(z) = \exp\left[-\left(\frac{z-60km}{25km}\right)^2\right] \qquad \text{for } z > 60km$$

$$X_{meso}(z) = \exp\left[-\left(\frac{z-60km}{15km}\right)^2\right] \qquad \text{for } z \le 60km$$

$$H_{meso}(\varphi) = -\exp\left[-\left(\frac{\varphi+20°}{15°}\right)^2\right] \qquad \text{for } \varphi \ge -20°$$

$$H_{meso}(\varphi) = -\exp\left[-\left(\frac{\varphi+20°}{30°}\right)^2\right] \qquad \text{for } \varphi < -20°$$

where z and φ are log-pressure height and latitude, respectively. Note that the negative latitude corresponds to the summer latitude.

A.2 "WEAKENED EASTERLY JET" INITIAL WIND

For the "weakened easterly jet" experiment, the initial zonal mean zonal wind is prescribed analytically with the same expression as in the control initial wind except now:

$$\bar{u}_{stra} = 25\frac{m}{s}E_{stra}(\varphi)F_{stra}(z) + 45\frac{m}{s}W_{stra}(\varphi)G_{stra}(z)$$

$$\bar{u}_{meso} = 40\frac{m}{s}E_{meso}(\varphi)F_{meso}(z) + 60\frac{m}{s}W_{meso}(\varphi)G_{meso}(z) + 65\frac{m}{s}X_{meso}(\varphi)H_{meso}(z)$$

and,

$$F_{meso}(z) = \exp\left[-\left(\frac{z-75km}{200km}\right)^2\right] \qquad \text{for } z > 75km$$

$$F_{meso}(z) = \exp\left[-\left(\frac{z-75km}{20km}\right)^2\right] \qquad \text{for } z \le 75km$$

$$E_{meso}(\varphi) = -\exp\left[-\left(\frac{\varphi+40°}{15°}\right)^2\right] \qquad \text{for } \varphi \ge -40°$$

$$E_{meso}(\varphi) = -\exp\left[-\left(\frac{\varphi + 40°}{35°}\right)^2\right] \qquad \text{for } \varphi < -40°$$

$$X_{meso}(z) = \exp\left[-\left(\frac{z - 55km}{30km}\right)^2\right] \qquad \text{for } z > 55km$$

$$X_{meso}(z) = \exp\left[-\left(\frac{z - 55km}{15km}\right)^2\right] \qquad \text{for } z \leq 55km$$

$$H_{meso}(\varphi) = -\exp\left[-\left(\frac{\varphi + 15°}{15°}\right)^2\right] \qquad \text{for } \varphi \geq -15°$$

$$H_{meso}(\varphi) = -\exp\left[-\left(\frac{\varphi + 15°}{30°}\right)^2\right] \qquad \text{for } \varphi < -15°$$

Again, the negative latitude corresponds to the summer latitude.

VITA

Varavut Limpasuvan was born on December 4, 1969 in Bangkok, Thailand. His family moved to Los Angeles, California on October 19, 1979. After graduating from Belmont High School in Los Angeles, he attended Occidental College and the California Institute of Technology where he received a B. A. in Physics and a B. S. in Engineering and Applied Sciences, respectively, in June 1992. He met his wife, Lourdes A. Luna, during his Senior year in High School. They were married in Kent, Washington on September 15, 1994. Their son, Ty, was born on March 14, 1997.

IMAGE EVALUATION TEST TARGET (QA-3)

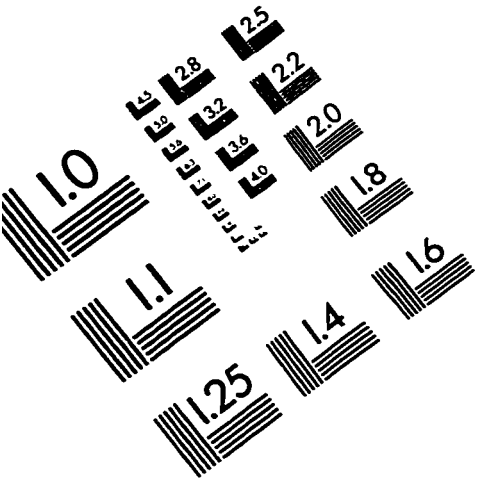

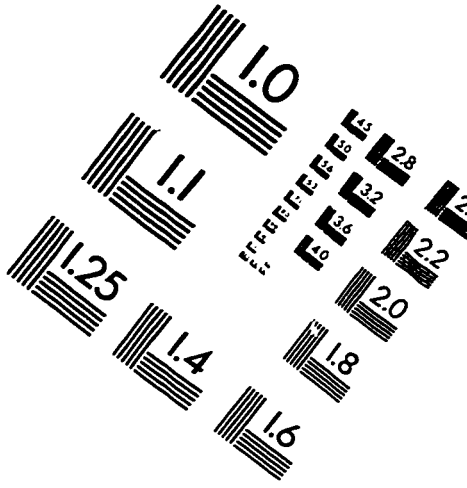

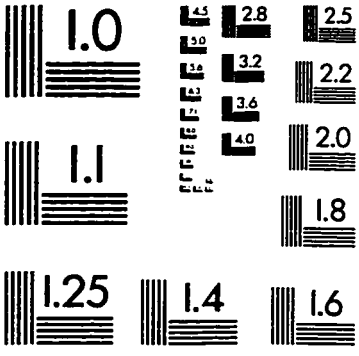

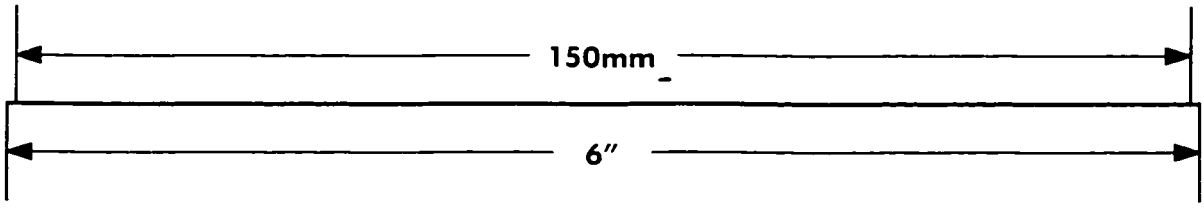

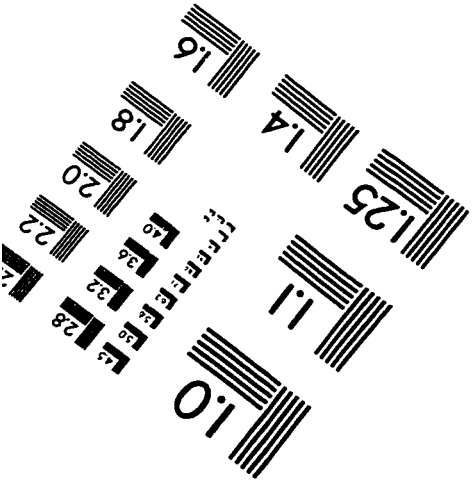

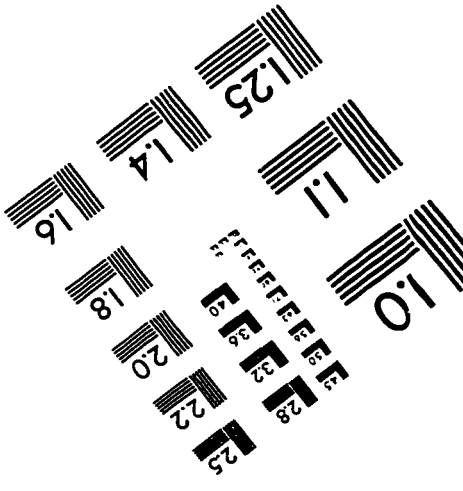

APPLIED IMAGE, Inc
1653 East Main Street
Rochester, NY 14609 USA
Phone: 716/482-0300
Fax: 716/288-5989